The upper troposphere/lower stratosphere in a changing climate – A global model study

Jan Moritz Menken

München 2026

The upper troposphere/lower stratosphere in a changing climate – A global model study

Jan Moritz Menken

Dissertation
an der Fakultät für Physik
der Ludwig–Maximilians–Universität
München

vorgelegt von
Jan Moritz Menken
aus Frankfurt am Main

München, den 06.03.2026

Erstgutachterin: Prof. Dr. Anja Schmidt
Zweitgutachter: Prof. Dr. Thomas Birner
Tag der mündlichen Prüfung: 22.04.2026

Zusammenfassung

Die obere Troposphäre/untere Stratosphäre (UTLS, engl. upper troposphere/lower stratosphere) bezeichnet die Region um die Tropopause. Die Verteilung von Treibhausgasen in der UTLS hat einen großen Einfluss auf das Klima an der Erdoberfläche. Allerdings ist die UTLS durch ein komplexes Zusammenspiel von Transportbarrieren und multiskaligen Prozessen gekennzeichnet, das zu starken Gradienten in der chemischen Zusammensetzung führt. Diese Komplexität stellt sowohl für Beobachtungen als auch für Modellsimulationen eine große Herausforderung dar. Um die Auswirkungen des Klimawandels zu untersuchen, sind numerische Modellsimulationen notwendig, doch selbst bei identischen Emissionen weisen die Modellresultate erhebliche Unterschiede auf. Um die Gründe für die Unterschiede zu beleuchten, werden Simulationen mit dem globalen Klima-Chemie Modell EMAC durchgeführt, in denen jeweils nur ein einziger Aspekt variiert wird. Der Einfluss von vier Modellkonfigurationen auf die simulierte UTLS wird untersucht: (1) die Newtonsche Relaxation der Troposphärendynamik, die einen direkten Vergleich zwischen Modellergebnissen und Beobachtungen begünstigen, (2) die Gitterauflösung, die für die Auflösung starker Gradienten entscheidend ist, (3) die Wahl der Konvektionsparametrisierung, die mit großen Unsicherheiten sowie dem troposphärischen Transport in die UTLS verbunden ist, und (4) der Einfluss der Konvektionsparametrisierung auf die UTLS unter dem Einfluss des Klimawandels.

Neben der Reduzierung der troposphärischen Temperatur- und Wind-Biases im Modell erhöht Newtonsche Relaxation den Wasserdampf-Bias in der unteren Stratosphäre erheblich und verstärkt die stratosphärische Zirkulation, was den simulierten Ozon-Bias weiter erhöht. Diese gegensätzlichen Einflüsse erschweren die Schlussfolgerung über die Fähigkeit der realistischen Simulation der UTLS im freilaufenden Modell.

Eine Erhöhung der horizontalen Auflösung für Klima-Chemie Simulationen über Klimaskalen reduziert die numerische Diffusion erheblich. Die Übereinstimmung der Modellergebnisse mit den Beobachtungen nimmt aufgrund einer niedrigeren Tropopause und einer langsameren stratosphärischen Zirkulation zu.

Die Wahl der Konvektionsparametrisierung hat erhebliche Auswirkungen auf die atmosphärische Dynamik, den konvektiven Transport in der Troposphäre sowie die stratosphärische Zirkulation. Durch den zusätzlichen Einfluss auf die chemischen Umsatzraten beeinflusst die Wahl die simulierte Zusammensetzung der UTLS, insbesondere die Verteilung von Wasserdampf und Ozon. Simulationen zum Ende des 21. Jahrhunderts mit verschiedenen Konvektionsparametrisierungen zeigen eine robuste Anpassung der simulierten UTLS an den Klimawandel. Wesentliche Unterschiede in der Anpassung sind auf die Regeneration von Ozon durch die Reduktion des menschengemachten katalytischen Ozonabbaus in der polaren Stratosphäre zurückzuführen.

Abstract

The upper troposphere/lower stratosphere (UTLS) is the transition region around the tropopause. Due to the significant radiative effect of greenhouse gases (GHGs) in the UTLS on the surface climate, their representation is essential for climate studies. However, the UTLS is characterised by a complex interplay of transport barriers and atmospheric processes operating across a wide range of temporal and spatial scales, leading to steep gradients in abundances of chemical constituents. This complexity poses major challenges for observations and realistic model simulations of the UTLS. Therefore, our knowledge about the UTLS is subject to considerable uncertainty. Numerical model simulations are necessary to investigate the effect of climate change, but even with the same forcing scenario, the model results show a large spread. To identify the causes of this spread, sensitivity simulations with the ECHAM/MESSy Atmospheric Chemistry (EMAC) Chemistry Climate Model (CCM) are performed by varying a single aspect at a time. The influence of four model configurations on the simulated UTLS characteristics are examined: (1) Newtonian relaxation of the tropospheric dynamics, which is favourable for a direct comparison between CCM results and observations, (2) the grid resolution, which is crucial to resolve steep gradients, (3) the choice of the convection parameterisation, which is associated with large model uncertainty and the transport of tropospheric constituents into the UTLS, and (4) the effect of the convection parameterisation on the UTLS under climate change.
Newtonian relaxation reduces temperature and wind biases in the troposphere and the lower stratosphere, but also significantly increases the moist bias in the lower part of the lowermost stratosphere (LMS) and alters the wave forcing. The enhanced stratospheric circulation thereby increases the ozone bias in the LMS. Therefore, the opposing effects complicate the drawing of conclusions about the model performance for the UTLS in a free-running simulation.
Increasing the horizontal resolution for climate-scale CCM simulations substantially reduces biases caused by numerical diffusion in the lower part of the LMS. Especially the lower tropopause and the slower stratospheric circulation improve the model performance relative to observations. An additional finer vertical resolution in EMAC yields only minor improvements in model results.
The choice of the convection parameterisation substantially affects the atmospheric transport, from the convective transport in the troposphere to the stratospheric circulation. In combination with its influence on chemical turnover rates, the choice affects the simulated composition of the UTLS, particularly the distribution of water vapour and ozone. Future projection simulations with different convection parameterisations show a robust response of the simulated UTLS to climate change. Significant differences in the response are due to the regeneration of ozone through decreased anthropogenic catalytic ozone depletion in the polar stratosphere.

Contents

Chapter 1

Introduction

1.1 Motivation

The climate science community has already stated in the First Assessment Report of the Intergovernmental Panel on Climate Change (IPCC) that anthropogenic emissions increase the natural greenhouse effect, which causes a changing climate system and warming of the Earth's surface (Houghton et al., 1990). The following IPCC reports strengthened and quantified the statement with new findings every time, but the core message stayed the same. Even if we were to stop all use of fossil fuels and land-use changes today, our current activities will still affect Earth's climate over the coming centuries (Chen et al., 2021a). But while the troposphere warms due to the emission of carbon dioxide (CO_2) and other greenhouse gases (GHG), the stratosphere cools (Manabe and Wetherald, 1967; Steiner et al., 2020; Gulev et al., 2021). The cooling in the stratosphere arises from the higher emissivity due to higher GHG abundances, in addition to a weaker outgoing longwave radiation due to the absorption by GHGs in the troposphere. In the lower stratosphere, the cooling observed today is dominated by a decrease of ozone (O_3), due to the anthropogenic emission of ozone depleting substances (ODS), most importantly chlorofluorocarbons (CFCs). Stratospheric cooling is one of the most evident signs that rapid climate change is caused by human activities rather than natural variability (Ramaswamy et al., 2001; Ramaswamy and Schwarzkopf, 2002; Shine et al., 2003; Pierrehumbert, 2010; Santer et al., 2023). Opposite temperature trends imply changes in both the vertical and horizontal temperature gradients between the tropical upper troposphere and the subtropical lower stratosphere, which in turn alter several atmospheric processes. Over the last decades, an upward trend in the tropopause has been observed (Seidel and Randel, 2006; Xian and Homeyer, 2019; Meng et al., 2021). A widening of the tropics, as projected by model studies, will be observed in the foreseeable future, if we further emit GHGs (Seidel et al., 2007; Staten et al., 2018) and global climate model simulations and reanalysis datasets indicate a strengthening of the Brewer-Dobson Circulation (Butchart, 2014; Garny et al., 2024). These changes affect the characteristics and mass exchange, and therefore the chemical composition, of the transition region between the troposphere and the stratosphere, the upper troposphere/lower stratosphere (UTLS).

The UTLS exhibits characteristics of both the troposphere and the stratosphere, which display strong gradients in many atmospheric species driven by their source regions, atmospheric lifetimes, and the role of the tropopause as a transport barrier. At the tropopause, the temperature decrease with altitude in the troposphere switches to a temperature increase in the stratosphere, changing from a less stable to a more stable stratification. Already small changes in the UTLS abundance of GHGs such as water vapour (H_2O), O_3 and methane (CH_4) have a significant climate impact (Forster and Shine, 1997; Forster and Shine, 2002; Soden et al., 2008; Solomon et al., 2010; Riese et al., 2012). Therefore, a high confidence about the composition of the UTLS is required for reliable climate change projections.

To quantify the UTLS composition and its changes associated with climate change, it is essential to have robust observations and consistent model simulations of the current state. However, global measurements and simulations of the UTLS are challenging. The UTLS is affect by processes on a wide range of temporal and spatial scales, from turbulence (Holton et al., 1995; Chau et al., 2025) and the interaction of clouds and aerosols with radiation, over the impact of warm conveyor belts (Spichtinger et al., 2005), the fast transport by deep convection and intrusion events by tropopause breaking events (Pan et al., 2004; Pan et al., 2009; Homeyer et al., 2014) to the large scale dynamical transport by the BDC. Many processes vary globally, with substantial large-scale differences between the tropics and the extratropics (Fueglistaler et al., 2009; Gettelman et al., 2011). Large-scale events or processes such as the Asian Summer Monsoon Anticyclone and the deep branch of the BDC further introduce inter-hemispheric and seasonal differences in the UTLS dynamics and composition (Rosenlof et al., 1997; Butchart, 2014; Vogel et al., 2016; Rolf et al., 2018). Global transport processes such as the BDC further reveal hemispheric asymmetries in the response to climate change (Plöger and Garny, 2022). The wide range of scales presents challenges for both observations and model simulations.

The UTLS is usually observed by measurements carried on three platforms: aircraft, balloon and satellite. Each platform has its benefits and drawbacks. Aircraft-borne instruments on passenger aircraft provide regular observations over a larger extent of the globe, spanning several decades, enabling the creation of climatologies of atmospheric trace gas species (Zahn et al., 2014; Cohen et al., 2018; Cohen et al., 2025; Konjari et al., 2025). They provide data with high horizontal and temporal resolution. However, the observations are restricted to the defined flight corridors, which are primarily located in the Northern Hemisphere (NH) and the upper troposphere (UT), and have hardly any vertical extent. Balloon-borne instruments provide vertically high-resolved observations spanning from the ground far into the stratosphere, making them very well suited to provide profiles and gradients in the UTLS (Degen et al., 2025). However, regular balloon starts are rare and very localised, and an individual flight does not provide horizontal coverage beyond the uncontrolled drift caused by the wind. Finally, satellite-borne instruments can provide global observations (sun-synchronous) or high-frequency observations of a specific section of the Earth (geostationary). Climatologies and longer time series can be created by combining observations from multiple satellites (Tummon et al., 2015; Davis et al., 2016). The global coverage comes at the cost of a coarser resolution in both time and space compared to the other two platforms. Furthermore, the data products mostly end in the UTLS, at the cloud top height, the tropopause or even higher in case of the merged data products, and exhibit the largest uncertainty in the UTLS for H_2O and O_3 (Hegglin et al., 2013; Tegtmeier et al., 2013; Hassler et al., 2014; Tummon et al., 2015). Despite these limitations, the observations have revealed significant discrepancies and biases between atmospheric models in the UTLS (Benito-Barca et al., 2025).

Free-running Chemistry Climate Models (CCMs) are capable of simulating the UTLS structure and trends qualitatively well, but exhibit biases relative to observations as well as a large spread between model results (Hegglin et al., 2010; Gettelman et al., 2010). What CCMs share is a tropopause that is too high compared to reanalyses (Abalos et al., 2026). Comparing the simulated UTLS composition with climatologies based on observations by aircraft-borne instruments shows an underestimation of tropospheric transport into the UT and an overestimation of the stratosphere-troposphere exchange (Cohen et al., 2025). Many models show temperature biases in the UTLS and at the cold point leading to biases of H_2O vapour in the stratosphere, with a too dry stratosphere in Coupled Model Intercomparison Project (CMIP) Phase 6 models, independent of the consideration of CH_4 oxidation (Keeble et al., 2021). In contrast, the lowest levels of the lowermost stratosphere (LMS) are too moist in the models due to overly diffusive transport schemes, which counteract the H_2O biases and affect both the radiative budget and the large-scale circulation (Stenke et al., 2007; Charlesworth et al., 2023). For O_3 in the UTLS, the significant uncertainties are reflected in the positive as well as negative trends in the lower stratosphere (LS) simulated over the last decades with state-of-the-art CCMs, while observations indicate a decline (Ball et al., 2018; Ball et al., 2019; Benito-Barca et al., 2025). Any temperature or H_2O bias is further affecting the O_3 abundance as well, for instance, due to the formation of Polar Stratospheric Clouds (PSCs).

To compare the composition simulated by a CCM with a specific observation in space and time, the meteorological conditions must be comparable, which cannot be achieved inherently by the model due to the omnipresent mismatch of initial conditions. A methodology for matching the meteorological fields between the model and the observed state is Newtonian relaxation, also known as nudging. It adds an ad hoc forcing term toward a reference state for all or a subset of the model's prognostic variables. The reference state is often taken from reanalysis datasets. Reanalysis datasets combine the global results of a high-resolution Numerical Weather Prediction (NWP) model with observations to form a consistent time series. They are presumably the closest estimate to the real atmospheric state. However, discrepancies exist between different reanalyses. Comparisons between reanalyses revealed differences between tropopause and subtropical jet (STJ) characteristics, as well as between the strength of the Brewer-Dobson Circulation (BDC), with significant implications for atmospheric transport (Abalos et al., 2015; Manney and Hegglin, 2017; Manney et al., 2017). The comparison of reanalyses to observations exhibits temperature biases at the cold point and the tropopause as well as H_2O biases in the lowermost stratosphere (Tegtmeier et al., 2020; Krüger et al., 2022). By using the reanalysis as reference datasets for nudging, the biases of meteorological variables are then introduced into the climate model. A former model intercomparison of nudged models revealed a larger spread in atmospheric circulation and composition than in their corresponding free-running simulations (Orbe et al., 2018; Orbe et al., 2020). The most extensive spread in atmospheric transport is found in the troposphere, particularly linked to convective transport (Orbe et al., 2017). Chrysanthou et al. (2019) found that nudging over the stratosphere affects large-scale transport and tropical upwelling, presumably by decoupling the residual circulation from its wave forcing. This leads to differences in atmospheric circulation between the nudged simulation and the reference reanalysis, as well as to a larger spread in circulation strength in nudged simulations than in free-running simulations. The errors introduced by nudging into transport processes accumulate at the destination (Davis et al., 2022). Therefore, the largest errors for the residual circulation as well as fast convective transport occur in the UTLS, affecting the local composition. The UTLS composition is therefore strongly affected by nudging. However, a detailed analysis of the effect of nudging on the climatological state of the UTLS composition has not yet been performed.

The uncertainties and discrepancies associated with the UTLS are also present in future projections. What adds to the uncertainty is our lack of confidence in the dynamical response to climate change, for instance, in the response of the large-scale circulation and its interactions with convection and clouds (Shepherd, 2014; Bony et al., 2015). The models differ more strongly in the projected temperature change in the 21st century in the UTLS than in the rest of the lower atmosphere (Lee et al., 2021). Stratospheric H_2O is expected to increase primarily in the LMS (Banerjee et al., 2019), causing the major part of the global mean radiative feedback. Ozone trends in the UTLS are projected to be the strongest in the entire atmosphere (Iglesias-Suarez et al., 2016), but with a smaller model spread than under present-day conditions (Friedel et al., 2023; Polvani et al., 2023). Furthermore, O_3 and the strength of the BDC exhibit large sensitivity to the projected GHG and ODS abundances, leading to a large spread across different climate change scenarios (Banerjee et al., 2018; Morgenstern et al., 2018; Polvani et al., 2019).

One fundamental issue that all models have is their discrete grid. With a finer grid, the resolution increases, and we expect convergence towards the real solution: more accurate distributions, gradients, and processes can be resolved and calculated. While it is nowadays technically possible to run a General Circulation Model (GCM) for more than a month at resolutions that allow the explicit calculation of convection (Hohenegger et al., 2020), this is not feasible for climate simulations, even more so for CCMs. Given the common horizontal grid resolution of a few hundred kilometres in climate simulations, many essential atmospheric processes occur on subgrid scales. The effect of each process on the large scales is estimated using parameterisations, simplified descriptions based on approximations, rather than calculating the actual process (Randall et al., 2003). And each climate model is a unique combination of different model descriptions and process parameterisations (see Figure 1.1 for a schematic overview), leading to the spread in model results, from local species distributions to the global climate feedback due to climate change (Dietmüller et al., 2014; Nowack et al., 2014; Marsh et al., 2016). The climate feedback spread has even increased between the last two Coupled Model Intercomparison Project (CMIP) phases, CMIP5 and CMIP6 (Tebaldi et al., 2021). Due to the very different model descriptions, no conclusions can be drawn about the contribution of single process parameterisations to the overall spread in model results. And since the UTLS is affected by many small-scale processes as well as large-scale dynamics with horizontal and vertical gradients, the errors from parameterisations accumulate in this region.

Parameterised convection significantly contributes to model discrepancies in the troposphere and the UTLS. It is responsible for fast vertical transport, enabling species with a short atmospheric lifetime emitted at or near the surface to reach the UTLS. Direct convective transport mostly ends in the upper troposphere. Still, convection has a non-negligible effect on the stratospheric H_2O abundance by the interaction of cirrus clouds in the tropical UT with transported air parcels (Schoeberl et al., 2018; Jensen et al., 2020; Dauhut and Hohenegger, 2022; Ueyama et al., 2023). The formation of clouds is further essential for the radiative balance of the atmosphere. But convective updrafts occur on scales of 1–100 m, and cloud microphysics are even smaller. Therefore, its effects must be heavily parameterised in climate models, introducing significant uncertainty into the simulations. For instance, the effect of convective mixing in the tropical lower and middle troposphere, and how it is parameterised, accounts for half of the variance in climate sensitivity (Sherwood et al., 2014). Only a limited number of studies have yet investigated the robustness of the model results to the convection parameterisation.

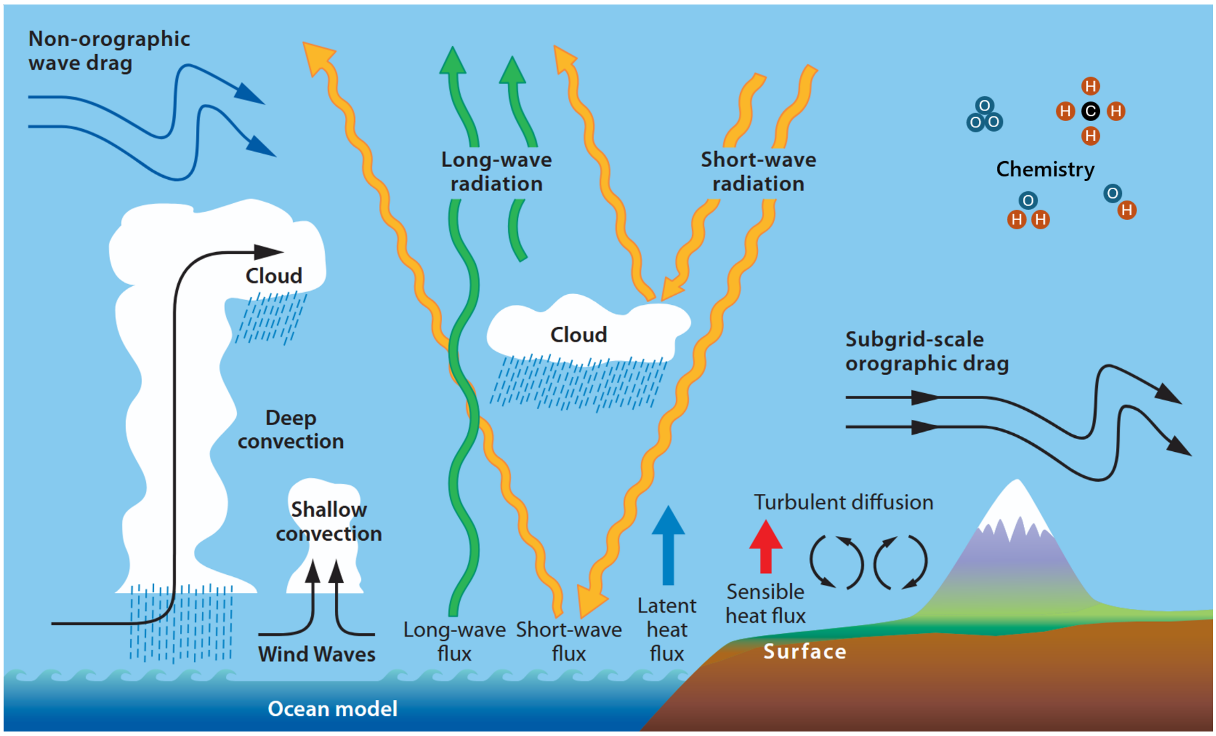

Figure 1.1: Schematic diagram of the different physical processes represented in the IFS model, providing an overview of processes which differ between different models, next to the dynamical core. Adapted from Figure 1.1 of IFS Documentation CY49R1 Part IV: Physical Processes, © European Centre for Medium-Range Weather Forecasts (ECMWF, 2024), licensed under CC BY 4.0.

They found the most substantial differences in H_2O in the UTLS under both present-day and future climate conditions (Tost et al., 2006b; Rybka and Tost, 2014). The studies focused on the troposphere, without fully resolving the stratosphere or atmospheric chemistry. If atmospheric chemistry is included in studies of the impact of the convection parameterisation, large relative differences are found for species with short atmospheric lifetimes (Tost et al., 2010), indicating significant differences in convective vertical transport. Tost et al. (2010) compared results from four months of flight campaigns, focusing on the troposphere. The simulations were nudged, and any feedback from the atmospheric chemistry was turned off. Therefore, it remains an open question how robust the UTLS composition is to the convection parameterisation when using a CCM, and how the convection parameterisation alone affects the model spread in future projections.

The most apparent improvement for accurately modelling the UTLS would be a higher vertical resolution to better represent the steep gradients and transport barriers (Wang et al., 2018). However, increases in vertical resolution directly increase the computational resources required to perform the simulation. It further requires a matching horizontal resolution to represent processes in space reasonably. This leads to an increase in time resolution to achieve a stable simulation and to a multi-fold increase in computing resources. This explains the relatively small increase in resolution over recent decades in climate-scale studies, especially in CCMs. With the improvements in computational resources (`https://www.top500.org/lists/top500/2025/11/`, `https://scied.ucar.edu/learning-zone/how-climate-works`

`/fast-computers-complex-climate-models`; last accessed: 01.03.2026) and the better parallelisation of recent models (Giorgetta et al., 2018; Crueger et al., 2018), an increase in the resolution over climate scales will become feasible. The extent to which the representation of the global UTLS will benefit is yet to be thoroughly investigated.

1.2 Research questions and outline

This work investigates the uncertainty of the simulated UTLS at climate scales for certain aspects of the climate model configuration. While future projections gain confidence through model intercomparison, I go one step further by isolating the impact of a single process parameterisation and quantifying the spread in simulated composition arising from uncertainty in its realisation. Concerning the UTLS representation, the presumably most considerable uncertainty in climate modelling arises from the convection parameterisation. Secondly, a significant improvement in modelling of the UTLS is expected from a finer resolution. CCMs have to rely on relatively coarse resolutions due to the high computational demands. Still, with modern High Performance Computing (HPC) systems, it is feasible to increase resolution in climate-scale simulations. I will investigate the dynamical effect of a feasible increase of model grid resolution for the UTLS. And finally, I compare the effect of nudging on the UTLS composition on the climatological scale. The effect of the accumulated transport errors in the UTLS due to nudging needs to be quantified to be considered in comparisons with observations. The gaps in our understanding pointed out here result in the following research questions:

1. How does Newtonian relaxation affect the simulated UTLS composition on climate scales? How do nudged and free-running simulations perform compared to observations?
2. What will be the benefit for the UTLS characteristics of a computationally feasible increase of the model grid resolution in EMAC?
3. How does the choice of the convection parameterisation affect the simulation of UTLS characteristics and composition?
4. In what ways are the projected UTLS responses on climate change dependent on the choice of the convection parameterisation?

The thesis is structured as follows: Chapter 2 introduces the UTLS and the relevant transport and chemistry processes affecting the UTLS composition on global climate scales. Chapter 3 introduces the CCM used throughout this thesis and its modular structure, which enables the sensitivity studies regarding the convection parameterisation. More detailed information is provided for the model setup aspects that are actively varied in the sensitivity studies. A significant effort was necessary to set up the simulations that represent the climate states for the beginning and the end of the 21st century consistently and to isolate the effects of the model configuration aspect. The utilised tuning process is introduced. Further observations and reanalysis datasets used for comparison are mentioned. The end of a chapter outlines the simulation strategy and highlights the differences between the model setups. In Chapter 4, I investigate the effect of nudging on the UTLS composition. Chapter 5 shows the sensitivity of the simulated UTLS under present-day climate conditions to the convection parameterisation and to the increase in the resolution on climate scales. In Chapter 6, I compare the future climate state with the present-day state for simulations with different convection parameterisations to analyse the dependence of future projections on the choice of convection parameterisation. All results are placed in the context of the literature at the end of each chapter. In Chapter 7, the general limitations of the methodology are discussed. The research questions are answered in Chapter 8, and an outlook for future work is provided.

Chapter 2

Scientific Background

2.1 Properties of troposphere and stratosphere

The troposphere is the lowest layer of the atmosphere, where weather that affects our daily lives takes place. Solar irradiation heats the surface, and with altitude the temperature decreases, leading to omnipresent turbulence and mixing, resulting in a relatively homogeneous distribution of trace gas species (tracers) (Seinfeld and Pandis, 2016). As the layer of the atmosphere in contact with the surface, the chemical composition is strongly influenced by both natural and anthropogenic emissions. Tracers with lifetimes of hours to days can reach the middle and upper troposphere through fast transport via convection, the vertical motion associated with density differences driven by thermal expansion (Tost et al., 2010). Convection further initiates cloud formation and precipitation, an essential removal process for soluble tracers and particles in the troposphere (Seinfeld and Pandis, 2016). The tropospheric zonal and vertical circulation patterns are characterised by three circulations: the Hadley cell in the tropics, the Ferrel cell in the mid latitudes and the Polar cell in the high latitudes. In the extratropics, the circulation is mainly driven by baroclinic waves (Gettelman et al., 2011). Turbulence induced by wave propagation into the upper troposphere initiates mixing between atmospheric layers. The Hadley cell in the tropics is thermally driven by diabatic heating from strong convection (ascending flow) at the latitude of the strongest solar irradiation around the equator, and by radiative cooling in the subtropics (descending flow). The ascent further includes an eddy-driven component due to Rossby wave breaking in the STJ region, leading to additional pumping in the tropics from above (Shepherd, 2007; Staten et al., 2018). The strong ascent of the Hadley cell leads to transport into the tropical upper troposphere and from there into the atmospheric layer above.

The layer above the troposphere is the stratosphere. The stratosphere is characterised by stable stratification, with increasing temperature with altitude. The temperature increase with altitude results from the absorption of solar ultraviolet (UV) radiation by O_3 (Seinfeld and Pandis, 2016). As altitude increases, so does the amount of high-energy irradiation, thereby enabling the photolysis of otherwise relatively stable molecules. The stratosphere extends to approximately 1 hPa, corresponding to an altitude of roughly 50 km, where the lapse rate becomes negative at the mesopause. The stratosphere would be in radiative equilibrium, and tracer abundances would be highest where they are produced without the transport by the Brewer-Dobson Circulation. The BDC is explained in more detail in the following sections.

2.2 The tropopause

The tropopause is the conceptual boundary between the troposphere and the stratosphere. Due to differences in stratification between the troposphere and the stratosphere, the tropopause acts as a transport barrier, inhibiting direct transport and vertical and horizontal mixing (Haynes and Shuckburgh, 2000; Haynes et al., 2001; Hegglin et al., 2009; Gettelman et al., 2011). Due to the latitudinal dependence of upward longwave radiation and large-scale transport between the troposphere and stratosphere, the tropopause itself exhibits pressure differences between the poles and the tropics (Thuburn and Craig, 2000). The tropopause is located at about 300 hPa (8 km) at the poles and increases to about 100 hPa (17 km) in the tropics. The steepest increase of tropopause altitude occurs in the subtropical regions, which are dynamically dominated by the subtropical jet (STJ). The STJ originates from strong solar irradiation and convective heating in the tropics, which initiates movement in the lower troposphere upward. Following mass conservation and the temperature gradients between low and high latitudes, a poleward transport in the upper troposphere is initiated, which is then redirected eastward by the Coriolis force. Without surface friction, angular momentum is conserved, and the reduced distance to the Earth's axis implies an increase in wind velocity, the STJ (Lee and Kim, 2003; Schneider, 2006). As a direct consequence of the intense heating in the tropics, the STJ is thermally-driven, in contrast to the eddy-driven jet (EDJ) in the mid latitudes (Messori et al., 2021). Another distinction is the vertical wind shear. The STJ occurs only in the upper troposphere with a strong vertical wind shear. In contrast, the EDJ in the mid-latitudes is driven by baroclinicity, which results from non-parallel density and pressure surfaces leading to the conversion of potential energy into kinetic energy. This conversion produces westerly winds in the lower troposphere, and therefore low vertical wind shear at the eddy-driven jet (Davis and Birner, 2016). The baroclinic eddies that lead to the EDJ further affect the tropopause structure in the mid-latitudes (Schneider, 2004). Finally, the tropopause exhibits an annual cycle, reflecting differences in solar irradiance and transport patterns.

While there is a precise semantic definition of the tropopause, the physical definition is ambiguous. Several concepts have been developed over the past few decades, driven by an increase in available information and by research across fields. The first concept was officially introduced by the World Meteorological Organization (WMO) in 1957, purely based on the temperature decrease with altitude, the lapse rate, and a somewhat arbitrary value of 2° C km^{-1} (WMO, 1957). This definition is known as the thermal or lapse rate, or the WMO tropopause. By this definition, more than one tropopause may be found at a given point in time in the vertical column. Double-tropopause events can occur near the STJ and indicate increased horizontal mixing (Pan et al., 2004; Pan et al., 2009). The WMO tropopause definition also considers vertical profiles independently, which may result in a horizontally discontinuous tropopause. A continuous tropopause, apart from the deep tropics around the equator, is defined by the dynamical tropopause. The dynamical tropopause is based on the potential vorticity (PV) field, which is increasing with altitude. This leads to higher PV values in the stratosphere than in the troposphere and the definition of the dynamical tropopause by selecting a suitable PV value. Since the dynamical tropopause provides a global, continuous, quasi-material surface (outside the deep tropics), the definition is especially valuable for the analysis of tropopause folding events (Reed, 1955; Gettelman et al., 2011). On an isentropic surface, PV can be written as

$$PV = \frac{\zeta_\theta + f}{\sigma} \quad , \tag{2.1}$$

written as in Gettelman et al. (2011). ζ_θ is the relative vorticity on isentropic surfaces, f the Coriolis parameter and σ the isentropic density. However, special care has to be taken at the equator, as the Coriolis parameter becomes zero and ζ_θ is not uniquely defined. The PV value is often selected to match the WMO tropopause; however, the most suited value depends on the investigated latitude. The values range between 1.5 and 4 PVU (potential vorticity unit, [PVU] = $10^{-6}\,\mathrm{K\,m^2\,(kg\,s)^{-1}}$) between pole and equator (Holton et al., 1995), with 3.5 PVU for mid-latitudes (Hoerling et al., 1991). At the tropopause, strong PV gradients are found, which are associated with strong vertical gradients in static stability, indicating a significant barrier to isentropic mixing (Haynes and Shuckburgh, 2000). The strong PV gradients are further used to adapt the PV tropopause definition from arbitrarily selected values to the gradient maximum (Kunz et al., 2011; Turhal et al., 2024). A third concept utilises the transport barrier and the chemical distinction between the troposphere and the stratosphere to define the so-called chemical tropopause. The chemical tropopause can either be calculated by the steep gradient of one tracer, for instance O_3 (Bethan et al., 1996), or by a tracer-tracer correlation between one tracer with a high abundance in the troposphere and one with a high abundance in the stratosphere (Zahn and Brenninkmeijer, 2003). The latter has the advantage of recognising transition layers. In contrast, the chemical tropopause, based solely on the gradient of a single tracer, is, on average, 800 m below the WMO tropopause (Gettelman et al., 2011). This highlights the spread in tropopause altitude due to different definitions. In model studies, the chemical tropopause can also be calculated using artificial tracers to eliminate chemical effects (Prather, 2025). Recently, a new definition of the tropopause was proposed, based on the vertical gradient of relative humidity with respect to ice, to account for diabatic processes that are crucial for the tropopause structure in midlatitudes (Reutter and Spichtinger, 2025). In summary, there are numerous definitions for the tropopause. All of them differ in the altitude at which the tropopause occurs, which makes the selection of a tropopause definition an essential decision for air mass studies and the creation of climatologies (Bauchinger et al., 2025).
In the tropics, the tropopause is not associated with a vertical transport barrier. Instead, in the tropics, the main upward transport from the troposphere into the stratosphere occurs, defining the starting point of the stratospheric Brewer-Dobson Circulation.

2.3 The Brewer-Dobson circulation

The BDC describes the global meridional mass circulation through the stratosphere (Butchart, 2014). Tropospheric air enters the stratosphere in the tropics, ascends, moves poleward, then descends in the higher latitudes and back into the troposphere. It was proposed to explain the stratospheric distribution of O_3 and H_2O by Dobson et al. (1929), Brewer (1949) and Dobson (1956), which led to its naming (see Figures 2.1 and 2.2). The BDC is driven by the dissipation of upward propagating atmospheric waves from the troposphere. Synoptic-scale Rossby waves dissipate in the lower stratosphere throughout the year, resulting in a poleward forcing. The poleward motion in the lower stratosphere is called the shallow branch of the BDC (Birner and Bönisch, 2011). Transport by the shallow branch occurs on timescales of days to months. In the middle and upper stratosphere, planetary-scale Rossby wave propagation is dependent on the season. Only in the absence of solar irradiation during the hemispheric winter does the temperature gradient between the cold polar vortex and the equator drive westerly winds, which are required for higher wave propagation (Shepherd, 2007). The dissipation of Rossby waves in the middle and upper stratosphere creates a poleward flow in the winter hemisphere. The polar flow in the middle and upper stratosphere is called the deep branch of the BDC. Transport by the deep branch occurs on timescales of months to years from the tropical lower stratosphere into the LMS of the winter hemisphere. To maintain mass conservation, air must be pumped from the troposphere into the stratosphere in the tropics, and it must move downward from the stratosphere into the troposphere in the extratropics. By the upward pumping in the tropical UT, colder air is transported into the LS, affecting the tropical lapse rate. Similarly, warmer air is transported down from the higher stratosphere into the LS in the extratropics, shifting the lapse rate turning point downward. This leads to a significant contribution of the BDC to the contrast in tropopause pressure between the poles and the tropics, accounting for more than half of the differences in polar and tropical tropopause altitude (Birner, 2010a).

To isolate the effect of transport by the BDC, a standard metric is the residual mean circulation using the Transformed Eulerian-Mean (TEM), which combines the contribution of eddies with the mean transport (Andrews and McIntyre, 1976). TEM reduces the BDC to a zonal mean vertical and polarward motion. Furthermore, the residual mean circulation in this formulation is a good approximation for the diabatic circulation. To also account for the effect of air-parcel mixing, the Age of Air (AoA) approach is used (Hall and Plumb, 1994; Garny et al., 2024). AoA is defined as the transit time of an air parcel between a selected location and a reference location, the latter often chosen to be the tropical tropopause or the surface in the tropics. While each location actually has an AoA spectrum instead of a single value, due to mixing and different transport processes, the mean transit time is often used as a representative value. There are several ways to study the stratospheric circulation using global atmospheric models. However, evaluating the results remains challenging, as estimations of AoA based on observations remain uncertain to this day, due to the sparse amount of global, continuous observations of almost chemically inert trace gases such as CO_2 and SF_6 and the missing of idealised trace gases, e.g. with no chemical reactions and a linear source at the surface (Engel et al., 2008; Engel et al., 2017).
The BDC explains the O_3 and H_2O abundances in the stratosphere in the midlatitudes and polar regions, where weak to no chemical production can take place. And the entire existence of the stratosphere is based on the chemical reaction of O_2 with UV photons. Atmospheric chemistry plays a crucial role in shaping life on Earth and in forming the atmosphere. Furthermore, the production and removal reactions depend heavily on atmospheric composition and solar irradiation, leading to substantial differences between the troposphere and the stratosphere.

2.4 Overview of the relevant atmospheric chemistry

This section follows the information provided by Seinfeld and Pandis (2016), unless otherwise stated. In addition to the exchange of chemical trace gases with the Earth's surface, many constituents are produced and destroyed in the atmosphere by physical processes, such as particle formation, and by chemical processes. Depending on the effectiveness of a constituent's loss processes, its lifetime in the atmosphere can range from seconds to thousands of years. Connected to the atmospheric lifetime is the distance over which the tracer can be transported before

being removed by a process. Highly reactive constituents such as radicals that have at least one unpaired valence electron, for instance hydroxyl radical ($HO\cdot$; in the following abbreviated to OH), react within seconds and are therefore transported only a few centimetres to metres. Tropospheric O_3 has a lifetime of some months and can be transported on mesoscales, ten to hundreds of kilometres, before being removed. Chemically more inert constituents, such as CH_4 and nitrous oxide (N_2O), can remain in the atmosphere for hundreds of years, leading to homogeneous distributions over global scales.
In the following, I will give an overview of the atmospheric chemistry of three GHGs: N_2O, CH_4 and O_3. They vary widely in chemical complexity and atmospheric distribution and serve as the basis for the chemical composition analysis in the sensitivity studies in this work.

2.4.1 Nitrous oxide

N_2O is a GHG with a global warming potential (GWP) over 100 years of 300, i.e. 300 times the radiative forcing of CO_2. Its largest natural sources are the ocean and the tropical soil. The agricultural soil and feedstock are the primary anthropogenic sources, leading to an increasing N_2O abundance in the atmosphere by about 1 ppb_v per year in the 21^{st} century (Lan et al., 2025). The atmospheric abundance increased from 280 ppb_v in 1850 to 325 ppb_v (parts per billion by volume) in around 2010. N_2O is chemically inert in the troposphere. The chemical sinks are in the upper stratosphere by photodissociation (90% of the sink)

$$N_2O + hv \longrightarrow O(^1D) + N_2 \qquad \text{(R 2.1)}$$

and the reaction with excited oxygen ($O(^1D)$) (10% of the sink)

$$N_2O + O(^1D) \longrightarrow 2\,NO \qquad \text{(R 2.2a)}$$

$$N_2O + O(^1D) \longrightarrow N_2 + O_2 \quad . \qquad \text{(R 2.2b)}$$

hv in Reaction R 2.1 represents the energy by radiation, h is Planck's constant, v the frequency of the photon, the ratio between the speed of light c and its wavelength λ.

2.4.2 Methane

CH_4 is the hydrocarbon with the largest atmospheric abundance. It is also a GHG with a warming potential more than 20 times that of CO_2, referring to the GWP over 100 years. Primary natural emission sources include wetlands, termites, and the oceans, with wetlands being the most significant contributor by an order of magnitude. Additionally, CH_4 is emitted by various anthropogenic sources, including fossil fuel energy production, ruminant livestock, and rice agriculture. Anthropogenic emissions have increased tremendously since the Industrial Revolution, leading to a rise in atmospheric abundance from 850 ppb_v before 1850 to more than 1800 ppb_v around 2010 (Seinfeld and Pandis, 2016; Lan et al., 2025). Methane is removed from the atmosphere mainly (90 %) by the reaction with OH,

$$CH_4 + OH \longrightarrow CH_3 + H_2O \quad , \qquad \text{(R 2.3)}$$

producing methyl radical (CH_3) and starting a long oxidation chain. The removal by Reaction R 2.3 is by an order of magnitude larger in the troposphere than in the stratosphere. Nevertheless, methane oxidation plays a crucial role in the stratosphere, as it is the primary chemical source of H_2O in the dry stratosphere. The atmospheric lifetime of CH_4 is 9.1 ± 0.9 years (Prather et al., 2012), resulting in a nearly homogeneous abundance throughout the well-mixed troposphere. Further chemical sinks are

$$CH_4 + O(^1D) \longrightarrow OH + CH_3 \qquad \text{(R 2.4a)}$$
$$CH_4 + Cl \longrightarrow CH_3 + HCl \qquad \text{(R 2.4b)}$$

and direct photolysis in the stratosphere (Saunois et al., 2020).

2.4.3 Ozone

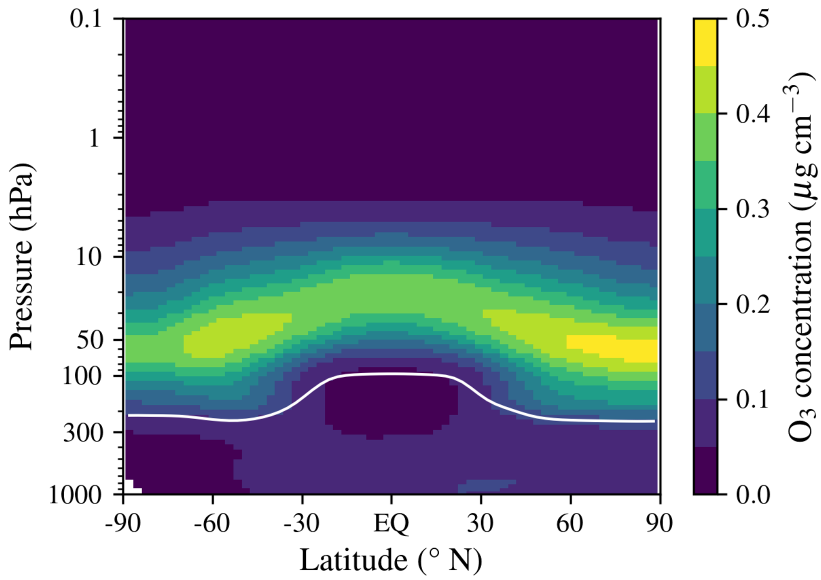

Figure 2.1: Ozone concentration as zonal mean climatology based on the 20 years of the REF_{today} simulation (introduced in Chapter 3). The white line indicates the WMO tropopause.

O_3 is the chemical constituent responsible for the increase in temperature with altitude in the stratosphere and dominates stratospheric chemistry. It is a GHG that protects living beings from harmful incoming UV radiation, UV-B radiation with a wavelength between 240 and 290 nm. The highest atmospheric concentration, exceeding 10^{12} molecules cm^{-3}, occurs at altitudes between 20 and 30 km, known as the ozone layer (Figure 2.1). The primary chemical production of O_3 occurs in the tropics due to the highest UV radiation and is then transported to the higher latitudes (Figure 2.1). Above the ozone layer, O_3 production decreases due to lower air density, leading to fewer production reactions. The importance of the ozone layer for the health of all living beings on Earth led to the signing of the Montreal Protocol on September 16, 1987, to ban the anthropogenic emissions of ODS (Ozone-Secretariat, 2020). Nowadays, the United Nations (UN) ozone treaty is universally ratified, and an observed recovery of the ozone layer has accompanied it. However, due to the long atmospheric lifetime of ODS, for instance, 45 years for CCl_3F (known as CFC-11) and 100 years for CCl_2F_2 (CFC-12), the removal continues over the 21st century (SPARC, 2013; Seinfeld and Pandis, 2016).

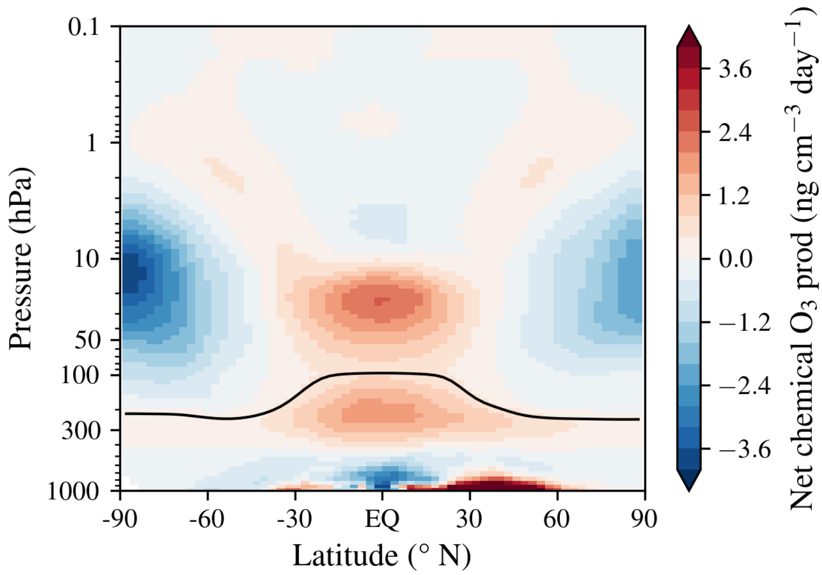

Figure 2.2: Net change in the ozone concentration by atmospheric chemical reactions as zonal mean climatology based on the 20 years of the REF_{today} simulation (introduced in Chapter 3). Positive changes (red colours) indicate net chemical production; negative values (blue colours) net chemical removal. The black line indicates the WMO tropopause.

The O_3 main stratospheric O_3 chemistry is described by the Chapman cycle (Chapman, 1930). In the stratosphere above 30 km oxygen (O_2) is dissociated by UV radiation ($\lambda < 240$ nm)

$$O_2 + h\nu \longrightarrow 2\,O \tag{R 2.5}$$

The atomic oxygen (O) reacts with another O_2 and a third reaction partner M to produce O_3

$$O + O_2 + M \longrightarrow O_3 + M \quad . \tag{R 2.6}$$

M is a necessary collision partner for the energy transfer. M is a substitute for O_2 or nitrogen (N_2), due to their omnipresent abundance. Reaction R 2.6 is the primary production of O_3 in the stratosphere. The O_3 is dissociated by UV radiation

$$O_3 + h\nu \longrightarrow O + O_2 \tag{R 2.7a}$$
$$O_3 + h\nu \longrightarrow O(^1D) + O_2 \tag{R 2.7b}$$

and provides the molecular oxygen again. Reaction R 2.7a requires radiation with wavelengths 400–600 nm, Reaction R 2.7b smaller than 320 nm. Excited oxygen ($O(^1D)$) collides with M very fast, so it resets to the ground state. The O_3 is removed if it reacts with molecular oxygen

$$O + O_3 \longrightarrow 2O_2 \quad . \tag{R 2.8}$$

Reactions R 2.6 and R 2.7a/R 2.7b have a much higher reaction rate than R 2.5 and R 2.8, leading to a continuous reaction between O_3 and O. Therefore, they are often discussed together, referred to as the odd oxygen family (O_x). The ratio between O_3 and O is dominated by O_3. The ratio in O_x as well as the entire Chapman cycle depends strongly on the altitude in the stratosphere. Above the ozone layer, the air density decreases further, which reduces the number of reaction partners, M, necessary for Reaction R 2.6. Below, the amount of UV radiation decreases, which is necessary to initiate the Chapman cycle. While most of the O_3 is produced in the tropical stratosphere due to the strongest irradiation, high abundances are also found in the high latitudes. The reason is that the lifetime of O_3 in the tropical stratosphere is weeks to months, which is sufficient for its transport to higher latitudes.

While the Chapman cycle describes the primary production of O_3, it does not account for the additional ozone-depleting reactions necessary to explain observations. Many of these reactions form catalytic cycles, so no large abundances are required to explain ozone depletion. Important cycles include the NO_x (NO + NO_2), the HO_x (OH + HO_2), the ClO_x (Cl + ClO) and the BrO_x (Br + BrO) chemical families. The chlorine and bromine chemical families are essential because they undergo catalytic loss reaction with O_3, one Cl molecule reacts on average with 10^5 O_3 molecules, which highlights the impact of even small amounts of ODS, molecules containing Cl or Br atoms. To end a catalytic cycle, the reactive species must be converted into a more stable product and can then be transported into the troposphere. Examples of reactions leading to meta-stable, also known as reservoir species, that stop catalytic cycles are

$$OH + NO_2 + M \longrightarrow HNO_3 + M \tag{R 2.9a}$$
$$Cl + CH_4 \longrightarrow HCl + CH_3 \tag{R 2.9b}$$
$$ClO + NO_2 + M \longrightarrow ClONO_2 + M \quad . \tag{R 2.9c}$$

And they are essential for explaining ozone depletion over Antarctica during spring. During the polar winter, the air cools strongly, creating westerly winds that isolate the polar region from the midlatitudes, forming the polar vortex. The polar vortex traps O_3-rich air in the polar region until it breaks down with the first irradiation in spring. Inside the polar vortex, the temperatures decrease below 183 K in the LS, at which the small amount of H_2O vapour in the stratosphere condenses and freezes and forms Polar Stratospheric Clouds (PSCs). They further consist of nitric acid trihydrate (NAT), a thermodynamically stable form of HNO_3. The NAT particles are sufficiently large to sediment, potentially leading to a loss of NO_x from the stratosphere (see R 2.9a), a process known as denitrification. The stable HCl gets absorbed by the PSCs very efficiently, and this enables the heterogeneous reaction on the PSCs surface

$$HCl\,(s) + ClONO_2 \longrightarrow Cl_2 + HNO_3(s) \tag{R 2.10}$$

to release Cl_2 from its chemically stable molecule. The symbol (s) indicates that the molecules are attached to the surface of the PSC ice crystals and are not present in their gaseous state. This heterogeneous reaction is much faster than a homogenous reaction purely in the gas phase.

When irradiation reaches the polar region in spring, Cl_2 is photolysed, and the free Cl atoms react with the O_3, leading to a massive ozone depletion by the ClO_x and BrO_x families. The Cl is rapidly catalytically recycled, leading to a net loss of O_3:

$$\begin{array}{rl} & Cl + O_3 \longrightarrow ClO + O_2 \\ & ClO + O \longrightarrow Cl + O_2 \\ \hline \text{Net:} & O + O_3 \longrightarrow 2\,O_2 \quad . \end{array}$$

Due to denitrification, Reaction R 2.9c cannot bind Cl as effectively as usual, resulting in greater depletion of O_3. Since the polar night is approximately 10 K colder over the Antarctic than over the Arctic, the Arctic polar vortex is weaker, and fewer PSCs are formed, resulting in a weaker ozone depletion in spring.

Although O_3 is mainly present in the stratosphere, its smaller abundance in the troposphere also plays a central role in tropospheric photochemistry. Tropospheric O_3 abundance is governed by the interaction of chemical families. The photolysis of nitrogen dioxide (NO_2) ($\lambda < 424$ nm)

$$NO_2 + h\nu \longrightarrow NO + O \tag{R 2.11}$$

produces O which initiates the main O_3 production by Reaction R 2.6. The NO_x cycle is terminated by

$$O_3 + NO \longrightarrow NO_2 + O_2 \quad \cdot \tag{R 2.12}$$

The O_3 abundance depends on the ratio between NO_2 and NO, i.e. the higher the ratio, the more O_3 is present. While the tropospheric O_3 abundance is low, it is crucial to produce the essential oxidant hydroxyl radical (OH), which drives tropospheric chemistry. Following Reaction R 2.7b, the photolysis of O_3 can produce $O(^1D)$. Together with the high abundance of H_2O in the troposphere it produces OH

$$O(^1D) + H_2O \longrightarrow 2\,OH \quad \cdot \tag{R 2.13}$$

As $O(^1D)$ is produced by photolysis of O_3 with UV radiation with $\lambda < 320$ nm, the highest production of OH in the troposphere occurs in the tropics. If OH reacts with a carbon-containing compound, hydroperoxyl radical (HO_2) is created in the oxidation chain, contributing to the HO_x cycle. If that is the case, it can lead to a higher O_3 abundance, if

$$HO_2 + NO \longrightarrow OH + NO_2 \tag{R 2.14}$$

effectively preventing the removal of O_3 by Reaction R 2.12.

The simplest carbon-containing compound, CO, creates HO_2 almost directly without intermediate steps, by

$$CO + OH \longrightarrow CO_2 + H \tag{R 2.15}$$

creating hydrogen (H) next to carbon dioxide (CO_2) which produces the HO_2

$$H + O_2 + M \longrightarrow HO_2 + M \quad , \tag{R 2.16}$$

producing one O_3 molecule per CO molecule as theoretically maximum net gain, CH_4 has a large oxidation chain, leading in theory to a maximum of

$$CH_4 + 10\,O_2 \longrightarrow CO + H_2O + 2\,OH + 5\,O_3 \quad \cdot \tag{R 2.17}$$

In the troposphere, O_3 is produced by the reaction of peroxyl radicals with NO, to 70 % by Reaction R 2.14 and about 20 % by the reaction $NO + CH_3O_2$, produced for instance during the CH_4 oxidation. The O_3 loss is dominated equally by the reactions R 2.13, if $O(^1D)$ leaves the O_x cycle, and the direct reaction O_3 + HO_2, and to a lesser extent by the reaction with OH (Wang et al., 1998; Seinfeld and Pandis, 2016). In addition to its protective role in the stratosphere for life on Earth, O_3 is harmful to living beings when in direct contact. And its tropospheric abundance is increased by anthropogenic emissions, for instance, of NO_x (see Figure 2.2 for chemical production at the surface from precursors).

The substantial differences in tropospheric and stratospheric chemistry, along with the atmospheric lifetimes of chemical constituents, result in distinct compositions in the two regions. Mixed compositions and steep gradients are found in the upper troposphere/lower stratosphere.

2.5 The upper troposphere/lower stratosphere

While the tropopause is a concept describing the boundary between the troposphere and the stratosphere, the conjunction of the troposphere and the stratosphere is better described as a transition layer surrounding the tropopause (Highwood and Hoskins, 1998; Thouret et al., 2006). The transition region is generally referred to as the upper troposphere/lower stratosphere (UTLS). The UTLS composition and properties are affected by many processes that further vary between the poles and the equator. Due to the two-way stratosphere-troposphere exchange (STE), the UTLS has properties of the troposphere as well as the stratosphere, creating important structures inside the UTLS. While the UTLS is defined as the region around the tropopause, its upper and lower boundaries are not strictly defined and vary between studies, for example, 5–22 km (Hegglin et al., 2010; Millán et al., 2024), 6–25 km (Riese et al., 2012), 8–20 km (Gettelman et al., 2011) and 10–22 km (Millan et al., 2025).

In the tropics, the tropopause does not inhibit bi-directional transport between the stratosphere and the troposphere, which creates an airmass with both tropospheric and stratospheric properties, known as the TTL, the tropical tropopause layer (Randel and Jensen, 2013). While horizontally bound by the strong decreasing tropopause altitude in the subtropics, the estimated vertical extent of the TTL varies between studies. Some studies refer to the TTL as the region from the main convective outflow to the cold point tropopause (Gettelman and Birner, 2007), while others use the point of zero radiative heating as the lower boundary (Fueglistaler et al., 2009). The TTL emerges as a result of convective transport, waves generated by convection, radiation, cloud microphysics and the BDC (Gettelman et al., 2010). The main transport path from the troposphere into the stratosphere by the BDC goes through the TTL, which therefore

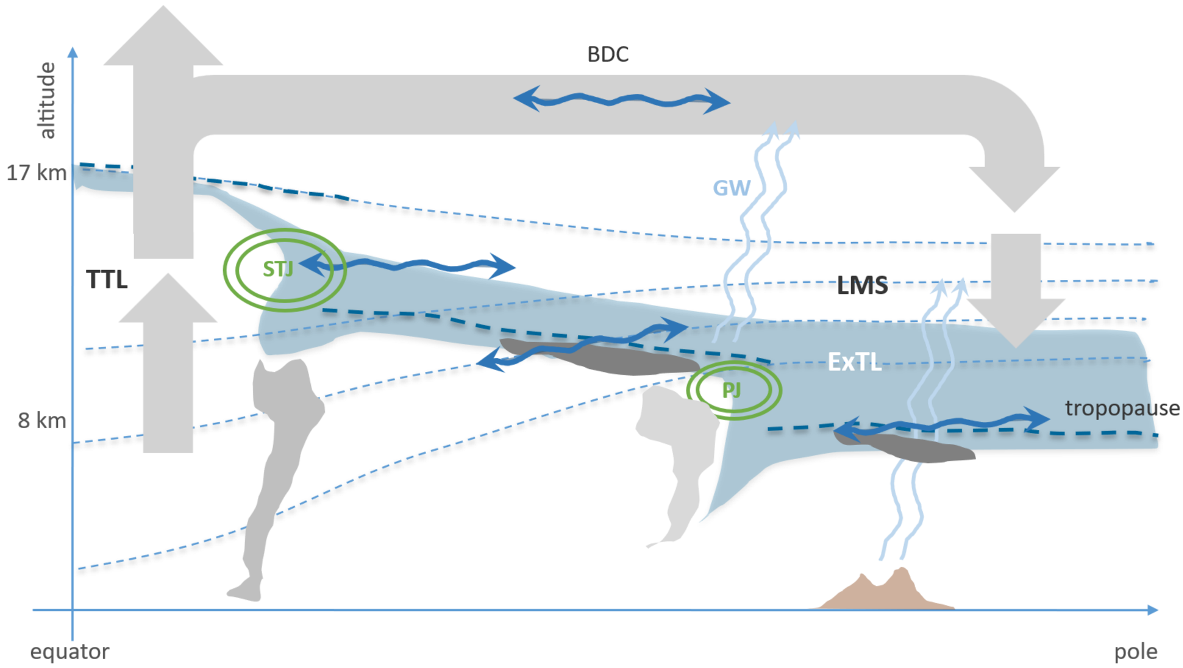

Figure 2.3: Schematic of the UTLS. The thick blue dashed line represents the lapse rate tropopause, which is broken in the vicinity of the subtropical jet (STJ) and polar jet (PJ) in green. Thin blue dashed lines represent potential temperature isolines (isentropes). The highest isentrope plots 380 K. The big grey arrows sketch the Brewer-Dobson Circulation (BDC) of the shallow and the beginning of the deep branch in the tropics, as well as the upward pumping in the tropical troposphere. Grey inhomogeneous patterns depict clouds, and the brown structure represents high orography at the surface. Both are sources for gravity waves (GW, light blue wavy arrows), which initiate mixing and turbulence around the tropopause. Thick dark blue two-sided wavy arrow indicate mixing between the troposphere and the stratosphere. These transport and exchange processes create three structures of the UTLS: the tropical tropopause layer (TTL), the extratropical tropopause layer (ExTL, blue area), around the tropopause and the lowermost stratosphere (LMS) between the tropopause and the 380 K isentrope. Graphic after the Collaborative Research Centre TR301 "TPChange", P. Hoor and V. Bense, personal communication.

exerts a strong influence on the trace gases that reach the stratosphere. In the case of water vapour, entry into the lower stratosphere through the TTL is determined by the cold point temperature, leading to freezing out of H_2O, the strength of the BDC, and the QBO, the Quasi-Biennial Oscillation (Dessler et al., 2014). The cold point temperature exhibits an annual cycle, with the coldest temperatures occurring in the NH winter, resulting in a tape recorder signal in tropical stratospheric H_2O abundance (Mote et al., 1996).

In the subtropics to both sides of the tropics, the tropopause altitude steeply decreases, coinciding with the location of the STJ. At the jet core, there are strong gradients in isentropic PV, associated with a horizontal transport barrier between the stratosphere and the troposphere that inhibits continuous transport. Wind speeds are higher in winter than in summer, leading to a stronger barrier. At the edges of the STJ, the region experiences significant wind shear, baroclinic instability, and wave breaking, resulting in turbulence, mixing, and bi-directional exchange events between the troposphere and the stratosphere (Lelieveld et al., 1997; Gettelman et al., 2011).

Polarward of the STJ in the midlatitudes follows the lowermost stratosphere (LMS). The LMS is defined as the part of the stratosphere between the tropopause and the 380 K isentrope (Holton et al., 1995). Due to the curvature of the tropopause, air masses can be exchanged between the LMS and the tropical UT through horizontal transport and adiabatic transport across the STJ region in situations with a weak transport barrier, as well as mixing at the jet boundaries. The 380 K isentrope closely matches the tropopause altitude in the tropics, and is therefore associated with the first isentrope that lies entirely in the stratosphere. From above, stratospheric air is transported into the LMS by the BDC. The transport into the LMS via different pathways varies throughout the season. In winter, transport is strongest from the stratosphere via the BDC, whereas in summer, transport from the troposphere dominates due to weaker PV gradients (Chen, 1995). In the polar region, the polar vortex can extend down from the upper stratosphere to the LMS, affecting transport and chemical composition, and isolating the polar region.

Analogously to the TTL, a transition layer is found with properties of tropospheric as well as stratospheric air masses around the lapse rate tropopause in the extratropics (Pan et al., 2004; Hoor et al., 2004; Hoor et al., 2010; Gettelman et al., 2011), called the extratropical tropopause layer (ExTL). Diabatic mixing is driven by baroclinic instabilities, leading to wave breaking in the ExTL. This layer is located around the WMO tropopause, extending from approximately 1 km below the tropopause to 1–1.5 km above it in the subtropics, and 3–4 km in the polar regions, as identified in observations (Hegglin et al., 2009; Zahn et al., 2014). The asymmetry of the ExTL around the tropopause is caused by the faster mixing timescales in the troposphere (Shepherd, 2007). The transport from the troposphere is weaker in the Southern hemisphere, leading to a lower upper limit of the ExTL. Furthermore, a seasonal variability has been found, with a maximum extent during summer (Tilmes et al., 2010). The ExTL is associated with strong vertical gradients in chemical constituents.

An essential process for the transport into the upper troposphere and which is associated with turbulence and mixing into the LS is convection. However, it is not straightforward to accurately represent its processes on the large scales of climate models.

2.6 Convection in climate models

Convection is associated with rapid vertical motion resulting from density differences caused by thermal expansion. The dry convection driven by density differences is accompanied by wet convection driven by diabatic heating and cooling associated with water-phase transitions in the atmosphere, which leads to cloud and precipitation formation. Convection in the atmosphere is driven by heat fluxes from the surface, radiative cooling by outgoing longwave radiation in areas without clouds, the large-scale dynamics, such as atmospheric waves, and meso- and synoptic-scale systems, for instance, MCSs, mesoscale convective systems (Bechtold, 2017; Rio et al., 2019). The occurrence and strength of convection vary significantly across the Earth due to differences in irradiance between the tropics and the poles, differences in heat flux between land and ocean surfaces, the daily cycle of the sun, orography, and sources of atmospheric waves. Air rises or sinks under unstable conditions. Rising air expands and cools, increasing relative humidity (RH). Once the saturation vapour pressure is reached, the water vapour condenses into water or even deposits as ice, and clouds form. During the phase transition, latent heat is released into the atmosphere, resulting in increased instability, upward transport (updraft), and feedback to the dynamics through the interaction of clouds with radiation, as well as the stimulation of turbulence and atmospheric waves (Bony et al., 2015).

During the formation of clouds by convection, air is exchanged with the surrounding environment. The process of mixing environmental air into a cloud is called entrainment. The environmental air is generally drier, leading to reduced relative humidity, increased evaporation, and a cooling effect. This can enhance the turbulence in the cloud (Bechtold, 2017). The opposite effect is called detrainment. Convection transports tracers from the surface into the UT on timescales down to hours, whereas vertical large-scale transport requires days to weeks. Therefore, convective transport enables tracers with a short atmospheric lifetime to reach the upper troposphere and the stratosphere (Tost et al., 2010). Since mass is conserved, the upward transported air must be balanced by a downward movement. While there is some rapid convective downward (downdraft) motion inside the cloud, the upward motion is mainly balanced by the slow downward motion outside the cloud, called subsidence.

In conclusion, convection plays a central role in tropospheric vertical transport, dynamics, and its interaction with both incoming and outgoing radiation. Nevertheless, convection poses a major challenge for weather and climate modelling and significantly contributes to the uncertainties in climate warming projections (Bony and Dufresne, 2005). The challenge of simulating convection lies in the scales on which convection occurs: single convective clouds and even MCSs occur on microscales (up to 100 m) to mesoscales (up to 100 km), usually much smaller than the horizontal grid resolution of weather and climate models. To incorporate this fundamental aspect of the troposphere, the effect of these processes at large scales is approximated. This approximation is known as a parameterisation (Randall et al., 2003).

Convection parameterisations must approximate all relevant convective processes in each grid cell at model grid scales, accounting for their different magnitudes. In practice, this begins with a criterion for whether convection occurs, i.e. the trigger of convection. If a convective event is triggered, the heat, moisture, and momentum exchange are calculated, and the vertical extent of the convection is determined. They are based on the total available energy, defined by the mass flux at the cloud base. The determination of the mass flux is referred to as the closure problem (Bechtold, 2017).

The trigger of convection usually differentiates at least between two convective classes, shallow and deep, by the height of the convective cloud (Rio et al., 2019). Since convection parameterisations were required from the beginning of weather and climate simulations (Manabe et al., 1965), many parameterisations have been developed in the second half of the 20^{th} century. With horizontal grid sizes of hundreds of kilometres in climate models, a widespread assumption in convection parameterisations is that convection and the large-scale forcings are in quasi-equilibrium, dating back to the work of Bjerknes (1938). Based on that assumption, the convection parameterisation of the mass flux approach was developed. It divides the grid box into a convective (cloudy) part and a cloud-free environmental part, describing the total up- and downdraft within the grid box. While it simplifies the calculation of vertical motion, the entrainment and detrainment rates must be specified in the parameterisation. Common approaches assume a plume or bulk model to describe the entire convection within a grid cell as a single cloud entity. On which levels entrainment and detrainment occur can either follow a predefined vertical distribution (e.g. Tiedtke, 1989) or a stochastic distribution of mixing to include episodic entrainment and detrainment, which better agrees with observations but is more complex and computationally more expensive (Emanuel, 1991; Raymond and Blyth, 1992). The convective tracer transport is also based on a bulk model, but entrainment and detrainment can occur on every level, defined by the mass flux profile (Lawrence and Rasch, 2005).

Finally, to calculate the convective quantities, the total available energy must be specified. This is achieved by estimating the total mass flux at the cloud base and applying closure assumptions. The total energy associated with the mass flux is used to estimate heat release, precipitation amount, vertical motion, the extent of the cloud, and the exchange with the environmental air. The closure assumptions often differ across the convective cloud classes used to define the convection trigger. Many closure assumptions, especially for deep convection, assume some relationship between the strength of the convection and Convective Available Potential Energy (CAPE), defined as

$$CAPE = \int_{base}^{top} g \, \frac{T_v^c - T_v^e}{T_v^e} \, dz \quad . \tag{2.6}$$

CAPE describes the available energy in the entire convective cloud from the cloud base to the cloud top based on the differences between the virtual temperature (T_v) inside the cloud (T_v^c) and the environment (T_v^e).

This is the concept of most convection parameterisations used in modern climate models. They were developed several decades ago for very coarse resolutions. Any cloud and precipitation organisation is not considered. Examples are mesoscale convective systems, characterised by a convective cloud at the front of the system and a large trailing stratiform cloud cover and precipitation, as well as the interaction between the two cloud types. Instead, they are mostly seen as the unresolved (convective) and the resolved (stratiform) parts of clouds and precipitation. While the convective regions are essential for vertical transport, the large stratiform areas strongly influence the temperature profile and the radiative budget. The large-scale effect is assumed to compensate for the missing interactions and organisation (Donner et al., 2001).

The crude approximations lead to several discrepancies between model simulation results and observations. In atmospheric models, the distribution between convective and stratiform precipitation is shifted too far towards convective precipitation in low-resolution models (Chen et al., 2021b). Additionally, light precipitation is triggered too frequently, leading to too rare heavy precipitation events; both phenomena are reduced with finer resolution (Dai, 2006; Huang et al., 2017). A common phenomenon in climate modelling is the double-intertropical convergence zone (ITCZ), which results from ocean-atmosphere feedback and too-frequent deep convection in the tropics (Lin, 2007). However, significant progress and improvements have been made by the individual convection modelling groups over the last few decades, accompanied by a steep increase in computational resources that has enabled higher-resolution simulations and the direct calculation of large convective events rather than a parameterisation. Rio et al. (2019) point out that part of the improvement in convection parameterisation is probably concealed due to the necessity of tuning for climate simulations to match the radiative imbalance of the climate system. It often involves modifying the parameters of the convection parameterisation, which affects cloud cover and precipitation. More information on climate model tuning is presented in Section 3.3.

Despite the progress in convection parameterisation, further improvements are necessary, especially in the representation of convective cloud ensembles, their organisation, and their interactions with large-scale processes. A detailed review was written by Rio et al. (2019). For instance, they point out that common assumptions, such as the quasi-equilibrium, no longer hold for horizontal grid sizes below 250 km. Further, unsaturated downdrafts must be considered, which is currently the case in only a few parameterisations (e.g., Emanuel, 1991).

For completeness, I would like to mention additional approaches that were developed for, or have become feasible with, the computational resources available today. Next to the first global cloud-resolving models over short timescales (Satoh et al., 2019), one approach is the use of super-parameterisations, which employ a 2D cloud-resolving model in each grid column of global simulations (Randall et al., 2003; Arakawa, 2004; Bechtold, 2017). However, they are not feasible for climate simulations. Nowadays super-parameterisation simulations are conducted over a few years only, and the implementation approach is a topic of current research (Grabowski, 2016; Rybka and Tost, 2020). Another approach is the use of machine learning algorithms trained on high-resolution datasets to provide a statistical solution for convection (Schneider et al., 2017; Gentine et al., 2018). They might be an addition to traditional convection parameterisations. However, they require substantial computational resources to train the algorithm and are only useful for investigating physical processes if they comply with physical laws.

Everything I introduced so far is changing rapidly due to anthropogenic climate change. Especially the temperature change in the UTLS is highly uncertain.

2.7 Atmospheric responses due to climate change

The anthropogenic emissions of GHGs, especially CO_2, lead to a warming of the troposphere and a cooling from the middle stratosphere to the mesosphere. The effect of greenhouse gases, primarily causing cooling of the middle and upper stratosphere, is known as the blocking effect. With higher greenhouse gas abundances, the atmosphere becomes optically thicker for the emitted longwave radiation. Greenhouse gases absorb outgoing longwave radiation, leading to local warming, and then emit it in all directions, thereby retaining a larger portion of the energy in the atmosphere. The local temperature determines the energy of the emitted longwave radiation required to achieve local radiative balance. The surface is warming, so outgoing longwave radiation increases. In the troposphere, longwave radiation originates mainly from the surface. The air above the surface warms (Goessling and Bathiany, 2016). In the stratosphere, the higher emissivity due to the greater abundance of GHGs dominates, resulting in a cooling effect. The cooling effect is further enhanced if the absorbed longwave radiation originates from the atmospheric GHGs below instead of directly from the surface. Over the satellite era, from 1986 to now, the observed cooling is between 1 and 2 K in the middle to upper stratosphere (Santer et al., 2023). The cooling stratosphere is one of the most significant pieces of evidence that the climate change we observe is caused by anthropogenic emissions, as a natural climate change would typically warm or cool the entire atmosphere, rather than exhibit the bimodal change (Santer et al., 2023). With a warming troposphere and a cooling stratosphere above, the anthropogenic climate change especially affects processes connecting the two regions, the upper troposphere/lower stratosphere (UTLS). Chemistry Climate Models project that the warming troposphere further leads to a warmer tropical cold point, which is the strongest contributor to a stronger transport of H_2O into the stratosphere over the 21^{st} century (Smalley et al., 2017).

The warming of the troposphere and the cooling of the stratosphere due to climate change lead to an expansion of the troposphere and a higher tropopause, which is observed over the last two decades (Forster and Tourpali, 2001; Xian and Homeyer, 2019; Meng et al., 2021) as well as simulated by model studies (Gettelman et al., 2010; Hegglin et al., 2010; Tegtmeier et al., 2020). Only the extratropical tropopause altitude in the SH is decreasing in some datasets, presumably connected to O_3 recovery in the LMS and a strengthening of the BDC (Birner, 2010b; Weyland et al., 2025). Additionally, the tropics are expanding, most likely due to upper-tropospheric warming, stratospheric cooling observed today due to O_3 depletion, anthropogenic pollution, and decadal variability and trends in SST (Staten et al., 2018). Dynamical changes affect storm track paths, the location of subtropical dry zones, and precipitation patterns (Seidel et al., 2007). The tropical widening over the last few decades can already be derived from model studies and reanalysis datasets; however, the widening rates differ depending on the metric (Birner, 2010a; Davis and Birner, 2017; Weyland et al., 2025). The metrics can be divided into those based on lower- or upper-tropospheric quantities (Staten et al., 2018), with the lower-tropospheric metrics agreeing more closely and estimating a tropical expansion of 0.5° decade^{-1}. Upper tropospheric metrics, such as the STJ position, vary more strongly among each other. Maher et al. (2019) found a weaker tropical expansion based on the STJ location as metric and presumes that the area is not dynamically coupled to the edge of the Hadley cell.

Chemistry Climate Models further predict a strengthening of the BDC caused by the warming troposphere, increased wave drag and an upward movement of the critical layer for Rossby wave breaking in the subtropical lower stratosphere (Shepherd and McLandress, 2011; Butchart, 2014). Many model projections agree on a 2 to 4 % increase per decade in the net upwelling mass flux at 70 hPa in the tropics. However, Oberländer-Hayn et al. (2016) question the metric. A fixed pressure level relative to the ground is biased by the expansion of the troposphere and the rise in tropopause altitude under future conditions. Using satellite-based temperature observations of the lower stratosphere reveals a strengthening of the BDC over the last four decades (Fu et al., 2019). While a good agreement has been found between trends in the shallow branch of the BDC between model results and observations, there is a large spread between the CMIP6 model results for the deep branch in the middle and upper stratosphere (WMO, 2018; Abalos et al., 2021). The BDC trend is affected by the increase of GHGs (faster circulation) and the decrease of ODS (slower circulation), leading to a projected reduction in the acceleration of the BDC in projections until 2100 (Polvani et al., 2019). The acceleration is such that the relative differences between the hemispheres in the BDC strength remain. Faster transport has a significant impact on the abundance and distribution of O_3 and the coupling between the troposphere and the stratosphere. The more vigorous upwelling of tropospheric air reduces O_3 in the tropical lower stratosphere, and a faster BDC in the stratosphere leads to a larger abundance in the polar stratosphere. Therefore, the transport between the troposphere and the stratosphere is projected to increase in both directions in the future (Abalos et al., 2017; Abalos et al., 2020).

Changes in atmospheric temperature affect the rate of chemical reactions. The primary production of O_3 by Reaction R 2.6 is inversely dependent on temperature, resulting in increased production in the context of climate change, and the heat release mitigates the cooling in the stratosphere O_3 (Jonsson et al., 2004). The continuous reduction of the atmospheric ODS abundance results in a reduction of PSCs and leads to O_3 recovery in the higher latitudes. With more O_3 entering the troposphere (Hegglin and Shepherd, 2009; Neu et al., 2014), the tropospheric chemistry may amplify due to a higher production of OH by Reaction R 2.13, leading to higher tropospheric oxidation of constituents such as CH_4.

Chapter 3

Methods and Data

To answer the research questions stated in my introduction, I require an atmospheric chemistry model that allows for isolated changes to the model setup. I use the Modular Earth Submodel System (MESSy) (`https://messy-interface.org/`; last accessed: 01.03.2026) and its ECHAM/MESSy Atmospheric Chemistry (EMAC) model configuration. In the following, I will introduce MESSy and EMAC, providing a more detailed description of the components required to build the different model setups used in the analysis.

3.1 Model description

3.1.1 MESSy – The framework

MESSy is an integrated software framework to combine numerical representations of components of the Earth system. The philosophy behind the framework is to modularise all processes necessary to simulate the Earth system and couple them in a standardised way (Jöckel et al., 2005). The modularisation provides the greatest freedom and flexibility to create a numerical model setup best suited to investigate the scientific question at hand. It further enables the independent development, modification, or addition of alternative descriptions of a process parameterisation or entirely new processes. This is possible because the coupling is generalised through clearly defined interfaces and handled separately by the framework.

The MESSy framework is divided into four distinct layers (see Figure 3.1), enabling a high degree of independence between the different process descriptions. The base model layer (BML) defines the dynamical core of the model. Its extent can range from only time integration in box models to a complete GCM in which individual components are removed or replaced by MESSy submodels. Connected to the BML is the base model interface layer (BMIL), the MESSy infrastructure. It defines which submodels are activated in a specific model setup (SWITCH), it controls the data exchange between the submodels (CHANNEL), the input to the model (IMPORT) with necessary grid transformations (GRID) and the output of the model (CHANNEL) and which chemical constituents are involved, if chemical processes are included (TRACER), and handles the time integration of the prognostic variables (TENDENCY) (Jöckel et al., 2008; Jöckel et al., 2010; Eichinger and Jöckel, 2014; Kerkweg and Jöckel, 2015; Kerkweg et al., 2018). In brackets are the names of the infrastructure submodels. The submodel interface layer

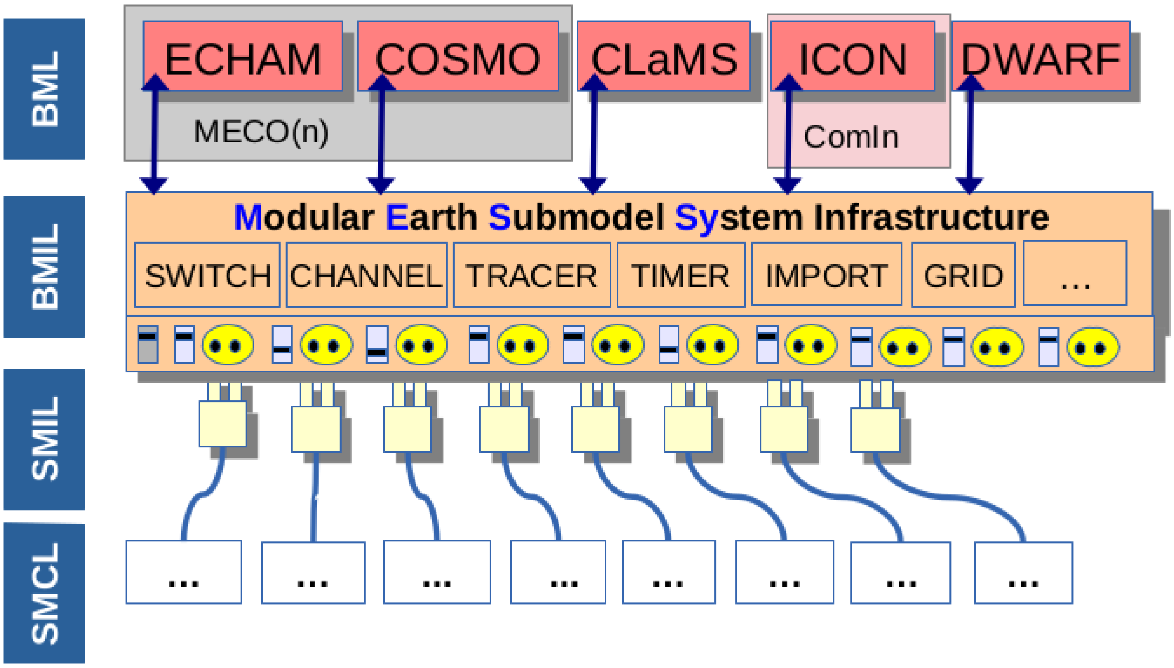

Figure 3.1: Schematic diagram of the MESSy framework. Abbreviations on the left are the four distinct layers of MESSy: base model layer (BML), base model interface layer (BMIL), submodel interface layer (SMIL) and submodel core layer (SMCL). Licensed by DLR under CC BY-NC-ND 3.0.

(SMIL) connects the BMIL to the submodel core layer (SMCL), the basemodel-independent core calculations of the process. SMIL and SMCL define a submodel representing a process or an online diagnostic. The SMIL collects all necessary information from the BMIL for the SMCL, and the results are transferred back to the BMIL so other submodels can further access them. The user interacts with the MESSy framework primarily via Fortran namelists to build the required complexity of the Earth system numerical model. Each submodel is controlled by its specific namelist file, which contains the control (CTRL) and coupling (CPL) namelists. In the namelist file, the import to the submodel is defined, a realisation of a selected process is specified, parameter values are set, additional tracers are created, and specific couplings between submodels are defined. These various configuration options enable the specific model setups. Depending on the setup, MESSy can be used to create atmospheric models of varying complexity and scales. The spectrum ranges from a box model to a fully coupled Earth System Models (ESM), encompassing high-resolution atmospheric event studies and climate simulations.

In the following sections, I outline the core model setup used for the simulations in this thesis.

3.1.2 ECHAM5/MESSy – The atmospheric general circulation model

Until today, the most essential basemodel in MESSy is the 5$^{\text{th}}$ version of the Atmospheric General Circulation Model (AGCM) ECMWF and Hamburg (ECHAM), called ECHAM5 (Roeckner et al., 2003; Roeckner et al., 2004), a derivative of the early Integrated Forecasting System (IFS) model from European Centre for Medium-Range Weather Forecasts (ECMWF). At the beginning of MESSy, Jöckel et al. (2005) used ECHAM5 to modularise it into the MESSy structure, translating all physical processes into separate submodels and coupling them via BMIL to the atmosphere model component of ECHAM5. The atmosphere model of ECHAM5, specifically the spectral dynamical core, large-scale advection, and the implementation of Newtonian relaxation (nudging), remains the original implementation. While the name ECHAM5 is kept, major bug fixes and changes in the ECHAM5 development were also implemented in MESSy. To run ECHAM5/MESSy, several submodels of physical processes have to be included. Different parameterisations exist for many of these processes, but the original ECHAM5 parameterisations are still included and, in many cases, remain the default. The calculation of cloud cover and cloud microphysics is done in the submodel CLOUD, and the submodel CONVECT calculates the convection. The cloud cover calculation in this thesis is based solely on specific humidity (Sundquist scheme). For the convection parameterisation, several realisations exist in MESSy. In addition to the original ECHAM5 (Tiedtke, 1989; Nordeng, 1994), the parameterisation by Emanuel and Živković-Rothman (1999) is used in this work. Their different approaches are further introduced in Section 3.1.6. The convective transport of trace gases is handled by the submodel CVTRANS. It is based on a bulk approach that incorporates the convective mass flux and the entrainment and detrainment rates from the selected convection parameterisation in CONVECT. Entrainment and detrainment of trace gases are allowed on all levels. E5VDIFF calculates the vertical diffusion and exchange of the prognostic variables between the surface and the atmosphere, as well as some tracer fluxes. An updated version, called VERTEX, was recently implemented in MESSy (Emmerichs et al., 2021). It includes code optimisations and bug fixes, as well as modifications to several internal calculations, such as the transfer coefficients for vertical diffusion, the roughness length over sea, and the kinematic heat and moisture fluxes. It is used here in several simulations instead of the E5VDIFF realisation. GWAVE calculates the momentum flux and wind drag due to non-orographic gravity waves. The submodel SURFACE calculates surface temperature and water content in various forms, including snow and ice amounts, soil water, and resulting heat fluxes, depending on the surface type. Finally, the interaction of radiation with different parts of the atmosphere has to be included. ORBIT calculates Earth's orbit around the Sun, defined by the radius, the Sun's declination, and right ascension, resulting in the solar zenith angle and day/night phases. With the optical properties of aerosols and clouds by AEROPT and CLOUDOPT, the surface albedo and the information about GHG abundances, RAD calculates the radiation flux in the Earth's atmosphere (Dietmüller et al., 2016) and creates a complete AGCM. Recently, the radiation scheme of ECHAM6, PSRAD (Pincus and Stevens, 2013), got added as an alternative parameterisation, which further adds a submodel to calculate the surface albedo (ALBEDO, Nützel et al. (2024)). The new parameterisation is used for many simulations in this work.

This setup has to be extended by an atmospheric chemistry submodel and the processes it requires to build ECHAM/MESSy Atmospheric Chemistry (EMAC), a Chemistry Climate Model (CCM).

3.1.3 EMAC – The chemistry climate model

To build the EMAC model, ECHAM5/MESSy AGCM gets expanded by the submodels necessary to simulate atmospheric chemistry. Next to the description of the chemical reactions and reaction rates, this includes both the emission and removal of atmospheric species.

At the centre of the chemistry component of MESSy is the MECCA submodel, which solves the partial differential equation (PDE) system describing the chemical mechanism in both the gas and aqueous phases as well as aerosol species of the atmosphere. While capable of up to 600 chemical species and more than 1600 reactions (Sander et al., 2019), this complexity is not feasible for global climate simulations. The chemical mechanism is typically reduced to the gas-phase chemistry of ozone, methane, odd nitrogen, alkanes and alkenes up to 4 C atoms, chlorine and bromine halogen chemistry, and the chemical reactions of isoprene and a few non-methane hydrocarbons (NMHC). The reduced mechanism is then referred to as the mainz isoprene mechanism (MIM) version 1 and is based on Pöschl et al. (2000). In total, MIM1 considers 155 species with about 310 reactions. The necessary photolysis rate coefficients are calculated by the submodel JVAL (Sander et al., 2014). MECCA also provides the option to add diagnostic tracers to individual chemical reactions, enabling determination of their effects on the overall abundance of the trace gas. It is a helpful tool for analysing the individual contributions of production and loss reactions to the overall abundance of a trace species, for example, O_3. In the CCM simulations for this work, I also utilised the submodel GMXe, which incorporates tropospheric aerosols into the simulation and calculates their properties and microphysical processes (Pringle et al., 2010). This affects heterogeneous reactions; therefore, the chemistry differs from a simulation without aerosols. Crucial for the O_3 chemistry are Polar Stratospheric Clouds (PSCs). The abundance of PSCs as well as the second-order reaction rates for the heterogeneous reactions on their surface and on stratospheric background aerosol in general are calculated by the submodel MSBM (Jöckel et al., 2010; Kirner et al., 2011).

Chemical species and aerosols are removed from the atmosphere by wet and dry deposition, along with sedimentation for aerosols. The submodel SCAV calculates wet deposition by precipitation, also known as scavenging (Tost et al., 2006a). It further calculates the aqueous-phase chemistry and the phase transitions between the aqueous and gaseous phases. Dry deposition is calculated by the submodel DDEP and depends on the surface properties and the near-surface turbulence. The submodel SEDI describes the process of sedimentation, which is the slow fall to the ground due to gravity (Kerkweg et al., 2006a). Therefore, especially larger, heavier aerosols are affected by sedimentation.

The chemical species and aerosols are emitted into the atmosphere, primarily at the surface. They can be divided into two sources: anthropogenic and natural. Anthropogenic emissions originate from various aspects of our lives, including the transport sector, agriculture, and energy production, leading to a heterogeneous distribution of the emissions. The emissions are collected and homogenised in extensive emission inventories, which then can be used as input to the CCM. These emissions are mainly independent of the meteorological situation and are directly emitted via the OFFEMIS submodel, which adds the emission as a tendency to the respective species. If the emission further depends on meteorology, it must be calculated during the simulation based on the specific conditions and external information. Sea salt and dust emissions, calculated by the submodel ONEMIS (Kerkweg et al., 2006b), are two examples. Considering a mask of biosphere types and dry particulate matter, BIOBURN calculates biomass burning emissions, which offer greater control than direct emissions from an emission inventory, e.g. (Kaiser et al., 2012). The submodel MEGAN calculates emissions of gas species and aerosols from the terrestrial ecosystem, taking meteorological conditions into account, such as temperature (Guenther et al., 2006). And finally, the submodel LNOX calculates the production of nitrogen oxide family, $NO + NO_2$ (NO_x) in the atmosphere by lightning. The calculation is based on the flash frequency and distribution, which are themselves determined by meteorological conditions, most notably the strength of convection (Tost et al., 2007). Several parameterisations exist in MESSy for this process; here, the realisation by Price and Rind (1992) is used, along with the modification by Luhar et al. (2021) for one set of simulations. Due to the strong dependence on convection, the annual global mean flash frequency and, consequently, the NO_x production must be rescaled to match observations for each simulation.

And with that, the EMAC model is primarily established. For many GHG and ODS, there exists no robust information about emission and removal fluxes, or components are missing, such as a complete carbon cycle for CO_2, and therefore the boundary conditions are prescribed by relaxing the surface value against the values collected in datasets based on observations. This is done via the submodel TNUDGE (Kerkweg et al., 2006a). For submodels such as MSBM, which operate only in the stratosphere, some tropopause information is required. For that, there is the diagnostic submodel TROPOP (now METEODIAG), which calculates several tropopause definitions, as well as the cold point, the potential temperature and the potential vorticity in MESSy (Jöckel et al., 2006). A detailed description of the implementation of the WMO lapse rate tropopause is provided in Appendix B. Additionally, several purely diagnostic submodels are used in the model setups of this work. VISO calculates user-defined iso-surfaces, for instance, the 380 K isentropic surface (Jöckel et al., 2010). VAXTRA regrids user-defined variables on a user-defined vertical grid, such as altitude, pressure, potential temperature or potential vorticity. The submodel PTRAC incorporates prognostic tracers with a wide range of possible properties, spanning from the defined mass and medium to the point at which processes affect the new tracer (Jöckel et al., 2008). TREXP offers the option to add point sources to a tracer or to add a lifetime (Jöckel et al., 2010). This completes the list of submodels used in this work. A summary is provided in the tables A.1 and A.2 in the supplement.

3.1.4 Newtonian relaxation

Any evaluation of the model results requires comparison with observations. To evaluate the chemical composition at a specific location and time, the meteorological conditions must be met, ensuring that transport by fronts and weather systems is similar. However, free-running atmospheric model simulations will never achieve this inherently. The main reasons are coarse resolution, parameterisations, model biases, and, first and foremost, the butterfly effect. A free-running simulation is initiated from an initial state, based on some reference for this specific time. After a few hours to days, the simulation diverges from the reference evolution due to small deviations, becoming independent of the initial state. Without continuous modifications in their meteorology to reflect the actual state, a direct instantaneous comparison with observations is futile. To facilitate a more accurate comparison with observations for hindcast simulations, Newtonian relaxation, often referred to by convenience as nudging, is employed.

With Newtonian relaxation, the meteorology is nudged towards the observed meteorological state at that time, used as a reference, by adding a forcing term that favours that state for variables such as temperature, wind, and surface pressure. This can be done over the entire atmosphere, or only over a horizontal or vertical region. The method is defined as

$$\left(\frac{dX_{MODEL}(t_0)}{dt}\right)' = \frac{dX_{MODEL}(t_0)}{dt} - \frac{1}{\tau}\Big(X_{MODEL}(t_0) - X_{REF}(t_0)\Big) \quad . \tag{3.1}$$

$X_{MODEL}(t_0)$ describes a multidimensional meteorological variable calculated at time t_0, τ is the relaxation time, which can differ for each nudged variable, and $X_{REF}(t_0)$ is the meteorological situation, which is assumed to describe the actual value and the model is nudged towards.

In the case of ECHAM5, the Newtonian relaxation is performed in the dynamical spectral core of the model. First, the model tendencies are calculated, and afterwards, the Newtonian relaxation is carried out. Following Krishnamurti et al. (1991) (Eq. 7.3), the finite difference form of equation 3.1 can be written as

$$X^m(t+\Delta t,k) = \frac{X^m{}_{prior}(t+\Delta t,k) + 2\Delta t \cdot N(X,k) \cdot X^m{}_{REF}(t+\Delta t,k)}{1+2\Delta t \cdot N(X,k)} \quad , \tag{3.2}$$

m is the spectral coefficient, k is the index of the vertical model level, and N is the reciprocal of the relaxation time τ. The equation includes twice the time step, Δt, because ECHAM uses the leapfrog scheme. It is called the nudging coefficient and defines the strength of the relaxation. X represents the variables relaxed against the reference dataset. In case of ECHAM these are

- divergence
- vorticity
- temperature
- and logarithm of the surface pressure,

as implemented by Jeuken et al. (1996). The Newtonian relaxation strength differs for each variable and with the vertical level. Typically, the nudging coefficient is set to 0 s^{-1} outside of the troposphere, which is equivalent to turning nudging off. As the atmospheric region with weather activities, the smallest temporal and spatial scales of atmospheric events, and the majority of observations, it is the area that benefits most from nudging for comparison and correction of the meteorological situation. Outside the troposphere, the detrimental aspects of nudging prevail and are therefore typically avoided altogether. As seen in equation 3.1, Newtonian relaxation nudges the model simulation by adding a unphysical ad-hoc forcing, dependent on the size of the difference between the intrinsic model results and the reference. This additional forcing perturbs the model's otherwise balanced energy system and can lead to results that are only indirectly affected by nudging and agree even less with observations. This can inadvertently affect the large-scale transport regimes over the entire stratosphere and, therefore, the simulation results everywhere.

In this work, the simulation using Newtonian relaxation is nudged toward ECMWF Reanalysis version 5 (ERA5) (Hersbach et al., 2020). Reanalysis datasets are a combination of Numerical Weather Prediction (NWP) model output and observations, creating a consistent time series that closely matches the global meteorological state. Nudging is focused on the vertical layer between about 700 hPa and 100 hPa to avoid spurious behaviour in the stratosphere due to decoupling of the stratospheric residual circulation from its wave forcing by nudging (Chrysanthou et al., 2019). To avoid hard spikes, the nudging strength is reduced stepwise over the levels around this area. The vertical nudging area is visualised in Figure 3.2.

The divergence is nudged in the main layer with a relaxation time of 48 hours, while the temperature and the logarithm of the surface pressure are nudged with a relaxation time of 24 hours,

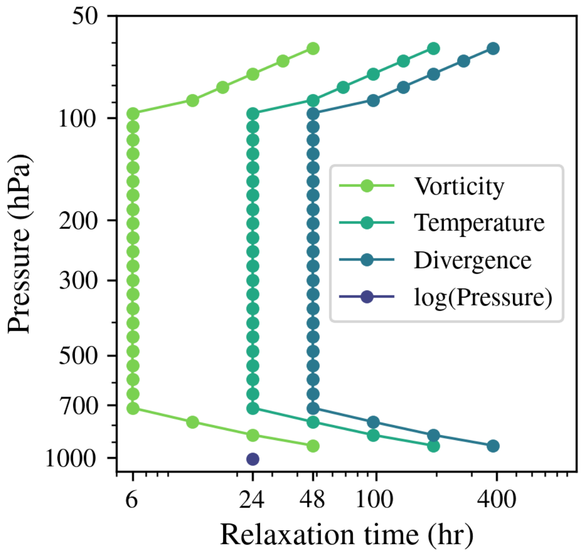

Figure 3.2: Relaxation time in the vertical direction of vorticity, temperature, divergence and the logarithm of the surface pressure, which are nudged against ERA5. The relaxation time is the reciprocal of the nudging coefficient and is therefore not defined outside the nudged vertical region.

and the vorticity is nudged strongest with a relaxation time of 6 hours. The values are based on numerical experimentation (Krishnamurti et al., 1991). No nudging is performed on the 0^{th} wave number, i.e. the global mean, however. This means that the EMAC simulation keeps its intrinsic temperature bias compared to ERA5. This decision was made because earlier experiments revealed a temperature bias by diabatic heating on short timescales when the global mean is also nudged.

3.1.5 The model grid resolution

In atmospheric models, the primitive equations are solved numerically, using vertical and horizontal discretisations to represent the model domain. The vertical discretisation is defined as isolines of constant altitude or pressure, or as hybrid levels that follow orography in the lower atmosphere and pressure isolines in the upper atmosphere. For the horizontal discretisation, spectral methods dominate in atmospheric models developed in the 20^{th} century, such as those used in ECHAM5 with a triangular truncation (Roeckner et al., 2003).

The advantages of spectral methods include an intrinsic high accuracy in calculating horizontal advection, exact results by accounting for quadratic nonlinearity terms, straightforward modelling of flows over the entire globe, and easy use of semi-implicit time integration schemes (Bourke, 1988). However, the dynamics are affected by nonlinear physical processes, which are only available in the grid space, such as convection and radiation. To include them, a transformation between spectral and grid space is required at each time step. In the transformation by Fast Fourier (longitude) and Legendre (latitude) transformation from the grid space into the spectral space, the PDE are translated into a set of ordinary differential equation. The products are computed on the grid, while the derivatives are computed in the spectral space. As only scalar quantities should be represented by a series of spherical harmonics, the primitive

Table 3.1: Grid points in longitudinal (N_{lon}) and latitudinal (N_{lat}) direction and horizontal resolution corresponding to the spectral resolutions used in this work.

	T42	T106
N_{lon}	128	320
N_{lat}	64	160
Hor. Res.	2.8° x 2.8°	1.125° x 1.125°

equations are in the vorticity and divergence formulation of the wind instead of the zonal and meridional components (Riddaway and Hortal, 2002).

In numerical calculations, the infinite series of spherical harmonics must be truncated. As spherical harmonics involve a summation over the indices of the zonal wavenumber and the total wavenumber, both must be truncated. Several types of truncation exist; a prevalent type is triangular truncation, which truncates both indices by the same constant, creating a triangular shape of included index combinations in the plane of the two indices (see Figure 1 in Jarraud and Simmons, 1983). The triangular truncation has the advantage of being isotropic, resulting in a uniform resolution over the sphere (Machenhauer, 1979). With the truncation at the same value, the spectral resolution using triangular truncation is directly identified by the abbreviation "T" followed by the highest resolved wavenumber, e.g. T21.

To obtain exact results before and after the transformation, the resolutions in spectral and grid spaces are not independent. Following the Gaussian quadrature, the integral over a polynomial can be described exactly if sufficient grid points are used. In the case of the spherical harmonics, the necessary grid points are the roots of the Legendre polynomial. While the longitudes are equidistantly spaced on each latitude around the globe, the latitudes along a longitude are not, the Gaussian latitudes. This is a mathematical necessity on the sphere, more roots of the Legendre polynomials for the Gaussian quadrature are found near the poles than near the equator due to the convergence of longitudes at the poles. To achieve exact results before and after the transformation between spectral and grid space, the transformation must avoid aliasing, which can lead to interpreting a wave with a short wavelength as one with a longer wavelength (Riddaway and Hortal, 2002). Sufficient grid points are required to represent the nonlinear interactions that lead to shorter waves. Using triangular truncation and under consideration of quadratic nonlinearities, the relation between the highest resolved zonal wavenumber N (spectral space) and the number of grid points (grid space), N_{lon} and N_{lat}, for an alias-free computation is

$$\begin{aligned} N_{lon} &\geq 3N+1 \\ N_{lat} &\geq \frac{3N+1}{2} \quad , \end{aligned} \tag{3.3}$$

e.g. (Machenhauer, 1979), a so-called quadratic Gaussian grid. The minimum number of grid points, with a factor-2 relationship between N_{lon} and N_{lat}, is typically used. The grid resolution in degrees is calculated as

$$Res_{lon} \approx \frac{360°}{GP_{lon}} = \frac{180°}{GP_{lat}} \approx Res_{lat} \quad . \tag{3.4}$$

In this work, the spectral resolution of the EMAC simulations is T42 and T106. The number of grid points and the resolution in degrees following Equations 3.3 and 3.4 are given in Table 3.1.

In the vertical, ECHAM uses a hybrid-pressure grid which follows the terrain in the lower levels of the domain. Throughout this work, I use an upper limit of the atmosphere at 0 hPa, with the highest half-level at 0.01 hPa ($\approx$ 80 km). Spurious wave reflection at the upper boundary is avoided by introducing a dampening of the wave amplitudes in the highest model levels, called the sponge layer. The setup with the highest half-level at 0.01 hPa is referred to as the 'Middle Atmosphere' (MA) domain altitude, which encompasses the atmosphere up to the stratopause, enabling simulation of the primary transport mechanism by the BDC. 90 and 191 vertical levels are utilised from the surface to the upper limit of the model domain. This results in twice as many vertical levels in the UTLS region, with a high vertical resolution, increasing from 25 to 48 levels with a layer thickness of 600 to 300 m, respectively, in the pressure range between 500 hPa and 50 hPa (see Figure B.1).

Spectral methods have the disadvantage that the calculations cannot be parallelised very efficiently on modern High Performance Computing (HPC) cluster architectures, since spectral calculations require global information rather than independent regional calculations. Furthermore, the number of calculations increases cubically with the highest resolved wavenumber. While 20 % of the computational cost is due to the Legendre transformation on a T63 spectral resolution, on a T252 resolution, the Legendre transformation accounted for 50 % of the computational cost on an early IFS version (Jarraud and Simmons, 1983). This gave rise to the finite elements methods developed in this century. One example for an atmospheric model using this method is the ICOsahedral Non-hydrostatic modelling framework (ICON) model.

3.1.6 Convection parameterisation

Convection and the concept of convection parameterisations are introduced in Section 2.6. In climate models, convection is often parameterised to adjust the energy and water budgets of a model column to achieve a more stable atmosphere (Tost et al., 2010). But there exists a variety of different approaches and realisations. In any case, different parameterisations affect atmospheric chemistry in the troposphere (Tost et al., 2010), including the simulated O_3 lifetime (Lelieveld and Crutzen, 1994).

In the following, I will introduce two convection parameterisations with different approaches in further detail: The parameterisation by Tiedtke (1989) with the Nordeng closure (Nordeng, 1994), and the parameterisation by Emanuel and Živković-Rothman (1999), based on Emanuel (1991). In both cases, the convective tracer transport is calculated by the submodel CVTRANS.

TIEDTKE

The convection parameterisation by Tiedtke (1989) with the Nordeng closure (Nordeng, 1994) (hereafter referred to as TIEDTKE) is the parameterisation used in most EMAC simulations and also used as the standard for all simulations used in this thesis, if not stated otherwise. It was developed for the IFS which needed an improved cumulus convection parameterisation, especially in the tropics around Indonesia.

The parameterisation is based on the mass flux approach, which requires the definition of a cumulus cloud model, closure assumptions for calculating the cloud mass flux, the discretisation of the vertical advection terms associated with cumulus-induced circulations, and a representation of different cumulus cloud types (Emanuel, 1991). Instead of characterising cumulus convection as a large ensemble of clouds with different sizes, cumulus clouds are defined by a bulk model, following the approach of Yanai et al. (1973). They demonstrated that a bulk model can accurately represent the realistic contributions of convection to the large-scale heat and moisture budgets. The bulk model is applied separately to cumulus updrafts and downdrafts, using bulk properties such as cloud-base mass flux and entrainment/detrainment rates.

The bulk properties differ between the considered convection types; TIEDTKE considers deep (penetrative), shallow, and mid-level convection. Deep convection requires synoptic-scale convergence, as is typically present in the tropics. Shallow convection occurs in situations without a large-scale convergent flow, for instance, in the ridge region of tropical easterlies or along the tradewinds in the presence of an inversion. Mid-level convection forms above the boundary layer as convective cells in warm fronts.

The most uncertain and challenging part in parameterising convection is defining the closure assumptions that determine the individual cloud properties (Tiedtke, 1989). The closure assumptions describe the criteria under which the cloud types form and the magnitude of the bulk. They were defined based on observations across all considered cumulus cloud types and later refined by Nordeng (1994).

EMANUEL

The convection parameterisation developed by Emanuel and Živković-Rothman (1999) and based on the ideas of Emanuel (1991) (hereafter referred to as EMANUEL) is the second parameterisation used to illustrate the differences in composition and dynamics resulting from the realisation of the convective processes alone. I selected this parameterisation because it follows a very different approach from the mass flux approach of TIEDTKE.

Emanuel (1991) argues that for an accurate description of cumulus convective transport, one needs to represent entrainment and microphysical processes in the clouds correctly. Emanuel and Živković-Rothman (1999) states that a good convection parameterisation should include major properties of cumulus clouds such as (I) the ability to penetrate to the level of neutral buoyancy of undiluted subcloud-layer air, (II) the mass of a convective cloud is composed mainly of entrained air, (III) the saturated downdrafts can be as strong as updrafts in non-precipitating cumulus clouds and (IV) the unsaturated downdrafts driven by evaporation of precipitation are essential agents of transport and are critical for restabilising the atmosphere to convection from the boundary layer.

Based on these properties, they rejected the use of a plume model and the need for cloud-type differentiation, opposing the standard approach and actively citing the work of Tiedtke (1989). Instead, EMANUEL is based on the buoyancy-sorting hypothesis (Raymond and Blyth, 1986), which assumes that mixing in clouds is highly episodic and inhomogeneous rather than assuming predefined mixing rates, yielding a single vertical distribution of entrainment and detrainment rates across all bulk clouds. The parameterisation is developed to represent the effects of updrafts and downdrafts at subcloud scales, of the order of 100m. EMANUEL includes the feature of reversible ascent, mixing with the environment and transport to a level at which further mixing would result in zero buoyancy.

The primary challenge lies in redistributing water and converting it into precipitation. Both processes are governed by microphysics and cloud dynamics, which must be simulated using model parameters. One simplification in that regard is that no interaction between cloud water and precipitation is allowed.

In summary, TIEDTKE and EMANUEL are two distinct approaches for convection parameterisation in large-scale models. Both are developed and evaluated against observations to improve their representation in the model, and neither can be ranked above the other. They demonstrate the variety of possible solutions for the problem of convective transport in global models, and I will investigate the impact this has on the UTLS region, particularly on its composition and large-scale dynamics.

3.2 Emissions and boundary conditions

A specific time or situation is defined by its boundary conditions. Without the correct emissions of an event or the global surface mixing ratios of GHGs, it is impossible to simulate a historical atmospheric state. To project the future climate, emissions and boundary conditions are estimated under defined scenarios to determine how the atmosphere will change. Therefore, they significantly impact the simulation's outcome and are a crucial consideration when setting up a model.

In model intercomparison studies, the same boundary conditions and emission inventories are specified in advance to attribute differences between the results to variations in model realisations. Here, the emissions and boundary conditions from the Chemistry Climate Model Initiative (CCMI)-2022 are used, which are mainly based on the Coupled Model Intercomparison Project (CMIP) phase 6 (Meinshausen et al., 2017). The boundary conditions differ from the CCMI-2022 protocol only for the ODS. In this regard, as here only the CMIP6 conditions are applied, not the WMO-2018 annual conditions. Furthermore, two additional species are included: CH_2Cl_2 and $CHCl_3$. Historical emissions and boundary conditions, based on observations, extend up to 2014 for CMIP6; thereafter, projections must be used. Following the CCMI-2022 protocol (Plummer et al., 2021), after 2014 the data of the projection Shared Socioeconomic Pathway (SSP) scenario SSP2-4.5 is used, which defines the "middle-of-the-road" scenario, with moderate population growth, a growth in GHG emissions similar to present-day and a target radiative forcing of 4.5 Wm^{-2} in the year 2100 compared to preindustrial conditions (Fricko et al., 2017; Gidden et al., 2019). The projection of the emissions and boundary conditions in the future is based on simulations with the reduced complexity carbon-cycle climate model MAGICC7.0 (Meinshausen et al., 2011a; Meinshausen et al., 2011b) under the SSP2-4.5 scenario (Meinshausen et al., 2020).

The GHGs and ODSs in this work are prescribed as mixing ratios at the lowest model level in all simulations. Table 3.2 shows the global annual mean boundary conditions for two specific years: 2012 as a representative of present-day conditions and 2100 for future conditions. The boundary conditions of 2012 have been selected after comparing the natural and anthropogenic boundary conditions over the first 20 years of the 21^{st} century to avoid years with strong outliers relative to the 20-year mean. The comparison has been visualised in Appendix D.1. It shows the overall increase in CO_2 and the replacement of CFC-11 and CFC-12 with other ODS, such as HFC-125. Table 3.3 provides an overview of the same representative years for the anthro-

Table 3.2: Greenhouse Gases and Ozone Depleting Substances surface boundary conditions as global mean molar fraction for today (2012) and future (2100) conditions, following the CMIP6 emission inventory and SSP2.4-5 projections. Values are rounded to the second decimal digit.

Tracer	Unit	Today	Future	Tracer	Unit	Today	Future
CO_2	ppm	393.02	602.78	CH_3Br	ppt	6.99	5.47
CH_4	ppb	1815.26	1683.16	HCFC-141b	ppt	22.54	1.02
N_2O	ppb	325.00	377.26	HCFC-22	ppt	220.11	0.66
CFC-11	ppt	236.21	53.93	HFC-125	ppt	11.74	288.38
CFC-12	ppt	525.83	214.80	HFC-134a	ppt	67.75	115.15
CCl_4	ppt	85.01	5.27	HFC-143a	ppt	12.85	229.65
CH_3CCl_3	ppt	5.25	0.00	HFC-152a	ppt	8.04	1.76
CH_3Cl	ppt	537.65	464.83	HFC-23	ppt	24.99	23.66
Halon-1211	ppt	3.96	0.04	HFC-32	ppt	5.64	0.01
Halon-1301	ppt	3.25	1.53	CH_2Cl_2	ppt	29.30	28.77
CFC-113	ppt	73.98	27.29	$CHCl_3$	ppt	8.84	6.56
CFC-114	ppt	16.34	10.44	HCFC-142b	ppt	21.62	0.54
CFC-115	ppt	8.41	8.66	Halon-2402	ppt	0.44	0.04

pogenic and natural emission fluxes imported into the simulation, grouped by emission sources. Overall, it shows a reduction in anthropogenic emissions, following the SSP2-4.5 scenario.

Next to the meteorology-independent emissions in Table 3.3, some emissions need to be calculated with respect to the meteorological situation during runtime. They are affected by quantities such as temperature and wind. For the production of NO_x by lightning (submodel LNOX) and by biogenic emissions (MEGAN), references for the emission amounts exist, which were targeted using scaling. In case of lightning NO_x, the observation is based on the Optical Transient Detector (OTD) satellite data, which gives a global annual mean flash frequency of 44 s^{-1} $\pm$ 5 s^{-1} and a mean NO_x production of 15.6 kg(N) $flash^{-1}$. Be aware that both variables exhibit high uncertainty (Price et al., 1997; Schumann and Huntrieser, 2007). The flash frequency in the simulations under present-day conditions is therefore scaled to provide a global annual mean NO_x production of slightly below 5 Tg(N) $year^{-1}$, which lies in the centre of the uncertainty range of Schumann and Huntrieser (2007).

For biogenic emissions calculated by MEGAN, the desired global mean values for 2000 are provided by A. Pozzer of the Max Planck Institute for Chemistry and listed in the MEGAN namelist. A table of the online-calculated and scaled emissions is presented in the following section, which outlines the individual EMAC simulations conducted for this thesis.

3.3 Tuning of a climate model

Regarding climate simulations, a crucial process often overlooked in the literature is the setup tuning. The climate model consists of the coupling of numerous atmospheric processes, several of which occur on subgrid scales and are approximated by parameterisations. To combine them into a harmonised system, it may be necessary to slightly modify some processes so that, in the end, the model better compares with observations and describes the current climate (Hourdin

Table 3.3: Annual global mean prescribed emissions clustered to tracer classes and sources for today (2012) and future (2100) following the CMIP6 emission inventory and SSP2.4-5 projections. Emissions are grouped into the emissions sectors biomass burning (BB), anthropogenic (ANTH), agricultural waste burning (AWB), shipping (SHIP), road traffic (ROAD) and Aircraft (AIRC), and the grouped species of non-methane hydrocarbons (NMHC). DMS_TERR is the abbreviation for terrestrial dimethyl sulfide. Emissions are rounded to the second decimal digit.

Emission	Unit	Today	Future	Emission	Unit	Today	Future
CO_BB	Tg(C)/yr	134.23	86.55	NO_BB	Tg(N)/yr	6.03	3.79
CO_ANTH	Tg(C)/yr	194.70	52.87	NO_AWB	Tg(N)/yr	0.34	0.34
CO_AWB	Tg(C)/yr	10.26	8.51	NO_SHIP	Tg(N)/yr	6.86	6.01
CO_biogenic	Tg(C)/yr	5.57	5.58	NO_ROAD	Tg(N)/yr	13.62	3.80
CO_SHIP	Tg(C)/yr	0.29	0.18	NO_AIRC	Tg(N)/yr	0.91	3.71
CO_ROAD	Tg(C)/yr	68.97	16.91	NH_3_BB	Tg(N)/yr	3.05	3.96
CO_AIRC	Tg(C)/yr	0.24	0.73	NH_3_ANTH	Tg(N)/yr	48.90	49.72
NMHC_BB	Tg(C)/yr	24.93	15.68	NH_3_AWB	Tg(N)/yr	0.42	0.13
NMHC_ANTH	Tg(C)/yr	30.69	15.18	NH_3_SHIP	Tg(N)/yr	0.01	0.01
NMHC_AWB	Tg(C)/yr	2.47	1.36	NH_3_ROAD	Tg(N)/yr	0.32	0.15
NMHC_SHIP	Tg(C)/yr	0.74	0.00	NH_3_AIRC	Tg(N)/yr	0.00	0.00
NMHC_ROAD	Tg(C)/yr	8.08	3.78	NH_3_bio	Tg(N)/yr	8.73	8.73
NMHC_AIRC	Tg(C)/yr	0.01	0.06	SO_2_BB	Tg(S)/yr	1.12	0.94
NMHC_biogenic	Tg(C)/yr	1.36	1.36	SO_2_ANTH	Tg(S)/yr	50.32	13.22
Aerosol_BB	Tg(C)/yr	17.61	11.14	SO_2_AWB	Tg(S)/yr	0.05	0.08
Aerosol_ANTH	Tg(C)/yr	24.97	4.52	SO_2_SHIP	Tg(S)/yr	4.48	0.00
Aerosol_AWB	Tg(C)/yr	0.72	0.82	SO_2_ROAD	Tg(S)/yr	1.95	0.89
Aerosol_SHIP	Tg(C)/yr	0.30	0.00	SO_2_AIRC	Tg(S)/yr	0.14	0.35
Aerosol_ROAD	Tg(C)/yr	2.11	0.74	DMS_TERR	Tg(C)/yr	0.34	0.34
Aerosol_AIRC	Tg(C)/yr	0.02	0.04	CH3I	Tg(C)/yr	0.02	0.02
Halocarbs	Tg(C)/yr	0.03	0.03				

et al., 2017). However, tuning is highly subjective and varies across model groups (Schmidt et al., 2017). While the overall procedure is similar, the targets may vary. This can further impact the model's performance in simulating specific climate variables. If the variable were used for some clustering in model intercomparison projects, the clustering could be biased. Therefore, the modelling groups are encouraged to document their tuning practices (Hourdin et al., 2017; Schmidt et al., 2017).

A climate simulation strives to represent the observed climate as closely as possible to draw any conclusions or comparisons to the real situation. Before the Industrial Revolution, a simulation of the climate system should show naturally forced variations around an equilibrium between incoming and outgoing radiation. With the Industrial Revolution and the systematic burning of fossil fuels, along with the ongoing emission of greenhouse gases, the climate system should exhibit an increasing positive imbalance: more energy is entering the Earth's climate system than leaving it. The mean temperature on Earth increases to reduce the radiative imbalance, following the Planck feedback, the most critical negative feedback process.

A climate simulation of the present-day climate should show a radiative imbalance at the top of atmosphere (TOA) of slightly below 1 Wm^{-2}. Johnson et al. (2016) states an energy imbalance of 0.71 $\pm$ 0.1 W m^{-2} for 2005 to 2015, Schuckmann et al. (2023) an imbalance of 0.76 $\pm$ 0.2 W m^{-2} for 2006 to 2020 (both calling it earth energy imbalance). The final model setup must be tuned to describe the required climate state accurately.

The practice of tuning involves making minor adjustments to parameters in the model's parameterisations within the model setup, thereby shifting the entire climate state towards the targeted state. An often-adapted parameterisation for tuning is the parameterisation of convection (e.g. Mauritsen et al., 2012). The entrainment rate of a convection type, the conversion rate from cloud water to precipitation, the homogeneity of ice clouds, or the rate of approach to quasi-equilibrium, to name a few, are typical parameters of a convection parameterisation that can be used for tuning. They affect the strength and lifetime of convection, as well as the amount of precipitation. A change in cloud cover directly affects the incoming and outgoing radiation. A change in precipitation affects atmospheric temperatures and the abundance of water vapour, altering its radiative feedback as a greenhouse gas. Changes of these parameters themselves are of a small nature, and for none of these values exists a physically valid argument for a specific value, since they are not observed values but necessary parameters for a simplification of the process of convection.

What can be observed in the atmosphere, however, are the radiative fluxes, the cloud cover, the amount of water vapour in the atmosphere and the total precipitation. And very often, there is not a single set of parameter values in the parameter phase space that optimises all of the mentioned climate quantities. Or at least finding the parameter combination would require an enormous number of test simulations over several years, with the full complexity of the climate model setup and systematic variation of all parameters across the parameter space. This requires a large number of resources and time, and must be done for every model setup. In practice, a subset of the atmospheric climate quantities is selected for optimisation, resulting in less-fitting values for the rest. However, even this might require a large number of test simulations, as tuning is often highly erratic. The parameters of a parameterisation are all interconnected and exhibit a highly nonlinear behaviour. This highlights the caveat of the tuning process.

For the simulations in this thesis I prioritized the radiative imbalance to fit an imbalance of slightly above 0.7 Wm^{-2} following the observations by Johnson et al. (2016), while trying to keep the climate state parameters of the global mean radiative components at the top of atmosphere (TOA), the cloud cover and the amount of precipitation as close to observations as possible. The global mean values of the observations are listed in Table 3.4. A list of the final tuning parameters is provided in Appendix Table C.1.

Table 3.4: Overview of used observational datasets to compare important climate indicators of the simulation results. *: Radiative imbalance is estimated using the in situ observations of the ocean heat uptake measured by the floating instruments of the Argo program, `https://argo.ucsd.edu/` (last access: 01.03.26). **: Calculated from the standard errors provided by the datasets, following Righi et al. (2020).

Climate indicator	Dataset	Temporal coverage	Mean	Uncertainty	Unit	Reference
Radiative imbalance	-*	2005–2015	0.71	0.1	W m^{-2}	Johnson et al. (2016)
LW all-sky	CERES EBAF Ed4.0	2005–2015	-240.1	2.5	W m^{-2}	Loeb et al. (2018)
SW all-sky	CERES EBAF Ed4.0	2005–2015	240.9	2.5	W m^{-2}	Loeb et al. (2018)
LW clear-sky	CERES EBAF Ed4.0	2005–2015	-268.7	4.5	W m^{-2}	Loeb et al. (2018)
SW clear-sky	CERES EBAF Ed4.0	2005–2015	286.7	5.0	W m^{-2}	Loeb et al. (2018)
LW cloudy-sky	CERES EBAF Ed4.0	2005–2015	27.9	4.4	W m^{-2}	Loeb et al. (2018)
SW cloudy-sky	CERES EBAF Ed4.0	2005–2015	-45.8	5.5	W m^{-2}	Loeb et al. (2018)
Cloud Cover	ESA cloud_cci	1982–2014	64.5	17.4**	%	Stengel et al. (2017)
Precipitation	GPCP v2.3	2009–2013	2.7	0.2	mm day^{-1}	Adler et al. (2018)
LWP ocean	MAC	1988–2016	83.0	10.2**	g m^{-2}	Elsaesser et al. (2017)

All these global-mean climate quantities are calculated by the emactuner Python class, written by Franziska Winterstein, based on previous work by Mattia Righi and the emacutils Python class.

3.4 Comparison datasets

To evaluate the overall performance of the model setups and to identify model biases in the UTLS, I compare them with observations. However, as mentioned in the introduction, the UTLS remains a region with large uncertainties in its structure and chemical composition, as obtaining consistent, long-term, and large-scale observations remains challenging.

For an evaluation of the entire UTLS on Earth, two primary data sources are available: reanalysis datasets and data products from retrievals based on measurements by satellite-based instruments. A reanalysis is created by combining an atmospheric model with observations. Many observations of climate variables, such as temperature and wind, date back to the mid-20th century, providing a long-term and consistent dataset. And since it combines model results with observations, it is closer to the real situation than the standalone model simulation. A very popular and state-of-the-art reanalysis dataset is ECMWF Reanalysis version 5 (ERA5) (Hersbach et al., 2020).

Meteorological data products based on retrievals from satellite observations have become increasingly available over the past few decades. They either provide a continuous view of the same region of Earth from a geostationary orbit or cover the entire Earth over a specific time period using a polar or sun-synchronous orbit. Satellites measure the radiation or the reflection of a laser to derive information about the atmospheric composition. Over the last few decades, sensors and retrieval algorithms have undergone significant improvements, enabling the derivation of not only total column information but also atmospheric profiles. Deriving gridded information on atmospheric gases from satellite signals using retrieval algorithms has significantly simplified their use by the scientific community. With a strong focus on H_2O and O_3, observations from several satellites are merged to create a consistent time series spanning a period longer than the lifetime of a single satellite, which is utilised in the scientific community: the Stratospheric Water and OzOne Satellite Homogenized data set (SWOOSH) dataset.

3.4.1 ERA5

Based on model output of the IFS combined with observations, the ERA5 product is created. It covers the entire globe at very high resolution, approximately 0.25° horizontally (T639), and has 137 vertical model levels with an hourly time resolution. Sixteen variables are available with a vertical profile, and more than 200 variables are available at specific levels. ERA5 were released in 2018; since then, the time coverage into the past has been gradually increased. Today, it is available from 1940 to the present.

It is one of the state-of-the-art reanalysis products available, enabling many process studies that were previously impossible. Nevertheless, it has some limitations and biases that one must be aware of. For instance, Krüger et al. (2022) showed a significant moisture bias in the LS in ERA5, which is probably connected to the one in IFS (Kaufmann et al., 2018). The moist bias in the LMS is a problem shared with many atmospheric models, likely due to overly diffusive transport schemes and the steep gradients in the UTLS (Charlesworth et al., 2023). A moist bias of about 50 % compared to satellite observations in the tropical lower stratosphere is still present in the most recent development cycle of IFS, making it one of the key targets for future developments (Chabrillat et al., 2025). One must keep in mind that IFS simulations for NWP and ERA5 were performed using parameterisations for the chemical sources and sinks of O_3 in the stratosphere, through a linear expansion with respect to the photochemical equilibrium, rather than interactive chemistry (Cariolle and Teyssèdre, 2007).

For my thesis, I use ERA5 as one dataset to estimate the model bias in the EMAC simulations. Additionally, I nudge one simulation towards ERA5 to estimate the effect of nudging on the UTLS composition on climate scales.

3.4.2 SWOOSH

The SWOOSH dataset is a merged dataset compiled from observations made by instruments on multiple satellites. Data from the satellite instruments Stratospheric Aerosol and Gas Experiment (SAGE) II and III, HALogen Occultation Experiment (HALOE), and Microwave Limb Sounder (MLS) on the satellites Upper Atmosphere Research Satellite (UARS) and Aura, respectively, are combined. For the primary product, data from SAGE, HALOE, and UARS MLS are corrected to better align with Aura MLS. All corrections and homogenizations are well documented, and alongside the combined and harmonised products, the uncorrected information is also available in the dataset. The combined data represent the weighted mean over all available satellite observations at the specified spatial and temporal points. Until the availability of data observed from Aura MLS, the combined data product contains data gaps. A filled data product is included, in which data anomalies in the latitude-time plane are interpolated to fill gaps and then added back to the seasonal cycle, creating a data product without missing data. The SWOOSH main products are H_2O and O_3 as monthly and zonal-mean gridded datasets. The time series spans from 1984 to the present. The dataset is provided at several latitudinal resolutions; throughout this work, the 2.5° resolution is used. The vertical resolution consists of 31 pressure levels, ranging from 316 to 1 hPa, which are identical to those of the AURA MLS version 4 products. Alternatively, SWOOSH information is available at 21 isentropic levels spanning the potential temperature range of 300–650 K. The SWOOSH dataset is still under development, and the time series is still being extended.

Providing a merged data product on a regular grid simplifies comparisons with atmospheric models and observations. However, some limitations need to be considered. When working with datasets based on satellite observations, there is always uncertainty in the retrieval algorithms. Several assumptions underlie the derivation of information about the gas abundance profile from satellite instruments. Depending on the variable, clouds and surface albedo can affect the instrument's view. And with averaging kernels, there are assumptions about the profiles of trace gases, often derived from a model simulation. And the lower in the atmosphere the product shall be, the higher the uncertainty in the value. SWOOSH focuses on the stratosphere, with its lower limit at 316 hPa; however, even at this level, many points are already removed by a quality flag. For H_2O, the developers of SWOOSH recommend using the data only between 100 and 1 hPa; all values below should be used with great caution.

I use SWOOSH as a second comparison dataset in the UTLS, especially for O_3. Regarding H_2O, this means I primarily consider a pressure range below the recommended altitude. However, a comparison on climate scales still offers valuable insights, and good and bad agreements can be captured. In addition to the combined and filled products of H_2O and O_3 (*combinedanomfillh2oq* and *combinedanomfillo3q*), I utilise the included temperature and geopotential height information, which are based on the Modern-Era Retrospective analysis for Research and Applications, Version 2 (MERRA2) reanalysis dataset.

3.5 Simulation strategy

To answer the research questions of this thesis, several EMAC simulations are necessary. While they are performed using the same MESSy model version, minor deviations occur, partly to address the questions and, to some extent, to incorporate the most recent model development. The simulations can be divided into two groups, each with a different optimal model configuration. All groups with interactive chemistry use the chemical mechanism used for CCMI-2022, *mecca_CCMI2-base-02*.

To investigate the EMAC model bias and the effect of Newtonian relaxation on the simulated climate state, two transient hindcast simulations are performed. This configuration involves adjusting boundary conditions and emissions over the specified period to match observed values. The simulations $SD_{transient}$ and $notSD_{transient}$ are transient simulations over the period 1998 to 2019. Specified Dynamics (SD) is a synonym for Newtonian relaxation. They are identical but for the activation of SD against ERA5 in $SD_{transient}$ as described in Section 3.1.4. To better control emissions from biomass burning, the BIOBURN submodel was activated. Fire type and vertical distribution of emissions are available from the Global Fire Assimilation System (GFAS), while the amount of dry matter burned was obtained from the Global Fire Emissions Database (GFED) since this information is only available before the year 2000. The NO_x production by lightning is calculated using the parameterisation for the flash frequency by Price and Rind (1992). $SD_{transient}$ and $notSD_{transient}$ further use the E5 radiation parameterisation, the original scheme of ECHAM5. The meteorological conditions and abundance of the long-living tracers CO_2 and SF_6 for the initialisation of the simulations are taken from an AGCM spin-up simulation I created. The initialisation of the chemical tracers is taken from the EMAC simulation RD1SD-base-01, which was created as an CCMI-2022 contribution. The sea surface temperature (SST) and sea ice concentration (SIC) data are obtained from the ERA5 dataset, ensuring consistency with the forcing by the Newtonian relaxation. The first two years of the simulations are used as spin-up for the full coupled EMAC simulation and are excluded from the investigation. Both simulation setups in the first group are not tuned.

The second group targets the sensitivity of the UTLS composition to the choice of convection parameterisation and resolution under present-day conditions, as well as the robustness of future projections. For future projections, free-running simulations are necessary, and, for consistency, simulations under present-day conditions must also be free-running to compare quasi-equilibrium climate states. A large number of years is necessary for a statistical analysis, which requires substantial computational resources. To reduce the number of years required to identify a signal, the simulations of the second group are time-slice (TS) simulations. To reduce noise from internal variability, the emissions and boundary conditions of a selected year are repeated for all subsequent years, and SST/SIC information is taken from 20-year climatologies.

After an analysis of the year-to-year differences in the emissions to find a year representative for the beginning of the 21st century (see Figures D.2, D.1), I selected the year 2012 for the simulations under present-day conditions. As all future conditions are based on the scenarios, I selected the assumptions for 2100 for the simulations under future conditions. The initial conditions are taken from the EMAC projection simulations prepared for CCMI-2022 under the SSP2.4-5 scenario, RD2-base-01, as a three-member ensemble average of the timestep before 01.01.2012 and 01.01.2100, respectively. To use consistent forcing based on SST/SIC information for present-day and future setups, I also had to rely on information from a model simulation under the SSP2.4-5 scenario. I used SST/SIC climatologies based on the first ensemble member of the MPI-ESM1.2-LR simulations from year 2017 prepared for CMIP6, which coupled the atmospheric model ECHAM version 6.3, the land model Joint Scheme for Biosphere Atmosphere Coupling in Hamburg (JSBACH) version 3.20, the ocean model Max Planck Institute Ocean Model (MPIOM) version 1.63 and the ocean biogeochemistry model Hamburg Model about Ocean Carbon Cycle (HAMOCC) version 6, the Max Planck Institute for Meteorology (MPI-M) Earth System Models (ESM) (Mauritsen et al. (2019), Müller et al. (2018)). The SST/SIC are used as climatologies for the period 2000–2019 for present-day conditions and for the period 2080–2099 for future conditions.

The simulations investigating the sensitivity of the UTLS composition under present-day conditions to the convection parameterisation are called $\mathrm{REF}_{\mathrm{today}}$ and $\mathrm{CONV}_{\mathrm{today}}$. $\mathrm{REF}_{\mathrm{today}}$ uses the TIEDTKE convection parameterisation, $\mathrm{CONV}_{\mathrm{today}}$ EMANUEL. The naming convention also states that TIEDTKE is the reference and default parameterisation, used for all simulations unless otherwise indicated. For the sensitivity study of the model resolution effect on the UTLS composition, I targeted doubling the resolution in both horizontal and vertical dimensions. Due to the triangular truncation of ECHAM, which allows only specific horizontal resolutions, I aimed for the T106L191MA resolution, which has not been used in EMAC studies at climate scales. Increasing the resolution from our standard T42L90MA to T106L191MA corresponds to an increase of more than a factor of 13 in the number of grid points. To fulfil the Courant-Friedrichs-Lewy (CFL) criterion, which describes the relationship between spatial grid size and time step length for a converging solution of a partial differential equation, the time step length of the simulation has to be reduced. For a stable solution, the criterion can be expressed as

$$\frac{u_x \Delta t}{\Delta x} + \frac{u_y \Delta t}{\Delta y} \leq 1 \quad , \tag{3.5}$$

where u_x and u_y are the magnitudes of the wind velocity in x and y direction, and Δx, Δy and Δt the spatial and temporal step sizes. For a stable simulation of an AGCM setup, it was necessary to reduce the time step even further to avoid instabilities due to wave breaking at the model's upper boundary, from 12 minutes in the T42L90MA setup to 2 minutes in the T106L191MA setup. This led to an enormous increase in the computational resources required to run the simulation and in the size of the resulting data output. During the test simulations, it became clear that it was not feasible to run EMAC on a high-resolution setup with interactive chemistry over decades in the time frame of this thesis. Therefore, I decided to run these sensitivity simulations as an AGCM simulation with diagnostics to investigate the differences in dynamics and draw conclusions about the composition changes. $\mathrm{AGCM}_{\mathrm{T42L90}}$, $\mathrm{AGCM}_{\mathrm{T106L90}}$ and $\mathrm{AGCM}_{\mathrm{T106L191}}$ are the simulations with increasing resolution. $\mathrm{AGCM}_{\mathrm{T42L90}}$ has a default horizontal resolution of T42 in spectral space and 90 vertical levels, but without interactive chemistry to identify changes due to missing chemistry rather than to the resolution change.

$AGCM_{T106L90}$ has a T106 spectral resolution, with 90 vertical levels, while $AGCM_{T106L191}$ additionally increases the vertical resolution to 191 levels.

These five simulations show the influence of the convection parameterisation and the resolution on the simulated UTLS under present-day conditions. To compare the five simulations and account for differences between simulated and observed climate, a tedious tuning of each simulation setup has been performed to match the radiative imbalance observed by Johnson et al. (2016). Especially the tuning of $CONV_{today}$ required a large number of test simulations due to limited experience with the Emanuel parameterisation in EMAC for climate studies. The final parameters are provided in Appendix C. Between REF_{today} and $CONV_{today}$, the tuning was performed using only the convection parameterisation parameters.

Finally, to investigate the robustness of climate change projections to convection parameterisations, I repeated the simulations REF_{today} and $CONV_{today}$, using the emissions and boundary conditions for 2100. The simulations are called REF_{future} and $CONV_{future}$.

To make a statement on the climate state of the UTLS region, the 20-year means are compared. Only $AGCM_{T106L191}$ is 10 years long due to the high computational resources required. For direct comparison, only the first 10 years of the reference dataset are used. Table 3.5 provides an overview of all the simulations performed as the basis for this thesis, highlighting the major differences in setup.

Table 3.5: Overview of performed simulations in this thesis. The setup changes between the simulations are highlighted in each column: 'TS?' indicates whether the simulation is a time-slice simulation. If False ('F'), the simulation is a transient simulation with varying emissions and boundary conditions. 'Chemistry?' points out if interactive atmospheric chemistry was included in the simulation. Column 'Today?' indicates whether the emission and boundary conditions are for present-day ('T') or future ('F') conditions. The column 'Used for RQ' lists the Research Questions asked in Section 1.2 that are investigated using the simulation. All simulations use the same setup described above and differ only in the aspects mentioned in the text.

Simulation	TS?	Chemistry?	Today?	Used for RQ
$SD_{transient}$	F	T	T	1
$notSD_{transient}$	F	T	T	1
$AGCM_{T42L90}$	T	F	T	2
$AGCM_{T106L90}$	T	F	T	2
$AGCM_{T106L191}$	T	F	T	2
REF_{today}	T	T	T	3,4
$CONV_{today}$	T	T	T	3,4
REF_{future}	T	T	F	4
$CONV_{future}$	T	T	F	4

There are some additional changes included in the setup between the first and second group. Since the setup must not change between the simulations under present-day and future conditions, the submodel BIOBURN was not used; instead, the CCMI-2022 emission inventory was used directly. To incorporate recent model development, I included the submodel MEGAN to improve the representation of biogenic emissions and replaced E5VDIFF with the updated

Table 3.6: Online-calculated emissions for present-day and future conditions. Emissions are global means over the entire simulation period, rounded to the second decimal digit.

Emission	Unit	REF_{today}	$CONV_{today}$	REF_{future}	$CONV_{future}$
NO_x_Lightning	Tg(N)/yr	4.71	4.99	5.16	5.58
NO_x_Soil	Tg(N)/yr	6.03	6.16	6.48	6.70
MEGAN_CO	Tg(C)/yr	45.54	65.29	52.07	78.86
MEGAN_NMHC	Tg(C)/yr	139.71	199.40	162.49	253.35
Dust	Tg/yr	2708.67	3120.74	2881.19	3250.25
Sea-salt	Tg/yr	4881.57	5027.69	4905.57	4973.13

version, VERTEX. For the flash frequency, the parameterisation by Luhar et al. (2021), a modification of that by Price and Rind (1992), was selected. Finally, as Nützel et al. (2024) found that part of the temperature bias at the tropical cold point in EMAC can be reduced when using PSrad instead of E5, I changed the radiation parameterisation between group one and two to PSrad.

Table 3.6 presents a list of online-calculated emissions for the four TS simulations with interactive chemistry. The emissions depend on meteorology, which differs across convection parameterisations and climate states in present-day and future scenarios. Their values are based on an exemplary year with both present-day and future forcing conditions. For the exemplary year, the two scaled simulations under present-day conditions differ significantly from expectations after scaling. For isoprene, the $CONV_{today}$ simulation agrees well with the desired emission size, while for the individual NMHC species, REF_{today} agrees better (not shown).

For the simulations without interactive chemistry, I need two additional modifications that may affect the UTLS structure. Firstly, the submodel CH4 was included. It calculates the chemical production of H_2O by the oxidation of CH_4 in the stratosphere, which is the most essential chemical source. Secondly, the abundance of GHG must be included in the simulation for a correct calculation of the radiative forcing. As the interactive-chemistry simulations were not finalised before the start of the AGCM simulations, climatologies based on the EMAC simulations for CCMI-2022, RD1-base-01, were used. However, as the ODS emissions differ between the CCMI-2022 setup and the setup used for this work, together with general setup differences and MESSy updates such as the change from E5rad to PSrad. Differences in the individual radiative forcing terms in RAD are expected. Figure D.3 visualises the relative differences in the GHG abundances considered in the RAD parameterisation.

Chapter 4

Effect of nudging on the UTLS characteristics on climate scales

In this chapter, I investigate how Newtonian relaxation affects the simulated UTLS on climate scales. While necessary for model comparison with observations, it remains an open question how it affects the climate state over decades of the EMAC simulation. Furthermore, the analysis offers insight into the model bias in EMAC and the impact that nudging has on it.
As described in Section 3.1.4, the nudging is performed only until the lower stratosphere. In the middle and upper stratosphere, the circulation develops solely from the model's physics. Furthermore, the wave-0 in spectral space is not nudged; therefore, no correction for the global mean model bias at each level is applied.
The chapter ends with a summary and a discussion of the results.

4.1 Differences in the UTLS

In my investigation, I focus on differences across three variables with varying direct nudging effects but high relevance for the climate: temperature, H_2O in the gaseous phase, and O_3. The temperature in the UTLS is nudged towards ERA5 and is therefore most directly affected by it. The abundance of H_2O in the gaseous phase is strongly dependent on the temperature of the air. The transport of H_2O into the upper troposphere is affected by convection in the troposphere, which also depends on temperature. However, because the ERA5 temperature field used for nudging includes diabatic heating and cooling from convective processes, the triggering of convection and cloud formation in $SD_{transient}$ will differ from both the free-running simulation $notSD_{transient}$ and ERA5. The abundance of H_2O in the lower stratosphere is further dependent on the tropical cold point temperature and, therefore, on temperature nudging. The effect of nudging on H_2O is smaller than that of temperature, but more factors affect the abundance; whether nudging improves the abundance relative to observations needs to be investigated. Nudging should have the most indirect effect on the abundance of O_3. Firstly, because O_3 is not directly affected by any of the nudged quantities, and secondly, because O_3 is produced mainly in the stratosphere, above the nudged region. Therefore, differences in O_3 abundance should primarily originate from dynamical differences in the troposphere driving the BDC. To evaluate differences between nudged and free-running simulations, their results are compared with the ERA5 reanalysis and the SWOOSH dataset, based on H_2O and O_3 measurements from satellites.

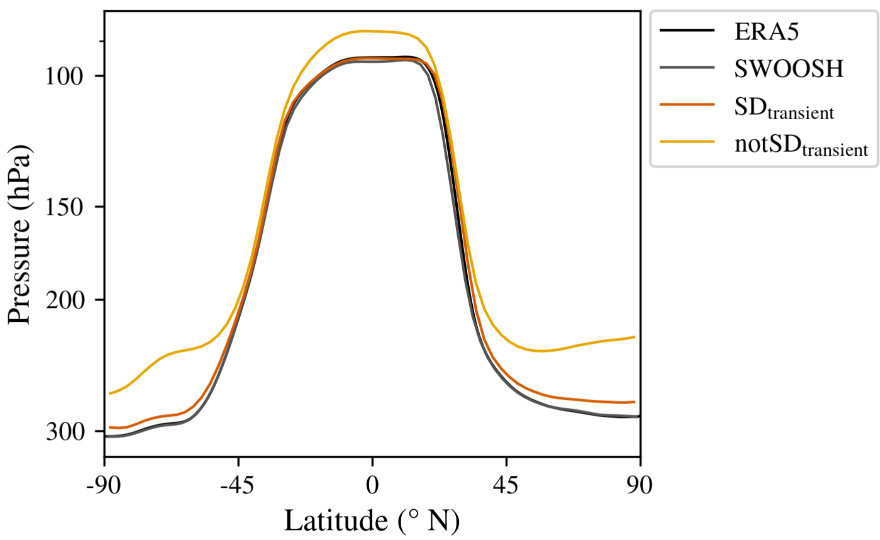

Figure 4.1: Zonal and temporal mean of the WMO tropopause pressure over the period 2000–2019 for the December-January-February (DJF) season.

Figure 4.1 compares 20-year mean WMO tropopause pressures in DJF between the datasets ERA5, SWOOSH, the nudged simulation SD$_{transient}$ and the free-running EMAC simulation notSD$_{transient}$. The WMO tropopauses for ERA5 and SWOOSH are calculated and provided by Hoffmann and Spang (2021). notSD$_{transient}$ shows that EMAC simulates a higher tropopause than observations, while nudging removes most of the bias, as seen for SD$_{transient}$. The WMO tropopauses of ERA5 and SWOOSH strongly overlap over all latitudes. The substantial similarity of the tropopause pressure between SD$_{transient}$ and ERA5 points to a minor effect of the different tropopause calculations, e.g. by other implementations of the second condition of the WMO tropopause.

Figure 4.2 shows the zonal mean statistics of the temperature over the 20 years of the DJF season for the temperature mean, the linear trend and the interannual variability. The linear trend is estimated by linear least-squares regression, and the interannual variability is calculated by subtracting the linear trend from the temperature time series, then computing the standard deviation. The zonal mean statistics are calculated on a tropopause-relative grid relative to the WMO tropopause to exclude the variability of the tropopause height.
ERA5 and SWOOSH closely agree on mean temperature statistics in the UTLS, since SWOOSH temperature information is based on the MERRA2 reanalysis dataset. The EMAC simulations SD$_{transient}$ and notSD$_{transient}$ are colder than the two reanalyses, as can be seen by eye at the tropical cold point temperature. Aside from the intrinsic temperature bias, nudging leads to similar temperature patterns in the UTLS in the case of SD$_{transient}$. The linear temperature trends in the UTLS are not statistically significant almost everywhere, as determined by a Student's t-test at the 0.05 confidence level. Including tropopause variability was not sufficient to detect statistically significant trends with this relatively simple approach. However, the trend pattern and strength correlate strongly between ERA5 and SD$_{transient}$. The opposite trend pattern in the tropics simulated in notSD$_{transient}$ confirms that the high correlation is due to nudging and that

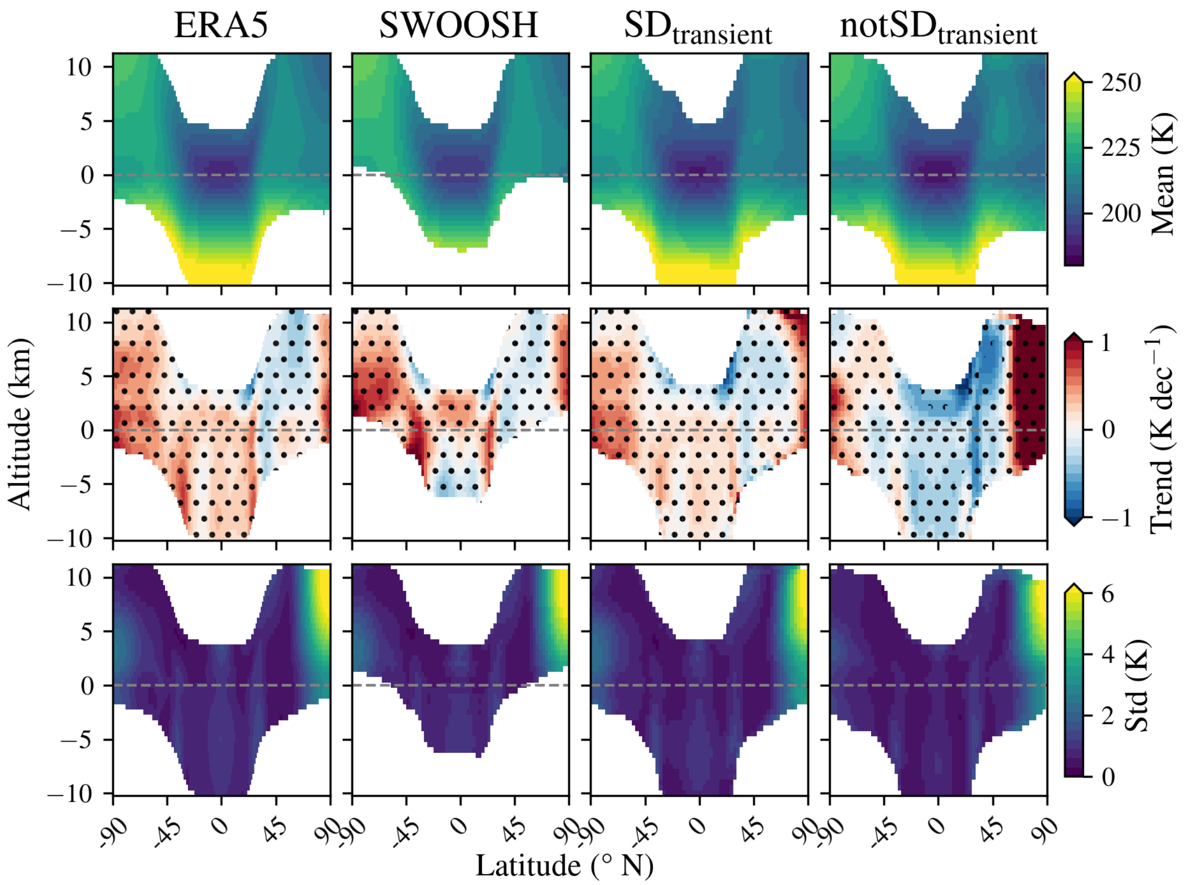

Figure 4.2: Zonal mean statistics of the temperature over the period 2000–2019 for the December-January-February (DJF) season in the UTLS. The data is shown on an altitude grid relative to the WMO tropopause of each dataset. The mean, the linear trend using a least-squares regression, and the detrended standard deviation (top to bottom) for ERA5, SWOOSH, $SD_{transient}$ and $notSD_{transient}$ (left to right) are shown. The dotted areas in the linear regression plots mask not statistically significant trends, as indicated by a confidence level of 0.05 and a two-sided Student's t-test. The grey dashed line indicates the tropopause.

nudging is necessary for EMAC to simulate temperature trends similar to those in reanalysis products. The interannual variability is comparable across all four datasets, as measured by the detrended standard deviation. All share a distinct maximum in the polar winter hemisphere, linked to variability in the polar vortex. Apart from the maximum, $notSD_{transient}$ tends to a lower detrended standard deviation compared to the other datasets in the UTLS, suggesting slightly lower variability, potentially linked to the lower grid resolution.

Figure 4.3 compares the temperature 20-year means in the UTLS against ERA5 to visualise the biases. The not statistically significant regions (stippling), determined by a Student's t-test at the 0.05 confidence level, correlate closely with regions of small differences between the datasets or with regions of large interannual variability at the polar vortex in the NH. Differences between ERA5 and MERRA2 (from the SWOOSH dataset) show a slightly warmer tropical cold point than ERA5 by about 2 K, but otherwise they agree strongly. Since the global mean temperature is not nudged, $SD_{transient}$ shows a uniform cold bias all over the UTLS region by about 3 K.

notSD$_{transient}$ simulates a tropical cold point temperature about 2 K colder than SD$_{transient}$, i.e. about 5 K colder than ERA5. However, the most significant cold bias is simulated around the tropopause in the high latitudes, by up to 10 K in the SH.

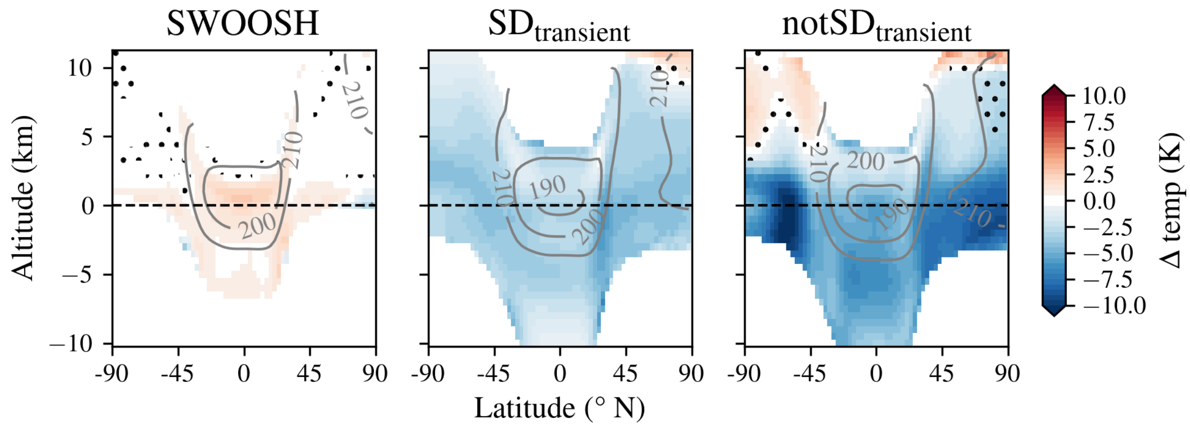

Figure 4.3: Temperature differences of SWOOSH (MERRA2), SD$_{transient}$ and notSD$_{transient}$ relative to ERA5, shown as zonal and temporal means for the period 2000–2019 for season DJF. Differences are shown on an altitude grid relative to the WMO tropopause. Grey solid lines indicate temperature contours, and the grey dashed line marks the WMO tropopause. The dotted areas denote regions that are not statistically significant according to a Student's t-test with a significance level of 0.05.

In the cases of H_2O and O_3, the linear trends in the UTLS are not statistically significant almost everywhere and the interannual variability is dominated by the strong vertical trends of both trace gases. While the trend pattern is still very similar between ERA5 and SD$_{transient}$ for H_2O, there is no resemblance for the O_3 trends. This is at least partly explained by the simplified parameterisations of the stratospheric O_3 chemistry in the IFS model for weather forecasts. Therefore, the statistics bear no further robust similarities or unexpected differences, and I restrict myself to the differences in the mean abundances in the UTLS.

The relative differences between the different datasets and SWOOSH reveal that ERA5 is moister than SWOOSH all over the UTLS, especially in the LMS of the summer hemisphere (Figure 4.4). While H_2O of SWOOSH has to be used with great cautious below 100 hPa (i.e. in the LMS and the tropical UT), due to the H_2O bias in ERA5 discussed in Section 3.4.1, it is justified to assume that SWOOSH is more accurate than ERA5 in the LMS. notSD$_{transient}$ simulates a moist bias in the lowest levels of the LMS which is comparable to ERA5. Apart from that, notSD$_{transient}$ is drier in the tropical UT and the stratosphere than SWOOSH. Comparing the H_2O abundance between SWOOSH and SD$_{transient}$ reveals that the stratospheric H_2O abundance is higher and the dry bias is reduced. However, the moist bias at the lowest levels is strongly enhanced. Larger regions in both hemispheres exhibit a H_2O abundance more than twice as large as in SWOOSH. Therefore, Newtonian relaxation increases the moist bias in the LMS. On a pressure grid, the more substantial moist bias is similarly simulated in both EMAC simulations; however, the higher tropopause, and therefore the higher transport barrier, for instance for convective transport, is responsible for it in the case of notSD$_{transient}$.
Both findings of the H_2O abundance are strongly correlated with the reduction of the cold bias in EMAC by nudging. The warmer tropical cold point in SD$_{transient}$ compared to notSD$_{transient}$

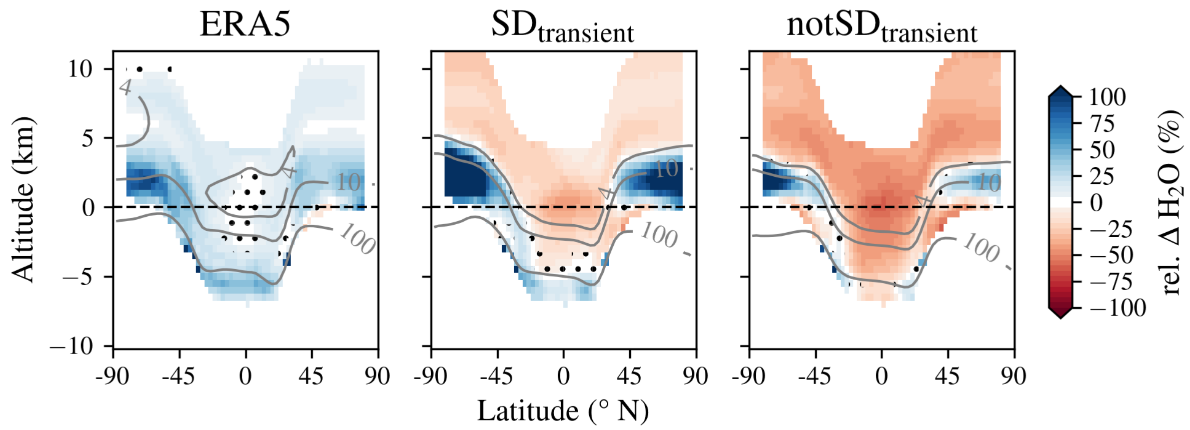

Figure 4.4: Water vapour relative differences of ERA5, $SD_{transient}$ and $notSD_{transient}$ relative to SWOOSH, shown as zonal and temporal means for the period 2000–2019 for season DJF. Differences are shown on an altitude grid relative to the WMO tropopause. Grey solid lines indicate water vapour contours, and the grey dashed line marks the WMO tropopause. The dotted areas denote regions that are not statistically significant according to a Student's t-test with a significance level of 0.05.

allows for more H_2O transport into the stratosphere. In contrast, the warmer lowest levels of the LMS lead to less freezing out of H_2O for direct transport over the tropopause in the midlatitudes. The drier UT is partly connected to the colder temperatures shown in Figure 4.3.

Figure 4.5 compares the O_3 abundance of the datasets, using SWOOSH as the reference. For O_3, the effect of nudging is mostly indirect, mainly due to differences in the atmospheric dynamics and from outside of the nudged region. As O_3 in the UTLS originates from the stratosphere, differences in the abundance are unaffected by tropopause height differences except for the closest region around the tropopause. With that limitation in mind, the O_3 comparison is performed on a pressure grid.
In the tropical UT, ERA5 and both EMAC simulations exhibit a higher O_3 abundance than SWOOSH by more than 50 %, whereas in the tropical LS, they show a slightly lower abundance. In the extratropical LS, relative differences between SWOOSH and ERA5 are mostly negligible. $SD_{transient}$ simulates a higher abundance in both hemispheres, while $notSD_{transient}$ simulates a higher O_3 abundance in the SH (summer) and a lower abundance in the NH (winter). The lower abundance of O_3 around the tropopause in $notSD_{transient}$ is expected, since the tropopause of MERRA2, as used by SWOOSH, is lower, resulting in a comparison of stratospheric air of SWOOSH with tropospheric air in O_3.
To understand the differences in the O_3 abundance between nudged and free-running EMAC simulations, I compare the transport processes towards the UTLS between both simulations.

4.2 Effect on transport processes towards the UTLS

I compare two transport processes into the UTLS between $SD_{transient}$ and $notSD_{transient}$ to understand the differences in the O_3 abundance. The first process is the fast convective upward transport into the upper troposphere. As convection is strongly restricted by the change in sta-

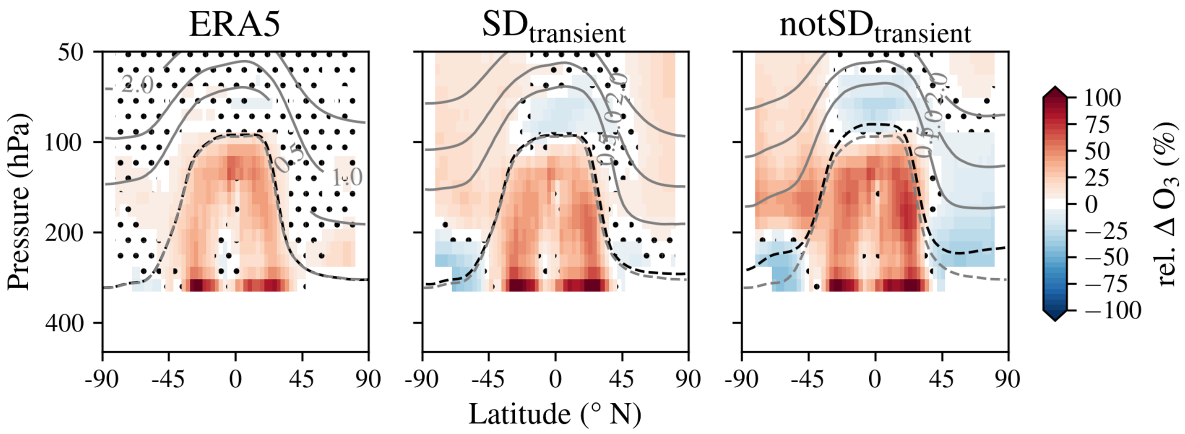

Figure 4.5: Ozone relative differences of ERA5, $SD_{transient}$ and $notSD_{transient}$ relative to SWOOSH, shown as zonal and temporal means for the period 2000–2019 for season DJF. Grey solid lines indicate ozone contours. Grey dashed lines mark the SWOOSH (MERRA2) WMO tropopause, black dashed lines mark the WMO tropopause of each individual dataset. The dotted areas denote regions that are not statistically significant according to a Student's t-test with a significance level of 0.05.

bility at the tropopause, so is its transport of trace gases. However, from the tropical upper troposphere, the trace gases can be transported by the pumping of the Brewer-Dobson Circulation, the second transport process I compare between the EMAC simulations. The stratosphere is not nudged, so the circulation is coupled to its wave forcing. Since the waves originate in the troposphere, their propagation into the stratosphere is affected by nudging of temperatures and winds, and therefore differs between simulations.

In the case of the EMAC setup in this thesis, nudging increases the convective updraft mass flux almost everywhere in the troposphere, leading to more transport in the tropical UT, as seen for instance for H_2O, shown in Figure 4.6. Only in the subtropics, especially around 45° S, $notSD_{transient}$ simulates stronger convective updraft, indicating a stronger convective triggering, suggesting differences in the westerly winds at the STJ region by nudging. To identify resulting differences in the transport from the troposphere to the stratosphere, I use an idealised diagnostic tracer. The E90 tracer has a constant boundary condition at the surface, an e-folding lifetime of 90 days, and no interactions with other tracers or feedback on the dynamics. Differences in the E90 tracer abundance between $SD_{transient}$ and $notSD_{transient}$ are solely connected to differences in the vertical transport. Figure 4.7 compares the E90 tracer abundance in the UTLS. Since the differences are largest around the tropopause, the comparison is performed on a vertical altitude grid relative to the WMO tropopause. In the troposphere, the pattern of the E90 tracer differences correlates with the differences in the convective updraft mass flux. Following the stronger vertical transport in the troposphere, the E90 abundance is larger above the tropopause in the extratropics. In the tropical LS, however, the E90 tracer abundance is slightly larger in $notSD_{transient}$. This is probably related to the higher tropopause, which increases cloud top height and slightly increases the E90 abundance.
The E90 tracer highlights transport barriers near the tropopause and the effect of tropopause-relative coordinates. Due to the higher tropopause in $notSD_{transient}$, a comparison on pressure coordinates (relative to the surface) results in a larger E90 abundance in $notSD_{transient}$ than in

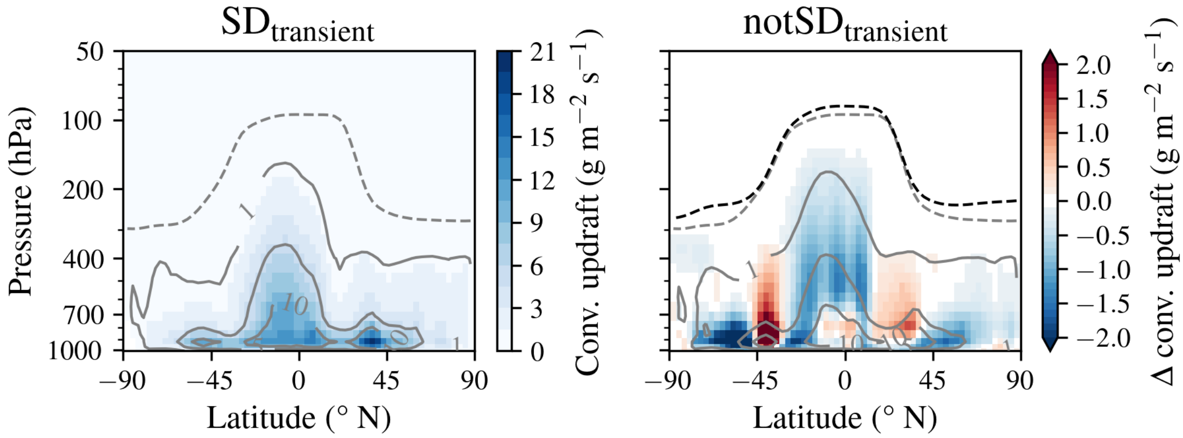

Figure 4.6: Convective updraft mass flux shown as zonal and temporal means for the period 2000–2019 for season DJF. The left panel shows the climatology for $SD_{transient}$, the right panel the difference between $notSD_{transient}$ and $SD_{transient}$. The grey dashed lines indicate the WMO tropopause of $SD_{transient}$, the black dashed line the tropopause of $notSD_{transient}$. Grey contour lines mark the convective updraft mass flux strength for 1, 5 and 10 $gm^{-2}s^{-1}$ for each simulation.

$SD_{transient}$ for all points above the tropopause of $SD_{transient}$. Tropopause-relative coordinates are necessary to include the effect in the comparison.

While the tropospheric transport leads to differences in the O_3-poor air that reaches the UTLS, the stratospheric transport by the BDC is responsible for the transport of O_3-rich air from the tropical stratosphere into the LMS. The differences in the transport strength are highlighted in Figure 4.8 by using the concept of Age of Air (AoA). The AoA is calculated by using an artificial diagnostic tracer with a linear increasing source at the surface and no sinks in the atmosphere. The calculation uses the convolution method as formulated by Wagenhäuser et al. (2024). As reference time series, I deseasonalised the diagnostic tracer time series in the tropics (-17.5°–17.5° N) at 100 hPa to remove differences in the tropical vertical transport in the AoA information. The 100 hPa level is selected to approximate the tropopause height. The tropopause height differs between $SD_{transient}$ and $notSD_{transient}$; however, its effect on vertical transport by the residual circulation is minor and does not affect the AoA result. The AoA reveals that the lowest part of the shallow branch of the BDC that is inside the nudged region is slower in $SD_{transient}$, indicated by an older AoA. In the middle and upper stratosphere, however, AoA is younger by up to 0.4 years, which is evidence for a faster transport by the BDC in $SD_{transient}$. The BDC is driven by the dissipation of Rossby waves, by the dissipation of synoptic scale Rossby waves in the subtropical lower stratosphere and by planetary scale Rossby waves in the upper stratosphere at the polar vortex. Since the sign of the AoA differences changes between the lower and middle/upper stratosphere, nudging must influence propagation differently. The lower AoA in the upper stratosphere for $SD_{transient}$ suggests that nudging from the troposphere to the lower stratosphere favours atmospheric conditions for the propagation of planetary waves.

Figure 4.9 compares the zonal wind field of the EMAC simulation with the data of ERA5. The nudging of the wind divergence and the vorticity until the lower stratosphere leads to

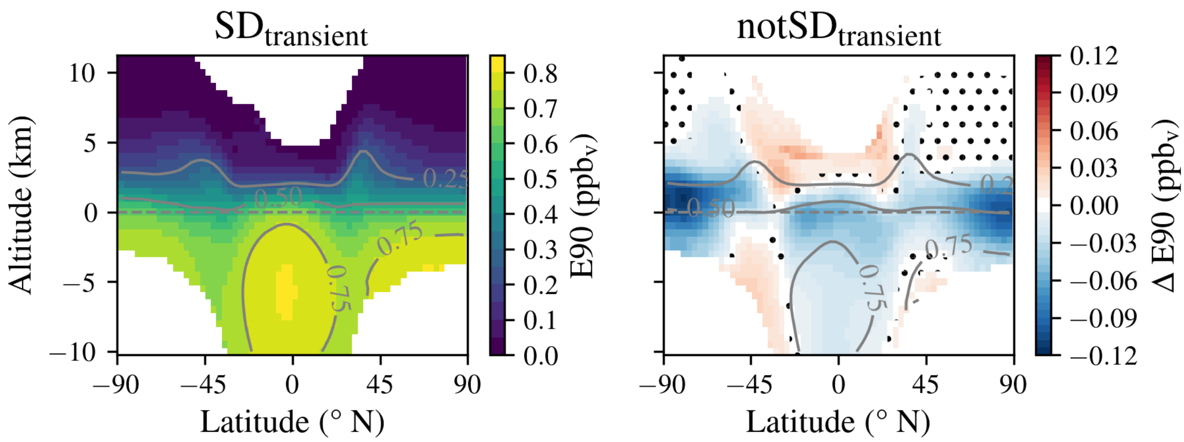

Figure 4.7: E90 tracer abundance shown as zonal and temporal means for the period 2000–2019 for season DJF on an altitude grid relative to the WMO tropopause. The left panel shows the climatology for $SD_{transient}$, the right panel the difference between $notSD_{transient}$ and $SD_{transient}$. The grey dashed line indicates the WMO tropopause. Grey contour lines show the E90 tracer abundance for each simulation. The dotted areas denote regions that are not statistically significant according to a Student's t-test with a significance level of 0.05.

the same zonal wind field between $SD_{transient}$ and ERA5. The free-running EMAC simulation $notSD_{transient}$ results in a smaller latitudinal extent of the strong westerlies at the summer STJ and generally stronger winds in the tropical UT. The stronger subtropical jet leads to a stronger vertical wind shear, which enhances the formation of convection, as seen by the similar pattern for the differences in the convective updraft (Figure 4.6). Over most of the stratosphere of the SH, EMAC simulates stronger easterlies and the change from easterlies to westerlies in the tropics is shifted northwards. In the northern hemisphere, however, the differences between $notSD_{transient}$ and ERA5 are smaller than between the nudged simulation $SD_{transient}$ and ERA5. Nudging of the troposphere and lower stratosphere initiates differences that accumulate in the dynamics of the upper stratosphere, reducing the zonal wind at the polar vortex by up to 8 ms^{-1}. The analysis of the Transformed Eulerian-Mean (TEM) following the formulation by Andrews et al. (1983) implemented into MESSy by Hella Garny associates the weaker polar vortex at least partly with a more substantial deceleration of the zonal wind by planetary Rossby waves. The Eliassen-Palm (EP) flux divergence describes the interaction of waves with the mean flow. The stronger negative divergence in the upper polar stratosphere simulated in $SD_{transient}$ compared to $notSD_{transient}$ (not shown) leads to a more substantial deceleration of the zonal wind and a weaker polar vortex.

The O_3 differences in the LMS results from a combination of processes and are not straightforward to disentangle. The O_3 abundance is generally low, less than 0.8 ppm_v, therefore even minor differences lead to the relative differences of up to 30 % compared to SWOOSH. The significantly stronger transport of O_3-poor air from the troposphere into the winter LMS in $notSD_{transient}$ than in $SD_{transient}$ is sufficient to simulate a lower O_3 abundance than SWOOSH. In case of $SD_{transient}$ the transport of O_3-rich air BDC dominates. In the summer hemisphere, tropospheric transport is weaker, and stratospheric transport dominates. Differences can originate from differences in the chemical removal process during spring, but this cannot be investigated at this point.

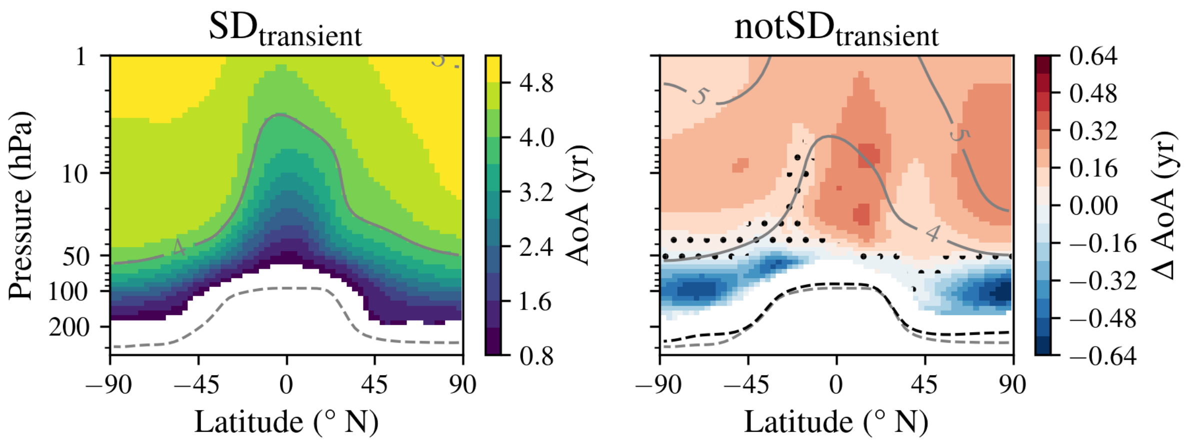

Figure 4.8: Age of Air shown as zonal and temporal means for the period 2000–2019 for season DJF. The left panel shows the climatology for $SD_{transient}$, the right panel the difference between $notSD_{transient}$ and $SD_{transient}$. The grey dashed lines indicate the WMO tropopause of $SD_{transient}$, the black dashed line the tropopause of $notSD_{transient}$. Grey contour lines show AoA for each simulation. The dotted areas denote regions that are not statistically significant according to a Student's t-test with a significance level of 0.05.

In summary, nudging strongly affects the UTLS dynamical characteristics and composition. The nudging of the temperature towards ERA5 reduces the temperature biases at the tropical cold point by about 2 K, and by up to 7 K in the SH around the tropopause. The nudging aligns the temperature profile towards ERA5, leading to a similar static stability and a WMO tropopause in EMAC that closely matches the tropopauses of the reanalysis datasets ERA5 and MERRA2 (based on the information included in SWOOSH). In contrast, the free-running EMAC simulation simulates a WMO tropopause which is up to 50 hPa lower in the extratropics. It shows why nudging is necessary to compare observations of the UTLS with model results. However, next to the positive effect on the stratospheric dry bias in EMAC, nudging increases the moist bias above the tropopause in the extratropics significantly, leading to a H_2O abundance more than twice as large as SWOOSH in both hemispheres. In case of the O_3 abundance in the UTLS, nudging increases the stratospheric transport into the winter hemisphere, leading to a slightly larger abundance than in SWOOSH. In comparison, the free-running EMAC simulation simulates a smaller abundance. The faster BDC is indicated by a younger AoA up to 0.4 years in the nudged EMAC simulation compared to the free-running EMAC simulation.

4.3 Discussion

The analysis revealed several disadvantages of Newtonian relaxation over climate scales and of the configuration in general. Firstly, the cold bias in the extratropics around the tropopause is driven by excessive numerical diffusion, common on the coarse grids of climate models in regions with steep gradients (Stenke et al., 2007). The transported H_2O in the lower stratosphere primarily causes cooling in the region, leading to a cold bias. The fix of the cold bias by changing the temperatures directly, rather than the cause of the cold bias, allows for less freezing out and more direct transport. This leads to the substantial enhancement of the moist bias.

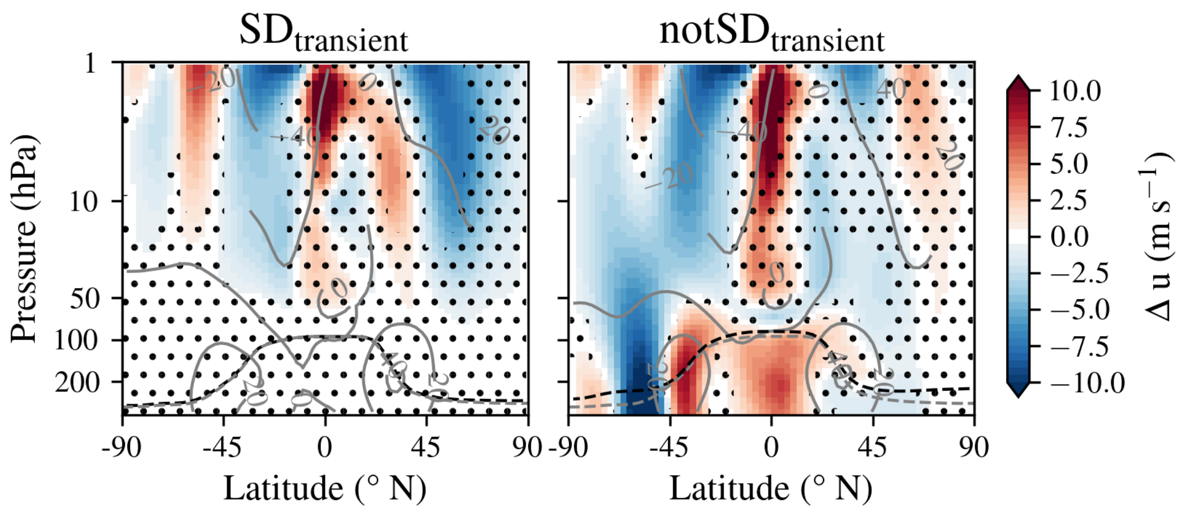

Figure 4.9: Zonal mean differences of SD$_{transient}$ (left) and notSD$_{transient}$ (right) relative to ERA5, shown as zonal and temporal means for the period 2000–2019 for season DJF. The grey dashed lines indicate the WMO tropopause of ERA5, the black dashed lines the tropopause of the shown dataset. Grey contour lines mark the climatological zonal wind field of the EMAC simulations in 20 ms^{-1} increments.

Secondly, the effect on the BDC. Following the results by Chrysanthou et al. (2019), which showed that nudging over the stratosphere decouples the residual circulation from its wave forcing leading to an unphysical transport, I restricted the nudging to the troposphere up to the lower stratosphere. However, as the driving Rossby waves originates from the troposphere, the forcing is still affected by nudging. My results revealed that nudging results in a faster BDC. The faster transport by the deep branch enhances the already too young AoA in models compared to observations (SPARC, 2010; Garny et al., 2024; Abalos et al., 2026). Nudging mainly affects the wave forcing by adjusting the temperature wind field in the troposphere, affecting wave triggering and wave propagation. To allow more waves to propagate into the stratosphere, westerly winds are necessary but they have to be slower than the phase speed of the propagating atmospheric waves, mainly planetary Rossby waves. With the weaker zonal mean wind at the polar vortex in the nudged simulation, planetary Rossby waves propagate higher, which is visible in the larger EP flux divergence, indicating more wave dissipation, stronger reduction of the mean flow and more vigorous pumping, leading to a faster transport. However, a more sophisticated dynamical analysis of the wave propagation differences is necessary to determine the strength of the contribution by waves and the effect by dynamical differences, for instance by differences in the horizontal temperature gradient, creating the polar vortex. To understand the effect of nudging for the synoptic scale Rossby waves and gravity waves, the analysis has to be expanded, for instance using a Fast Fourier Transformation and analysing the different wave numbers.

Thirdly, when free-running and nudged simulations are compared, the differences are inevitably influenced by different climate states. Between SD$_{transient}$ and notSD$_{transient}$there is a difference of 4 Wm^{-2} in the radiative imbalance at the TOA. It is not possible to achieve the same climate state without tuning both simulations independently, but then the nudging effect is no longer isolated. Therefore, the different climate parameters are always a direct consequence of nudging and must be taken in mind in the analysis.

Nudging improves the representation of transport barriers, thereby enhancing the inter-comparison with observations, since simulated air mass characteristics are more realistically distinguished between the troposphere and the stratosphere. Next to a more accurate location of the transport barrier, also the strength of the transport barrier will better align with the reference if a higher resolution dataset such as ERA5 is utilised. However, deficiencies in the LMS composition and the substantial effect on the stratospheric residual circulation indicate that Newtonian relaxation introduces biases into the model results in the UTLS. Therefore, any conclusion about the model's performance from comparisons between observations and nudged simulations over longer timescales must be drawn with care, especially for trace gases such as O_3 with dependence on the stratospheric circulation strength. The benefit of Newtonian relaxation lies in the comparison of tropospheric trace gases and anthropogenic emissions on short timescales, in which the composition is affected by tropospheric transport and the accurate location of weather systems.
For climate studies, free-running model simulations have to use a physically conserved system and to be able to draw conclusions on the model configuration and model performance. Therefore, I don't use any Newtonian relaxation for the following studies in this thesis.

Chapter 5

Sensitivity of the simulated UTLS characteristics to grid resolution and convection parameterisation

In this chapter, I investigate the sensitivity of the simulated UTLS dynamics and composition to EMAC setup changes under present-day conditions by increasing the resolution and using a different convection parameterisation. Since the simulations had to be performed with differently optimised parameter sets (as a result of the tuning for radiative imbalance), I first compare the climate states across the different simulations. This includes the convection, as its parameters are adapted during the tuning process. Afterwards, I focus the sensitivity analysis of the simulated UTLS first on the atmospheric dynamics and subsequently on the chemical composition. The latter is limited to analysing the effect of the chosen convection parameterisation, since the high-resolution could not be performed with interactive chemistry. However, as AGCMs as close as possible to the EMAC simulations with interactive chemistry, they already provide insights into the effects on dynamics and transport to and through the UTLS.
To reduce interannual variability, all simulations in this chapter are time-slice (TS) simulations that repeat the boundary conditions of 2012. The exceptions are diagnostic transport tracers, which require a transient increase of the surface boundary conditions, such as for the calculation of AoA. Therefore, only climatological averages are reasonable for comparison, and fewer years are required for robust climatologies. All simulations were performed over 20 years, but the simulation with finer horizontal and vertical resolution was performed over 10 years due to computational feasibility during my thesis. The effect will be discussed at the end of the chapter.

5.1 The climate states after tuning

A prerequisite for a meaningful analysis in the following chapters is a comparable radiative imbalance for the simulations under present-day conditions. Otherwise, the simulations would drift to a different climate equilibrium. The tuning is performed by varying the parameters of the convection parameterisation to achieve the same radiative imbalance, as discussed in Section 3.3. The tuning is further described in Appendix C, which lists the final tuning parameters for each simulation. Since the tuning is performed using convection parameters, the convection must be investigated separately from the other model results and is compared in this section.

5.1.1 Global climate parameters

Figure 5.1 shows the global and climatological mean radiative components at the top of atmosphere (TOA) for all simulations under present-day conditions. The individual panels show the net longwave (LW) against the shortwave (SW) radiation components. Incoming energy into the Earth's climate system is defined as positive. The horizontal and vertical grey lines define the observed values listed in Table 3.4, and the lighter grey area represents the corresponding uncertainty range. Diagonal lines indicate the sums between the LW and SW components, as shown in the individual subplots. Red colours indicate a positive imbalance between LW and SW, leading to more energy being directed into the climate system. Blue colours show a negative imbalance and less energy in the system when comparing the two radiative components in the subplot.

Panel a. shows the total LW and SW components, referred to as 'all-sky'. For present-day conditions around the year 2010, observations lie both around a value of -240 W m^{-2} and 240 W m^{-2} respectively, with slightly more net incoming SW than outgoing LW radiation, leading to a radiative imbalance of about 0.8 W m^{-2}. All tuned simulations under present-day conditions show an imbalance very close to that observed. However, they differ in the contributions made by the LW and SW components. The three simulations with varying resolutions, $AGCM_{T42L90}$, $AGCM_{T106L90}$, and $AGCM_{T106L191}$, show net component values that are close to the observations. For $AGCM_{T106L90}$, the net radiative components are both higher, cancelling each other out, resulting in the same total imbalance. All tuned simulations with the Tiedtke convection parameterisation reproduce the total radiative components at the TOA well, in agreement with observations. For the simulation with the Emanuel convection parameterisation $CONV_{today}$, however, I achieved tuning to the observed total radiative imbalance only with radiative LW and SW components lower than observations by more than 10 W m^{-2}, far outside the uncertainty range. The respective tuning parameters are acceptable, as the imbalance aligns with the target value. But it suggests further differences in the clouds and cloud-related quantities. As the two convection parameterisations are different by design, differences are expected.

Panel b. shows the 'clear-sky' LW and SW components at the TOA, defined as the radiative components in a cloud-free atmosphere. The spread between the simulations is smaller than for the 'all-sky' components in panel a., and all simulations lie within the uncertainty range of the 'clear-sky' estimates by Loeb et al. (2018) based on observations. The darker grey background indicates the range of uncertainty for both 'clear-sky' data products. Furthermore, all simulations estimate a net positive radiative imbalance in the 'clear-sky' estimation; more energy enters the Earth's climate system than leaves it. All simulations yield a SW 'clear-sky' radiation, with a similar value around 288 W m^{-2}, inside the uncertainty range of observations. The large agreement is expected due to the missing cloud reflection of the incoming irradiation. The Tiedtke simulations have a larger LW 'clear-sky' component than the simulation with the Emanuel convection parameterisation, REF_{today} is larger than $CONV_{today}$ by more than 4 W m^{-2}. The differences indicate differences in the GHG abundance in the atmosphere and differences in the location. The three AGCM simulations have a slightly larger LW component, which increases further with higher resolution. All but $AGCM_{T106L191}$ are below the uncer-

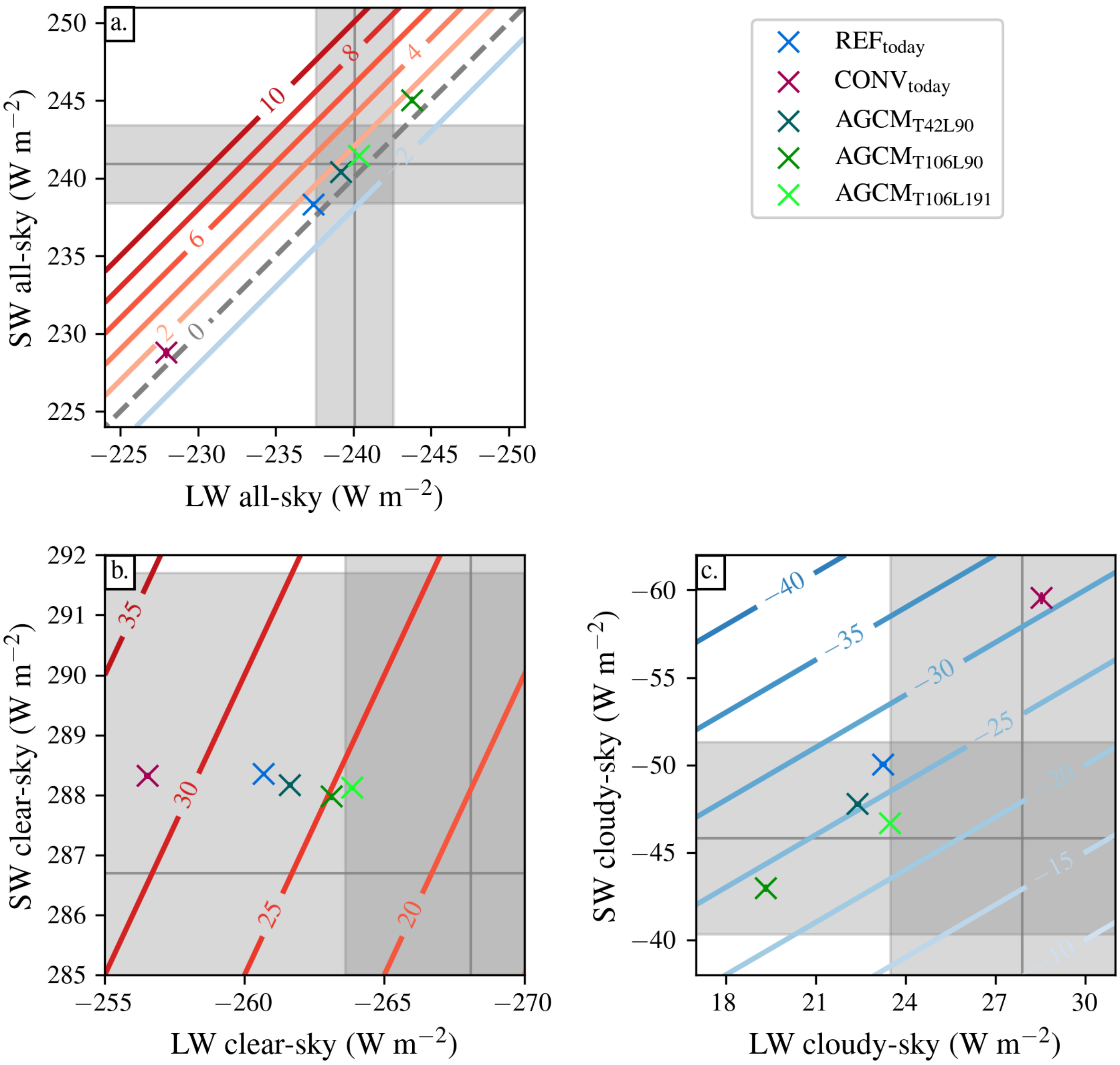

Figure 5.1: Radiative imbalance of all tuned simulations performed and analysed throughout this thesis. Plots show the mean and standard deviation (small) of the radiative components over the entire simulation. Panel a. shows the shortwave (SW) against the longwave (LW) component of the 'all-sky' net radiation at the top of the atmosphere (TOA), meaning a global mean over the entire Earth. Panel b. shows the radiative fluxes of the 'clear-sky' components. Panel c. shows the 'cloudy-sky' component of the net LW and SW radiation, the counterpart to panel b. Coloured diagonal lines represent lines of constant radiative imbalance concerning the shown radiative component, since the radiative imbalance is the sum of the two components. Grey lines and areas indicate the mean and uncertainty range of observations for the radiative components, as provided by Loeb et al. (2018) and listed in Table 3.4.

tainty range of the LW 'clear-sky' observations. Between simulations with varying resolutions, higher resolution increases LW 'clear-sky' radiation.

Panel c. shows the 'cloudy-sky' LW and SW component at the TOA, the counterpart to 'clear-sky' and just the part of the radiative components that result from interaction with clouds. The primary source of SW radiation is solar irradiance; its reflection leads to a net negative effect. LW radiation is mainly outgoing from the Earth; therefore, its absorption and emission downward is a positive effect on the radiation balance at the TOA. The reflection of incoming SW radiation by clouds creates a SW flux more than twice as large as the LW flux that is emitted back to the surface. While the Tiedtke simulation results are within the uncertainty of SW 'cloudy-sky' observation-based estimates, but are lower than the LW observation-based estimates uncertainty, $CONV_{today}$ is close to the mean estimate of LW 'cloudy-sky' but has a 10 W m^{-2} larger SW component. These differences in the 'cloudy-sky' components are the main reason for the differences in the 'all-sky' radiation. REF_{today}, $AGCM_{T42L90}$ and $AGCM_{T106L191}$ are close to LW uncertainty range of observations while $AGCM_{T106L90}$ is lower by about 3 W m^{-2}. Figure 5.1 shows that the differences between the simulations in the SW radiation originate from the differences in the 'cloudy-sky' components, i.e. the abundance of clouds. In contrast, the LW radiation differences differ in the 'clear-sky' component due to differences in the distribution of GHGs and the differences in the abundance of clouds.

Figure 5.2 visualises the differences of important cloud and precipitation climate parameters between the tuned simulations. Panel a. shows the global mean precipitation rate against the global mean cloud cover. Grey lines and background shadings show the means and uncertainty ranges from the observation datasets. While all simulations are within the uncertainty range for the global cloud cover observations, all simulations with the Tiedtke convection parameterisation but REF_{today} yield a too high precipitation rate, with REF_{today} being close to the upper end of the uncertainty range of observations by Adler et al. (2018). The cloud cover in the Tiedtke simulations is lower than the observed mean. $CONV_{today}$, with the Emanuel convection parameterisation, has a precipitation rate lower than the observed mean value and a higher cloud cover. This indicates a lower conversion rate of cloud water to precipitation and a longer cloud lifetime.

Panel b. splits the precipitation rate into the two types in MESSy, convective and large-scale precipitation. They are based on the two MESSy submodels that convert the H_2O in the atmosphere into precipitation, CLOUD (large-scale precipitation) and CONVECT (convective precipitation). Their ratio is an indicator of the performance of the convection parameterisation. Due to the tuning using parameters of the convection parameterisation, the trigger for precipitation can be too high, and CLOUD compensates by producing more precipitation. This unrealistic behaviour should be avoided. For the Tiedtke simulations, CONVECT is responsible for 2/3 of the total precipitation rate, except for $AGCM_{T106L191}$ where it is almost evenly distributed among the two. For $CONV_{today}$, the ratio is reversed; CLOUD is responsible for 2/3 of the total precipitation rate. The higher contribution from convective precipitation is favourable, but this ratio had to be accepted to achieve the targeted radiative imbalance.

Panel c. shows the global mean liquid water path (LWP) over the ocean against each simulation's vertically integrated water vapour. LWP is defined as the vertical integral of water in the liquid state in the atmosphere. Together, they provide information on the total abundance of all water in the atmosphere, except for ice. For LWP over the ocean, observations are available to evaluate model performance. Consistent with the lower precipitation rate, $CONV_{today}$ results in higher atmospheric H_2O abundance in both the gaseous and liquid phases than simulations using the Tiedtke parameterisation. Its LWP over the ocean is slightly higher than the observed mean value. The Tiedtke simulations have LWP below the observed uncertainty range, and higher-resolution simulations are even lower. $AGCM_{T106L191}$ has a H_2O vapour amount in the

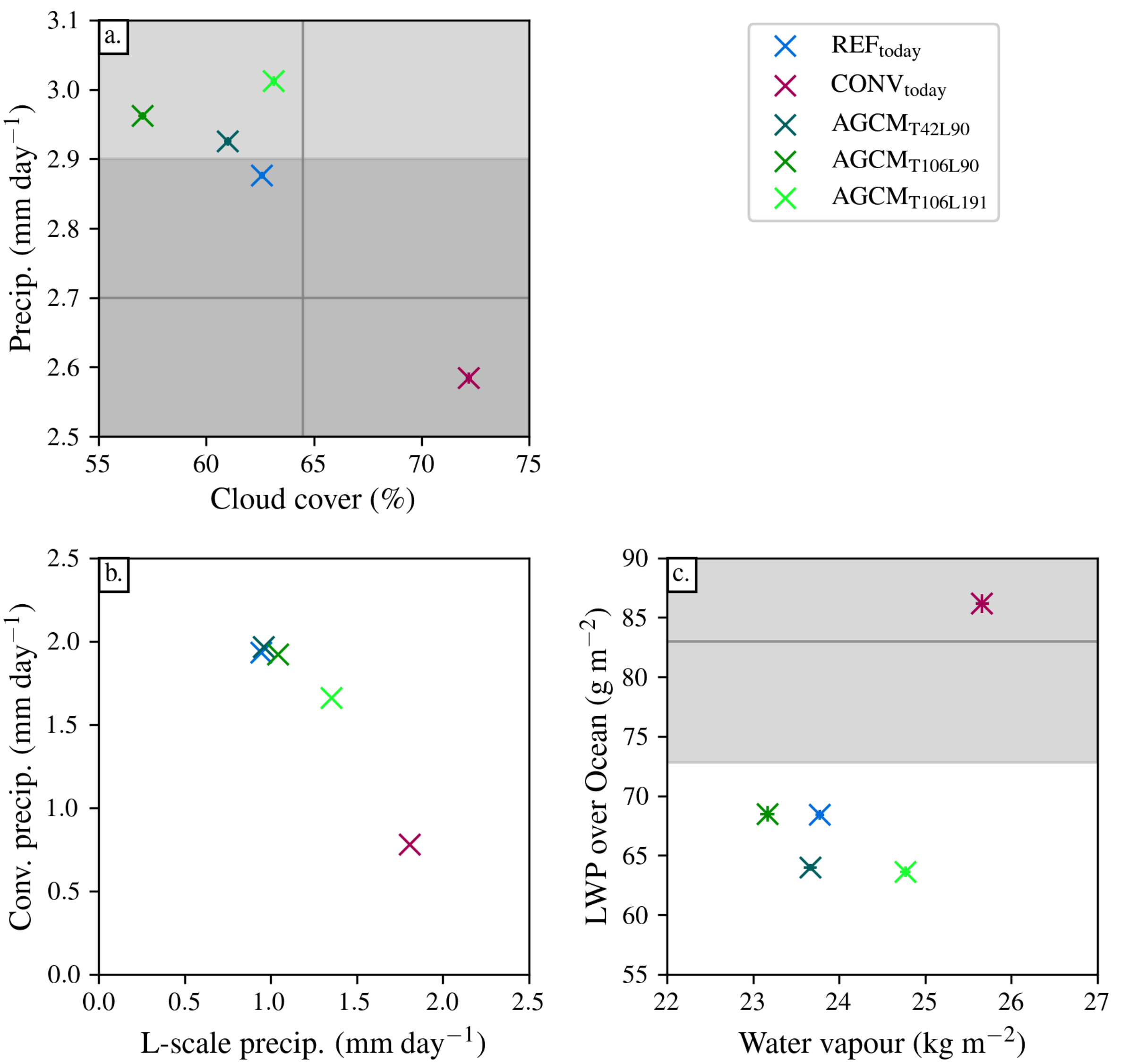

Figure 5.2: Precipitation and water amount of all simulations performed in this thesis. Plots show the global climatological mean and standard deviation (small). Panel a. shows the total precipitation against the cloud cover. Panel b. splits the total precipitation. into the internal precipitation types in MESSy; hence, observations lack this differentiation, and no global reference data exist. Panel c. shows the liquid water path (LWP) over the ocean, the total mass of liquid water in the vertical column per area, against the mass of water vapour (no observations available). Grey lines and areas show the observed global mean values and their uncertainty range. The observation of the precipitation rate is provided by Adler et al. (2018), of the cloud cover by Stengel et al. (2017) and of the LWP over the ocean by Elsaesser et al. (2017).

atmosphere higher than the other Tiedtke simulations but lower than CONV$_{today}$.

The cloud- and water-related climate parameters differ most between simulations with different convection parameterisations. Therefore, I go one step further and compare their spatial differences over the Earth. Figure 5.3 compares the differences in the climatological mean precipitation rate on Earth of REF$_{today}$ and CONV$_{today}$ again with the Global Precipitation Climatology

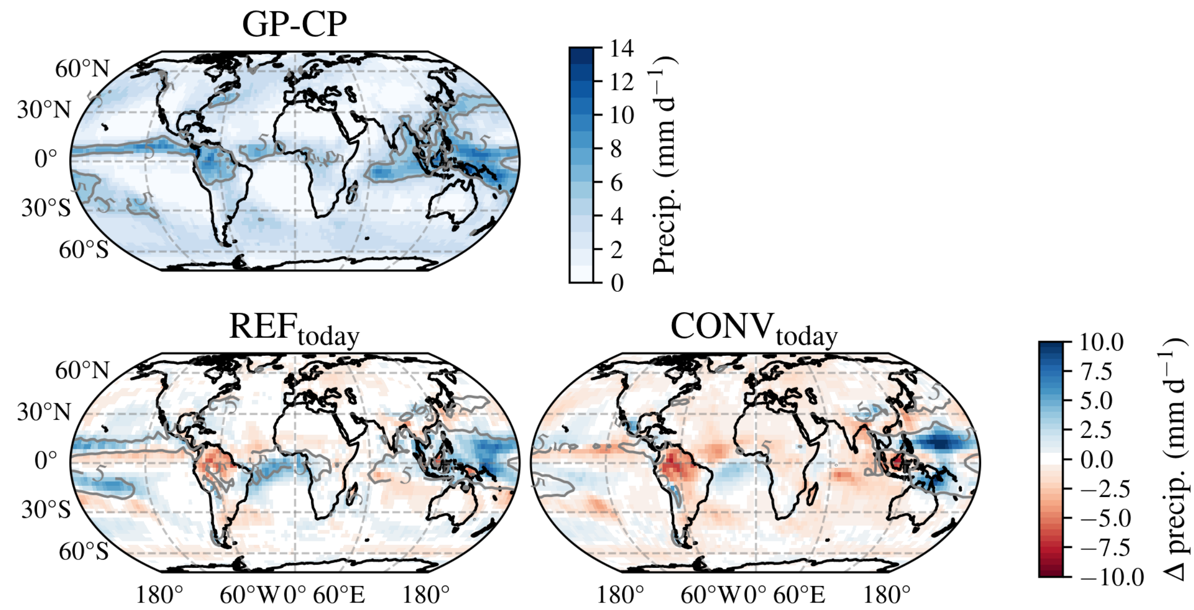

Figure 5.3: Comparison of the annual mean climatological precipitation rates resulting from the TS simulations REF_{today} and $CONV_{today}$ with the GPCP satellite product of the year 2012 (Adler et al., 2018).

Project (GPCP) observational dataset. The highest precipitation rate is measured within the intertropical convergence zone (ITCZ), especially over the Pacific Ocean, over Indonesia. The lowest precipitation rates are measured above the Atlantic and Pacific Oceans in the subtropics. Both simulations show a very similar structure of differences compared to GPCP over the Earth. The largest differences occur in the tropics and subtropics. Instead of an intense precipitation band over the Pacific Ocean at the equator, the simulations have two ITCZs, one north and one south of the equator. This phenomenon of a double-ITCZ is a common artefact in many Atmosphere Ocean General Circulation Models (AOGCM) (Lin, 2007), such as the MPI-ESM model, from which I used the SST/SIC data as forcing data for EMAC (see Section 3.5). The simulations show lower precipitation rates at the ITCZ and higher rates in the subtropics of the SH. The exception is the region of strong precipitation east of Indonesia, where the simulations exhibit an even more substantial precipitation than observed. Most positive differences are more substantial in REF_{today}, while $CONV_{today}$ has more substantial negative differences in the precipitation rate. Except for east of Indonesia, where $CONV_{today}$ also has a stronger precipitation rate. Both simulations simulate a zonal-mean precipitation pattern consistent with GPCP (not shown).

Figure 5.4 compares the cloud cover of REF_{today} and $CONV_{today}$ with observations. Clouds cover a large portion of the Earth. Both EMAC setups simulate lower cloud cover in the mid-latitudes of both hemispheres and higher cloud cover over the polar regions. They exhibit the most substantial negative cloud cover differences, particularly in the subtropics west of the continents, including North and South America, Africa, and Australia. In the tropics, the two simulations differ. REF_{today} tends to a lower cloud cover than observations, while $CONV_{today}$ shows a substantially higher one. These findings are consistent with the theory. Within the ITCZ occurs the most intensive precipitation on Earth. A slower conversion of cloud water and

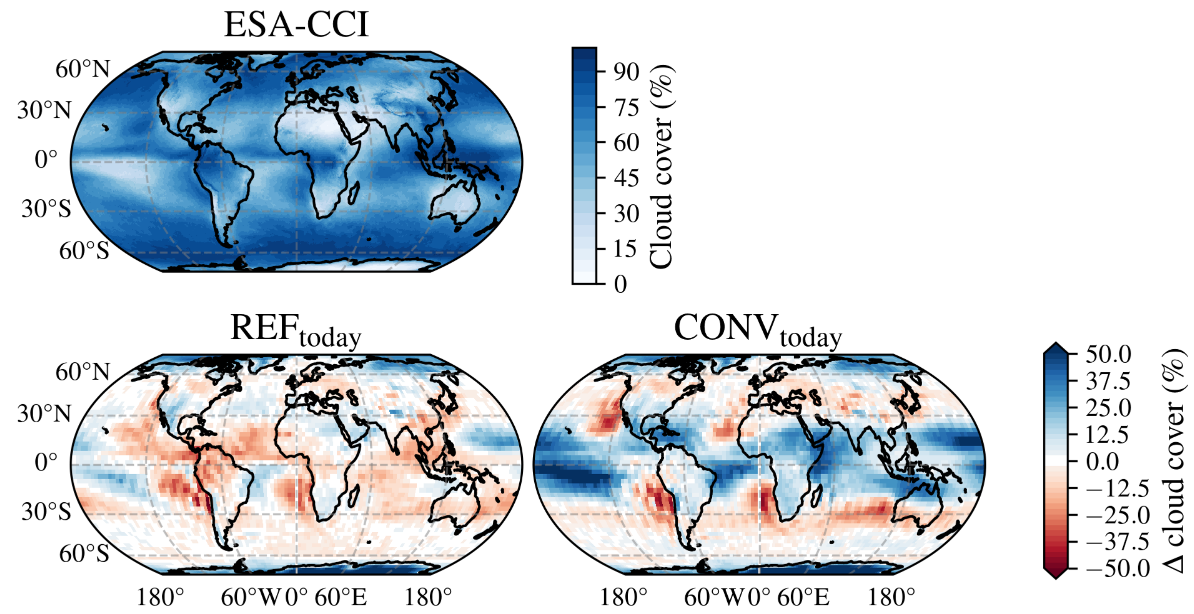

Figure 5.4: Comparison of the climatological total cloud cover resulting from the TS simulations REF$_{today}$ and CONV$_{today}$ with the European Space Agency (ESA) Climate Change Initiative (CCI) global satellite product of the year 2012 (Stengel et al., 2017).

ice into precipitation results in the largest differences in the tropical region.

5.1.2 Comparison of convective quantities

Convection plays a significant role in the fast vertical transport from the boundary layer into the UTLS and substantially contributes to cloud formation. Here, I investigate the differences in the convective quantities between the tuned simulations. During the tuning process, the convection parameterisation parameters were adjusted to improve the simulation of the radiative imbalance. The direct effect on the convective quantities is unintentional and may lead to spurious behaviour. This should be kept in mind and can explain differences between simulations with the same convection parameterisation but different resolutions.

Figure 5.5 shows the cloud cover differences between the tuned simulations, using REF$_{today}$ as the reference. The cloud cover is highest in the UT of the SH polar region in the case of REF$_{today}$ and CONV$_{today}$. It does not occur in any of the AGCM simulations and is likely to be connected to Polar Stratospheric Clouds (PSCs) in the LMS region in both hemispheres. The largest cloud cover in the polar UT is found in the winter hemisphere when comparing seasonal means, supporting the hypothesis that larger cloud cover is associated with PSCs. The cloud cover calculation in all these simulations is based solely on relative humidity, which depends on water vapour abundance and temperature. Investigating the water vapour and temperature on a pressure grid (not shown) reveals that, in the case of AGCM$_{T42L90}$, the polar UT is drier than REF$_{today}$, and the temperatures are similar. In the case of AGCM$_{T106L90}$ and AGCM$_{T106L191}$, the water vapour abundance is similar or even larger, but the polar UT is colder by about 2 K. Both cases result in a lower relative humidity and a lower cloud cover. The largest difference in cloud cover in CONV$_{today}$ compared to REF$_{today}$ occurs in the tropical UT, reaching slightly above the

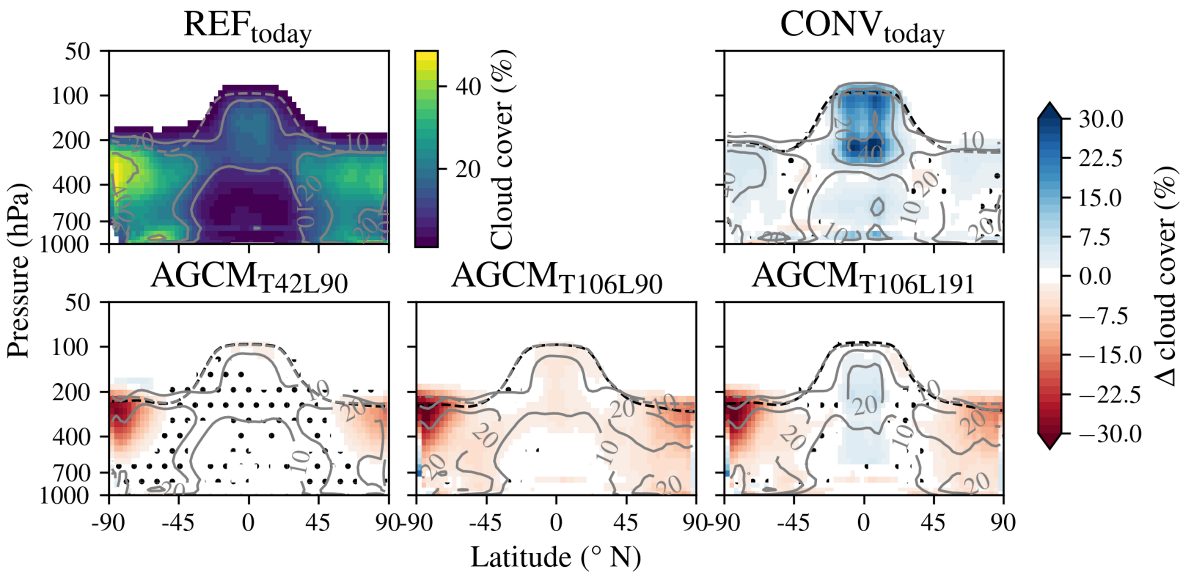

Figure 5.5: Annual climatological differences of the zonally averaged cloud cover between each simulation and REF$_{today}$. For REF$_{today}$ the climatological cloud cover is shown. The grey dashed line marks the WMO tropopause of REF$_{today}$, the black dashed line marks the WMO tropopause of the individual simulation. Solid grey lines mark contour lines of the cloud cover field. Regions with a cloud cover below 1 % are masked out. The dotted areas denote regions that are not statistically significant according to a Student's t-test with a significance level of 0.05.

tropopause. The larger cloud cover, especially in the tropical UT in the climatological mean, corresponds to a higher frequency or a longer lifetime of convection. Except for the UT in the polar region, AGCM$_{T42L90}$ shows only minor and mostly not statistically significant differences in cloud cover. In AGCM$_{T106L90}$ the cloud cover is slightly lower, while in AGCM$_{T106L191}$ the cloud cover is larger in the tropics. The change cannot be attributed solely to the higher vertical resolution or to the different set of parameters in the convection parameterisation, but rather is probably a combination of both.
Tropopause height differences will affect cloud top heights between the simulations and might be visible in the tropical UT of AGCM$_{T106L90}$ compared to REF$_{today}$. While the tropopause height differs the most at higher latitudes, there the influence is masked by the cloud cover reduction due to missing chemistry in AGCM$_{T42L90}$, AGCM$_{T106L90}$ and AGCM$_{T106L191}$.

Figure 5.6 shows the convective vertical updraft (solid) and downdraft (dashed) mass fluxes in the tropics, zonally averaged between -10°–10° N. All simulations with the Tiedtke convection parameterisation exhibit a peak in updraft mass flux near the surface, followed by a steady decrease to 100 hPa. The convective updraft mass flux in the Emanuel convection parameterisation misses the strong peak near the surface and shows an almost constant updraft flux until above 200 hPa. Then the updraft weakens continuously in CONV$_{today}$, but at a lower rate than the Tiedtke simulations. This leads to a stronger convective vertical updraft mass flux in the Emanuel convection parameterisation in the UTLS in the tropics compared with Tiedtke. At the lower boundary of the tropical UT, around 350 hPa, and slightly below the tropopause, the convective updraft is of similar magnitude. This leads to weaker transport into the UT

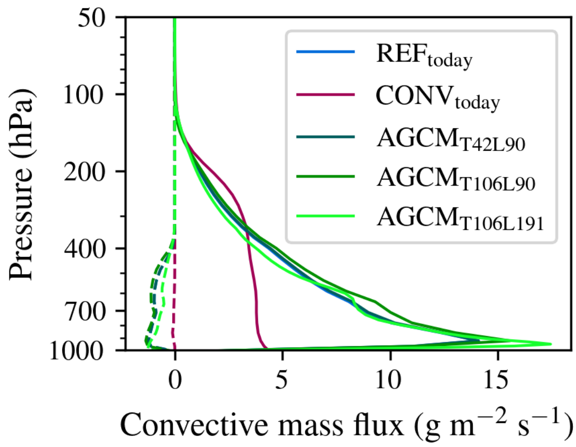

Figure 5.6: Climatological mean of convective mass fluxes, zonally averaged and averaged over the tropics (-10°–10° N). Solid lines denote updraft mass flux (defined as positive), and dashed lines denote downdraft mass flux.

but stronger transport into the LS, since everything that enters the UT in Emanuel is transported more strongly toward the tropopause. The convective downdraft mass flux (dashed) is one order of magnitude smaller than the updraft in the troposphere for the Tiedtke convection parameterisations and even two orders of magnitude smaller for Emanuel. Therefore, the slow transport by the subsidence balances the fast updraft mass flux by convection there. The results show that the convective mass flux to the tropopause is strongly affected by the choice of the convection parameterisation. It is noteworthy that all four Tiedtke simulations agree very well in terms of the strength of convective updrafts and downdrafts. This leads to the conclusion that neither the interactive atmospheric chemistry nor the model resolution has a significant influence on the convection parameterisation, despite the necessary adaptations of the parameter set to match the radiative imbalance.

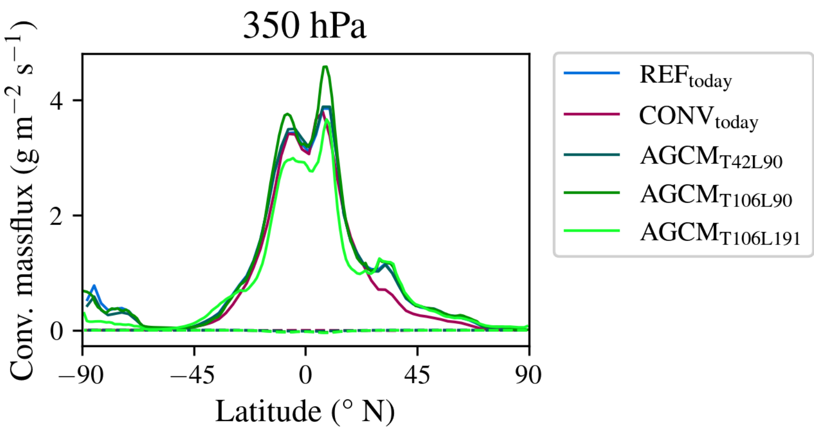

Figure 5.7: Zonally averaged convective updraft (solid lines) and downdraft (dashed lines) mass fluxes at 350 hPa as climatological mean.

Figure 5.7 shows the zonal average of the convective up- (left) and downdraft (right) at 350 hPa, used as a measure for the convective transport into and out of the UT. All simulations have a similar updraft strength at that pressure level. The most substantial differences between REF_{today} and $CONV_{today}$ appear over the SH polar region, where Emanuel lacks vertical updrafts. In the tropics, REF_{today}, $CONV_{today}$ and $AGCM_{T42L90}$, agree closely. While sharing the latitudinal structure, $AGCM_{T106L90}$ exhibits a slightly stronger convective updraft in the tropics, whereas $AGCM_{T106L191}$ simulated a weaker updraft in the tropics as well as in the SH polar region compared to $AGCM_{T42L90}$. The convective downdraft mass flux at 350 hPa is more than two orders of magnitude smaller than the updraft for all simulations; therefore, the fast updraft at 350 hPa is balanced by the slow subsidence. This implies that convection in the UTLS primarily leads to convective upward transport, rather than enhanced vertical mixing.

5.2 Effect on dynamical characteristics

From now on, the analysis focuses on the DJF climatological average instead of the annual climatological average. With that, it is possible to disentangle the model setup effects from those caused by the seasonality of various processes, such as photolytic chemical reactions. I begin with an analysis of differences in dynamics and large-scale transport processes, followed by an investigation of changes in atmospheric chemistry that significantly impact UTLS composition.

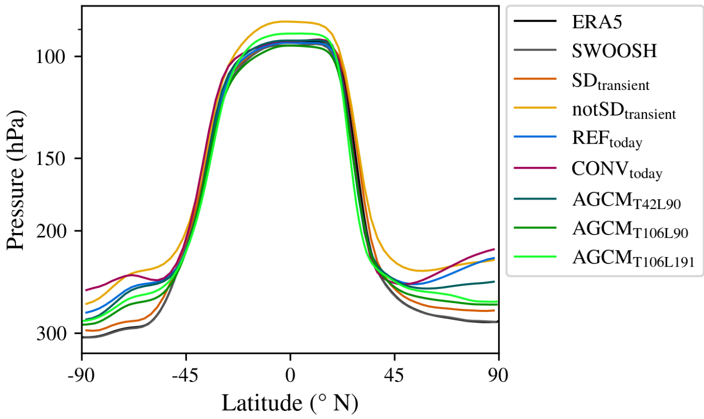

Figure 5.8: Climatological DJF mean of the diagnosed zonally averaged tropopause following the WMO definition. WMO tropopauses of ERA5 and SWOOSH (MERRA2) are provided by Hoffmann and Spang (2021).

Figure 5.8 compares the WMO tropopause pressure across all simulation results under present-day conditions, as well as the datasets ERA5 and SWOOSH (MERRA2), to assess agreement with high-resolution reanalyses directly. While all EMAC simulations, except $notSD_{transient}$ agree closely with the observations in the tropics, the differences are larger in the higher latitudes. An increase in horizontal resolution in $AGCM_{T106L90}$ and $AGCM_{T106L191}$ results in a lower tropopause (higher pressure), indicating an improvement relative to the reanalysis datasets. The effect is more substantial in the NH, the hemisphere in winter. Interestingly, $AGCM_{T106L90}$ simulates a lower tropopause than $AGCM_{T106L191}$ does, which also incorporates a higher vertical resolution. In the tropics, $AGCM_{T106L191}$ simulates the highest tropopause among all TS simulations. Therefore, $AGCM_{T106L90}$ performs best among all free-running EMAC simulations concerning the tropopause pressure. In the SH, the tropopauses between the simulations with the Tiedtke convection parameterisation agree well, $CONV_{today}$ shows the highest tropopause, even higher than $SD_{transient}$ in the polar region. In the NH, REF_{today} and $CONV_{today}$ show lower tropopause pressure at higher latitudes, whereas this is not observed in the reanalyses or AGCM simulations. This implies an effect of atmospheric chemistry on the vertical temperature profile, in combination with differences in the composition of GHGs in the atmosphere (Figure D.3.

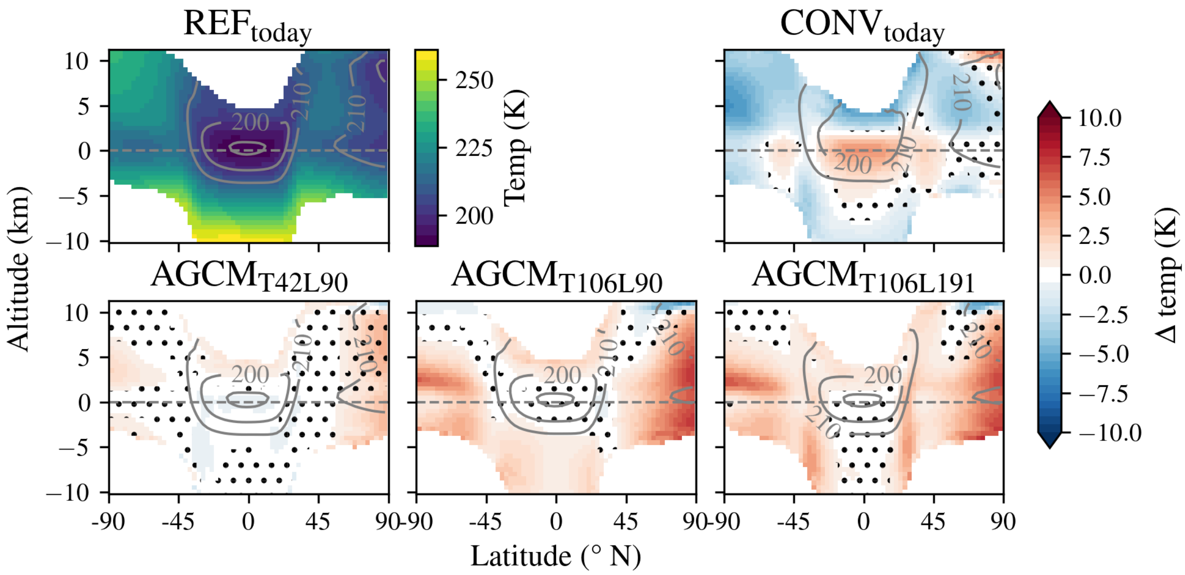

Figure 5.9: Temperature differences between the sensitivity simulations and the reference simulation REF_{today} (upper left). Shown are zonal mean temperature differences between the climatological mean temperatures in season DJF in the UTLS on an altitude grid relative to the WMO tropopause pressure (grey dashed lines) of the corresponding simulation results. REF_{today} shows the temperature climatology. Grey solid lines represent temperature contour levels for each simulation. Dotted areas are not statistically significant, according to a Student's t-test at a 0.05 confidence level based on DJF means per year.

Figure 5.9 shows the temperature in the UTLS region of REF_{today} and the temperature differences of the sensitivity simulations. To account for the differences in tropopause pressure and the major differences in the temperature occurring around the tropopause, the comparison is performed on an altitude grid relative to the WMO tropopause. To maintain focus on the UTLS region, only the EMAC data in the range of 500–50 hPa are interpolated onto the relative grid. Compared to REF_{today}, $CONV_{today}$ is warmer around the tropical tropopause and the cold point, and colder elsewhere, with a maximum in the LMS of the Southern Hemisphere. The double sign change in the tropical temperature differences implies different temperature gradients and, therefore, differences in the static stability with different convection parameterisations. Furthermore, since Emanuel simulates warmer temperatures around the tropical cold point, the Tiedtke convection parameterisation is at least partly responsible for the cold bias at the tropical cold point seen in most EMAC simulations. Without chemistry, but with the same resolution ($AGCM_{T42L90}$), the temperature differences are small and not statistically significant, as determined by a Student's t-test and a confidence level of 0.05. However, it is not possible to isolate the effect of the chemistry on the temperature, since the GHG abundances in REF_{today} are higher in the lower atmosphere than in the climatologies used as input for the radiation scheme in the simulations without chemistry (see Figure D.3). This leads to additional tropospheric warming, which blurs the effect of interactive chemistry. In the northern hemisphere, the polar UTLS in $AGCM_{T42L90}$ is warmer. On a pressure grid, the temperature differences in the polar UT are insignificant, indicating differences in the temperature profile due to a lower cloud cover. Increasing the horizontal and vertical resolutions ($AGCM_{T106L90}$ and $AGCM_{T106L191}$) results in a warmer UTLS, with maxima in the temperature differences in the LMS in both hemispheres, more pronounced in the winter hemisphere. As seen in chapter 4, EMAC in its default resolution and the Tiedtke convection parameterisation simulates a cold bias at the tropical cold point and the LMS above the tropopause. Therefore, the finer resolution reduces the cold bias in the LMS. At the tropical tropopause, differences are not statistically significant.

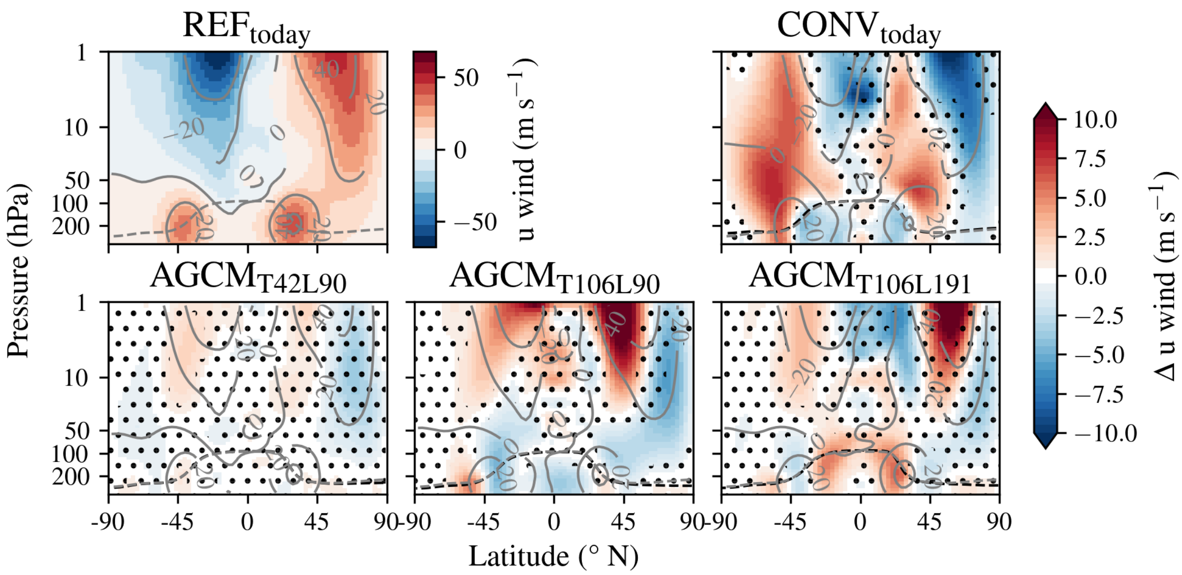

Figure 5.10: Zonal wind differences between the sensitivity simulations and the reference simulation REF_{today} (upper left). Shown are zonal mean differences between the climatological mean zonal wind in season DJF over the stratosphere. REF_{today} shows the climatology. Grey solid lines are zonal wind contour levels of the individual simulation. The grey dashed line is the climatological mean of the WMO lapse rate tropopause of REF_{today}, and in black the tropopause of the individual sensitivity simulation. Dotted areas are not statistically significant, according to a sStudent's t-test at a 0.05 confidence level based on DJF means per year.

Figure 5.10 compares the zonal wind speed between the sensitivity simulations over the stratosphere. $CONV_{today}$ simulates a substantially different wind field than REF_{today}, pointing to substantial dynamical differences due to the convection parameterisations. In $CONV_{today}$ the STJ is located further poleward than REF_{today}, and it further exhibits a weaker stratospheric polar jet. Additionally, the strong wind speeds around the STJ and the stratospheric polar vortex are less separated, the zonal wind speed between the two jet streams is faster in the case of $CONV_{today}$.

Interactive chemistry has almost no effect on the zonal wind, leading to small and mostly not statistically significant zonal wind differences between $AGCM_{T42L90}$ and REF_{today}. Increasing the resolution, however, shifts the STJ and the polar vortex. The largest differences are found at the strong wind speeds in the upper stratosphere. Interestingly, $AGCM_{T106L90}$ simulates larger differences in the zonal wind in the stratosphere compared to REF_{today} than $AGCM_{T106L191}$.

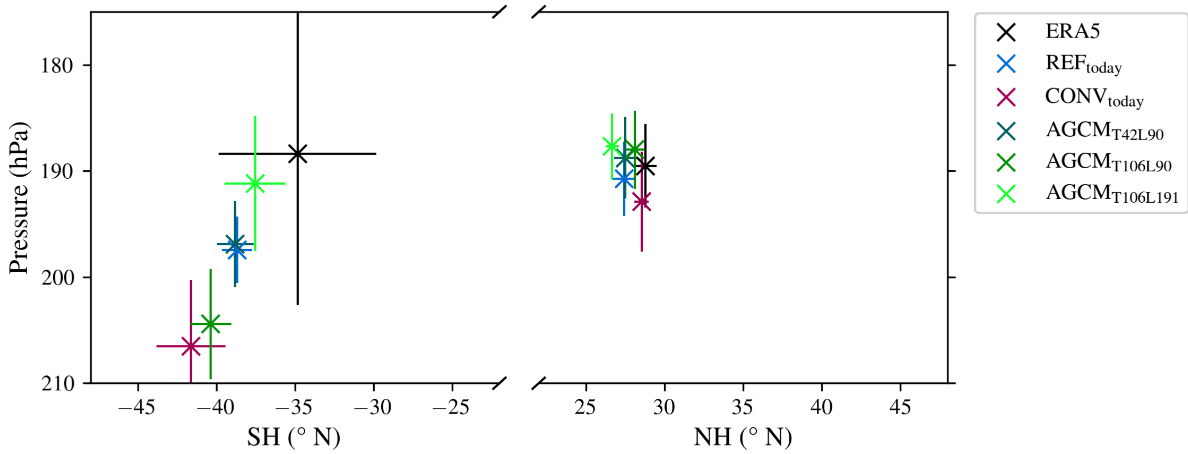

Figure 5.11: Climatological STJ position in DJF for the sensitivity simulations and ERA5. The mean position (cross) and standard deviation (error lines) in latitude and pressure are shown.

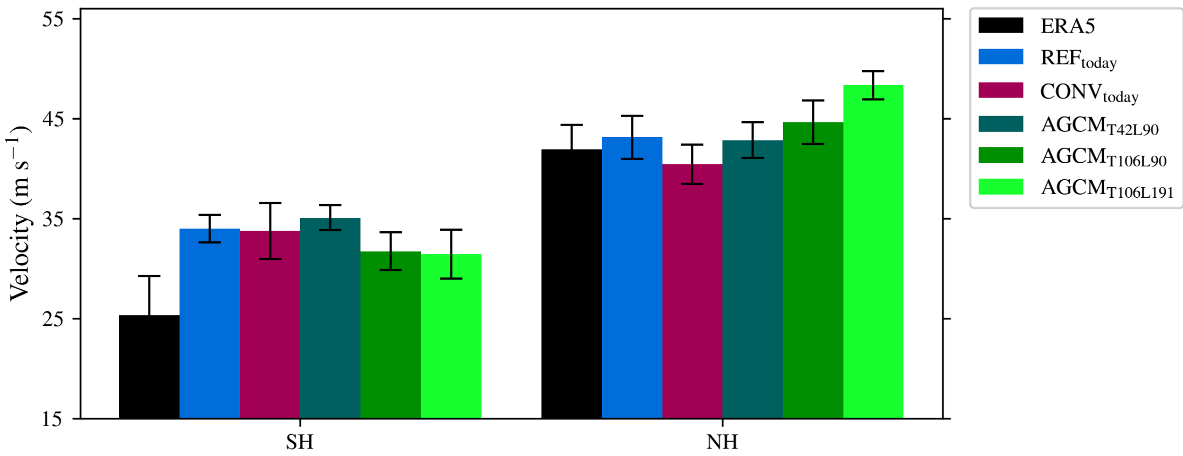

Figure 5.12: Climatological STJ mean (bars) wind speed and standard deviation (error bars) in DJF for the sensitivity simulations and ERA5.

Increasing the vertical resolution counteracts the effect of increasing the finer horizontal resolution. This effect can be seen clearly for the contradicting zonal wind differences in the tropical UT, close to the STJ.

Figure 5.11 compares the differences in the STJ core location. The latitude of the STJ core is calculated using the TropD package written by Adam et al. (2018). The pressure at the core is calculated by calculating the zero crossing of the gradient of the zonal wind speed at the STJ latitude in the logarithmic pressure profile. While all simulations agree closely with the position of ERA5 for the STJ in the winter hemisphere (NH), the location varies substantially with the weaker STJ in the summer hemisphere (SH). CONV$_{today}$ simulates the lowest STJ across all simulations, the furthest away of the STJ location in ERA5. In ERA5, the summer STJ is equatorward of the EMAC simulations. The much larger variability is caused by transient changes over 20 years rather than time-slice simulations, and is probably further enhanced by the higher resolution. AGCM$_{T106L191}$ matches the location of the STJ in the SH the closest among all simulations, while $AGCM_{T106L90}$ is further away, closely to $CONV_{today}$. The different STJ location is consistent with the discrepancy in the tropical UT zonal winds.

The comparison of the wind speed at the STJ core (Figure 5.12) reveals that the differences in the maximum wind speed are not correlated with differences in the location. While the wind speed of the stronger winter STJ is matched very closely by the simulations with the default T42L90MA resolution, $AGCM_{T106L90}$ and $AGCM_{T106L191}$ calculated higher wind speeds, with $AGCM_{T106L191}$ calculating higher wind speeds by about 3 ms^{-1} compared to ERA5. The weaker STJ in the summer hemisphere is overestimated by all EMAC simulations. The convection parameterisation and the use of interactive atmospheric chemistry have little effect on the STJ wind speed, and higher resolution reduces it only slightly. The differences in the STJ may affect the location of wave dissipation in the LS as well as the occurrence of mixing.

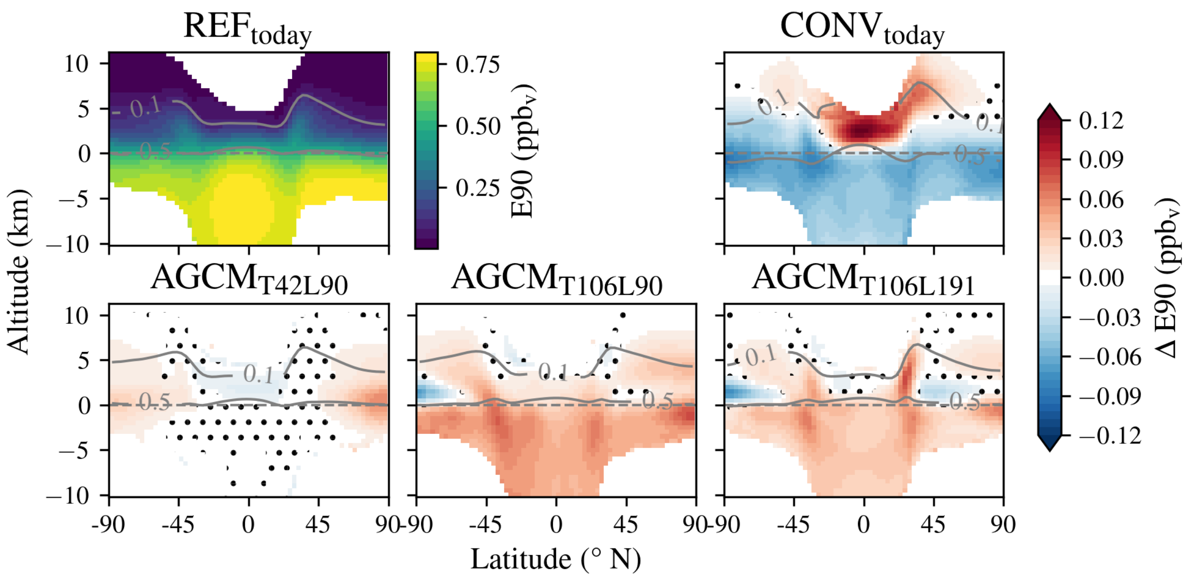

Figure 5.13: Same as 5.9 but for the diagnostic E90 tracer.

To investigate differences between simulated tracer transport to the UTLS region and throughout the atmosphere driven by large-scale processes, I use artificial, inert diagnostic tracers. They are independent of other tracers, have single and idealised sources and sinks, and do not exert any feedback on the dynamics. Therefore, they can be used to isolate the effect of transport by reducing the noise due to additional sources and variability.

The E90 tracer has a constant boundary condition at the surface, an e-folding lifetime of 90 days, and no interactions with other tracers or feedback on the dynamics. With its idealised exponential decay and its homogenous source at the surface, it can be used to investigate the transport strength from the surface into the UTLS region. Figure 5.13 shows the differences in the E90 tracer abundance between the sensitivity simulations and REF_{today} in the UTLS region. As the differences are maximised around the tropopause, the comparison is performed in tropopause-relative coordinates. The Tiedtke simulations yield a larger E90 abundance in the UT and LMS, and the Emanuel simulation $CONV_{today}$ yields a higher abundance in the tropical LS. The result shows a stronger transport from the troposphere into the stratosphere using the Emanuel convection parameterisation. $AGCM_{T42L90}$ simulates a smaller E90 abundance in the

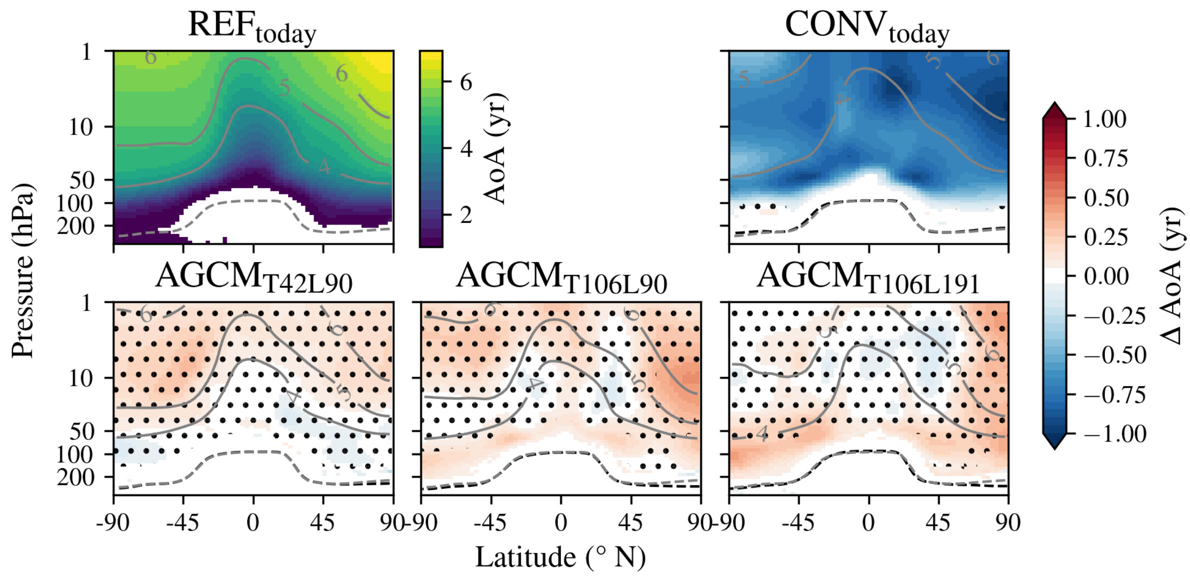

Figure 5.14: Same as Figure 5.10 but for AoA. The reference point is at 100 hPa in the tropics.

tropical LS but a larger one in the LMS regions, suggesting a stronger transport through the STJ region in simulations without interactive chemistry. Increasing the resolution increases E90 abundance in the UTLS, except in the LMS directly at the tropopause. In AGCM$_{T106L90}$ this is mainly the case in the SH, in AGCM$_{T106L191}$ the reduction appears in both hemispheres. At the latitudes of the STJs and below the tropopause in the NH polar regions, positive maxima in the E90 abundance difference are found. They suggest a stronger transport barrier at the tropopause in combination with the jet differences. While the transport through the STJ regions is reduced, a finer resolution appears to exhibit more transport into the LS on the upper edge of the STJ, encouraged by a slightly shifted and stronger jet compared to REF$_{today}$. The result is stronger above the STJ in the NH, the stronger winter jet.

As seen in Figure 5.6, the convective updraft by the Emanuel scheme is weaker than by the Tiedtke scheme below the UT and stronger in the UT. The main outflow region of Emanuel lies higher than that of Tiedtke, allowing for easier transport into the tropical stratosphere. However, the generally stronger updraft in Tiedtke results in a higher abundance in the UT. The higher abundance in the UT is responsible for the higher abundance in the LMS, as it is dominated by adiabatic and horizontal transport through the STJ region from the UT. Due to the significant differences in the convective updraft and the height of the main convective outflow, the E90 tracer abundances in the UTLS differ strongly between REF$_{today}$ and CONV$_{today}$. These differences prevent any conclusion about the strength of the transport barrier between simulations with different convection parameterisations. For AGCM$_{T106L90}$ and AGCM$_{T106L191}$, the results of the E90 tracer abundance cannot be explained by the differences in the convective transport. While the stronger updraft mass flux at 350 hPa for AGCM$_{T106L90}$ compared to AGCM$_{T42L90}$ is consistent with the larger E90 abundance, AGCM$_{T106L191}$ contradicts the hypothesis to attribute the increase solely to the convective updraft mass flux.

To investigate differences in the simulated stratospheric large-scale transports, I rely on AoA. As in Chapter 4, AoA is calculated using the convolution method as formulated by Wagenhäuser et al. (2024). However, due to different available information, the calculation in this

chapter is based on a CO_2 tracer. Therefore, deviations in AoA are expected between chapters, but within a chapter the definition is consistent and allows statements about the strength of the BDC. Choosing 100 hPa in the tropics as the reference location removes differences in convective transport in the tropical troposphere as seen in Figure 5.6. 100 hPa in the tropics matches closely with the tropopause pressure. Since the vertical transport does not vary strongly at the tropopause, differences in the tropopause pressure between the simulations do not affect the result of the AoA calculation.
Figure 5.14 shows the comparison of the AoA between the different simulations. A younger AoA denotes a faster transport. $CONV_{today}$ simulates a faster transport through the stratosphere, which is faster in the NH (winter) than the SH (summer), as a result of a faster transport by the BDC. Without interactive chemistry, the stratospheric transport tends to be slower; however, most of the differences in AoA are not statistically significant, except for a slower transport by the shallow branch in $AGCM_{T106L90}$ and $AGCM_{T106L191}$. They both show older AoA in the polar winter stratosphere, indicating a stronger polar vortex, which is consistent with the comparison of the zonal wind (Figure 5.10).
Since AoA in the middle and upper stratosphere can be dominated by a faster transport of the shallow branch, I further compare the meridional and vertical residual wind speeds, Figure 5.15 and 5.16 respectively, following the formulation of the Transformed Eulerian-Mean (TEM) theory by Andrews et al. (1983), implemented into the MESSy tools by Hella Garny. The analysis reveals that the entire stratospheric circulation is increased in the case of $CONV_{today}$ compared to REF_{today}, for the shallow and the deep branch of the BDC. An increase (decrease) in v^* in the upper stratosphere at the polar vortex is connected to a stronger (weaker) deceleration of the zonal wind by wave interaction, as resulting from the comparison of the EP flux divergence (not shown), indicating more (less) wave driving. The comparison of v^* further reveals for $CONV_{today}$ a reduced poleward transport by the residual circulation in the tropical UT in both hemispheres compared to REF_{today}. It indicates weaker horizontal transport of the tropical UT into the extratropical LS, contributing to reduced E90 abundance and a negative maximum in the differences in the STJ region. For $AGCM_{T106L90}$, a weaker v^* in the tropical UT is simulated mainly around the equator. In the case of $AGCM_{T106L191}$ on the other hand, the poleward transport to the STJ in the northern hemisphere is increased. In the upper stratosphere, v^* confirms the reduced poleward motion due to the stronger polar vortex in the case of $AGCM_{T106L90}$ and $AGCM_{T106L191}$.
The comparison of w^* confirms the higher reaching convective updraft in the tropical UT reaching above the tropopause in the case of $CONV_{today}$. In the stratosphere, the vertical residual wind is statistically significantly stronger until the upper stratosphere. In simulations with a finer resolution, the vertical meridional wind in the stratosphere is weaker, consistent with the older AoA compared to REF_{today}.

The investigation of transport mechanisms in the troposphere and stratosphere reveals substantial differences between the sensitivity simulations, which will contribute to differences in the UTLS composition.

5.3 Effect on chemical composition

While technically the simulations $AGCM_{T42L90}$, $AGCM_{T106L90}$ and $AGCM_{T106L191}$ are AGCM simulations without detailed atmospheric chemistry, there is one exception: H_2O. For a real-

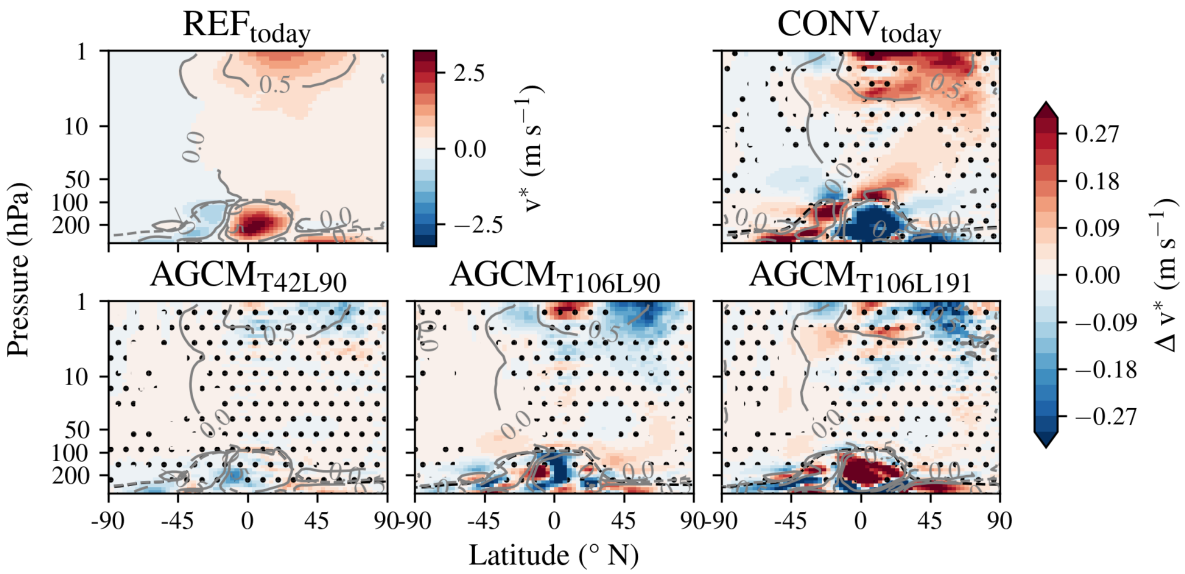

Figure 5.15: Same as Figure 5.10 but for meridional residual wind speed v^*. Positive wind speeds are northwards.

istic H_2O distribution in the stratosphere, the primary chemical production by CH_4 oxidation has to be included. This is done for the three simulations using the submodel CH4. Apart from the analysis of the H_2O vapour abundance in the UTLS, the other trace gas differences under present-day conditions can only be investigated for sensitivity to the convection parameterisation using REF_{today} and $CONV_{today}$.

The H_2O vapour abundance in the UTLS region is shown in Figure 5.17 as relative difference to REF_{today}. The comparison is performed on tropopause-relative vertical coordinates, as the differences with $AGCM_{T106L90}$ and $AGCM_{T106L191}$ are largest around the tropopause. Due to the generally dry nature of the stratosphere, differences in the total abundance by a few ppm_v result in large relative differences. $CONV_{today}$ yields a higher H_2O abundance in the entire UTLS, small relative differences in the UT and directly above the tropopause in the extratropics and polar regions. In the tropical UT and LS $CONV_{today}$ reaches 200 % higher abundances than REF_{today}. The three AGCM simulations yield a drier stratosphere than REF_{today}. This is at least partly caused by the lower CH_4 abundance in the climatology used for the RAD scheme compared to REF_{today} (see Figure D.3). Differences in the LS between $AGCM_{T42L90}$ and $AGCM_{T106L90}$ and $AGCM_{T106L191}$ appear only in the LMS regions, where a finer resolution results in a smaller H_2O abundance. The effect is more pronounced in the SH (summer), and in $AGCM_{T106L191}$ where the vertical resolution is further enhanced. The drier LMS in $AGCM_{T106L90}$ and $AGCM_{T106L191}$ implies a reduction of the moist bias in EMAC, independent of the vertical coordinate. $AGCM_{T42L90}$ has very small and mostly not statistically significant relative differences compared to REF_{today}. The higher H_2O abundance in the polar UT in the NH is an artefact from the tropopause differences and the steep H_2O gradients in the UT. On a pressure grid relative to the surface, the polar UT is drier in $AGCM_{T42L90}$ than in REF_{today}. The artefacts occur for all simulations in vertical profiles with tropopause pressure differences. $CONV_{today}$ has a higher tropopause than REF_{today} in the SH polar latitudes, leading to negative differences on the tropopause-relative grid but simulates a higher H_2O abundance everywhere

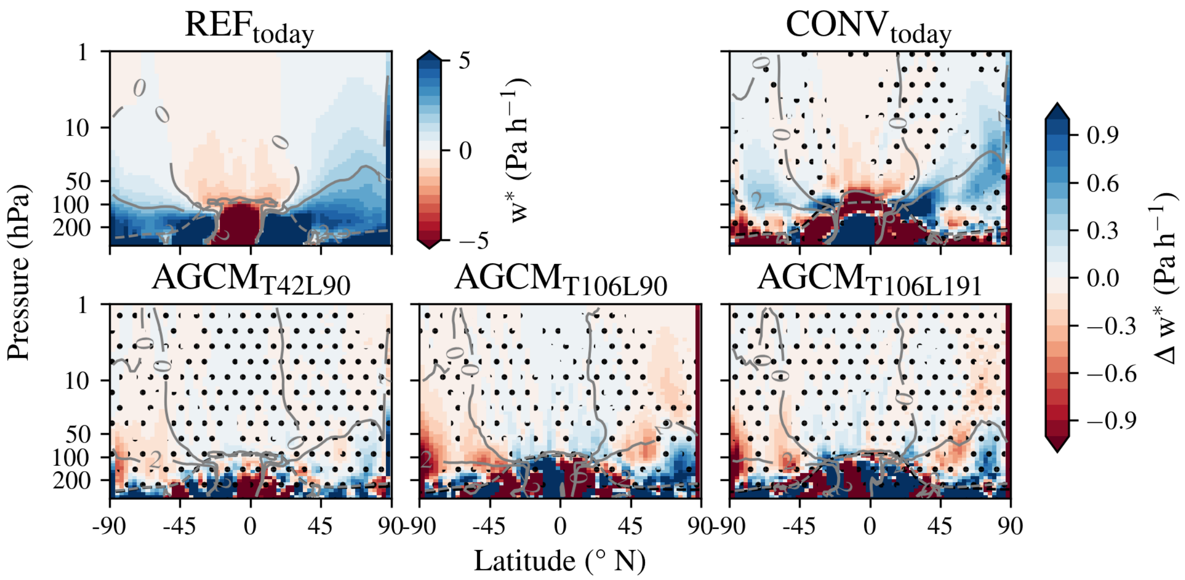

Figure 5.16: Same as Figure 5.10 but for vertical residual wind speed w*. Positive wind speeds are downwards.

on the pressure grid. AGCM$_{T106L90}$ has a lower tropopause, with a maximum for NH polar latitudes, leading to a larger abundance on the tropopause-relative grid, but on a pressure grid, the relative differences are small. In the tropics, the small differences on the tropopause-relative grid correspond to a drier tropical UT on a pressure grid. For AGCM$_{T106L191}$ the grid transformation to tropopause-relative amplifies the already larger H_2O abundance over the entire UT. The result highlights the risk of grid transformations for regions with steep gradients.

To understand the stratospheric H_2O vapour abundance differences, I compare the tropical cold point temperatures in further detail. The tropical cold point temperature is crucial for the amount of H_2O vapour that can be transported from the moist troposphere into the dry stratosphere. The lower the temperatures, the more H_2O vapour is frozen out, and the drier the stratosphere becomes. Figure 5.18 shows the temperature at the cold point, based on the online calculated diagnostic of the minimum temperature in the tropics (10° S–10° N average). While interactive chemistry and grid resolution have hardly any influence on the cold point temperature, the differences between REF$_{today}$ and CONV$_{today}$ are almost 5 K.

Due to a strongly non-linear relation between temperature and the H_2O amount that can be present as vapour, also relatively small temperature differences have a substantial impact on the H_2O vapour amount entering the stratosphere. This saturation H_2O vapour pressure is described by the Clausius-Clapeyron equation over ice and can be approximated by

$$e_s(\mathrm{T}) = e^{9.550426 - \frac{723.265}{\mathrm{T}} + 3.53068 \cdot ln(\mathrm{T}) - 0.00728332 \cdot \mathrm{T}} \quad , \tag{5.1}$$

following Murphy and Koop (2005). The temperature T is in units of K, and the calculated saturation pressure e_s is in units of hPa.

Figure 5.19 shows the theoretically possible H_2O vapour amount at the tropical cold point in units of ppm$_v$ based on e_s and a relative humidity of 100 %. It shows that, due to the almost 5 K

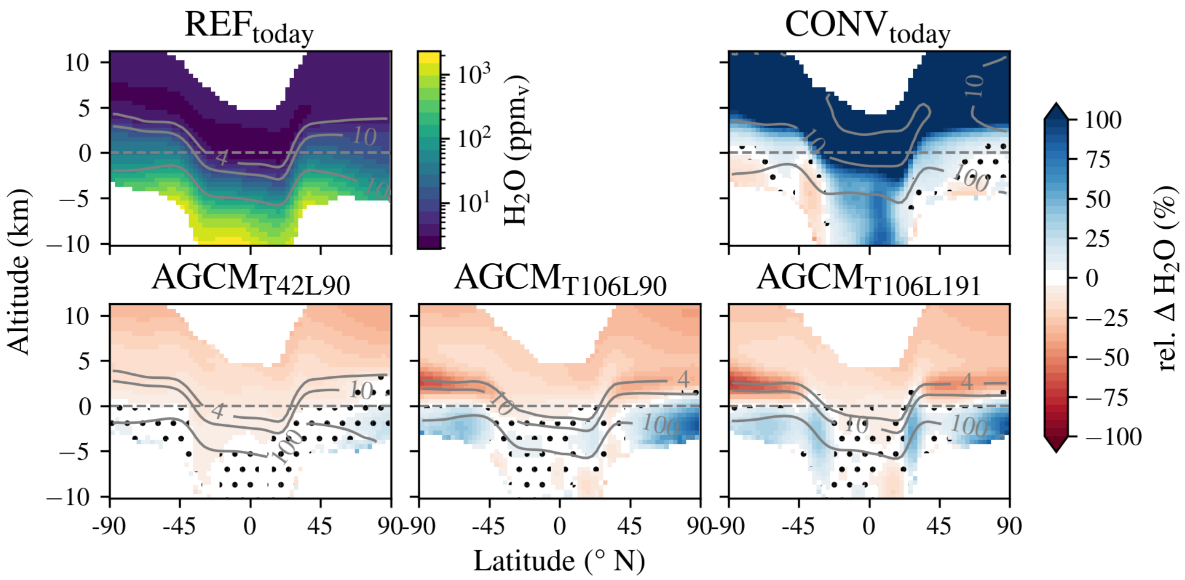

Figure 5.17: Relative differences of H_2O between the sensitivity simulations and the reference simulation REF_{today} (upper left). Shown are zonal mean differences between the climatological mean water vapour in season DJF in the UTLS on an altitude axis relative to the WMO tropopause pressure of the corresponding simulation results. REF_{today} shows the H_2O climatology. Grey solid lines are H_2O contour levels. The grey dashed lines are the climatological mean of the diagnosed tropopause based on the WMO definition. Dotted areas are not statistically significant, according to a Student's t-test at the 0.05 significance level based on DJF seasonal means per year.

warmer cold point temperature, twice as much H_2O vapour can enter the stratosphere through the cold point. The hashed areas show the simulated amount of H_2O vapour at the cold point. A larger fraction of the theoretically possible amount is present at the cold point in $CONV_{today}$ compared to REF_{today} and the other simulations with the Tiedtke parameterisation. This leads to the conclusion that EMAC's stratospheric H_2O vapour bias strongly depends on the applied convection parameterisation.

In the following, I investigate the sensitivity of the simulated chemical composition of the UTLS to the applied convection parameterisation. Figure 5.20 shows the distribution and relative difference of N_2O in $CONV_{today}$ compared to REF_{today}. N_2O is a greenhouse gas with a long lifetime in the atmosphere. It has a nearly homogeneous abundance in the UT and decreases with increasing altitude, similar to CO_2. $CONV_{today}$ yields a higher abundance in the upper LS in the mid latitudes, following a stronger poleward transport as seen by the comparison of AoA and the meridional residual circulation component v^*. In the LMS, there is a lower abundance than in REF_{today}, which is in agreement with the stronger horizontal transport from the tropical UT to the LMS, as found by the analysis of the E90 tracer. The stronger BDC leads to a faster transport from the higher stratosphere into the LMS, which has a lower N_2O abundance, which adds to the lower N_2O abundance found in $CONV_{today}$.

A major driver of atmospheric chemistry is the photolysis rate of constituents. Photolysis in the atmosphere is linked to irradiation, which provides the energy needed for chemical reactions

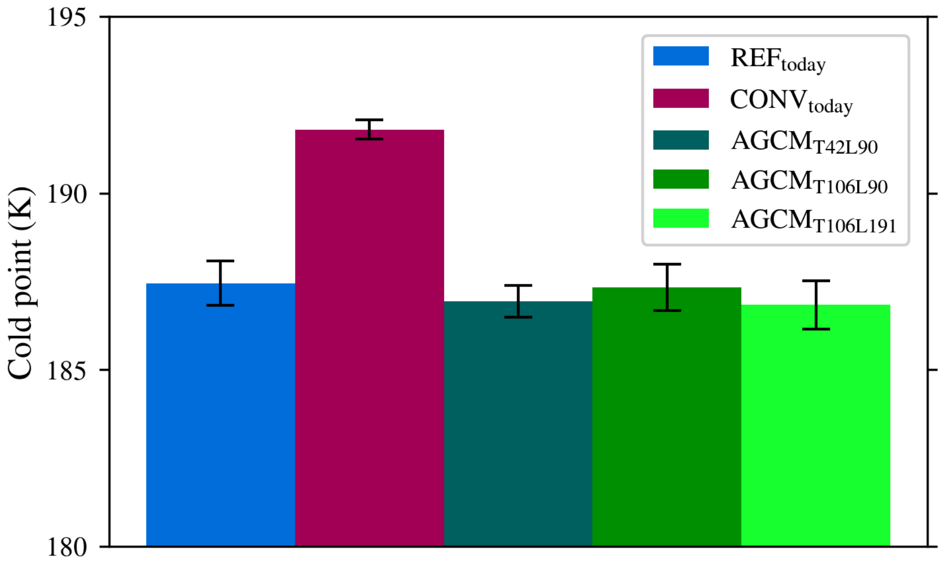

Figure 5.18: Comparison of cold point temperatures. The calculation uses the online-calculated cold point temperature, averaged over -10°–10° N latitude range, as the climatological mean for all DJF seasons. Error bars represent the interannual variability, calculated as the standard deviations over the period.

and breaks chemical bonds, creating highly reactive radicals. The photolysis rate coefficient for each molecule, referred to as the J value, depends on several atmospheric properties. Therefore, the difference in the J value of an arbitrarily selected constituent between the two simulations can be used for a qualitative statement about the general change direction. Figure 5.21 shows the J value of O_2. It is strongest in the upper stratosphere of the tropics, where intense irradiation is prevalent. But photolysis already occurs in the tropical LS. CONV$_{today}$ yields a higher photolysis rate in the tropical LS, by about 15 %. Photolysis is increased due to several factors that affect it, such as temperature, O_3 concentration, and clouds.

Figure 5.22 shows the differences between the simulated abundance of CH_4 in the UTLS region. CH_4 is mainly emitted at the surface, leading to a vertical gradient in the abundance, but is chemically more active than N_2O. CONV$_{today}$ shows a higher CH_4 abundance in the LS in the mid-latitudes and tropics, similar to N_2O, and a lower abundance everywhere else. The relative differences are mostly statistically significant but small, with a maximum positive relative difference of 5 %, due to the long atmospheric lifetime of CH_4. The smaller relative differences between REF$_{today}$ and CONV$_{today}$ for CH_4 than for N_2O are related to the overall lower abundance of N_2O, leading to a stronger relative increase. The transport differences affect CH_4 similarly to N_2O. Additionally, CH_4 is affected by differences in the turnover rates of chemical reactions, most notably by differences in the CH_4 oxidation by OH.

The hydroxyl radical plays an essential role as an oxidant and dominates the atmospheric lifetimes of many chemical substances such as CH_4 and CO. The differences between the simulated OH abundances in the UTLS region are shown in Figure 5.23. As a radical, it has a very short atmospheric lifetime but a fast production rate, for instance, through photolysis, which leads to very small abundances at night, such as in the polar regions of the winter hemisphere. In the UTLS, OH has the highest abundance at the upper edge in the tropics and the summer hemi-

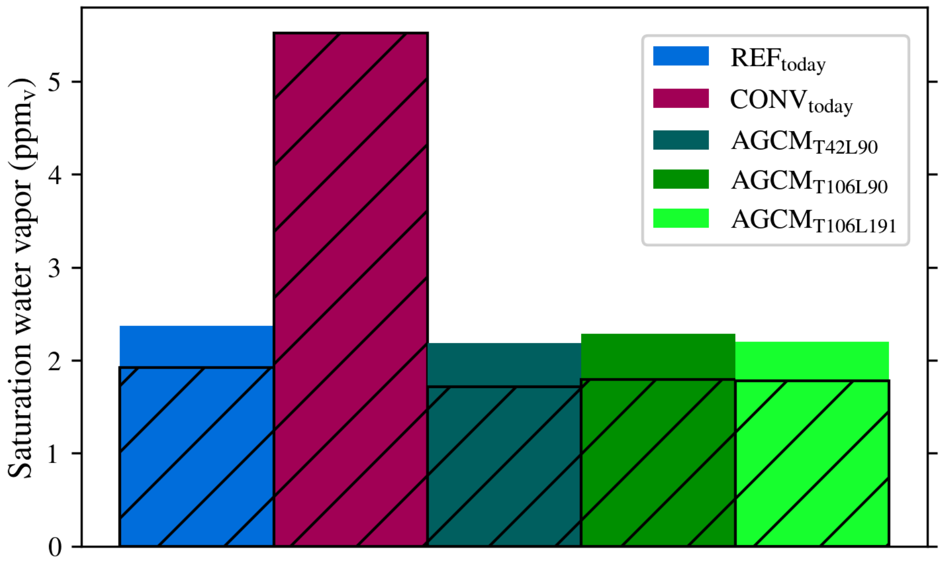

Figure 5.19: Theoretically possible H_2O vapour abundance at the tropical cold point, based on the estimations of the Clausius-Clapeyron equation over ice by Murphy and Koop (2005). The cold point calculation is the same as for Figure 5.18. The hashed areas indicate the simulated H_2O abundance at the tropical cold point.

sphere (SH), as well as in the tropical UT. In CONV$_{today}$, the OH abundance is primarily larger all over the UTLS. A higher OH abundance leads to a shorter atmospheric lifetime of CH_4 and is the second explanation for a lower abundance of CH_4 in most of the UTLS.

As introduced in Sections 2.3 and 2.4, the abundance of O_3 is strongly affected by chemical sources and removal processes as well as transport by the BDC. It combines the results of the simulated transport and chemistry found so far and concludes the investigation. Figure 5.24 shows the simulated O_3 abundance in the UTLS and the relative differences between CONV$_{today}$ and REF$_{today}$. The O_3 abundance increases towards the higher stratosphere with maxima at the upper edge of the LS in the mid-latitudes. In CONV$_{today}$ the O_3 abundance is larger in the NH, around the tropopause in the tropics and subtropics and in the UT in the southern hemisphere. In the tropical UT, the O_3 abundance is smaller due to the stronger convective transport of air from lower regions of the troposphere with lower O_3 abundance into the UT in REF$_{today}$. In the overall low abundance of O_3, this is sufficient to lead to a larger O_3 abundance in REF$_{today}$ than in CONV$_{today}$. The smaller O_3 abundance in the LMS of the SH by about 20 % contradicts an explanation of the differences by a stronger stratospheric transport into the LMS and points to chemical differences due to the choice of the convection parameterisation.

To understand the complex pattern of the O_3 differences, I use the diagnostic output of the atmospheric chemistry module MECCA for the individual O_3 chemical production and loss rates. Figure 5.25 shows the net O_3 tendency calculated by the kinetics solver. Since the tendency depends on the total abundance, it is expressed as a percentage of the abundance at each grid point to ensure comparability across simulations. In the UTLS region, O_3 is mainly produced with the strongest production relative to the abundance in the tropical UT. The very small chemical tendencies in the UTLS highlight the importance of transport for the O_3 distribution. The negative tendency in the extratropical LS indicates a net chemical loss in this region. In CONV$_{today}$,

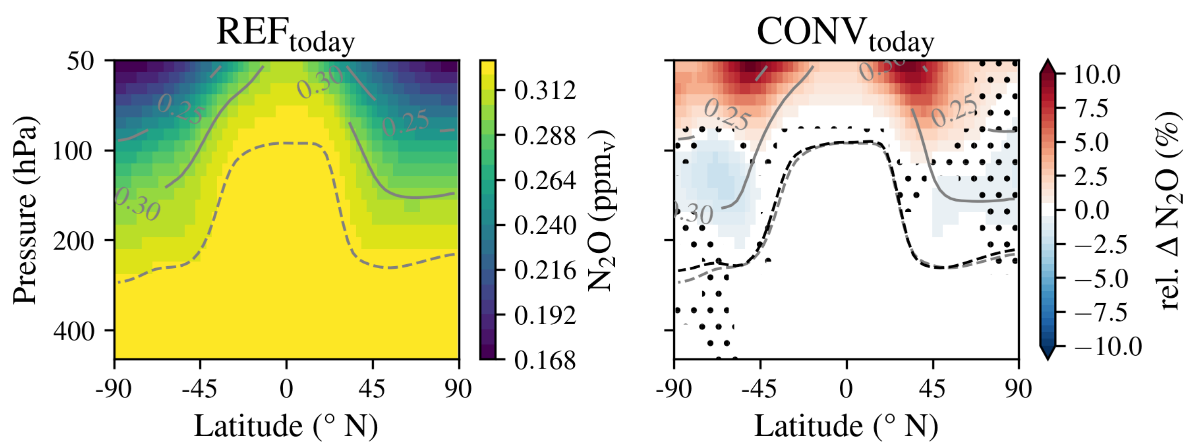

Figure 5.20: Comparison of N_2O distribution in the UTLS as climatological and zonal mean in DJF. Shown is the mixing ratio in REF$_{today}$ (left) and the relative difference of CONV$_{today}$ compared to REF$_{today}$ (right). Grey contour lines mark mixing ratios. The grey dashed line indicates the WMO tropopause of REF$_{today}$, the black dashed line the WMO tropopause of CONV$_{today}$. Dotted areas are not statistically significant, according to a Student's t-test at a 0.05 confidence level based on DJF seasonal means per year.

the production in the tropical UT is shifted northward to be more directly at the equator. In the summer hemispheric UTLS, the net chemical O_3 tendency is larger as well as in the tropical LS. In the winter hemispheric UTLS the tendency is smaller. The largest differences occur at the lower edge of the topical UT, where CONV$_{today}$simulates a lower net tendency.

Figure 5.26 shows the chemical production of O_3 expressed as a percentage of the abundance at each grid point to determine whether the differences in the net chemical tendency in the UTLS occur due to chemical production or removal differences. The comparison reveals that the shift in the net chemical tendency in the tropical UT originates a shift in the chemical production. Furthermore, the chemical production in CONV$_{today}$ is larger in the tropical LS and the summer hemisphere (SH). In the LS of the winter hemisphere (NH) and at the lower edge of the tropical UT, the chemical loss is larger. This stronger chemical loss contributes to the smaller abundance in the tropical UT, while the larger production in the UT of the summer hemisphere is likely to drive the larger O_3 abundance in CONV$_{today}$ than in REF$_{today}$ in the region. However, the stronger stratospheric circulation results in a stronger stratosphere-to-troposphere transport in the extratropics to balance the stronger mass transport into the stratosphere in the tropics. The downward transported O_3 can contribute to the larger abundance even though the abundance in the LS is lower than in REF$_{today}$. In the winter hemisphere, the analysis of chemical tendencies revealed that chemistry cannot be the source of the differences; therefore, the stronger stratospheric circulation governs them. In the winter hemisphere, the O_3 transport is further enhanced by the deep branch.

Looking further into the individual production terms for O_3 reveals that the reaction of NO with HO_2 to produce NO_2 (not shown), which leads to O_3 formation (see chapter 2), accounts for about 80 % of the total chemical production in the tropical UT. The shift in chemical production can also be attributed to this reaction. Figure 5.27 shows that the shift is connected to a shift and different distribution in the NO_x emission by lightning. In CONV$_{today}$ the production and

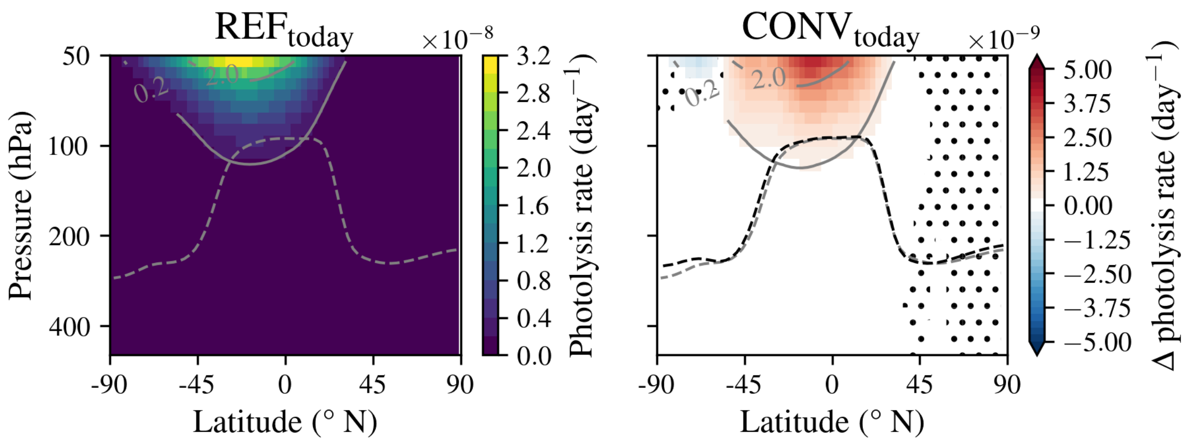

Figure 5.21: Same as 5.20 but for the photolysis rate. Shown is the difference between the simulated photolysis rates of O_2, but the change is consistent for all photolysis rates.

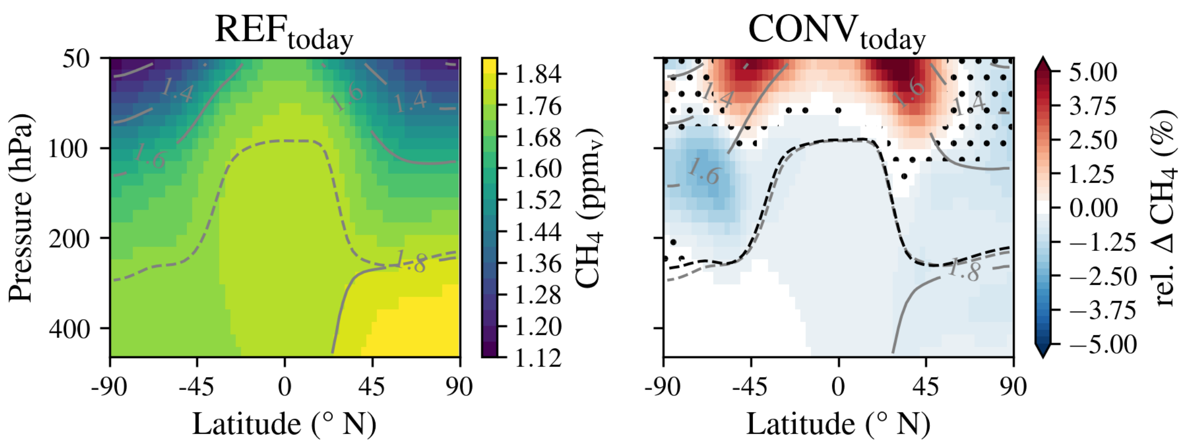

Figure 5.22: Same as 5.20 but for CH_4.

emission of NO_x by lightning occurs higher and is spread over a broader area in the tropics than in REF$_{today}$.

The lower abundance of O_3 in the summer hemispheric LS (SH) cannot be explained by transport differences or chemical production or loss rates in DJF. One important group of chemical losses of O_3 in the LS are reactions with ODS, catalytic reactions with radicals that contain Cl and Br at the surface of PSCs. The PSCs form in winter, but the catalytic reactions require photolysis, leading to O_3 depletion in spring. While the emissions of ODS are identical in both simulations, the atmospheric conditions to form PScs are not. Table 5.1 lists the climatological mean PSC surface area in the winter season of each hemisphere. It shows a much larger PSC surface area in CONV$_{today}$ due to the moister stratosphere and the lower temperatures than in REF$_{today}$. Figure 5.28 shows the chemical loss by all ODS that contain Cl in the season September-October-November (SON), the spring season in the SH, to identify their impact on the O_3 abundance in the DJF. Consistent with the higher PSC surface area, CONV$_{today}$ yields a significantly larger chemical loss than REF$_{today}$. The loss by the Cl group is three times that of the Br group, due to its larger emissions and atmospheric abundance. The higher loss rates

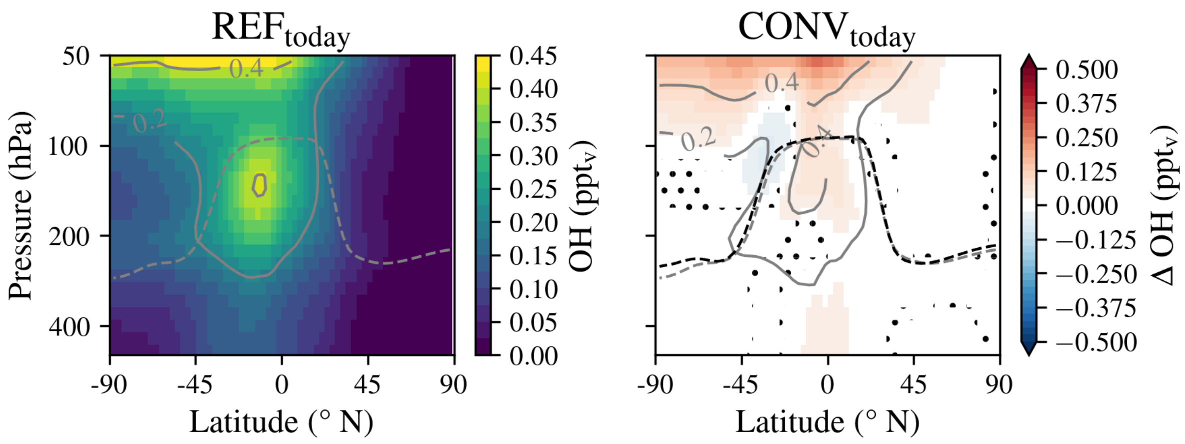

Figure 5.23: Same as 5.20 but for the absolute differences in OH.

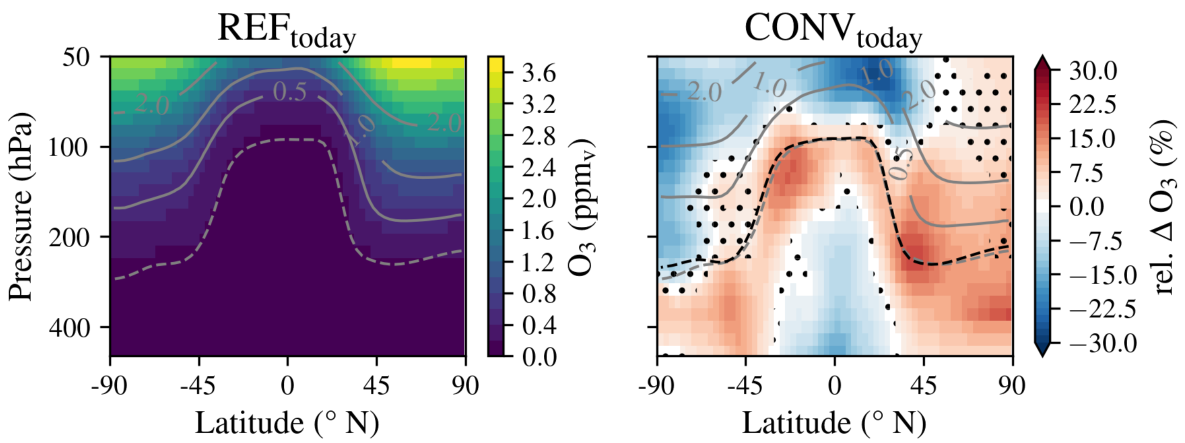

Figure 5.24: Same as 5.20 but for O_3.

in the preceding season explain the lower O_3 abundance in the LS of the southern hemisphere during DJF. The more substantial chemical loss partly prevails into the summer seasons of the SH, despite the stronger O_3 transport by the stratospheric circulation. Therefore, the choice of the convection parameterisation strongly affects the O_3 abundance in the UTLS due to transport as chemical turnover rate differences.

In summary, I successfully tuned all sensitivity simulations to a radiative imbalance at the top of atmosphere of about 0.8 Wm^{-2}, consistent with observed values for the beginning of the 21st century.
While the cloud cover and the convective mass flux are only weakly affected by the grid resolution of the model, the choice of the convection parameterisation has a strong effect on the maximum updraft strength and on the height of the main convective outflow in the tropical UT. This leads to significant differences in the UTLS composition in the tropics as well as in the LMS.
The location of the tropopause improves with a finer resolution, in the winter hemisphere, almost as much as the effect of nudging using ERA5, even though the resolutions differ substantially. The sensitivity of the tropopause to the choice of convection parameterisation is strongest

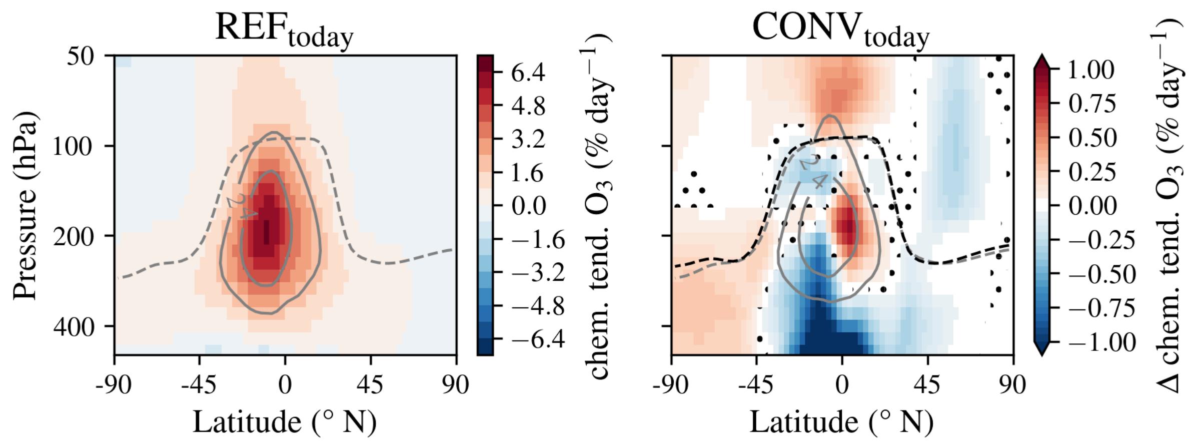

Figure 5.25: Same as 5.20 but for the absolute differences of the net chemical tendency of O_3 in the UTLS region.

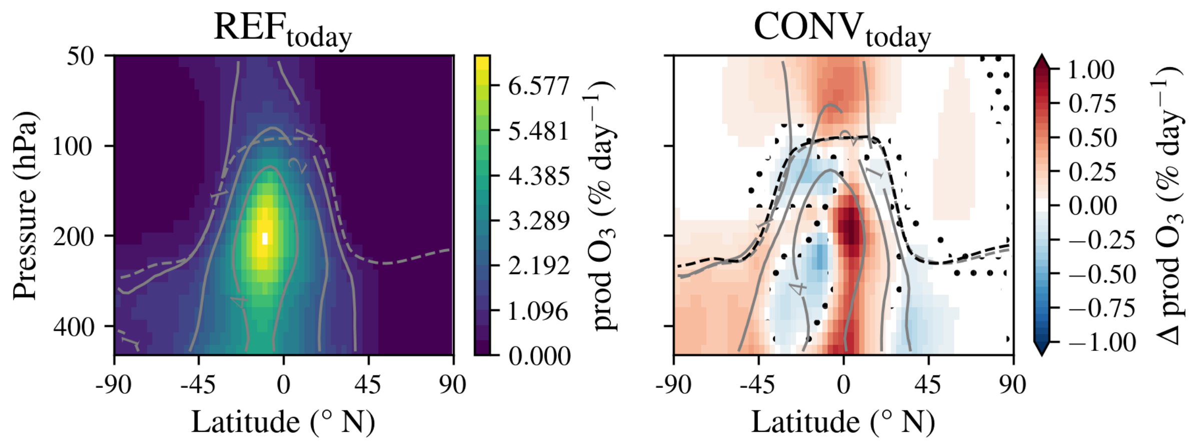

Figure 5.26: Same as 5.20 but for the absolute differences of the chemical production of O_3 in the UTLS region.

in the southern hemisphere, linked to O_3 differences, while the simulation of PSCs and their feedback on the temperature profile results in a higher tropopause than in AGCM simulations.
With a finer resolution, more atmospheric waves can be explicitly resolved, affecting the temperature and wind fields and leading to a stronger polar vortex. The stratospheric circulation tends to be slower, especially in the winter hemisphere. The convection parameterisation affects atmospheric temperature through GHG composition and differences in cloud abundance. A higher GHG composition in the LS leads to colder temperatures, which in turn reduces the wind speed in the stratosphere in the high latitudes, leading to a weaker polar vortex and a faster stratospheric circulation. Therefore, the choice of the convection parameterisation affects the dynamics of the atmosphere far above the region of direct influence.
A finer grid resolution reduces the moist bias in the LMS above the tropopause from more than 100 % to less than 50 % compared to SWOOSH (see Appendix D.2), the cold point temperature and therefore the dry bias in the stratosphere is not affected at all. The cold point temperature, however, is strongly affected by the choice of the convection parameterisation. Using

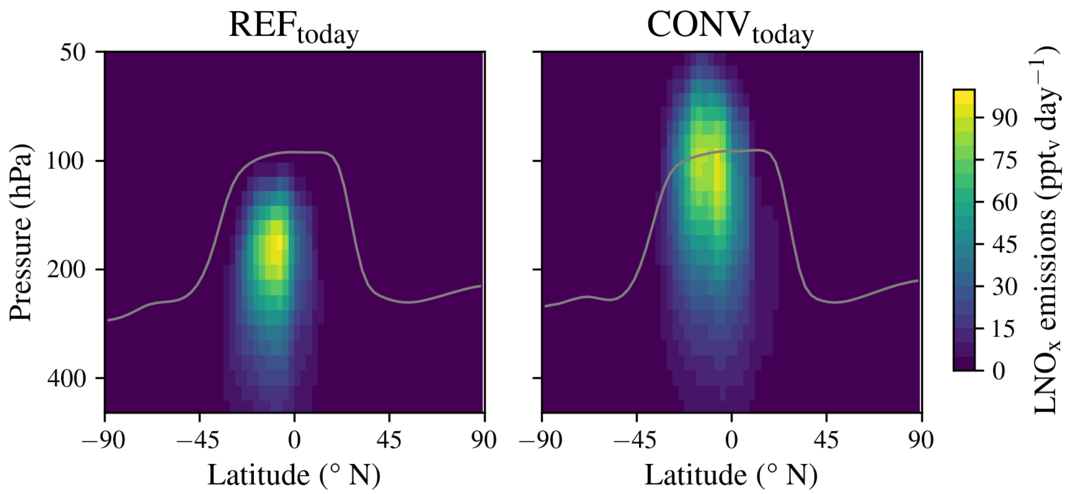

Figure 5.27: Same as 5.20 but for emission tendency of NO_x by lightning. Comparison of the emission tendency of NO_x by lightning in the UTLS as climatological and zonal mean in DJF. Shown is the tendency for REF_{today} (left) and $CONV_{today}$ (right). Grey contour lines mark the WMO tropopause of the individual simulation.

Table 5.1: The climatological mean of the PSC surface area in the simulations REF_{today} and $CONV_{today}$ in the winter of each hemisphere, DJF in NH and JJA in SH. The surface area is rounded to the next integer in km^2.

Sim	NH (km^2)	SH (km^2)
REF_{today}	318154	801907
$CONV_{today}$	1005309	1908068

the Emanuel convection parameterisation instead of Tiedtke, annuls the tropical cold point bias, creating a moist bias rather than a dry bias in the stratosphere of about 200 % compared to SWOOSH.
Finally, the choice of the convection parameterisation significantly affects the UTLS chemical composition. In addition to its dynamical effects on transport processes in the troposphere and stratosphere, it also influences photolysis rates and OH abundance, thereby strongly affecting chemical turnover rates. The OH abundance varies by up to 100 % in the LS. Most importantly, the convection parameterisation modifies the conditions for the formation of PSCs, resulting in relative differences in the O_3 abundance in the LS by up to 30 % under present-day conditions.

5.4 Discussion

During the course of this thesis, it was only feasible to perform the simulation with finer horizontal and vertical resolutions over 10 years, rather than 20 years for the other TS simulations. A comparison of a 10-year climatology with a 20-year climatology of the reference simulation REF_{today} revealed that the differences are generally small. The temperature differences are below 0.5 K everywhere below 10 hPa, higher in the atmosphere, the 10-year climatology tends to be warmer with a maximum of 1 K in the polar mesopause. In case of the zonal wind, the largest difference occurs for a vertical pattern of positive and negative differences in the stratosphere

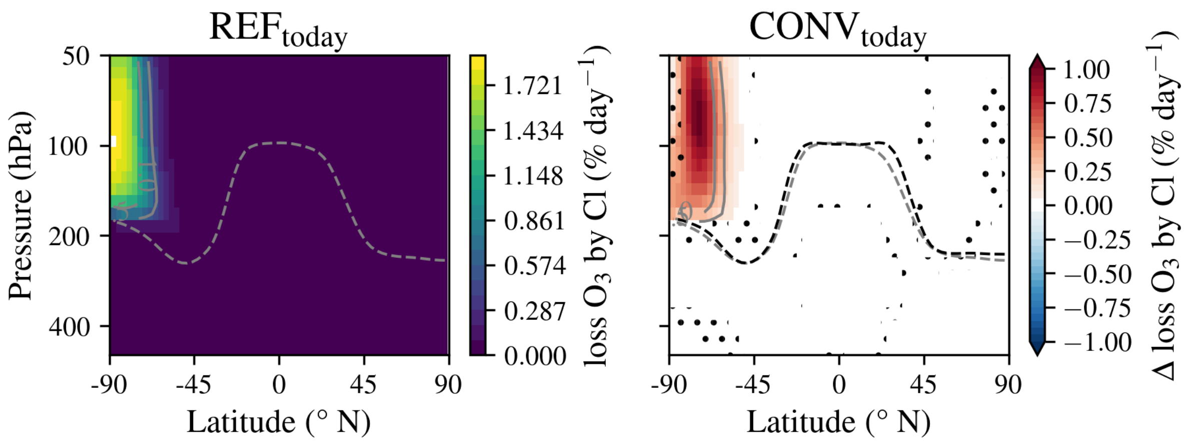

Figure 5.28: Same as 5.20 but for the absolute differences in the chemical loss of O_3 by the LossO3Cl group in the UTLS region during the SON season.

above the equator by up to 3 ms^{-1}, indicating the stratospheric vertical variability between the boundary of westward and eastward winds between the hemispheres. However, repeating the test with the simulation AGCM$_{T106L90}$ results in a similar magnitude of differences but a different pattern throughout the atmosphere. Only the general vertical zonal wind pattern is also found between the two climatologies for AGCM$_{T106L90}$. Therefore, no assumption about the changes in AGCM$_{T106L191}$ if 20 years were used for the climatologies can be made.

The investigation of resolution dependence on the UTLS structure in EMAC revealed an improved representation of temperature and water vapour distribution with finer resolution model setups compared to SWOOSH, especially in the LMS. Small differences are expected due to the transient nature of observations and the TS configuration for the EMAC simulations. The representation (when model results are compared with observations) improves primarily when the horizontal resolution is increased, and is further improved only slightly when the vertical resolution is increased as well. An increase of the model grid resolution strongly reduces the cold and the moist biases in the LMS. With finer grid resolution, steep gradients are better resolved, and numerical diffusion is reduced (Stenke et al., 2007). Too large numerical diffusion can be caused by insufficient vertical or horizontal resolution, or by both combined. The warmer LMS reduces the horizontal temperature gradient, affecting the wind field in the UTLS region. The observed weaker westerlies above the subtropical jet allow less Rossby wave propagation, which might explain the stronger polar vortex due to weaker wave dissipation, as indicated by the PV flux divergence, leading to a reduction in the zonal wind. A stronger polar vortex contributes to the colder polar temperatures. Furthermore, the higher resolution is especially beneficial in regions with strong gradients as in the vicinity of jets. Part of the differences in stratospheric temperatures and winds result from the finer grid resolution. A more detailed analysis of the wave driving is necessary to quantify its contribution to the differences.
Roeckner et al. (2004) stated for already much coarser vertical resolutions that the ratio between the horizontal and vertical resolution is important, whether an increase in one direction improves the simulated model results. Furthermore, they found tropospheric warming and a poleward shift of the STJ with increased horizontal resolution, and the opposite effect with increased vertical resolution. Since the vertical resolution is high in the standard configuration T42L90MA compared to other climate models, a beneficial effect of the horizontal resolution

increase is expected. While the finer vertical resolution would be desirable for UTLS composition studies, the matching finer horizontal resolution is probably not yet computationally feasible, at least for climate studies. For the EMAC standard-resolution T42L90MA, the horizontal resolution appears to be the limiting factor, leading to better representation when only the horizontal resolution is increased to T106 ($AGCM_{T106L90}$), since the vertical resolution is already rather high (about 600 m, see Figure B.1), at least in comparison to other models, as investigated by Richter et al. (2014) and Wang et al. (2018) with a finer grid resolution of about 500 m. Both studies also found improved representations of the LMS temperature and H_2O abundance compared to simulations with coarser vertical resolution. In contrast to Wang et al. (2018), I found no clear improvement in the higher vertical resolution ($AGCM_{T106L191}$) simulation of UTLS temperature and H_2O abundance compared to the lower vertical resolution ($AGCM_{T106L90}$) and ERA5. Furthermore, $AGCM_{T106L90}$ compares better with ERA5 for the zonal wind from the upper troposphere over the entire stratosphere. The discrepancy between the results may be due to differences in the reference datasets, the simulated periods, or free-running versus time-slice simulations. The fewer number of years for the climatology of $AGCM_{T106L191}$ can also contribute to the lower performance, especially for the zonal wind difference above the equator. Last but not least, the effect of the finer vertical resolution might be model-dependent. The cause of the contradictory results cannot be identified without reducing the number of differences through further simulations.

With increased resolution, my results indicate a slower residual circulation in the stratosphere, which better aligns with observations (Garny et al., 2024), although older AoA in the middle and upper stratosphere are mostly not statistically significant. $AGCM_{T106L191}$ simulates even higher wind speeds, especially for the polar vortex. A potential explanation is parameterised gravity waves, which have a significant effect on the wind speeds in the upper stratosphere (Giorgetta et al., 2006; Eichinger et al., 2020). The generation of parameterised gravity waves is mainly defined by the threshold of the root-mean-square wind speed, which is used globally, and studies have shown a high sensitivity to this parameter (Jöckel et al., 2006). For the higher vertical resolution, a different threshold might be more favourable. Furthermore, Eichinger et al. (2023) showed that improved horizontal propagation of gravity waves in EMAC results in better simulations of the stratospheric circulation and the polar vortex.

While the influences of the tuned convective differences cannot be prevented, the analysis of the cloud cover differences revealed only minor differences between the AGCM simulations. The differences between the H_2O abundances are not statistically significant in the tropical UT, but the LS is similarly drier in all three AGCM simulations. The drier stratosphere can be attributed to a lower chemical production of H_2O. As I described in Section 3.5, the three AGCM simulations include the primary chemical source of H_2O in the stratosphere, the oxidation of CH_4. But CH_4 itself is not considered in the simulations, and a climatology is used instead. It is the same climatology as used for the GHGs for the radiation scheme. These climatologies were created from the EMAC contribution to CCMI-2022, RD1SD-base-01, which simulated several differences in atmospheric composition driven by differences in the model setup. Therefore, the differences between $AGCM_{T42L90}$ and REF_{today} do not isolate the effect of interactive chemistry on the UTLS climate state. For CH_4, the abundance in the stratosphere is larger in REF_{today}(see Figure D.3), resulting in an enhanced CH_4 oxidation and an enhanced chemical production of H_2O compared to $AGCM_{T42L90}$. But the effect is uniformly distributed across the LS, and the main results of the resolution analysis remain unaffected. This is supported by the fact that the relative differences are independent of the resolution. The differences in GHG abundances under the radiation scheme further explain the need for retuning between REF_{today} and $AGCM_{T42L90}$. Consistent GHG climatologies based on REF_{today} would have been ideal for isolating the effect of the grid resolution.

The investigation of the effect of the convection parameterisation revealed a substantial impact on transport into the UTLS region. In addition to the direct effect, i.e., differences in cloud formation, location, and extent, these factors affect the temperature field by diabatic heating and then the wind field, leading to differences in the creation, propagation, and dissipation of Rossby waves. The setup incorporating the Emanuel convection parameterisation, $CONV_{today}$, simulates a younger AoA by up to one year in the winter upper stratosphere compared to the simulation with the Tiedtke parameterisation, REF_{today}. As shown in the analysis, the Emanuel convection parameterisation leads to greater cloud cover, especially in the tropical UT. The connected stronger diabatic heating leads to stronger horizontal temperature gradients between tropics and polar regions, similar to the effect of climate change. The stronger temperature gradients create stronger winds in the UTLS region. In the stratosphere, Emanuel increases the abundance of GHGs with the main source from the troposphere, such as CH_4, N_2O and especially H_2O, leading to a cooling due to the larger emissivity (Ramaswamy et al., 2001). Since the increase in GHGs originates from transport differences from the troposphere into the stratosphere, the cooling is strongest in the tropics, and therefore reduces the horizontal temperature gradient, leading to weaker winds, which is also seen in the zonal wind differences between the simulations. The strength of the zonal wind in the winter stratosphere determines the extent to which planetary Rossby waves can propagate into the upper stratosphere. Westerlies are required for the general propagation, but the zonal wind has to be slower than the phase speed of the Rossby waves. If the zonal wind is too fast, the wave hits a critical layer and dissipates. In the case of the Emanuel convection parameterisation, EMAC simulates stronger westerly winds above the STJ in the winter hemisphere in the climatological mean, leading to more frequent westerlies between the STJ and the polar vortex, allowing more propagation. Additionally, the weaker polar vortex moves the critical layer for the Rossby wave propagation higher. This mechanism explains how convection affects the stratospheric circulation as seen by the analysis of AoA. However, the differences in temperature and wind are also affected by dynamical feedbacks rather than solely by radiative differences. The strength of the individual contributions cannot be determined without further analysis of the wave activity. To determine the contribution from differences between the synoptic-scale and the planetary Rossby waves, a fast Fourier transformation can be used (e.g. Harzer et al., 2025). The wave numbers 1 to 3 are associated with planetary waves, and the synoptic scale waves with smaller wave numbers. To investigate the upward propagation of Rossby waves, investigations on the longitude-pressure plane through the polar vortex are necessary, rather than the zonal mean analysis. Another reason, in theory, would be gravity waves, which can be triggered by convection. However, convection as a source of gravity waves is not yet considered in MESSy; therefore, they can be ruled out as a reason for the differences.
To my knowledge, the effect of the convection parameterisation on the strength of the stratospheric circulation has not been shown before. With all that said, in my studies, the simulation REF_{today} with the Tiedtke convection parameterisation performs better in the simulation of the UTLS than $CONV_{today}$ with the Emanuel parameterisation, when compared to ERA5 and SWOOSH (Appendix D.2). Too much H_2O enters the stratosphere in $CONV_{today}$, and the stratospheric circulation is even faster than already compared to observations (Abalos et al., 2026). REF_{today} simulates a dry bias in the lower stratosphere, similarly to most CMIP6 models

(Keeble et al., 2021). The compensating effects of stronger circulation and stronger chemical loss of O_3 by PSCs lead to small relative differences compared to SWOOSH under present-day conditions.

The analysed strength of the convective updraft and downdraft mass fluxes is consistent with those found by Tost et al. (2010). Quantitative differences are expected due to the tuning and investigation of 20-year climatological averages in my study versus a mean over four months (September to December) analysed by Tost et al. (2010). They further compared three additional convection parameterisations, in addition to Tiedtke and Emanuel, and showed that neither Tiedtke nor Emanuel simulates strong outliers in convective mass fluxes compared to the other three parameterisations. Evaluating simulated convective mass fluxes is complicated because direct atmospheric measurements are not possible; they can only be estimated. One estimate uses the definition of the mass flux by Arakawa and Schubert (1974) as the product of the air density, the cloud area fraction, and the net vertical wind velocity. Kumar et al. (2016) used 3-hourly radar observations above Darwin, Australia, to define the cloud area fraction and estimated the vertical wind velocity based on the echo top height of a radar to estimate the convective mass fluxes on AGCM grid scales. They estimated a mean convective mass flux of 5 $gm^{-2}s^{-1}$, 6 km above the surface and a linear decrease to 1 $gm^{-2}s^{-1}$ at 14 km, in the tropical UT. These estimates, based on observations, match well with the 20-year average of convective updraft of $CONV_{today}$ in the tropics (compare Figure 5.6). However, Savazzi et al. (2021) used the same observational data but with a 10 minute sampling frequency and estimated a convective mass flux of 17 $gm^{-2}s^{-1}$, 4 km above the surface and a linear decrease to 2 $gm^{-2}s^{-1}$ at 14 km, in the tropical UT. These estimates, based on observations, match better with the climatological averages of REF_{today} in the tropics. Savazzi et al. (2021) attribute the significant differences to the different sampling frequency of the observations; a shorter sampling frequency captures strong convective events directly, rather than smoothing them out when there are no further events in the same period. With this spread in the convective mass fluxes from observations estimated on the grid scales of AGCM models, the results for the convective mass flux from both convection parameterisations are within the uncertainty range.

The investigation of the model performance with different convection parameterisations to match global mean observations of climate-state parameters revealed a grouping for radiative and water-related parameters. REF_{today} with the Tiedtke parameterisation closely matches the radiative LW and SW fluxes at the TOA, and shows larger differences for the precipitation rate and the LWP. The latter two are well simulated by $CONV_{today}$. A larger water content in the atmosphere in $CONV_{today}$ is associated with the larger cloud cover, suggesting a longer lifetime of the clouds. The larger cloud cover in $CONV_{today}$ compared to REF_{today} occurs mainly in the tropical UT, which agrees with satellite observations and higher-resolution simulations (Chepfer et al., 2010; Crueger et al., 2018). However, the climatologically averaged convective cloud height calculated by the Emanuel parameterisation exceeds the tropopause in the tropics. Observations do not support such a high frequency of overshooting convection in the tropics (Jensen et al., 2020). The differences in the GHG composition and distribution are responsible for differences in the LW clear-sky component, keeping more outgoing LW radiation trapped in the atmosphere in the case of the Emanuel convection parameterisation. One possible explanation for the differences in the climate state parameters is the different approach of the Emanuel parameterisation. Emanuel (1991) aimed to develop a physically sound parameterisation of convection, including subcloud-scale behaviour and exchange, based on the buoyancy sorting

hypothesis. On the other hand, he evaluated the parameterisation using a column model rather than a global circulation model. The role of clouds in the climate system was subordinate to the convection processes. In contrast, Tiedtke (1989) developed a parameterisation for IFS instead. He focused on the effect on the global scale.
The potentially strongest bias in the results, favouring the Tiedtke parameterisation, was the tuning starting point. Since Tiedtke has been the default convection parameterisation in EMAC over the last two decades, the cloud parameterisation is optimised for simulations with Tiedtke. Due to the strong coupling between the cloud and convection parameterisations, an optimal tuning might require adapting both parameterisations together. However, to isolate the effect of the choice of convection parameterisation, I had to restrict the tuning process to the convection parameterisation's parameters. To my knowledge, I performed the first EMAC simulation with the Emanuel parameterisation in the "Middle Atmosphere" configuration, including atmospheric chemistry over climate scales. The last time an EMAC simulation using Emanuel was tuned was more than a decade ago (Tost et al., 2010), for a simulation over four months. Significant effort was required to tune the $CONV_{today}$ to match the radiative imbalance observed around 2010, while preserving some convective precipitation rather than relying solely on the cloud parameterisation to create precipitation to remove excessive water in the atmosphere. Since the radiative longwave and shortwave components do not match the observed values, there is room for improvement. And I am not claiming that I have found the best parameter configuration if only the parameters of the Emanuel parameterisation are modified. Therefore, it is likely that the model results with the Emanuel convection parameterisation can be improved, especially if the cloud parameterisation is also adjusted. A tedious additional investigation would be necessary.

To my knowledge, there is one AGCM that used the Emanuel convection parameterisation as its default parameterisation: the Laboratoire de Météorologie Dynamique (Zoom capability) (LMDZ) version 4 (Hourdin et al., 2006). For the 4^{th} version, they switched from the original Tiedtke parameterisation (Tiedtke, 1989) to the Emanuel parameterisation (Emanuel, 1991; Emanuel, 1993). Additionally, they included the cloud parameterisation by Bony and Emanuel (2001). After a tuning process for the new setup, the representation of the Hadley-Walker circulation improved (Hourdin et al., 2006). By comparing the model results with Tiedtke and Emanuel, they also found a colder lower stratosphere and colder tropics in their Emanuel simulation than in their Tiedtke simulation. As Hourdin et al. (2006) compared AGCM simulation setups, the dynamical effect of the different heating rates by Emanuel contributes to the temperature differences in the stratosphere. Surprisingly, they still found a much larger specific humidity in most of the troposphere and the lower stratosphere in the Tiedtke simulation, which contrasts with my results and the strong influence of temperature on H_2O abundance. Only in the tropical UT Emanuel simulates a slightly higher specific humidity. Different versions of both parameterisations can partly explain the diverging results, as LMDZ did not include the improved closure criteria by Nordeng (1994) for the Tiedtke parameterisation and did not use the changes by Emanuel and Živković-Rothman (1999) for the Emanuel parameterisation. Another reason is the adaptation of the cloud scheme, which I kept untouched.

The sensitivity studies of the choice of convection parameterisation under present-day conditions revealed substantial differences in the UTLS and atmospheric transport processes. This raises the question of whether the choice leads to a different response to climate change.

Chapter 6

Robustness of future projections

In this chapter, I investigate how the response of the simulated UTLS on a projected climate change depends on the choice of the convection parameterisation. To assess robustness, I visually compare the response, defined as the change in the climate state (20-year mean) between future and present-day conditions. The time-slice simulations REF_{future} and $CONV_{future}$ are identical to their corresponding present-day simulations REF_{today} and $CONV_{today}$ besides the climate forcing by the SST/SIC climatology and the emissions.

6.1 Comparison of the UTLS response to climate change

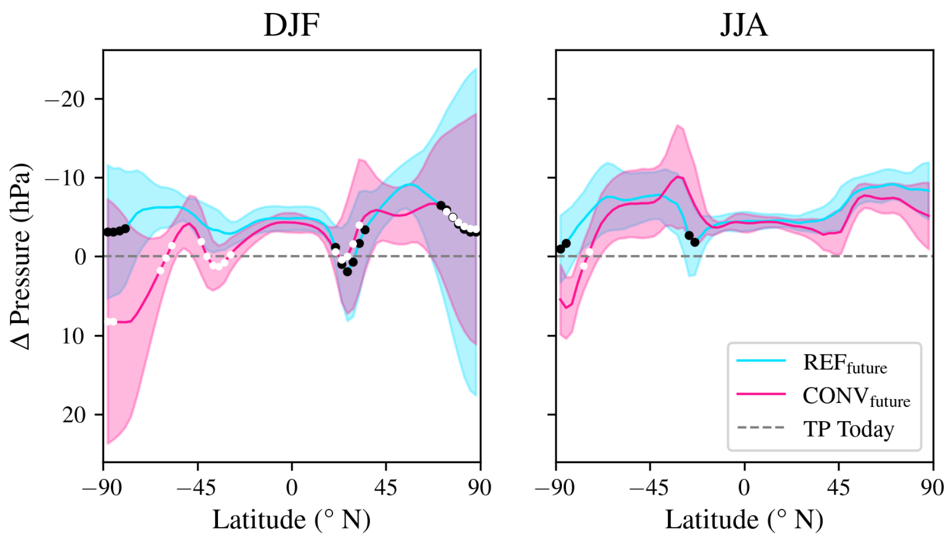

Figure 6.1: Climatological and zonal mean of the WMO tropopause pressure change in DJF (left) and JJA (right). The change is shown relative to the tropopause height under present-day conditions. Shaded areas show the standard deviation under present-day conditions. The pressure axis is decreasing. A negative pressure change indicates a higher tropopause. Dots indicate not statistically significant tropopause pressure changes, black for REF, white for CONV.

Figure 6.1 shows the response in the WMO tropopause pressure due to climate change between future and present-day conditions as zonal mean for the season DJF and JJA. The tropopause pressure generally decreases, resulting in a higher tropopause altitude. REF_{future} and $CONV_{future}$ agree the most in the tropics and the northern hemisphere, the winter hemisphere, with a 5 hPa pressure decrease in the tropics. Since the tropopause pressure differences agree well across all latitudes, this implies a stronger tropopause shift in the tropics, due to the logarithmic decrease in atmospheric pressure. The projections disagree most strongly in the SH polar region during DJF. REF_{future} has a pressure decrease of -2.5 hPa, $CONV_{future}$ a pressure increase of more than 7.5 hPa. However, as $CONV_{today}$ simulates a lower tropopause pressure than REF_{today}, see Figure 5.8, the tropopause pressure of the lapse rate tropopause agrees better under future simulations with different convection parameterisation, leading to a more robust climate state than under present-day conditions. The tropopause pressure comparison further reveals that the tropopause differences between present-day and future are smaller than those found between the sensitivity studies investigated in the two previous chapters. This reduces the beneficial effect of tropopause-relative coordinates in relation to the introduction of transformation errors, especially in the vicinity of steep gradients.

Figure 6.2 shows the temperature response under climate change, defined as the change between the future and the present-day climatologies of DJF. The response is further compared on a vertical pressure grid (top row) and on a tropopause-relative altitude grid to visualise the effect of the grid transformation for the small change in tropopause pressure. On the pressure grid, both setups show a warming of the troposphere, with the strongest warming by up to 3 K in the tropical UT. The tropical LS tends to cool, even more so between REF_{future} and $CONV_{future}$. In the extratropical LS, the two setups agree on the warming in the SH (summer) and show no statistically significant differences in the NH (winter). The simulated temperature response of the LMS of the southern hemisphere is the strongest difference between the Tiedtke and Emanuel simulations. While the Tiedtke simulation under future conditions warms by about 2 K as a response to climate change, the Emanuel simulation warms by up to 5 K, resulting in the largest response in the UTLS region. If tropopause-relative coordinates are used, the robust warming signal in the tropical UT is strongly reduced, leading to not statistically significant temperature changes and even a cooling signal in the Tiedtke simulations at the lower edge of the tropical UT. The differences between the coordinate systems suggest that the upward shift of the tropopause following the tropical expansion compensates for a strong part of the warming, if the UTLS is defined by the range around the tropopause rather than a fixed pressure range. This effect mainly occurs in the vicinity of steep vertical gradients, as small changes already have a significant effect, which explains why the extratropical LS is only weakly affected. However, the grid transformation from pressure to tropopause-relative introduces an error in the transformed data, since interpolation is most error-prone in regions of steep gradients.

The horizontal warming differences predict differences in the dynamical response between hemispheres and between model setups. Figure 6.3 shows the response in the zonal mean wind speed in the stratosphere. The pattern of the stratospheric response between the Tiedtke simulations correlates strongly with the differences REF_{today} and $CONV_{today}$(compare Figure 5.10). The westerlies above the STJ are stronger, and the polar vortex is weaker, in addition to a stronger stratospheric circulation. However, the strength of the response is half that of the differences between the sensitivity simulations in the last chapter, which explains the mostly not statistically significant response. A consistent response to climate change across the setups is found in the tropics, with a statistically significant increase in westerly winds at the STJ re-

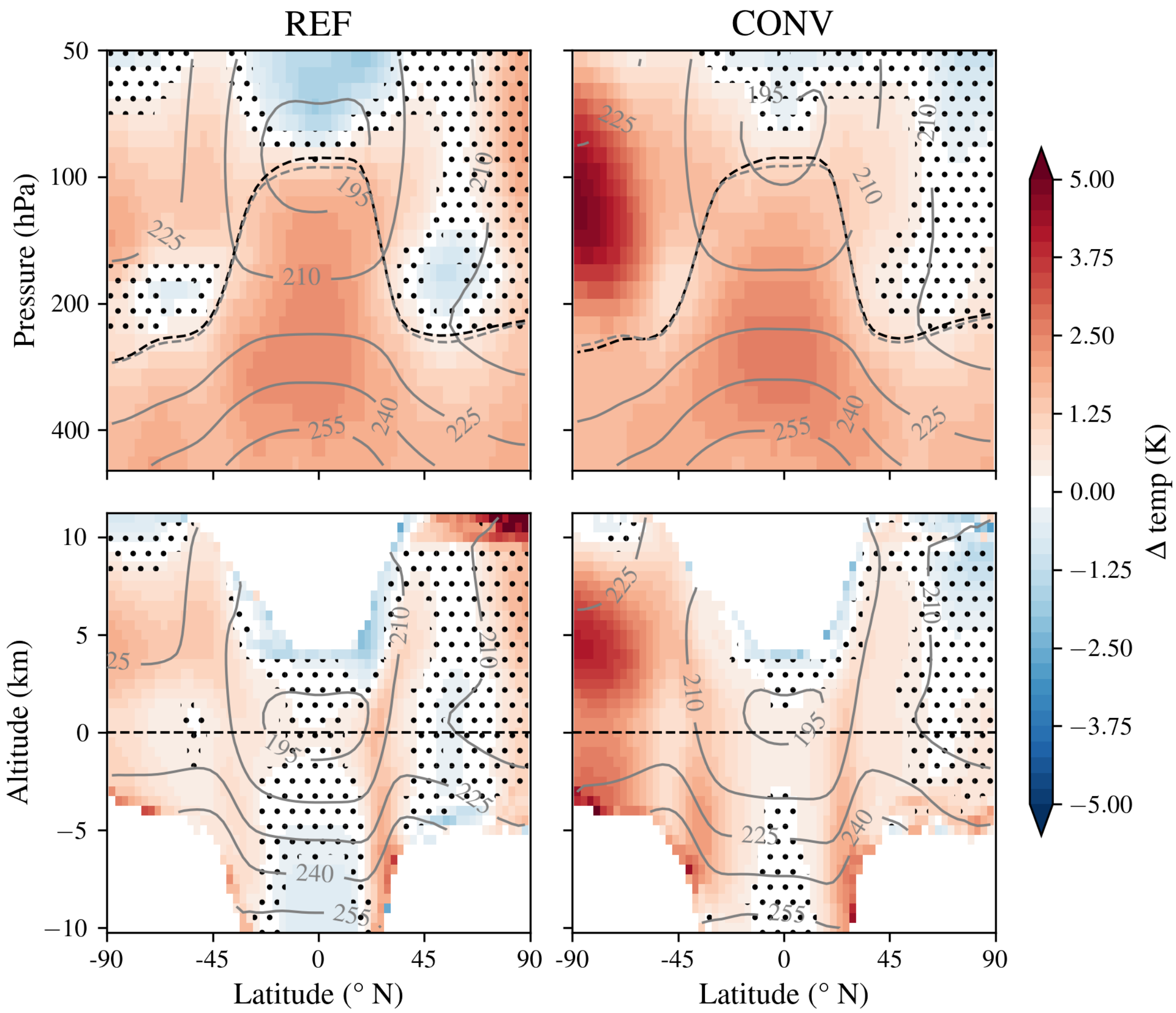

Figure 6.2: UTLS temperature response to climate change between the simulations with the Tiedtke convection parameterisation (REF, left) and with the Emanuel parameterisation (CONV, right) under future and present-day conditions as climatological and zonal mean of the DJF season. The top row shows the temperature change at pressure levels, the bottom row shows the temperature change on an altitude grid relative to the WMO tropopause. For the bottom row, the visualised data corresponds to the 500–50 hPa pressure range, to focus on the differences in the UTLS region. Grey dashed lines are the respective zonal mean WMO tropopause climatologies of the present-day simulations, and the black dashed lines show the climatologies of the future simulations. Grey contour lines depict the temperature field under present-day conditions. In the dotted regions, the temperature changes are not statistically significant according to a two-sided Student's t-test at a 0.05 confidence level.

gion and above, indicating more consistent westerlies in the DJF season and better conditions for Rossby wave propagation in the winter hemisphere. In the extratropics, the zonal wind response between the Emanuel simulations is weaker, and in the middle and upper stratosphere of the winter hemisphere, it is even opposite to the response in the Tiedtke simulations. Therefore, the simulated future climate states from simulations with different convection parameterisations agree better than the climate state under present-day conditions, indicating a decreasing model spread due to convection parameterisation with climate change.

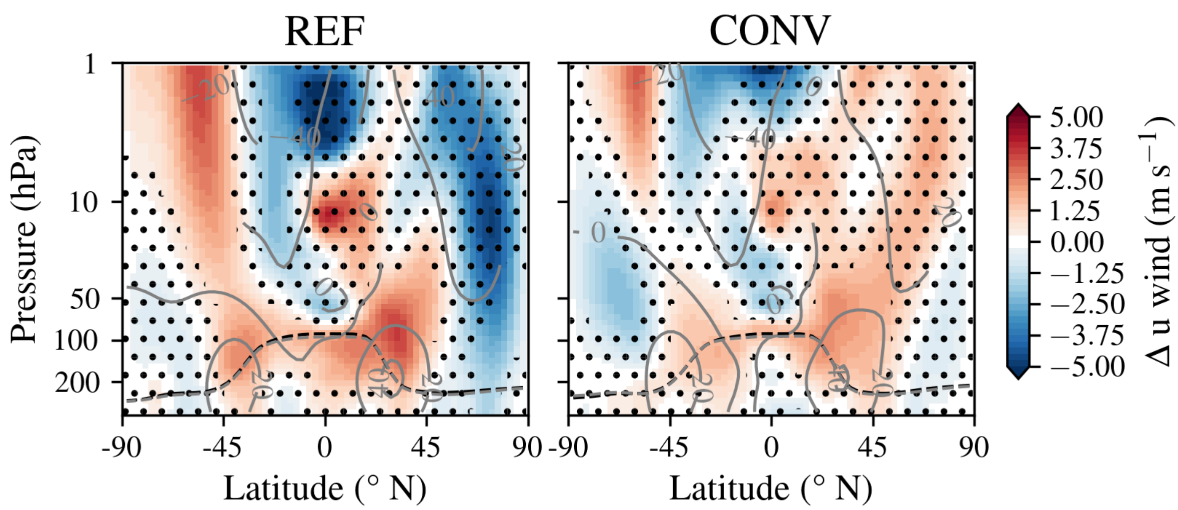

Figure 6.3: Stratospheric zonal wind response to climate change between the simulations under future and present-day conditions as climatological and zonal mean of the DJF season. On the left, the response for the setup with the Tiedtke convection parameterisation (REF), on the right, for that with the Emanuel parameterisation (CONV). Grey dashed lines indicate the respective mean WMO tropopause under present-day conditions, black dashed lines indicate the future conditions. Grey contour lines depict the zonal wind field under present-day conditions. In the dotted regions, the changes are not statistically significant according to a two-sided Student's t-test at a 0.05 confidence level.

The simulated response in the strength of the BDC is investigated by comparing AoA between the present-day and future simulations. The AoA calculation for all four simulations is based on an idealised tracer with a linear increasing abundance at the surface with no atmospheric sinks. As in the chapters before, the AoA calculation uses the convolution method and the tropics at 100 hPa as the reference point. The fixed pressure at the reference location does not account for the tropospheric expansion and differences in the tropospheric vertical transport; however, as the vertical transport around the tropopause does not vary strongly with pressure, the effect on the AoA calculation is also small. Figure 6.4 shows the response of AoA over the entire stratosphere. Both simulations show a younger AoA throughout the stratosphere, indicating faster transport compared to corresponding simulations for present-day conditions. The larger and statistically significant change in AoA is simulated between the Tiedtke simulations $\mathrm{REF}_{\mathrm{future}}$ and $\mathrm{REF}_{\mathrm{today}}$. To distinguish between an AoA change dominated by the shallow branch or a change by the entire BDC, I calculate the response of the meridional and vertical wind components of the residual circulation, D.8 and D.9, respectively. Most changes in the stratosphere are not statistically significant because the differences between the simulations are smaller. However, the sign of the differences indicates an increase in the shallow and the deep branch, which is more pronounced between the Tiedtke simulations. The faster circulation ultimately indicates stronger wave dissipation in the upper stratosphere and, therefore, more or stronger planetary Rossby wave propagation.

To investigate the future response of the tropospheric transport into the UTLS, I rely again on the diagnostic E90 tracer (Figure 6.6). The comparison between future and present-day conditions

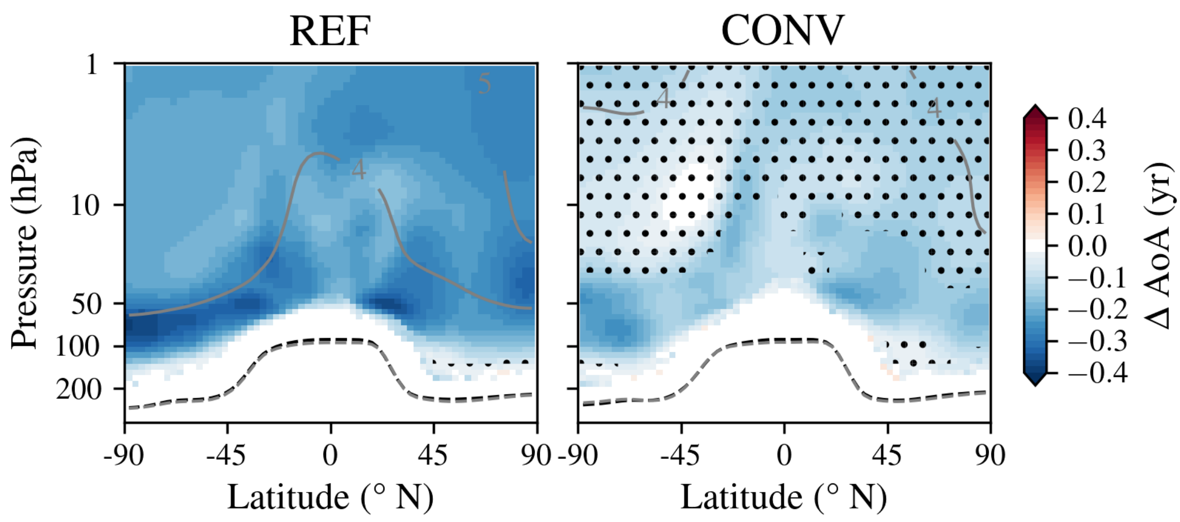

Figure 6.4: Same as Figure 6.3 but for the response of AoA.

reveals an increase in the vertical transport in the tropical LS, which is then transported into the LMS by the shallow branch. The strength of the increase reaches up to 25 %, if the tropospheric expansion is not considered and decreases to less than 10 % if it is, using a tropopause-relative grid. Similarly, the E90 tracer abundance increase around the tropopause in the extratropics is connected to the upward shift of the tropopause, since the increase disappears on a tropopause-relative grid. The weaker abundance of the E90 tracer in the UT can be explained by a reduction in the convective updraft mass flux in the lower and middle troposphere, as shown in Figure 6.5. In the tropical UT, however, the convective updraft mass flux increases in both future setups, leading to greater transport into the tropical LS. The response pattern of the convective mass flux to climate change is consistent between the two convection parameterisations. Due to the substantially different updraft strengths in the lower and middle troposphere, as visualised by the contour lines, Emanuel's response is smaller, except in the tropical UT.

So far, I have found a very similar response of the UTLS to climate change across simulations with different convection parameterisations. Therefore, the UTLS composition will change consistently if the trace gas is mainly affected by transport processes, such as N_2O and CH_4, as seen in the previous chapter. Due to their long atmospheric lifetimes, their UTLS abundance is driven by projected changes in their emissions and surface boundary conditions until 2100. Table 3.2 summarised the projected surface boundary condition changes between 2012 and 2100 in the SSP2-4.5 scenario. nitrous oxide is projected to increase, while the anthropogenic CH_4 emissions are projected to decrease, leading to a smaller mixing ratio at the surface. Both surface emission changes are directly projected into the response of the UTLS composition, with consistent results across both setups. nitrous oxide increase homogenously by about 15 % in the UT and LMS, then the increase enhances towards the upper edges of the polar LS to about 25 % increase for the smallest absolute abundances. methane decreases homogenously by about 7 % in the UT, then the decrease reduces towards the upper edges of the polar LS to insignificant changes at the smallest absolute abundances. The gradient occurs due to the relative differences.
The response of the OH abundance in the UTLS is very small. In the summer hemisphere, the

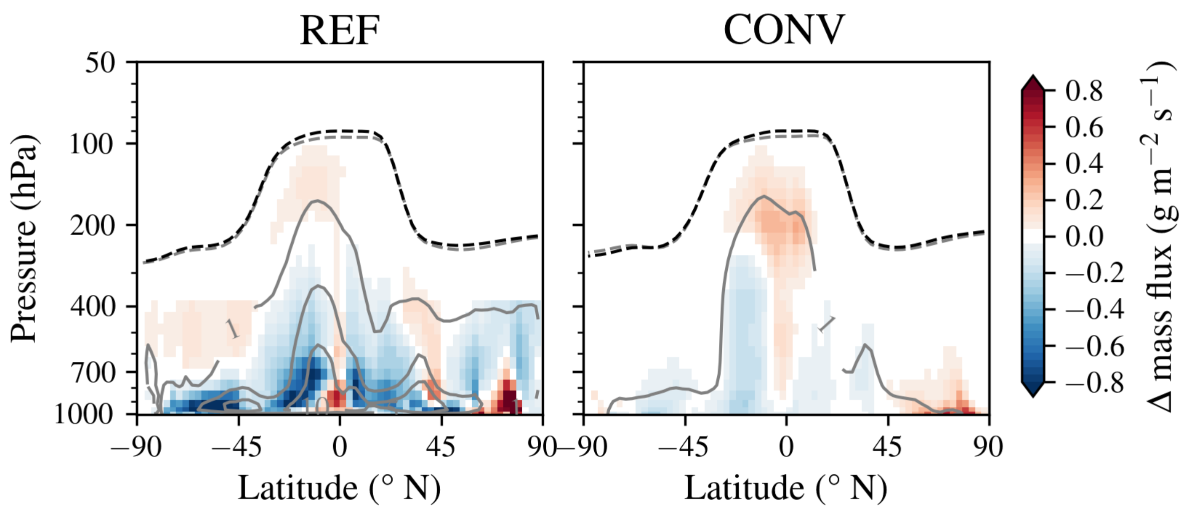

Figure 6.5: Convective mass flux differences between the simulations under future and present-day conditions as climatological and zonal mean of the DJF season. On the left, the difference for the setup with the Tiedtke convection parameterisation (REF), on the right, for that with the Emanuel parameterisation (CONV). The dashed lines indicate the WMO tropopause, shown in grey from the present-day simulations and in black from the future simulations. Grey contour lines mark the convective updraft mass flux strength for 1, 5 and 10 $\mathrm{g m^{-2} s^{-1}}$ for each simulation under present-day conditions.

abundance decreases by less than 10 %, in the tropical UT, the abundance slightly increases by a similar amount. Due to its central role in atmospheric chemistry, the small differences cannot be attributed to individual reactions, and a deeper analysis than is possible within this thesis would be necessary. All figures are available in the Supplement (Figures D.10 and D.11).

The special role of the temperature for H_2O vapour in the atmosphere is visible in Figure 6.7. The H_2O abundance increase correlates strongly with the corresponding temperature response in the UTLS, leading to the strongest increase by about 30 % in the tropical UT on a pressure grid relative to the surface. On a tropopause-relative grid, the logarithmic decrease of H_2O and the small increase in the tropopause pressure result in a small and even not statistically significant H_2O response to climate change, similar to the temperature response. However, the risk of spurious behaviour by the grid transformations is largest H_2O in the tropical UT due to the logarithmic decrease. In the extratropics, the grid transformation has a negligible effect on the comparison. In the tropical LS, the H_2O abundance is smallest on a pressure grid and slightly increases on a pressure-relative grid. The stronger warming of the tropical cold point in the Emanuel setup explains the larger H_2O abundance in the LS. In the Tiedtke simulations, the larger abundance in the tropical UT enables stronger horizontal transport through the STJ. The response is weaker for the Emanuel simulations, probably due to the already substantially larger H_2O abundance in the LS under present-day conditions. Overall, the magnitude of the projected H_2O change is consistent between the Tiedtke and Emanuel simulations, despite the large relative differences in the stratosphere under present-day conditions, and the spread from the convection parameterisation in UTLS H_2O persists.

Finally, Figure 6.8 shows the response of the UTLS O_3 distribution between both setups. Both

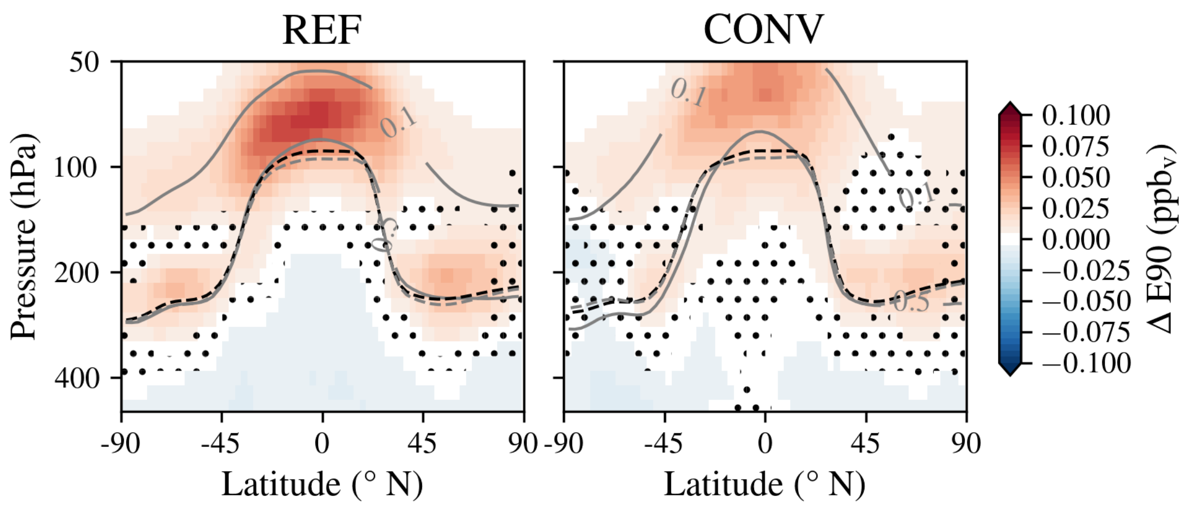

Figure 6.6: Response of the E90 abundance to climate change between the simulations under future and present-day conditions as climatological and zonal mean of the DJF season. On the left, the response for the setup with the Tiedtke convection parameterisation (REF) is shown, on the right, for that with the Emanuel parameterisation (CONV). Grey dashed lines indicate the respective mean WMO tropopause under present-day conditions, black dashed lines indicate the future conditions. Grey contour lines depict the E90 abundance under present-day conditions. In the dotted regions, the changes are not statistically significant according to a two-sided Student's t-test at a 0.05 confidence level.

strongly agree on the pattern, with a reduction in the tropical abundance and an increase in the LS in the extratropics. The reduction in the tropics is partly driven by stronger vertical transport and by increased chemical loss below 200 hPa (not shown). The largest O_3 increase is simulated for both convection parameterisations in the LMS of the SH. The strength, however, is twice as strong in $\text{CONV}_{\text{future}}$, leading to a 30 % larger O_3 abundance in $\text{CONV}_{\text{future}}$ than in $\text{REF}_{\text{future}}$. The region of the most substantial increase correlates with the stronger temperature response seen in Figure 6.2. The diagnostic output of the chemical reactions, as described in the previous chapter, confirms that the future increase of O_3 is driven by a reduction of the catalytic loss cycles in the LS. Figure D.13 displays the change in the chemical loss by Cl-containing radicals in season SON. The reduction follows the ban on ODS emissions and a reduction of their atmospheric abundance in the 21$^{\text{st}}$ century (see Table 3.2). Under future conditions, the stronger stratospheric circulation is no longer balanced by the stronger catalytic removal simulated under present-day conditions, explaining the stronger increase in the O_3 abundance in the LMS.

In summary, the response to climate change projected by the SSP2-4.5 scenario is very robust between simulations that differ only in their choice of the convection parameterisation. Furthermore, the response is smaller than the sensitivity of the choice itself. In both setups, the tropical tropopause pressure decreases by about 5 hPa, leading to a higher tropopause. The tropical UT warms by about 3 K, and the warming in the LMS of the southern hemisphere (summer) correlates strongly with the different strength of the O_3 recovery due to the reduction of ODS in the future scenario. The tropospheric transport and the strength of the stratospheric circulation increase, and differences in the strength lead to a smaller model spread under future conditions

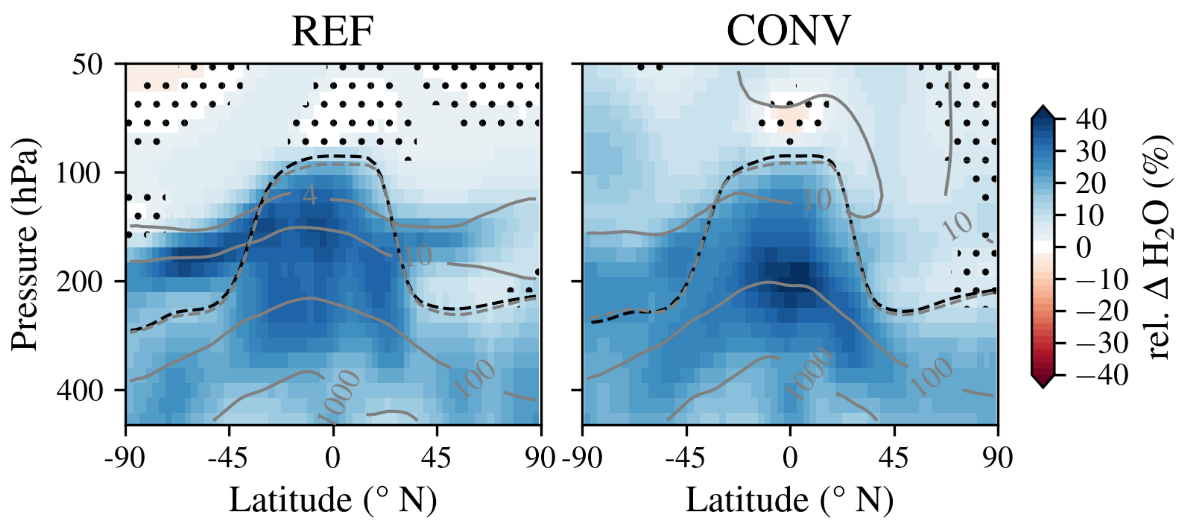

Figure 6.7: Same as in Figure 6.6 but for H_2O as relative differences. Grey contour lines depict the H_2O mixing ratio under present-day conditions in ppm$_v$.

than under present-day conditions. Last but not least, the response of the UTLS composition changes is consistent across the setups, except for the O_3 recovery in the LMS. The projected future changes are largely independent of the applied convection parameterisation.

6.2 Discussion

Over the 21st century, the strength of the BDC is projected to increase further, although less than the increase simulated over the last 20 years of the 20th century. Polvani et al. (2019) and Eichinger et al. (2019) found a reduction of the AoA trends between the last 20 years of the 20th and the 21st century as an indicator for the change of the BDC strength. They found a trend half as strong under future conditions over the CCMVal-2 and CCMI simulations. The multimodel mean AoA decreases by about 0.05 years per decade from 2000 to 2080, vertically averaged between 100 and 1 hPa (Polvani et al., 2019). At 50 hPa, Eichinger et al. (2019) found a mean AoA reduction from 2090s and 1990s for the CCMI REF-C2 models between 0.2 and 0.6 years in the tropics and a larger model spread in the extratropics. They further used an AoA relative to the tropopause. The response in the Tiedtke simulations is a AoA reduction of about 0.2 years at the boundary of the uncertainty range; however, this is also due to the shorter time difference between the start and end points by two decades. Since the first decades show the largest decrease in AoA, the response by the Tiedtke simulations agrees with that of the CCMI simulations. The response in the Emanuel simulations is smaller, as expected, given the already significantly faster stratospheric circulation. Abalos et al. (2021) investigated AoA trends in the CMIP6 1pctCO2 experiment and found the strongest decrease of AoA in the LMS, the upper stratosphere and polar stratosphere, with which my results are consistent.
To investigate the changes of the fast transport from the tropics in the UTLS between the time-slice simulations under future and present-day conditions, I used the diagnostic E90 tracer. Similar to studies using CCMI simulation results, I found larger future abundances in the tropical LS and the LMS, and lower abundances in the UT and the middle troposphere, compared to

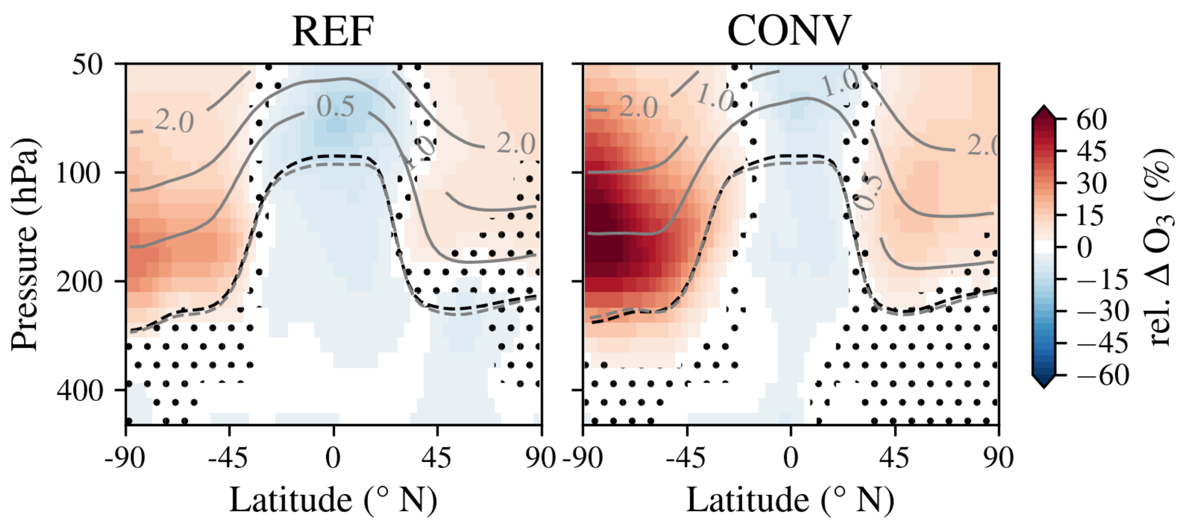

Figure 6.8: Same as in Figure 6.6 but for O_3 as relative differences. Grey contour lines depict the O_3 mixing ratio under present-day conditions in ppm_v.

present-day (Abalos et al., 2017; Abalos et al., 2020). This implies faster and higher-reaching transport. The lower E90 abundance in the UT is linked to a lower convective mass flux simulated with both convection parameterisations, which is confirmed by theory and previous studies (Held and Soden, 2006; Hwang et al., 2011).

For an evaluation of the vertically resolved temperature and zonal wind changes projected at the end of the 21st century, I compare my results with the current state of knowledge documented in the IPCC report (IPCC, 2021). While these reports synthesise our scientific understanding and serve as the rationale for the CMIP simulations, they focus primarily on surface climate and surface changes, rather than on vertically resolved changes under future conditions. Nevertheless, Lee et al. (2021) compared the temperature change in the 21st century for the SSP1-2.6 and SSP3-7.0 scenarios. They found that the warming in the tropical UT is strongest between 2 and 5 K, depending on the scenario, and is consistently simulated with both convection parameterisations in this thesis. The LMS warms or cools depending on the scenario, however, with a low model agreement. Following the observed cooling of the LMS over the last decades of the 20th century due to the O_3 depletion (e.g. (Ramaswamy et al., 2001)), the warming in the LMS under future conditions is associated with the O_3 recovery. Due to the stronger O_3 depletion in the simulation using the Emanuel convection parameterisation, the stronger recovery leads to a stronger warming in the LMS compared to the simulations using the Tiedtke convection parameterisation. This suggests that atmospheric chemistry drives the deviation from IPCC. For CMIP6, which was the basis for the IPCC (2021), none of the models used a tropospheric interactive chemistry scheme, and only 9 include some form of stratospheric chemistry. The others prescribe species such as O_3 (Keeble et al., 2021).

Following the analysis of the response of the zonal wind due to climate change for the CMIP6 models, Lee et al. (2021) found a strengthening of the westerlies above the STJs by up to 3 and 6 ms^{-1} for SSP1-2.6 and SSP3-7.0, respectively. While I simulated the same pattern of zonal wind changes with both convection parameterisations, the strength of the changes above the STJ region is close to the response to the SSP1-2.6 scenario, in the case of the Emanuel convection parameterisation, even smaller. The smaller response in the Emanuel simulations

might be due to the fact that the differences between the Tiedtke and Emanuel simulations under present-day conditions resemble the zonal wind response to climate change, potentially leading to a weaker necessary change to match future conditions. To my knowledge, three climate models incorporate a version of the ECHAM model. They therefore should simulate the closest response to EMAC to the same climate forcing: the AOGCMs AWI-CM and MPI-ESM (before they changed to ICON), and the CCM SOCOL (e.g. Chiodo et al., 2023). Of course, next to the climate studies using the AGCM ECHAM and a SST/SIC climatology (e.g. Koskentausta et al., 2025). Semmler et al. (2020) contributed to CMIP6 with the AOGCM AWI-CM-1-1 and simulated a zonal wind response between 4–6 ms^{-1} to the SSP3-7.0 scenario over annual means between the climatologies 2071–2100 and 1985–2014, corresponding to the multi-model response in CMIP6. This could indicate a smaller response to projected climate change in EMAC. However, so far I found no response for the SSP2-4.5 scenario, and the climatology periods differ, which prevents a final conclusion.
For the global precipitation change, Tebaldi et al. (2021) estimated a 4 % mean increase for 2100 and a 2–7 % 1.64σ interval compared to the mean of 1995–2014, based on the CMIP6 SSP2-4.5 simulation results. The precipitation change calculated with the Tiedtke simulations exhibits a 2.85 % increase, with the Emanuel simulation only 1.51 %. The smaller increase of precipitation in the future simulation with Emanuel may indicate a lower dependence of the convection on temperature changes or an inconsistency in the SST forcing data.
Under SSP2-4.5, the stratospheric H_2O above the LMS is projected to increase by 0.6 ppm_v from the first 15 years of the 21^{st} century to the last, with a temperature increase of 1.5 K at 100 hPa (Keeble et al., 2021). While the temperature response at 100 hPa is similar in both setups, the increase in stratospheric H_2O is not. REF_{future} simulates an increase of slightly more than 0.1 ppm_v, $CONV_{future}$ more than 1 ppm_v, similar to the substantial differences in the stratospheric H_2O abundance.
For O_3, the CMIP6 multi-model mean projects an O_3 increase in the stratosphere and a decrease in the troposphere (Keeble et al., 2021; World Meteorological Organization, 2022). At the tropical tropopause, O_3 decreases by 15–20 % for the CMIP6 model results, which is slightly stronger than for the EMAC simulations. The smaller decrease corresponds to the positive O_3 bias in the troposphere simulated by EMAC (e.g. compare Figure D.7). The strongest increase of more than 30 % is projected in the LMS of the SH, matching the O_3 response for the Tiedtke simulations closely. In contrast, the Emanuel convection simulations overestimate O_3 depletion under present-day conditions, leading to a O_3 recovery that is twice as strong on a percentage basis. Under future conditions, $CONV_{future}$ simulates a O_3 abundance in the LMS up to 30 % larger than REF_{future}. Since CCMI is completely based on CCM model results, this would be the more suitable comparison. However, CCMI did not compare O_3 mean changes in the UTLS vertically resolved, and the forcing and emission data differ from those of CMIP6 and SSP2-4.5. Furthermore, even the 2022 Ozone Assessment report, used for their investigation CMIP6 model results (World Meteorological Organization, 2022). The CMIP6 data comprise results from models with no chemistry (prescribed O_3), simplified chemistry, and interactive stratospheric chemistry. Therefore, O_3 chemistry is the first to be included, thanks to the ongoing research on stratospheric O_3 and O_3 depletion over the last decades.
The strength of the O_3 increase is dominated by the strength of the removal reactions on PSCs. Friedel et al. (2023) found large differences between the impact of PSCs simulated with different models in CCMI and CCMI-2022, which is consistent with the effect of different convection parameterisations found in this study. The differences are projected to decrease under future

conditions, leading to a stronger agreement between the models for the strength of O_3 minima in the polar regions (Friedel et al., 2023; Polvani et al., 2023). The O_3 recovery in the LMS together with the stronger BDC results in an enhanced O_3 transport from the stratosphere into the troposphere (Abalos et al., 2020; World Meteorological Organization, 2022). The effect is stronger in the Emanuel simulations in the SH, as reflected by the larger O_3 increase.

The comparison between temperature, H_2O, O_3, and PSCs in the LMS of the SH during DJF between present-day and future conditions highlights their strong coupling. Stratospheric H_2O is more abundant in the simulations using the Emanuel convection parameterisation than in those using the Tiedtke convection parameterisation. The smaller abundance of the GHGs H_2O, N_2O, and CH_4 leads to cooling of the LMS (Ramaswamy et al., 2001), which is likely enhanced by the dynamical feedback of Emanuel on the dynamics compared to Tiedtke (Hourdin et al., 2006). The lower temperatures and the higher H_2O abundance favour the formation of PSCs, thereby reducing O_3 abundance and further enhancing cooling. Over the 21st century, the abundance of ODS in the atmosphere decreases due to the ban on their emissions, leading to the O_3 recovery. Due to the stronger loss due to PSCs in the Emanuel simulations, the O_3 recovery in the future scenario is stronger, which in turn leads to a stronger radiative heating in the LMS and a stronger temperature response. This proposed mechanism to explain the strong differences in the response is consistent with the attribution studies of Ramaswamy and Schwarzkopf (2002) and Shine et al. (2003) and others.

Chapter 7

Discussion of methodological choices and their limitations

In the previous chapters, I presented my results and put them in context with literature. This chapter discusses the applied methodologies and their limitations.

7.1 The choice of the tropopause and a tropopause-relative representation

I selected the WMO lapse rate tropopause as the boundary between the troposphere and the stratosphere throughout this thesis for several reasons. Firstly, at the coarse resolution of CCM simulation over climate scales, the model cannot simulate tropopause folding events or tropopause breaks. Therefore, the lapse rate tropopause provides one global tropopause surface. Secondly, the dynamical tropopause shows spurious behaviour in the tropics due to a change in sign of the planetary vorticity at the equator. This led to a combination of the dynamical tropopause outside the tropics and another definition in the tropics. For instance, Hoffmann and Spang (2021) used the 380 K isentrope in the tropics and the 3.5 PVU dynamical tropopause elsewhere. In EMAC, a combination of the dynamical and lapse rate tropopause is implemented. The default value for the dynamical tropopause is 3.5 PVU, the default switch between the two definitions occurs at 30° N/S. However, simulations with a finer grid resolution showed a lower lapse-rate tropopause, creating kinks at 30° N/S. Therefore, the definition would need to be revised to avoid a spurious comparison between the simulations. This finding motivated me to introduce the combined tropopause based on the dynamical tropopause and the 380 K isentrope into MESSy. The default settings are at the equator (5° N/S), the 380 K isentrope, and, otherwise, the lower of the 380 K and the 2 PVU dynamical tropopause, which always selects the 2 PVU outside the tropics but with a less strict latitude criterion for the switch. Thirdly, the lapse rate tropopause is used for region-dependent processes during the simulation and therefore best aligns with the results. Examples of processes are chemical reactions that occur only in the troposphere or the stratosphere, and the MSBM submodel for the formation of PSCs. Test simulations with the newly implemented combined tropopause used during runtime revealed that the radiative imbalance at the TOA is strongly sensitive to the tropopause definition. This is further an indication of the strong effect of the UTLS region on the radiative forcing. It would have been necessary to retune the simulations significantly and even rerun some of them to ensure consistency. Therefore, I decided against changing the tropopause definition and use the lapse rate tropopause in my investigations to be as consistent with the simulation as possible, which should have the largest effect for UTLS studies.

Using tropopause-relative vertical coordinates eliminates the local effect of tropopause pressure differences, which are evident in both the sensitivity simulation results and the present-day and future scenarios. Eliminating the seasonal variability of the tropopause pressure from the time series further simplifies the identification of robust trends in the LMS (Thompson et al., 2021). However, not on the monthly means used to derive the trends in this thesis. Furthermore, as the tropopause is not lifted uniformly between poles and equator, e.g. as seen in Figures 5.8 and 6.1, non-local effects can be concealed (Match and Gerber, 2025). Especially in the vicinity of steep vertical gradients, such as those for H_2O and temperature in the tropics, the grid transformation is prone to errors. Therefore, the main benefit occurs when the differences are primarily around the tropopause.
The tropopause can further be seen as a transport barrier, in addition to the boundary between the troposphere and the stratosphere. Using this property, tropopause-relative coordinates can be used to investigate the strength of the transport barrier across simulations. However, there is no universal tropopause definition that fits the transport barrier equally well for all trace gases, as shown by the tropopause pressure differences among the lapse rate, dynamical, and chemical tropopauses. Using the same definition across all datasets and for all quantities ensures that each data point is assigned to the same layer, enabling comparisons of different variables based on their position relative to the tropopause. Furthermore, the selected lapse rate tropopause is based on a strict definition, apart from differences in the implementation of the second criterion, with clear thresholds and straightforward global calculation. Better-suited tropopause definitions for describing the transport barrier for a trace gas, such as the dynamical or chemical tropopause, vary with latitude and across species. These benefits lead me to conclude that it is better to include minor misrepresentations due to misclassified individual data points around the tropopause than to ignore the transport barriers at the tropopause altogether.

7.2 The statistical significance of the differences

To assess the variability and significance of differences between the sensitivity studies and observations, I used an independent two-sided Student's T-test, treating each data point as independent. However, every grid point of the atmosphere is coupled to its neighbours, large regions such as the LMS are affected by the same processes and will behave similarly. Therefore, the statistical analysis should include some information about the other grid points. This can be achieved by calculating a so-called field significance. It adjusts the independently calculated p-values at each grid point based on the total quantity of grid points and p-values. One method to do so is the false discovery rate (Wilks, 2016). However, adjusting the p-values by the false discovery rate marks each difference in the UTLS as not statistically significant. The reason is the small data sample: when comparing data as zonal and seasonal means, there are only 20 seasonal values for each grid point in the pressure/altitude-latitude plane. The false discovery rate also does not account for the reduction in interannual variability resulting from the application of the TS configuration. Therefore, the field significance is not applicable to my studies. The statistical significance, based on the independent Student's t-test with a significance level of

0.05 applied in this study, mainly classifies regions with small differences or large interannual variability as not statistically significant. Therefore, the results agree with our physical understanding and can support a statement about them, but they cannot be used to draw independent conclusions.

A similar deficit occurs for the trend analysis performed in Chapter 4. By performing a linear trend analysis only on the time series of the variable, large-scale processes that affect the atmosphere over years are not accounted for. This complicates any trend analysis, especially in a highly variable region such as the UTLS. Removing the variability of the tropopause height was insufficient. A method for accounting for variability due to large-scale processes is multiple linear regression. For instance, Benito-Barca et al. (2025) used multiple linear regression to calculate statistically significant O_3 trends in the lower stratosphere over 20 years of data.

7.3 The missing ocean component

Another factor contributing to the differences between the resulting climate state parameters is the SST/SIC forcing used in the simulations. Braconnot et al. (2007) found SST differences by up to 2 K in the tropics, between simulations with the Tiedtke and the Emanuel convection parameterisation. This confirms a significant effect from the convection parameterisation on the SST, next to the omnipresent effect from the ocean temperatures on the generation of convection. In this work, no ocean component was coupled to the CCM EMAC, therefore, the ocean forcing data had to be prescribed. The data is taken from an MPI-ESM simulation with the AGCM ECHAM and the Tiedtke convection parameterisation. Any effect of the convection parameterisation on SST/SIC spatial patterns introduces an inconsistency if the resulting data are used to drive a model utilising another convection parameterisation, such as in $\text{CONV}_{\text{today}}$ and $\text{REF}_{\text{future}}$. Therefore, SST forcing data will better align with the behaviour and generation of convection with the Tiedtke simulations. The impact of the inconsistency for the Emanuel simulations cannot be quantified without additional simulations with independent SSTSIC forcing data. However, it is likely to affect global precipitation rates and cloud cover, influencing the performance of the climate state parameters.
The inconsistency may also contribute to the increasing radiative imbalance at the TOA under future forcing conditions and to a lower increase in the precipitation rate. While the radiative imbalance at the TOA in $\text{REF}_{\text{future}}$ decreases to 0.58 Wm^{-2}, it increases in $\text{CONV}_{\text{future}}$ to 3 Wm^{-2}. The hypothesis cannot be confirmed without performing further simulations with a consistent SST/SIC forcing dataset, or with an interactively coupled ocean model component.

Furthermore, an interactive ocean model is necessary to investigate the sensitivity of my results on the surface warming in climate change. I showed in this thesis that the convection parameterisation significantly affects the GHG composition in the UTLS, and therefore the surface temperature (Forster and Shine, 1997; Riese et al., 2012). One intermediate step is to investigate radiative forcing differences driven by these GHG composition differences in the UTLS, using diagnostic calculations with the MESSy radiation scheme or a stand-alone radiation kernel.

7.4 The single SSP scenario

The SSP scenarios cover a wide range of idealised projections of the global climate. It enables model intercomparison and the investigation of uncertainty spread by removing avoidable differences, such as differences in emission inventories, to the greatest extent possible. I chose the SSP2-4.5 scenario for the future boundary conditions in 2100. It is defined as a "middle of the road" scenario, extrapolating the current trend into the future, assuming international cooperation does not expand and that global income inequality increases. With an additional radiative forcing of 4.5 Wm^{-2} in 2100 compared to 1850, the best estimate based on the CMIP6 models is a projected warming of 2.7 °C in 2100 relative to the period 1850–1900 (IPCC, 2021). Unfortunately, by comparing the development of the mean surface temperature over the last decade since the start of the SSP scenarios, we find that the scenarios underestimate the observed surface warming. If the current trend in surface warming continues, we will reach 1.5° C mean surface warming by 2030 (Copernicus, 2026). The last few years have seen a decline in efforts to mitigate emissions. Based on these developments, a SSP scenario with a higher estimated forcing by 2100 might be more realistic. Furthermore, the robustness of climate projections to the convection parameterisation might vary significantly, depending on the sensitivity to larger forcing. Therefore, additional projection simulations based on different forcing assumptions are necessary. To cover the entire range of forcing scenarios, simulations using the highest scenario would be a suitable complement to the investigations in this thesis, SSP5-8.5. Comparing the UTLS composition changes between different climate forcing scenarios reveals whether the convection parameterisation is sensitive to radiative forcing.

Finally, both future simulations in this thesis and all model projections based on SSP scenarios significantly underestimate future climate uncertainty and the UTLS composition (Chim et al., 2025). No assumptions about volcanic eruptions are included, however, small-to-medium volcanic eruptions occur frequently and have a significant effect on total radiative forcing by affecting the aerosol composition in the UT and the transparency of ice clouds (Schmidt et al., 2018). This deficiency is removed from the forcing data of the most recent version of CMIP, CMIP7 (Aubry et al., 2025). Therefore, CMIP7 will inevitably differ from previous versions. Still, it will create a more realistic UTLS composition and aerosol load, and will change the UTLS composition and its radiative effect.

7.5 The model spread by single configuration aspects

Throughout my thesis, I aimed to isolate the effect of specific model configurations, isolating only one aspect at a time, on the simulated results. My results indicate that decisions, such as those for the convection parameterisation, have a significant impact across the atmosphere, even in regions where they have no direct effect. Such dedicated studies to isolate the effects of a single aspect of climate models are necessary to attribute deficiencies in complex models to specific processes within the model configuration. In all MIPs, the models differ with respect to many model components and process parameterisations, nicely listed by Morgenstern et al. (2017). An attribution of differences between simulation results of different models to individual differences is therefore hardly possible, if at all. Sometimes the same model component or process parameterisation is used with the same ancestor, leading to a closer agreement between the models (Knutti et al., 2013; Kuma et al., 2023). Nevertheless, such model families can only provide indications on the effects of components and parameterisations, motivating further sensitivity studies. To identify the global effect of single processes, isolated variation of individual parameterisations, one at a time, is the only option, and it must be investigated across different models to filter out biases from other components.

Chapter 8

Conclusions and Outlook

In this final chapter, I will answer my research questions formulated in Chapter 1.2. Afterwards, I provide an outlook on future research, motivated by the results.

8.1 Answers to the research questions

1. How does Newtonian relaxation affect the simulated UTLS composition on climate scales? How do nudged and free-running simulations perform compared to observations?

Newtonian relaxation affects the representation of the position of transport barriers in the simulated UTLS and the dynamical transport throughout the model atmosphere (see Chapter 4). It reduces temperature and wind biases and decreases the deviation of the tropopause pressure simulated in EMAC from that in high-resolution reanalysis datasets. Therefore, Newtonian relaxation solves the problem of a too high tropopause that many state-of-the-art CCMs calculate. This is favourable to enable a reasonable comparison with observations, since more realistically simulated transport barriers are a prerequisite for comparing observed and simulated air samples from corresponding regions. However, the benefit of Newtonian relaxation for the simulated UTLS composition is strongly limited to a subset of variables, for instance, H_2O in the stratosphere, by the reduction of the cold bias at the tropical cold point in EMAC. The configuration of Newtonian relaxation typically applied in EMAC, including in the simulation presented in this study, ends above the UTLS as previous studies have shown that Newtonian relaxation in the stratosphere decouples the stratospheric circulation from its wave forcing, leading to spurious behaviour and divergence from the reference. However, Newtonian relaxation indirectly influences the stratospheric circulation, as it is driven by the dissipation of Rossby waves generated in the troposphere. The wave generation in the troposphere is, in turn, directly influenced by Newtonian relaxation. In this Newtonian relaxation configuration in EMAC, Newtonian relaxation decreases the stratospheric circulation strength in the shallow branch of the BDC, but substantially increases the circulation strength in the deep branch. The quantification of the differences using AoA revealed younger AoA in the middle and upper stratosphere by up to 0.4 years, in the deep branch of the BDC. Therefore, Newtonian relaxation enhances the already too fast stratospheric circulation relative to AoA estimates based on observations. As a consequence, the faster transport by the deep branch increases the simulated O_3 abundance in the LMS in the winter hemisphere, and therefore increases the positive O_3 bias present in the

results of free-running EMAC simulations.
The Newtonian relaxation configuration reduces regional temperature biases but not the global mean, leading, for instance, to a strong reduction of the LMS cold bias in nudged versus free-running simulations. However, this correction cannot fix the cause of the issue: the too strong numerical diffusion. The reduction of the cold bias leads to more water vapour transport across the tropopause into the lower part of the LMS, leading to H_2O mixing ratio more than twice as large as in the observational dataset SWOOSH in both hemispheres. However, for most of the stratosphere, H_2O abundance is governed by the tropical cold point temperature; reducing its cold bias therefore reduces the stratospheric dry bias in simulations affected by Newtonian relaxation.
My investigations revealed that the benefit of Newtonian relaxation is limited for UTLS studies. It is preferable to ensure a good representation of the tropopause when comparing observed stratospheric air samples with stratospheric air in the model, and likewise for tropospheric samples. The benefit decreases with increasing atmospheric lifetime and increasing effect of stratospheric transport. The stronger a constituent is affected by the stratospheric circulation, the greater the deviation of the Newtonian-relaxed results from the free-running EMAC simulation results, and, to an increasingly lesser extent, the results of a simulation affected by Newtonian relaxation can be used as an indicator of the free-running model's performance.

2. What will be the benefit for the UTLS characteristics of a computationally feasible increase of the model grid resolution in EMAC?

With the increase of the horizontal grid resolution from the default T42L90MA resolution to T106L90MA, EMAC reduces several of its biases in the UTLS, defined as deviation from observations and reanalysis data (see Chapter 5 and Appendix D.2). The better representation of the steep gradients in the extratropics reduces the numerical diffusion, leading to a stronger transport barrier, which reduces the moist bias in the LMS above the tropopause. This reduces the radiative cooling effect of H_2O in the lower part of the LMS and therefore reduces the cold bias from about -8 K to about -5 K compared to ERA5. In this context, it is important to note that the moist and cold bias is still present in IFS (and therefore ERA5) results in the lower part of the LMS, despite the fact that IFS is operated at a much finer horizontal (about 9 km compared to 125 km grid size at the equator in EMAC T106) and finer vertical (137 vs 90 levels until 0.01 hPa) resolution. The reduction of the cold bias in the LMS further changes the temperature profile and reduces the tropopause height, reducing the tropopause height difference between EMAC results and reanalysis data by 50 %. Temperature differences in the tropical UT are insignificant, resulting in a reduction of the horizontal temperature gradient and further to no effect on the cold bias at the tropical cold point and the dry bias in the stratosphere. The stratospheric AoA is older when simulated at T106 resolution by up to 0.5 years in the winter stratosphere, reflecting slower transport by the residual circulation, which better agrees with observations. The older AoA in the polar winter stratosphere is associated with a stronger polar vortex.
The investigation of different vertical resolutions in connection with the spectral resolution T106 revealed that the default vertical resolution of 90 vertical levels yields results closer to observational and reanalysis data than the simulation with 191 levels. In the vicinity of strong winds, such as the STJ and the polar vortex, the finer vertical resolution leads to even higher wind speeds in comparison to ERA5, especially for the polar vortex.

The analysis revealed that increasing the horizontal resolution strongly improves UTLS dynamics, reduces several model biases in the UTLS, and further improves UTLS composition by slowing the stratospheric circulation. An additional increase in vertical resolution provides little to no benefit, underscoring the influence of the ratio of horizontal to vertical resolution on model improvement.

3. How does the choice of the convection parameterisation affect the simulation of UTLS characteristics and composition?

Different convection parameterisations differ substantially in their calculated cloud and H_2O abundances in the troposphere, and consequently in their influence on the dynamics. Therefore, the choice of the convection parameterisation in a model has a strong influence on the simulated UTLS composition (see Chapter 5). The UTLS composition is directly affected by the fast convective transport of constituents into the upper troposphere. Moreover, convection influences the generation of Rossby waves in the troposphere and their propagation into the stratosphere, thereby influencing transport throughout the atmosphere.
The simulated convective vertical transport strength and the simulated height of main convective outflow in the UT have a substantial effect on the resulting UTLS abundance of species with an atmospheric lifetime of weeks to months. The larger cloud cover in the tropical UT simulated with the Emanuel convection parameterisation leads to a complete removal of the cold bias at the tropical cold point of about 5 K in comparison to ERA5, which is present when simulated with the Tiedtke convection parameterisation. As a consequence, the simulation with Emanuel results in a stratospheric moist bias of about 200 %, while the Tiedtke simulation results in a dry bias of 25 % in comparison to SWOOSH, as seen in most CCMs. The induced effect of convection on the dynamics alters temperatures in the LMS by several Kelvin, thereby affecting the formation of PSCs and the O_3 minima in spring. Convection further significantly affects the entire stratospheric circulation by altering stratospheric temperature gradients and wind fields, leading to AoA variations by up to 0.8 years in the deep branch of the BDC. Furthermore, an analysis of the residual circulation using the Transformed Eulerian-Mean results in differences in the Rossby wave propagation to the upper stratosphere, indicated by differences in the Eliassen-Palm flux divergence, which contributes to the differences in the circulation strength. A quantitative analysis of the differences in the wave propagation is subject to further investigations.
Overall, this shows that varying only the convection parameterisation in the model has a substantial impact on the UTLS composition and dynamics across the middle atmosphere. The extent of this effect has not been shown before and could partially explain the spread in results from different models performed with the same boundary conditions, as is usually done in MIPs. For instance, the convection parameterisation can be one reason for model differences in the strength of O_3 minima in spring and the O_3 recovery in the 21st century. Furthermore, the impact on the UTLS GHG composition might partly explain the spread of model results of simulated surface warming in climate projections. Attributing part of the model spread in surface warming to convection will highlight what we need to work on and maybe even allow us to reduce the uncertainty in our current knowledge about surface warming.

4. In what ways are the projected UTLS responses on climate change dependent on the choice of the convection parameterisation?

The comparison of the mean state between future projections and present-day simulations reveals consistent responses across different convection parameterisations (see Chapter 6). Therefore, in the case of a moderate climate change, as defined by the future scenario SSP2-4.5, the change is robust to the choice of the convection parameterisation. Differences in the strength of the dynamical response, such as the stratospheric circulation and the polar vortex, lead to a reduction of the model spread under future conditions. Temperature, H_2O and O_3 responses on climate change in the LMS of the southern hemisphere are driven by O_3 recovery and the sensitivity of the turnover rates of the chemical removal of O_3 on PSCs under present-day conditions. The formation of PSCs reduces under future conditions due to the ban on CFCs emissions, and the differences in the strength of the stratospheric circulations are no longer balanced in the future, leading to a change in sign of the O_3 abundance differences. The radiative heating of O_3 in the stratosphere leads to the stronger warming of the LMS, which allows for a higher H_2O abundance. In summary, the projected change (in terms of sign and magnitude) of the UTLS composition under climate change is, to a large degree, unaffected by the choice of the convection parameterisation.

8.2 Outlook

All sensitivity studies have shown significant differences in AoA, indicating an effect on the stratospheric circulation. To differentiate between differences in mean flow advection and transport due to wave eddy mixing, a budget analysis can be performed (e.g., Harzer et al., 2023). Basing the analysis on the diagnostic tracers without chemical sources and sinks used for the calculation of AoA further removes the source term from the budget equation.

The choice of the convection parameterisation has a strong effect on the simulated abundance of GHGs in the UTLS, especially for H_2O. Several previous studies showed that the surface climate is susceptible to GHG changes in the UTLS. In my study, I quantified the effect of the convection parameterisation on simulated UTLS composition. In the next step, it is required to estimate the impact of convection on the radiative forcing in the UTLS. This could potentially be achieved by utilising additional diagnostic calls in the radiation calculation with input from differently simulated UTLS compositions. Alternatively, a radiative kernel can be used. If the analysis results in significant differences in the radiative forcing, CCM simulations with different convection parameterisations and an interactive ocean component are justified to quantify differences in surface warming.

I further found a consistent response to climate change across simulations with different convection parameterisations, but strictly speaking only for the SSP2-4.5 scenario. However, different forcing scenarios span a range of possible changes, and the system response is not linearly related to the forcing. The convection parameterisations might respond differently to larger forcing. Therefore, I propose to add future projections based on the SSP5-8.5 scenario.

Finally, I showed that a finer horizontal resolution leads to substantial improvements in the simulated UTLS characteristics. My sensitivity simulation regarding the model resolution had to be performed without atmospheric chemistry due to the high computational costs. To make simulations with finer resolution computationally feasible for our CCM, we need to advance the development of ICON/MESSy. The goal is to replace the ECHAM atmospheric model with its spectral representation by ICON, which uses finite-element methods instead. The finite elements enable better parallelisation of the dynamical core calculations, leveraging modern HPC infrastructure. Based on my findings, ICON/MESSy is expected to improve the UTLS composition through its finer horizontal resolution.

Acronyms

M molar mass (g mol^{-1}). 127

R universal gas constant; $N_A \cdot k_B$ ($\mathrm{Jkg}^{-1}\mathrm{K}^{-1}$). 127

R_s specific gas constant; dry air = 287.05 $\mathrm{Jkg}^{-1}\mathrm{K}^{-1}$. 127, 128

T temperature (K). 127

T_v virtual temperature. 22

V volume (m^3). 128

Γ lapse rate (K m^{-1}). 127

Γ_{TP} lapse rate threshold of the WMO tropopause; -0.002 Km^{-1}. 129

λ photon wavelength; $\lambda = c/\nu$. 13

ϕ latitude. 129

ρ density (kg m^{-3}). 128

σ isentropic density; $\sigma = \rho \left(\frac{\partial\theta}{\partial z}\right)^{-1}$. 11

θ potential temperature (K). 127

ζ_θ relative vorticity on an isentropic surface. 11

c speed of light (vacuum); $c = 2.9979 \cdot 10^8$ m s^{-1}. 13

c_p specific heat capacity at a constant pressure; in air = 1005.46 $^{-1}\mathrm{K}^{-1}$. 127

f Coriolis parameter; $f = 2\Omega\sin(\phi)$. 11

g gravitational acceleration (m s^{-2}). 128

h Planck's constant; $h = 6.626 \cdot 10^{-34}$ J s. 13

i model level index. 128

i' model interface index. 128

m mass (kg). 128

n amount (mol). 128

$p_{TP+2000m}$ pressure 2000 m above the tropopause pressure. 129

p_{TP} tropopause pressure. 129

ν photon frequency; $\nu = c/\lambda$ s^{-1}. 13

z altitude (m). 127

Br bromine. 83

CH_3 methyl radical. 14

CH_4 methane. 2, 80, 81, 97, 140

CO_2 carbon dioxide. 1, 13, 18, 31, 37, 79

Cl chlorine. 83

H_2O water vapour. 2

HO_2 hydroperoxyl radical. 17, 82

H hydrogen. 18

M third molecule for reactions; N_2 or O_2. 15

N_2O nitrous oxide. 13, 79, 80, 97

N_2 nitrogen. 15

NO_2 nitrogen dioxide. 17, 82

NO nitric oxide. 82

$O(^1D)$ excited oxygen. 13, 15

O_2 oxygen. 15, 80

O_3 ozone. 1, 13, 81

OH hydroxyl radical. 13, 17, 80, 81, 140

O atomic oxygen. 15

AGCM Atmospheric General Circulation Model. 28, 29, 45, 47, 61, 88, 90, 91, 107

AoA Age of Air. 12, 55, 57, 58, 61, 75, 76, 79, 88, 89, 96, 97, 100, 111–114

AOGCM Atmosphere Ocean General Circulation Model. 66, 102

BDC Brewer-Dobson Circulation. 1–4, 9, 11, 12, 18–20, 24, 25, 35, 49, 54–58, 76, 79, 81, 96, 100, 103, 111, 113

BMIL base model interface layer. 27–29

BML base model layer. 27, 28

BrO_x reactive bromine family, Br + BrO. 16, 17

CAPE Convective Available Potential Energy. 22

CCI Climate Change Initiative. 67

CCM Chemistry Climate Model. vii, 2–6, 24, 29, 30, 102, 105, 107, 111, 113, 114

CCMI Chemistry Climate Model Initiative. 37, 44, 88, 100, 102

CFCs chlorofluorocarbons. 1, 114

ClO_x reactive chlorine family, Cl + ClO. 16, 17

CMIP Coupled Model Intercomparison Project. 3, 4, 37, 89, 100–102, 108

DJF December-January-February. 50–58, 70–73, 79, 82–84, 86, 93–96, 98, 99, 103, 136–139

ECHAM ECMWF and Hamburg. 28, 29, 32, 33, 35

ECMWF European Centre for Medium-Range Weather Forecasts. 28

EDJ eddy-driven jet. 10

EMAC ECHAM/MESSy Atmospheric Chemistry. vii, 27, 29, 31, 111

ERA5 ECMWF Reanalysis version 5. 32, 42, 43, 51, 52

ESA European Space Agency. 67

ESM Earth System Models. 28, 45

ExTL extratropical tropopause layer. 19, 20

GCM General Circulation Model. 4, 27

GFAS Global Fire Assimilation System. 44

GFED Global Fire Emissions Database. 44

GHG greenhouse gas. vii, 1, 2, 4, 13, 14, 23, 24, 29, 31, 37, 47, 62, 64, 71, 85, 88–90, 103, 107, 113, 114

GPCP Global Precipitation Climatology Project. 65, 66

GWP global warming potential. 13

HALOE HALogen Occultation Experiment. 43

HAMOCC Hamburg Model about Ocean Carbon Cycle. 45

HO_x hydrogen radical family, OH + HO_2. 16, 17

HPC High Performance Computing. 6, 35, 115

ICON ICOsahedral Non-hydrostatic modelling framework. 35

IFS Integrated Forecasting System. 28, 35, 42, 43, 52, 91

IPCC Intergovernmental Panel on Climate Change. 1, 101

ITCZ intertropical convergence zone. 23, 66

JJA June-July-August. 93, 94

JSBACH Joint Scheme for Biosphere Atmosphere Coupling in Hamburg. 45

LMDZ Laboratoire de Météorologie Dynamique (Zoom capability). 91

LMS lowermost stratosphere. vii, 3, 4, 12, 19, 20, 24, 52, 53, 55, 56, 59, 74, 81, 87, 88, 99–103, 106, 111–113

LS lower stratosphere. 3, 12, 16, 20, 53, 74, 76, 88

LW longwave. 62, 90

LWP liquid water path. 64, 65, 90

MCSs mesoscale convective systems. 21, 22

MERRA2 Modern-Era Retrospective analysis for Research and Applications, Version 2. 44, 52

MESSy Modular Earth Submodel System. 27, 29, 31, 64

MIM mainz isoprene mechanism. 30

MIP Model Intercomparison Project. 108, 113

MLS Microwave Limb Sounder. 43

MPI-M Max Planck Institute for Meteorology. 45

MPIOM Max Planck Institute Ocean Model. 45

N highest resolved spectral zonal wavenumber. 34

N_{lat} number of latitudes. 34

N_{lon} number of longitudes. 34

NAT nitric acid trihydrate. 16

NH Northern Hemisphere. 2, 20, 51, 73

NMHC non-methane hydrocarbons. 30, 39, 47

NO_x nitrogen oxide family, NO + NO_2. 16–18, 30, 31, 38, 44, 82, 83, 134

NWP Numerical Weather Prediction. 3, 32, 43

O_x odd oxygen family, O + O_3. 16, 18

ODS ozone depleting substances. 1, 4, 14–16, 25, 31, 37, 47, 83, 99, 103, 135, 140

PDE partial differential equation. 30, 33

ppb$_v$ parts per billion by volume. 13

ppm$_v$ parts per million by volume. 56, 102

PSCs Polar Stratospheric Clouds. 3, 16, 17, 25, 30, 67, 83, 85, 86, 102, 103, 105, 113, 114

PV potential vorticity. 10

PVU potential vorticity unit, [PVU] = $10^{-6}\,\mathrm{K\,m^2\,(kg\,s)^{-1}}$. 11

QBO Quasi-Biennial Oscillation. 20

RH relative humidity. 21

SAGE Stratospheric Aerosol and Gas Experiment. 43

SAOD Stratospheric Aerosol Optical Depth. 133

SD Specified Dynamics. 44

SH Southern Hemisphere. 24, 56, 57, 66, 73, 81, 84, 99, 103

SIC sea ice concentration. 44, 66, 93, 107

SMCL submodel core layer. 28

SMIL submodel interface layer. 27, 28

SON September-October-November. 83, 87, 99, 140

SSP Shared Socioeconomic Pathway. 37, 38, 108

SST sea surface temperature. 24, 44, 66, 93, 102, 107

STE stratosphere-troposphere exchange. 3, 18

STJ subtropical jet. 3, 9, 10, 19, 20, 24, 54, 56, 72–76, 87, 89, 94, 98, 101, 112

SW shortwave. 62, 90

SWOOSH Stratospheric Water and OzOne Satellite Homogenized data set. 42, 43, 51

TEM Transformed Eulerian-Mean. 12, 56, 76, 113, 138

TOA top of atmosphere. 39, 40, 58, 62, 84, 90, 105, 107

TS time-slice. 44, 61, 86, 87, 93, 106

TTL tropical tropopause layer. 18–20

UARS Upper Atmosphere Research Satellite. 43

UT upper troposphere. 2–4, 12, 20, 21, 53, 54, 72–74, 76, 88, 90, 91, 97, 101, 108, 113

UTLS upper troposphere/lower stratosphere. v, vii, 1–6, 18, 19, 23, 24, 35, 46, 50–53, 55, 57, 59, 76, 81, 82, 84, 86–89, 93, 98, 100, 102, 105–108, 111–115

UV ultraviolet. 9, 12, 15

WMO World Meteorological Organization. 10, 79, 127

Appendix A

Overview of the MESSy submodels included in the simulations

Table A.1: MESSy infrastructure framework.

Submodel	Description	Reference
CHANNEL	Data exchange between submodels control of output and restart files	Jöckel et al., 2010
GRID	Grid definition and transformation	Kerkweg et al., 2018
IMPORT	Data import from external files	Kerkweg and Jöckel, 2015
QTIMER	Simulation wall-clock time and restart trigger	Jöckel et al., 2010
TENDENCY	Tendency per process for prognostic variables	Eichinger and Jöckel, 2014
TIMER	Time and date control	Jöckel et al., 2010
TRACER	Data and meta data handling for chemical species	Jöckel et al., 2008

Table A.2: MESSy submodels used in this work. See `https://messy-interface.org/`; last accessed: 01.03.2026.

Submodel	Description	Reference
AEROPT	Aerosol optical properties	Dietmüller et al., 2016, Nützel et al., 2024
AIRSEA	Emission and deposition over the ocean	Pozzer et al., 2006
ALBEDO	Surface albedo	Nützel et al., 2024
BIOBURN	Biomass burning emissions	Kaiser et al., 2012
CLOUD	ECHAM5 cloud scheme	Roeckner et al., 2003
CLOUDOPT	Cloud optical properties	Dietmüller et al., 2016, Nützel et al., 2024
CONVECT	Convection schemes Tiedtke, Emanuel	Emanuel and Živković-Rothman, 1999, Roeckner et al., 2003, Tost et al., 2006b

Table A.2 continued from previous page

Submodel	Description	Reference
CVTRANS	Convective tracer transport	Tost, 2006
DDEP	Dry deposition	Kerkweg et al., 2006a
E5VDIFF	ECHAM5 Land-Atmosphere exchange (not for tracers) and vertical diffusion	Roeckner et al., 2003
GMXE	Tropospheric aerosol microphysical processes	Pringle et al., 2010
GRID	Grid definition and transformation	Kerkweg et al., 2018
GWAVE	ECHAM5 non-orographic gravity wave scheme	Roeckner et al., 2003
IMPORT	Data import from external files	Kerkweg and Jöckel, 2015
ISOPCOR	Cosmogenic isotopes	Poluianov et al., 2016
JVAL	Photolysis rate coefficients	Sander et al., 2014
LNOX	NOx production by lightning	Tost et al., 2007
MECCA	Atmospheric chemistry	Sander et al., 2019
MEGAN	Emissions from ecosystems	Guenther et al., 2006
METEODIAG	Meteorological diagnostics	Jöckel et al., 2006
MSBM	Heterogenous reactions in polar stratospheric clouds and stratospheric background aerosols	Jöckel et al., 2010
OFFEMIS	Tracer tendencies from offline emission files	Kerkweg et al., 2006b
ONEMIS	Tracer tendencies from online calculated emissions	Kerkweg et al., 2006b
ORBIT	Earth's orbit parameters	Dietmüller et al., 2016
OROGW	ECHAM5 subgrid scale orographic wave drag parameterisation	Roeckner et al., 2003
PTRAC	Add prognostic tracers	Jöckel et al., 2008
QBO	Assimilation of QBO zonal wind observations	Jöckel et al., 2006
RAD	Radiation schemes E5rad: ECHAM5 (+ extensions) PSrad: ECHAM6	Dietmüller et al., 2016, Nützel et al., 2024
SCAV	Wet deposition and liquid phase chemistry in precipitation	Tost et al., 2006a
SCALC	Online calculations	Jöckel et al., 2016
SEDI	Sedimentation scheme	Kerkweg et al., 2006a
SURFACE	ECHAM5 surface subroutines	Roeckner et al., 2003
TBUDGET	Production cycles for tracers	Jöckel et al., 2016
TNUDGE	Tracer nudging to defined fields	Kerkweg et al., 2006b
TREXP	Adds prognostic tracers with lifetime or point sources	Jöckel et al., 2010
UBCNOX	Effect of energetic particles on NOx	Funke et al., 2016
VAXTRA	Online vertical grid transformation	MESSy consortium

Table A.2 continued from previous page

Submodel	Description	Reference
VERTEX	Alternative to E5VDIFF Includes bug fixes	Emmerichs et al., 2021
VISO	Iso-surfaces and -maps	Jöckel et al., 2010

Appendix B

The implementation of the WMO lapse rate tropopause in MESSy

The WMO defined the tropopause in 1957 as such:

"1. The first tropopause is defined as the lowest level at which the lapse rate decreases to 2° C/km or less, provided also the average lapse rate between this level and all higher levels within 2 km does not exceed 2° C/km." – (WMO, 1957)

The lapse rate Γ in the atmosphere is defined as the temperature T change with altitude z,

$$\Gamma = -\frac{dT}{dz} \quad . \tag{B.1}$$

Since many atmospheric models employ a pressure-related vertical axis, calculating the WMO lapse rate tropopause in GCMs necessitates some assumptions and intermediate steps to derive the lapse rate on the model levels. The implementation of the WMO tropopause in MESSy follows the method written down by Reichler et al. (2003). Here, I provide further details on the implementation, which was used in the simulations presented in this work.

The first assumption is that adiabatic processes around the tropopause govern the change of the temperature with decreasing pressure. Any rise of an air parcel from point (T_1, p_1) to (T_2, p_2) then has a constant potential temperature θ,

$$T_1 \left(\frac{p_0}{p_1}\right)^{R_s/c_p} = \theta = T_2 \left(\frac{p_0}{p_2}\right)^{R_s/c_p} \tag{B.2}$$

with the specific gas constant of dry air, R_s, and the specific heat capacity at a constant pressure c_p. For air, this is $R_s/c_p = 287.05/1005.46$. In the following, the constant will be abbreviated with $\kappa = R_s/c_p$. The assumption leads to the linear relation.

$$T \propto p^\kappa \tag{B.3}$$

between temperature and pressure. Assuming further hydrostatic equilibrium,

$$\frac{dp}{dz} = -\rho g \quad , \tag{B.4}$$

with the density of air ρ, and the gravitational acceleration g, and the dry air as an ideal gas

$$\begin{aligned} pV &= nRT \\ &= \frac{m}{M} RT \\ p &= \frac{m}{V}\frac{R}{M} T \\ &= \rho R_s T \quad . \end{aligned} \tag{B.5}$$

V is the volume of the gas, n its amount, R the universal gas constant, m the mass of the gas, and M the molar mass of the gas. The ratio R/M is the specific gas constant R_s, in this case of dry air. Under these assumption, Equation B.1 can be rewritten to

$$\Gamma = -\frac{\partial T}{\partial p^\kappa}\frac{\partial p^\kappa}{\partial p}\frac{\partial p}{\partial z} \quad (extension) \tag{B.6}$$

$$= -\frac{\partial T}{\partial p^\kappa} p^{\kappa-1}\kappa \frac{\partial p}{\partial z} \quad (derivation) \tag{B.7}$$

$$= \frac{\partial T}{\partial p^\kappa} p^{\kappa-1}\kappa g \rho \quad (hydrostatic) \tag{B.8}$$

$$= \frac{\partial T}{\partial p^\kappa} p^{\kappa-1}\kappa \frac{gp}{R_s T} \quad (ideal\, gas) \tag{B.9}$$

$$= \frac{\partial T}{\partial p^\kappa}\frac{p^\kappa}{T}\frac{\kappa g}{R_s} \quad . \tag{B.10}$$

This equation is used to calculate the lapse rate in EMAC, solving the derivative by using finite differences on the discrete model levels i. To facilitate comparison with the actual implementation, I count the model levels as defined in EMAC from the top, so a higher model index $i+1$ corresponds to a lower level. To reduce the number of calculations, the vertical region to find the tropopause is restricted to 600-50 hPa. Equation B.10 is then used to calculate the lapse rate on all model interfaces, the vertical boundary between two grid boxes, by utilising the T and p^κ values at the model levels and their linear relation:

$$\Gamma_{i'} = \frac{T_i - T_{i+1}}{p_i^\kappa - p_{i+1}^\kappa}\frac{\frac{1}{2}(p_i^\kappa + p_{i+1}^\kappa)}{\frac{1}{2}(T_i + T_{i+1})}\frac{\kappa g}{R_s} \quad . \tag{B.11}$$

i' is the interface index half a level above model level i. The total number of interfaces is $\sum i' = 1 + \sum i$. Afterwards, we loop over all interfaces from bottom to top of the defined tropopause region and check whether the first criterion is fulfilled, i.e.

$$\Gamma_{i'} > \Gamma_{TP} = -0.002\,\frac{\mathrm{K}}{m} \tag{B.12}$$

If this is the case, the tropopause pressure, which is defined as the pressure at which the lapse rate equals the first tropopause criterion, is calculated using linear interpolation from the lapse rate at the interface and the interface below.

$$\Gamma_{TP} = \Gamma_{i'+1} + \frac{\Gamma_{i'} - \Gamma_{i'+1}}{p_{i'}^{k} - p_{i'+1}^{k}} \cdot (p_{TP}^{\kappa} - p_{i'+1}^{\kappa}) \tag{B.13}$$

and solved for p_{TP}

$$p_{TP} = \left(\frac{\Gamma_{TP} - \Gamma_{i'+1}}{\frac{\Gamma_{i'} - \Gamma_{i'+1}}{p_{i'}^{k} - p_{i'+1}^{k}}} + p_{i'+1}^{\kappa} \right)^{\frac{1}{\kappa}} \quad . \tag{B.14}$$

To test for the second criterion of the WMO definition, first, the pressure $dz = 2000$ m above p_{TP} is calculated, using the assumption of hydrostatic equilibrium and the ideal gas law again,

$$\begin{aligned} \frac{dp}{dz} &= -\rho g \\ &= -\frac{p_i}{T_i}\frac{g}{R_s} \\ dp &= -\frac{p_i}{T_i}\frac{g}{R_s} \cdot dz \\ p_{TP+2000m} &= p_{TP} - \frac{p_i}{T_i}\frac{g}{R_s} \cdot 2000 \quad . \end{aligned} \tag{B.15}$$

Starting from the interface level that initially satisfies the first criterion, the mean lapse rate between this level and the interface immediately above is calculated and evaluated to determine if the criterion remains fulfilled. If so, the next higher interface is included in the calculation of the mean lapse rate. This iterative process continues until one of two conditions is met: either the pressure at the interface falls below $p_{TP+2000m}$, or the mean lapse rate decreases below the threshold value Γ_{TP}.

In the first case, the tropopause pressure level is identified for the given timestep, latitude, and longitude, as defined by the WMO lapse rate criterion. In the second case, the calculated tropopause pressure is deemed invalid, and the procedure restarts at the next higher interface level that meets the first criterion.

Suppose the highest model level in the 600-50 hPa range is reached during the test before both the first and the second criterion are fulfilled. In that case, no tropopause pressure can be calculated (again for this timestep, latitude, and longitude). In this special case, the missing values are filled with a simple latitude ϕ dependent climatological tropopause, defined as

$$p_{TP} = 300\,\text{hPa} - 215\,\text{hPa} \cdot cos^2(\phi) \quad . \tag{B.16}$$

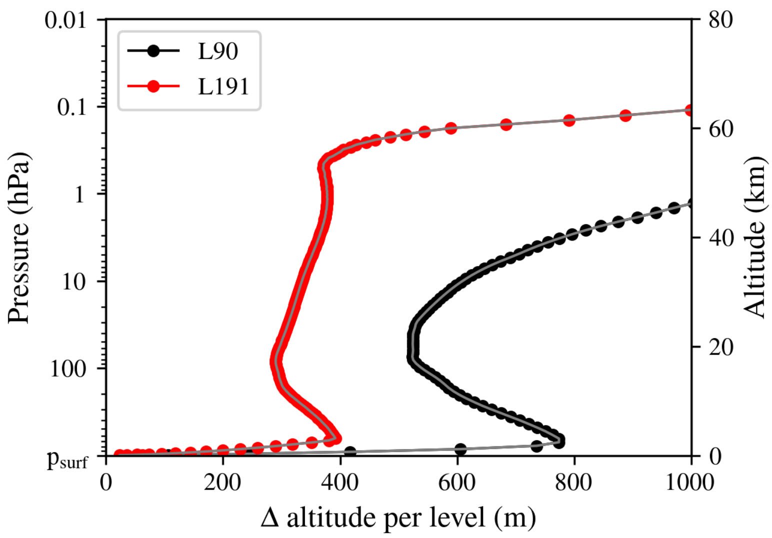

Figure B.1: Visualisation of altitude differences between grid points for the two vertical resolutions used in this work, L90 (black) and L191 (red). The markers are the model levels, and the grey lines follow their midpoints.

Appendix C

Tuning parameters of the time-slice simulations

To simulate today's climate system, the simulations with present-day conditions in this thesis are tuned to have a global mean radiative imbalance of 0.8 Wm^{-2} following the observations by Johnson et al. (2016). The tuning process is necessary because the resolution of the model strongly affects the behaviour of a parameterisation. In the case of the convection parameterisation, the cloud cover and precipitation are affected, which in turn affects the radiative imbalance and the total water content in the atmosphere. The parameters are based on specific parameterisations and are therefore not directly comparable.

For the tuning, I adapted three parameters per simulation, one for the cloud optical properties and two for the convection parameterisation, similar to most modeling centers (Hourdin et al., 2017). "zinhoml2" is an array for the critical relative humidity to form clouds for the three convection types: shallow, mid-level and high (Mauritsen et al., 2019). Increasing the relative humidity threshold results in a reduction of cloud cover in the simulation and directly affects the radiative imbalance.

"cprcon" and "cmfctop" are parameters of the Tiedtke convection parameterisation. "cprcon" is the parameter for determining the conversion from cloud water to rain. Increasing this parameter leads to a reduction in cloud cover and a lower water amount in the atmosphere, resulting from increased precipitation. "cmfctop" is the relative cloud mass flux at the level above non-buoyancy. It describes the transport of cloud water from the boundary layer into the free atmosphere by shallow clouds. Above the level of buoyancy, the cloudy water evaporates. Therefore, a stronger mass flux leads to less cloud cover (Mauritsen et al., 2012).

"damp" and "alpha", on the other hand, are parameters of the Emanuel parameterisation. They affect how fast the cloud-base updraft mass flux approaches the quasi-equilibrium of the sub-cloud layer (Emanuel and Živković-Rothman, 1999). The parameter settings used for the simulations are listed in Table C.1. The table is designed to facilitate the reproduction of the simulations. Just by its value, the effect of the parameters cannot be grasped, especially for those of the convection parameterisations, because they are coefficients of more complex and entangled equations. The simulations regarding the effect of nudging on climate scales and the effect under future conditions were not tuned. The nudged simulation $SD_{transient}$ is perturbed by the nudging term towards a different climate state than the model would have reached on its own; therefore, it will not necessarily achieve the targeted radiative imbalance. To isolate the effect of nudging, the not-nudged simulation $\mathrm{notSD}_{\mathrm{transient}}$ was also not tuned. And the future simulations $\mathrm{REF}_{\mathrm{future}}$ and $\mathrm{CONV}_{\mathrm{future}}$ are projections of their corresponding present-day simulations, $\mathrm{REF}_{\mathrm{today}}$ and $\mathrm{CONV}_{\mathrm{today}}$ respectively. Therefore, their model parameters must be identical.

Table C.1: Overview of tuning parameters for each of the tuned simulations in this thesis towards present-day conditions. zinhoml02 is a CLOUDOPT parameter, cprcon and cmfctop of the Tiedtke convection parameterisation, damp and alpha of the Emanuel convection parameterisation.

Simulation	zinhoml02	cprcon	cmfctop	damp	alpha
$\mathrm{AGCM}_{\mathrm{T42L90}}$	0.8, 0.4, 0.8	$4. \cdot 10^{-4}$	0.18	na	na
$\mathrm{AGCM}_{\mathrm{T106L90}}$	0.8, 0.4, 0.8	$4. \cdot 10^{-4}$	0.165	na	na
$\mathrm{AGCM}_{\mathrm{T106L191}}$	0.8, 0.4, 0.8	$1. \cdot 10^{-4}$	0.35	na	na
$\mathrm{REF}_{\mathrm{today}}$	0.9, 0.45, 0.9	$4. \cdot 10^{-4}$	0.164	na	na
$\mathrm{CONV}_{\mathrm{today}}$	0.9, 0.45, 0.9	na	na	0.3	0.0358075

Appendix D

Supplementary figures

D.1 Input for simulations under present-day conditions

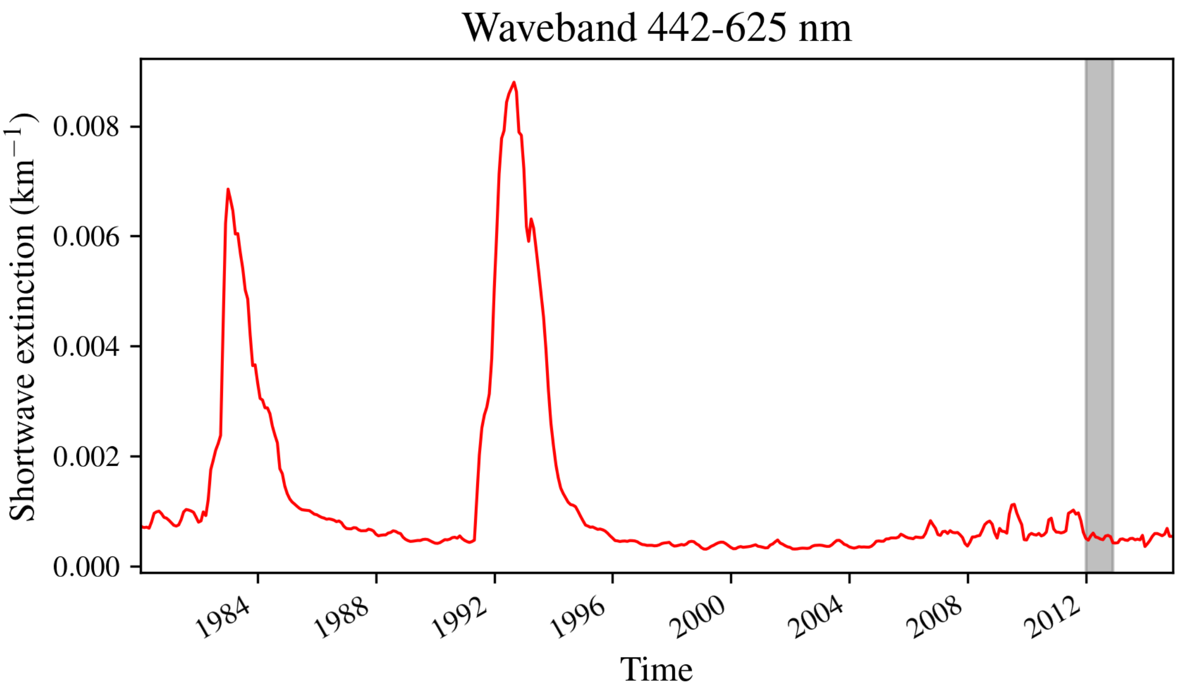

Figure D.1: Global mean Stratospheric Aerosol Optical Depth (SAOD) based on CMIP6 inventories, used as a proxy for volcanic activity. Shown is the shortwave extinction in the stratosphere around 100 hPa for the wavelength band 442-625 nm. The timeseries starts in 1980 to include the effect of the largest volcanic eruptions in the 20th century, El Chichón in 1982 and Pinatubo in 1991 for comparison. Their effect on the global mean SAOD is delayed by about half a year. No information is included in SSP scenarios starting in 2015. The grey area marks the monthly emissions of 2012, which were used for the TS simulations under present-day conditions.

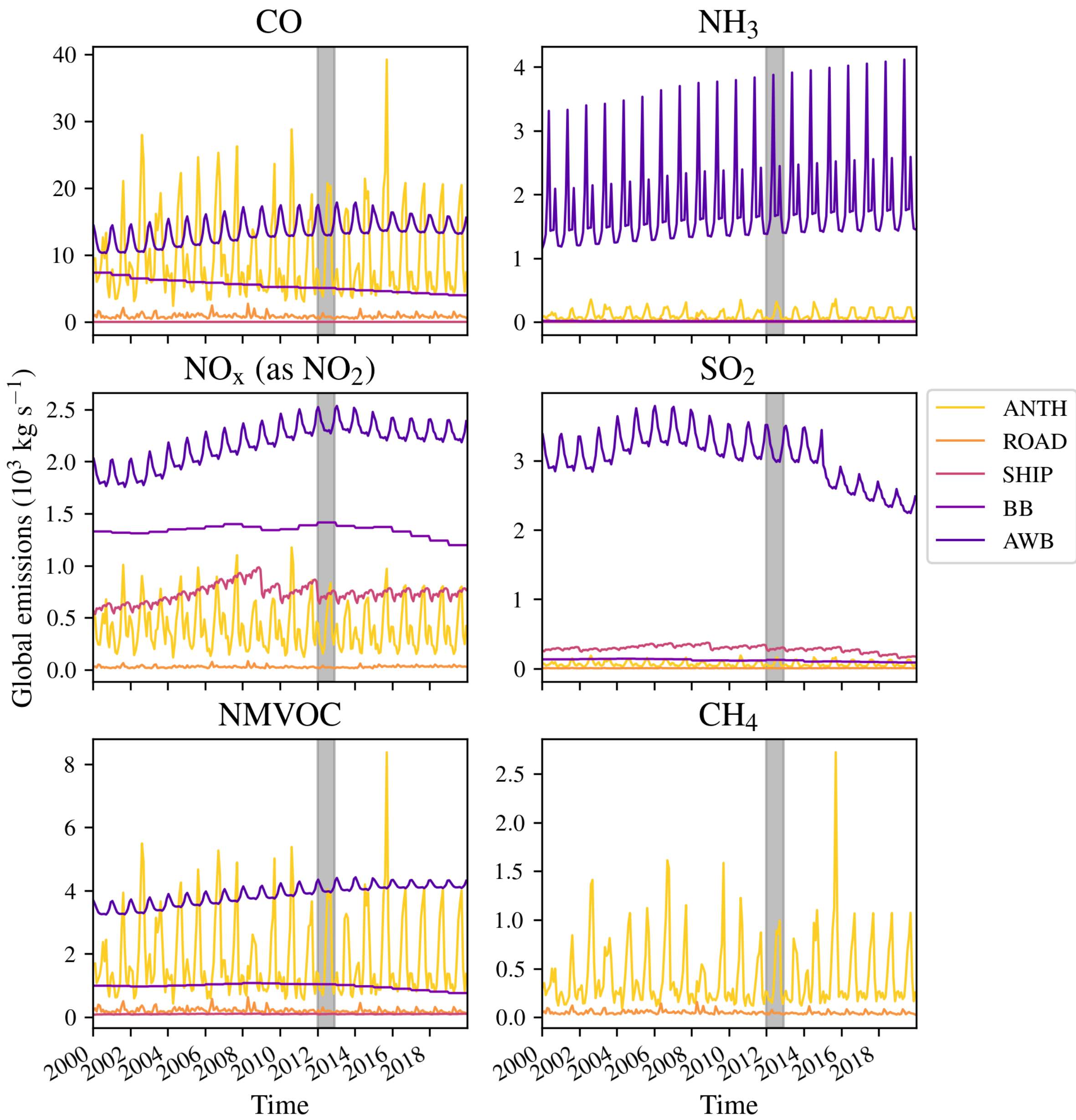

Figure D.2: Global emissions fluxes based on CCMI-2022 emission inventory, used as input data for the simulation in this thesis under present-day conditions. Emissions are grouped into the following sectors: anthropogenic (ANTH), road traffic (ROAD), shipping (SHIP), biomass burning (BB), and agricultural waste burning (AWB). NO_x is represented as NO_2 equivalent. The emissions are grouped by emission sectors. Until 2015, emissions were based on observations, thereafter, on the SSP2.4-5 scenario. The grey area marks the monthly emissions of 2012, which were used for the TS simulations under present-day conditions.

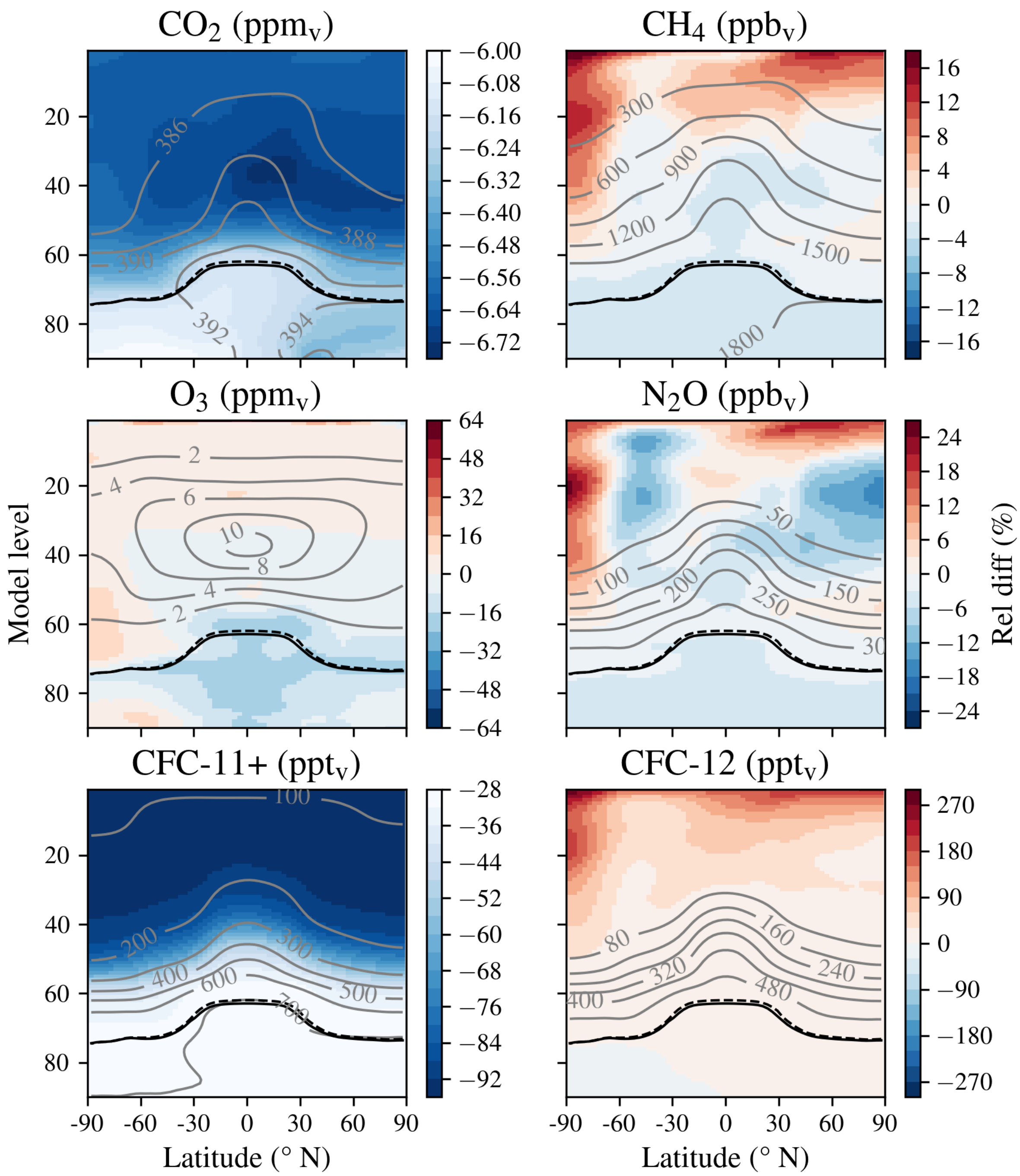

Figure D.3: Relative difference between the RAD input fields of chemical tracers based on the RD1-base-01 simulation and the same tracers from the REF_{today} simulation performed in this thesis, as (RD1-base-01 - REF_{today})/REF_{today} · 100. CFC-11+ is the weighted cumulative abundance of CFC-11 and additional ODS. The relative differences are based on the 2000–2019 temporal and zonal means. Grey contour solid lines indicate the abundance (unit added to the panel title in brackets) of REF_{today}, dashed lines are the WMO tropopause of RD1-base-01 (grey) and REF_{today} (black). Differences arise from considering more ODS in this simulation than in the CCMI-2022 protocol, and from general model differences, such as different RAD parameterisations.

D.2 Time-slice results compared to observations

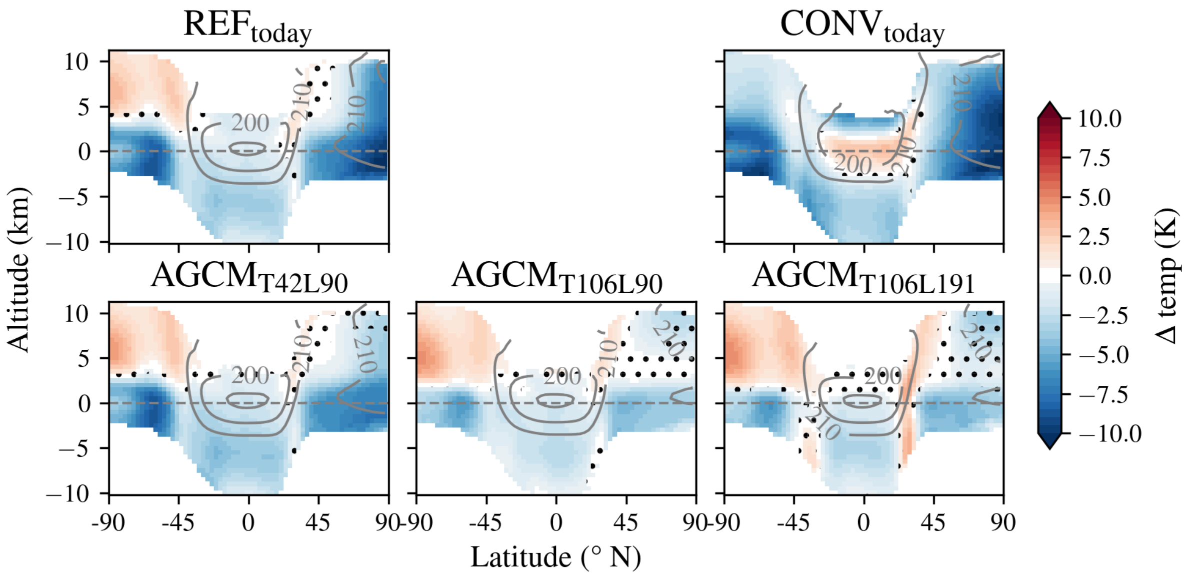

Figure D.4: Temperature differences between the sensitivity simulations and ERA5. Shown are zonal mean differences between the climatological mean temperatures in season DJF in the UTLS on an altitude grid relative to the WMO tropopause pressure (grey dashed lines) of the corresponding simulation results. Grey solid lines represent temperature contour levels for each simulation. Dotted areas are not statistically significant, according to a Student's t-test at a 0.05 confidence level based on DJF means per year.

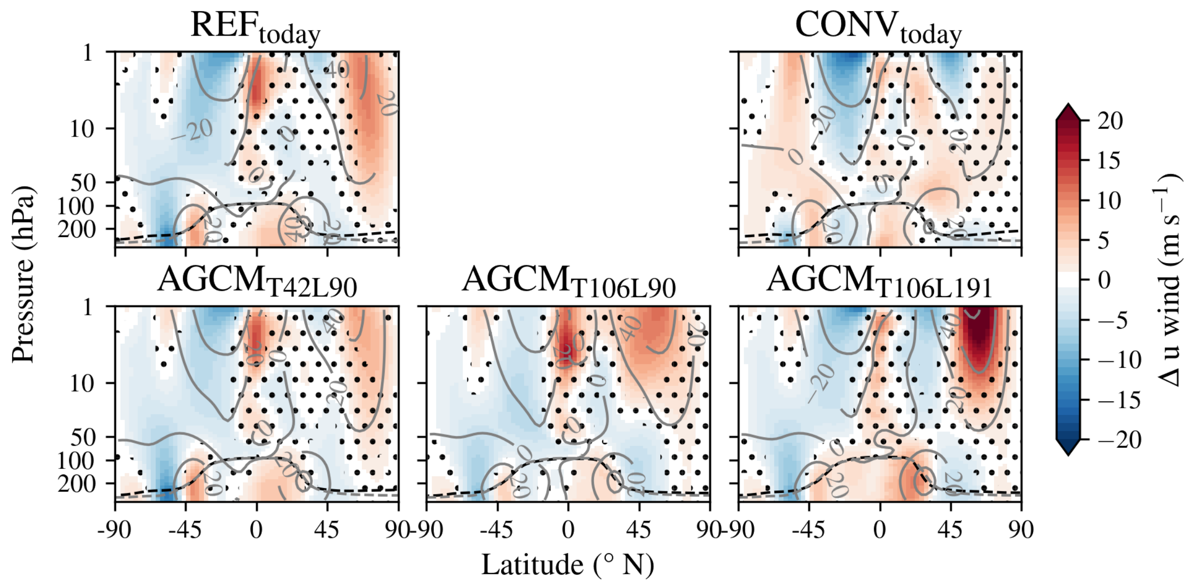

Figure D.5: Zonal wind differences between the sensitivity simulations and ERA5. Shown are differences between the climatological mean zonal wind in season DJF over the stratosphere. The grey dashed line is the climatological mean of the WMO lapse rate tropopause of ERA5, and in black the tropopause of the individual sensitivity simulation. Grey solid lines represent zonal wind contour levels for each simulation. Dotted areas are not statistically significant, according to a Student's t-test at a 0.05 confidence level based on DJF means per year.

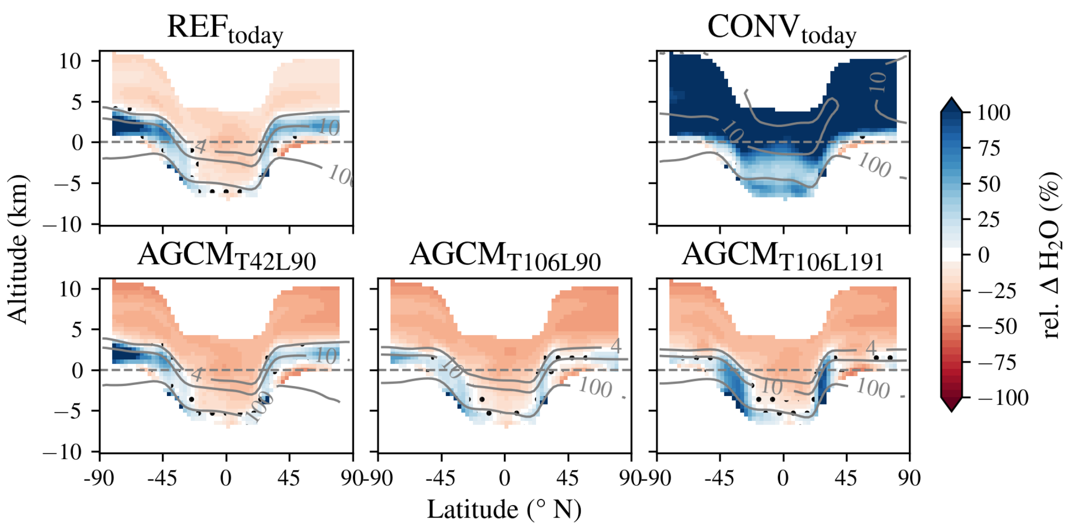

Figure D.6: Same as Figure D.4 but for the relative differences of H_2O compared to SWOOSH.

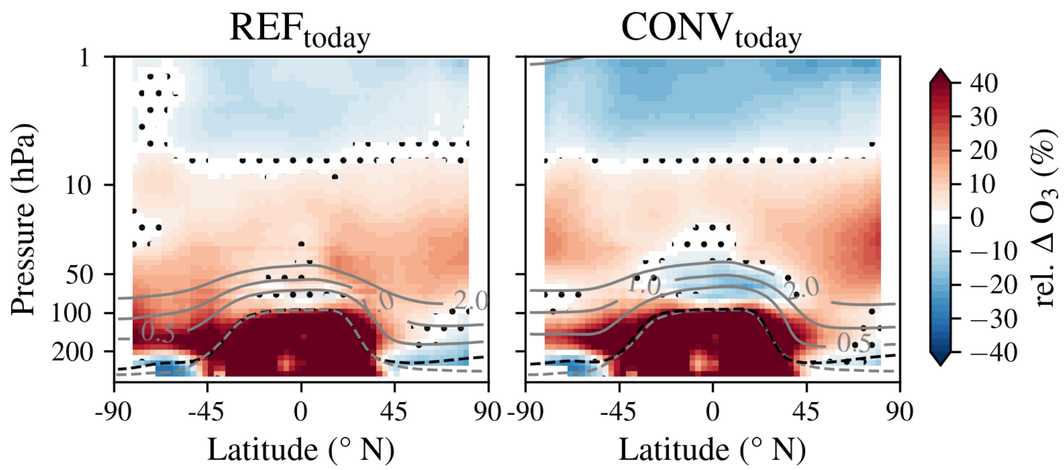

Figure D.7: Ozone relative differences between the sensitivity simulations and SWOOSH. Shown are differences between the climatological mean O_3 in season DJF over the stratosphere. The grey dashed line is the climatological mean of the WMO lapse rate tropopause of SWOOSH, and in black the tropopause of the individual sensitivity simulation. Grey solid lines are O_3 contour levels of the individual simulation. Dotted areas are not statistically significant, according to a Student's t-test at a 0.05 confidence level based on DJF means per year.

D.3 Further responses to climate change

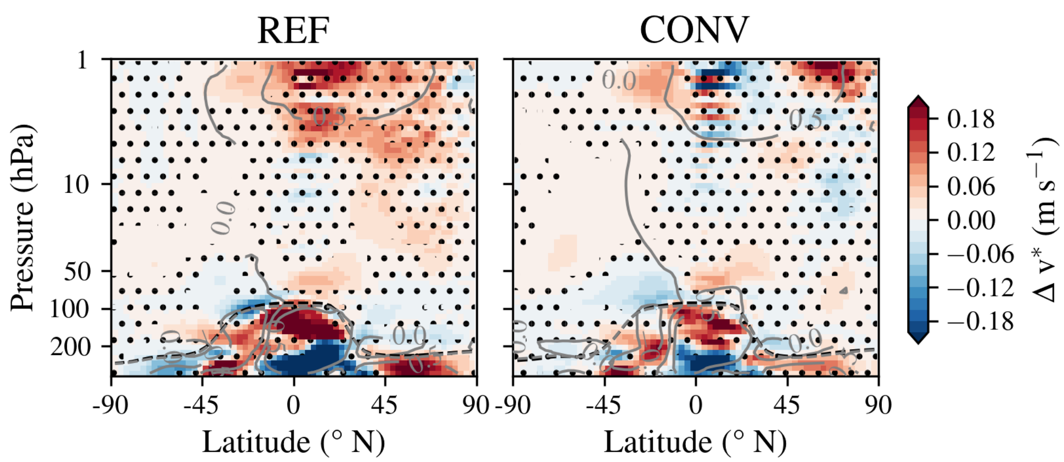

Figure D.8: Response of the meridional wind speed component of the residual circulation v* based on TEM to climate change between the simulations under future and present-day conditions as climatological mean of the DJF season. On the left, the response for the setup with the Tiedtke convection parameterisation (REF) is shown, on the right, for that with the Emanuel parameterisation (CONV). Grey dashed lines indicate the respective mean WMO tropopause under present-day conditions, black dashed lines indicate the future conditions. Grey contour lines depict v* under present-day conditions. In the dotted regions, the changes are not statistically significant according to a two-sided Student's t-test at a 0.05 confidence level.

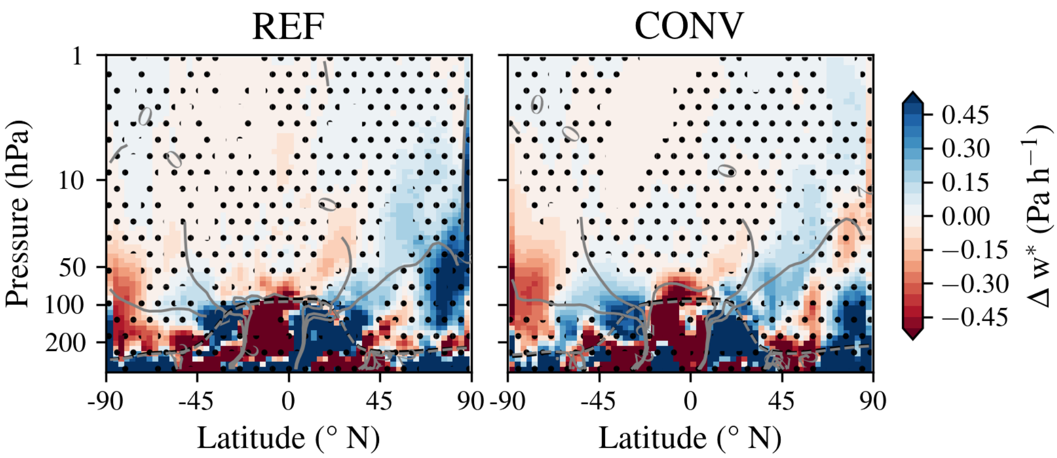

Figure D.9: Same as Figure D.8 but for the vertical wind speed component of the residual circulation w*.

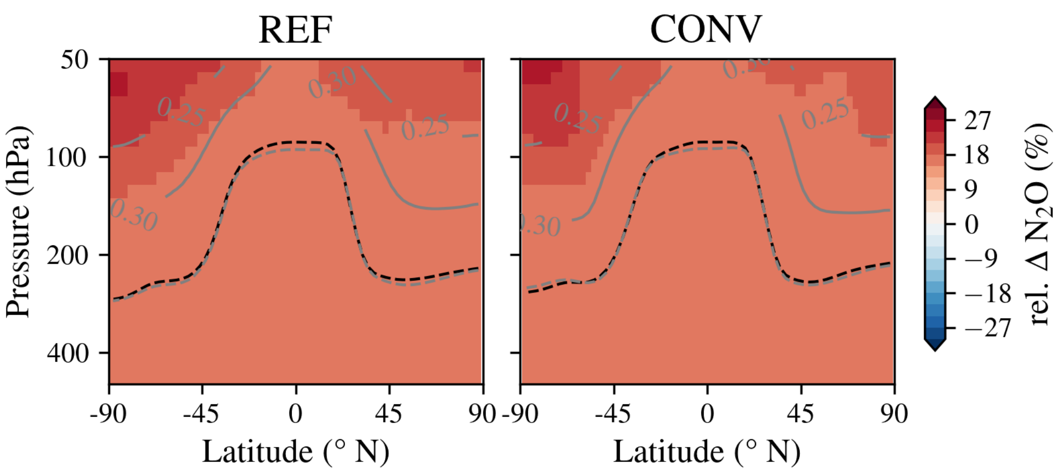

Figure D.10: Response of the N_2O abundance to climate change between the simulations under future and present-day conditions as climatological and zonal mean of the DJF season. On the left, the response for the setup with the Tiedtke convection parameterisation (REF) is shown, on the right, for that with the Emanuel parameterisation (CONV). Grey dashed lines indicate the respective mean WMO tropopause under present-day conditions, black dashed lines indicate the future conditions. Grey contour lines depict the N_2O abundance under present-day conditions in ppm_v. In the dotted regions, the changes are not statistically significant according to a two-sided Student's t-test at a 0.05 confidence level.

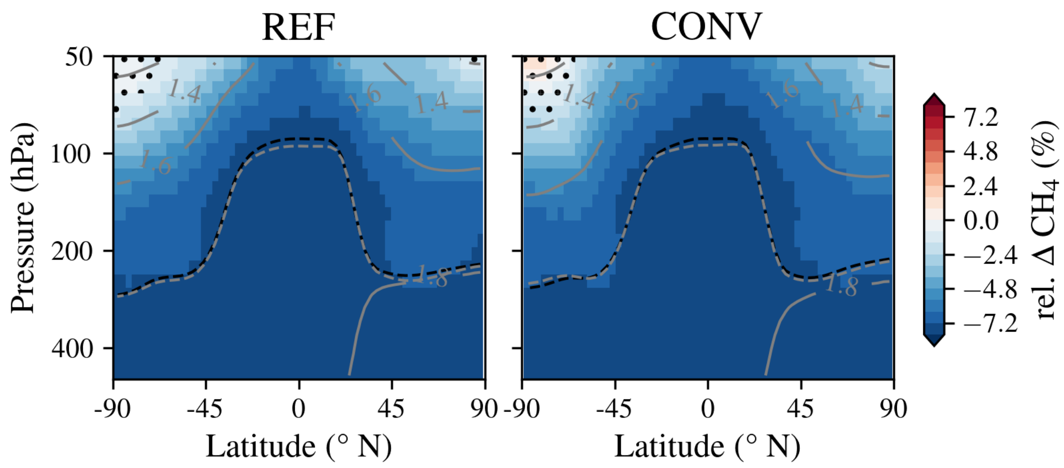

Figure D.11: Same as in Figure D.10 but for CH_4.

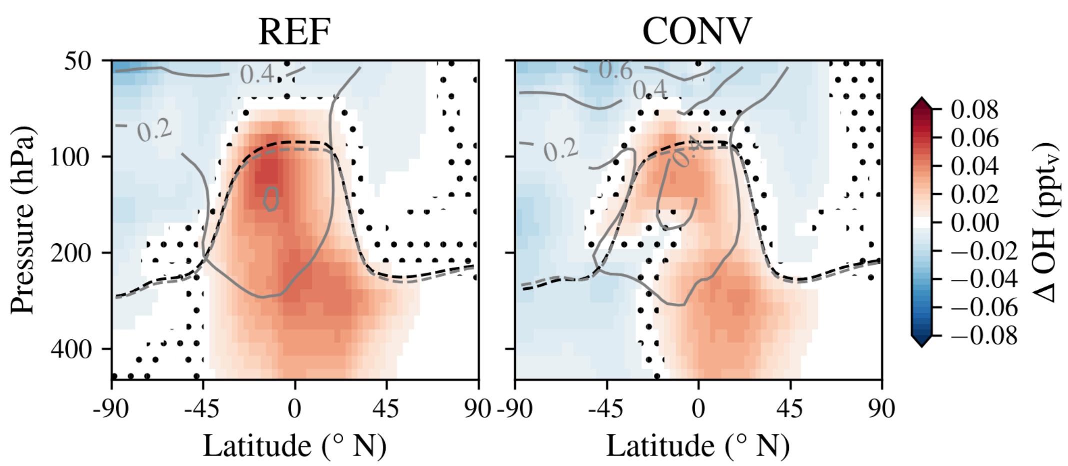

Figure D.12: Same as in Figure D.10 but for OH as absolute differences.

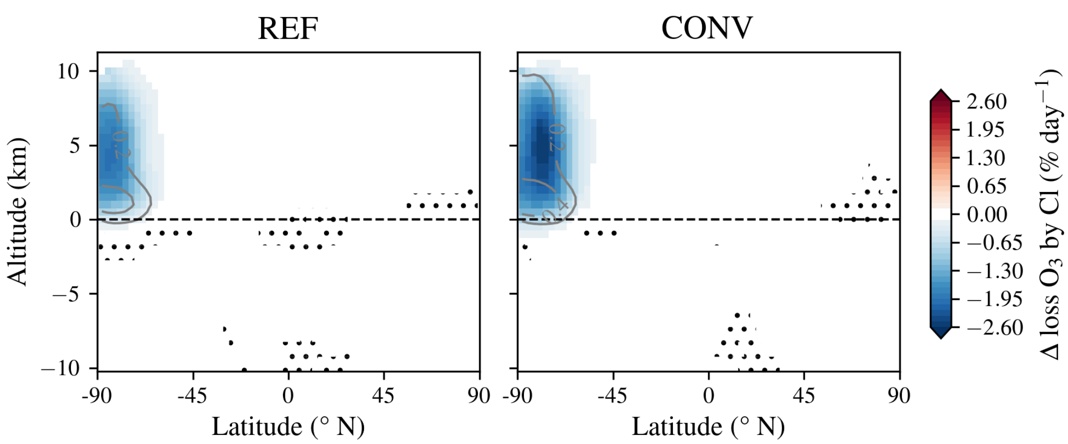

Figure D.13: Same as in Figure D.10 but for chlorine-containing ODS as absolute differences in the SON season.

Bibliography

Abalos, M., T. Birner, A. Chrysanthou, S. Davis, A. de la Cámara, S. Dhomse, H. Garny, M. I. Hegglin, D. Hubert, O. Ivaniha, J. Keeble, M. Linz, D. Minganti, J. Neu, D. Plummer, L. Saunders, K. Shah, G. Stiller, K. Tourpali, D. Waugh, N. L. Abraham, H. Akiyoshi, M. P. Chipperfield, P. Jöckel, B. Josse, O. Morgenstern, T. Sukhodolov, S. Watanabe, and Y. Yamashita (2026). "Evaluation of stratospheric transport in three generations of Chemistry-Climate Models". In: DOI: 10.5194/egusphere-2025-6549.

Abalos, M., N. Calvo, S. Benito-Barca, H. Garny, S. C. Hardiman, P. Lin, M. B. Andrews, N. Butchart, R. Garcia, C. Orbe, D. Saint-Martin, S. Watanabe, and K. Yoshida (2021). "The Brewer–Dobson circulation in CMIP6". In: *Atmospheric Chemistry and Physics* 21.17, pp. 13571–13591. ISSN: 1680-7324. DOI: 10.5194/acp-21-13571-2021.

Abalos, M., B. Legras, F. Ploeger, and W. J. Randel (2015). "Evaluating the advective Brewer-Dobson circulation in three reanalyses for the period 1979–2012". In: *Journal of Geophysical Research: Atmospheres* 120.15, pp. 7534–7554. ISSN: 2169-8996. DOI: 10.1002/2015jd023182.

Abalos, M., C. Orbe, D. E. Kinnison, D. Plummer, L. D. Oman, P. Jöckel, O. Morgenstern, R. R. Garcia, G. Zeng, K. A. Stone, and M. Dameris (2020). "Future trends in stratosphere-to-troposphere transport in CCMI models". In: *Atmospheric Chemistry and Physics* 20.11, pp. 6883–6901. ISSN: 1680-7324. DOI: 10.5194/acp-20-6883-2020.

Abalos, M., W. J. Randel, D. E. Kinnison, and R. R. Garcia (2017). "Using the Artificial Tracer e90 to Examine Present and Future UTLS Tracer Transport in WACCM". In: *Journal of the Atmospheric Sciences* 74.10, pp. 3383–3403. ISSN: 1520-0469. DOI: 10.1175/jas-d-17-0135.1.

Adam, O., K. M. Grise, P. Staten, I. R. Simpson, S. M. Davis, N. A. Davis, D. W. Waugh, T. Birner, and A. Ming (2018). "The TropD software package (v1): standardized methods for calculating tropical-width diagnostics". In: *Geoscientific Model Development* 11.10, pp. 4339–4357. ISSN: 1991-9603. DOI: 10.5194/gmd-11-4339-2018.

Adler, R., M. Sapiano, G. Huffman, J.-J. Wang, G. Gu, D. Bolvin, L. Chiu, U. Schneider, A. Becker, E. Nelkin, P. Xie, R. Ferraro, and D.-B. Shin (2018). "The Global Precipitation Climatology Project (GPCP) Monthly Analysis (New Version 2.3) and a Review of 2017 Global Precipitation". In: *Atmosphere* 9.4, p. 138. ISSN: 2073-4433. DOI: 10.3390/atmos9040138.

Andrews, D. G., J. D. Mahlman, and R. W. Sinclair (1983). "Eliassen-Palm Diagnostics of Wave-Mean Flow Interaction in the GFDL "SKYHI" General Circulation Model". In: *Journal of the Atmospheric Sciences* 40.12, pp. 2768–2784. ISSN: 1520-0469. DOI: 10.1175/1520-0469(1983)040<2768:etwatm>2.0.co;2.

Andrews, D. G. and M. E. McIntyre (1976). "Planetary Waves in Horizontal and Vertical Shear: The Generalized Eliassen-Palm Relation and the Mean Zonal Acceleration". In: *Journal of* *the Atmospheric Sciences* 33.11, pp. 2031–2048. ISSN: 1520-0469. DOI: 10.1175/1520-0469(1976)033<2031:pwihav>2.0.co;2.

Arakawa, A. (2004). “The Cumulus Parameterization Problem: Past, Present, and Future”. In: *Journal of Climate* 17.13, pp. 2493–2525. ISSN: 1520-0442. DOI: 10.1175/1520-0442(2004)017<2493:ratcpp>2.0.co;2.

Arakawa, A. and W. H. Schubert (1974). “Interaction of a Cumulus Cloud Ensemble with the Large-Scale Environment, Part I”. In: *Journal of the Atmospheric Sciences* 31.3, pp. 674–701. ISSN: 1520-0469. DOI: 10.1175/1520-0469(1974)031<0674:ioacce>2.0.co;2.

Aubry, T. J., M. Toohey, S. Khanal, M. M. Chim, M. Verkerk, B. Johnson, A. Schmidt, M. Kovilakam, M. Sigl, Z. Nicholls, L. Thomason, V. Naik, L. Rieger, D. Stiller, E. Ziegler, and I. Smith (2025). “Stratospheric aerosol forcing for CMIP7 (part 1): Optical properties for pre-industrial, historical, and scenario simulations (version 2.2.1)”. In: DOI: 10.5194/egusphere-2025-4990.

Ball, W. T., J. Alsing, D. J. Mortlock, J. Staehelin, J. D. Haigh, T. Peter, F. Tummon, R. Stübi, A. Stenke, J. Anderson, A. Bourassa, S. M. Davis, D. Degenstein, S. Frith, L. Froidevaux, C. Roth, V. Sofieva, R. Wang, J. Wild, P. Yu, J. R. Ziemke, and E. V. Rozanov (2018). “Evidence for a continuous decline in lower stratospheric ozone offsetting ozone layer recovery”. In: *Atmospheric Chemistry and Physics* 18.2, pp. 1379–1394. ISSN: 1680-7324. DOI: 10.5194/acp-18-1379-2018.

Ball, W. T., J. Alsing, J. Staehelin, S. M. Davis, L. Froidevaux, and T. Peter (2019). “Stratospheric ozone trends for 1985–2018: sensitivity to recent large variability”. In: *Atmospheric Chemistry and Physics* 19.19, pp. 12731–12748. ISSN: 1680-7324. DOI: 10.5194/acp-19-12731-2019.

Banerjee, A., G. Chiodo, M. Previdi, M. Ponater, A. J. Conley, and L. M. Polvani (2019). “Stratospheric water vapor: an important climate feedback”. In: *Climate Dynamics* 53.3–4, pp. 1697–1710. ISSN: 1432-0894. DOI: 10.1007/s00382-019-04721-4.

Banerjee, A., A. C. Maycock, and J. A. Pyle (2018). “Chemical and climatic drivers of radiative forcing due to changes in stratospheric and tropospheric ozone over the 21st century”. In: *Atmospheric Chemistry and Physics* 18.4, pp. 2899–2911. ISSN: 1680-7324. DOI: 10.5194/acp-18-2899-2018.

Bauchinger, S., A. Engel, M. Jesswein, T. Keber, H. Bönisch, F. Obersteiner, A. Zahn, N. Emig, P. Hoor, H.-C. Lachnitt, F. Weyland, L. Ort, and T. J. Schuck (2025). “The extratropical tropopause – trace gas perspective on tropopause definition choice”. In: *Atmospheric Chemistry and Physics* 25.21, pp. 14167–14186. ISSN: 1680-7324. DOI: 10.5194/acp-25-14167-2025.

Bechtold, P. (2017). *Atmospheric moist convection*. eng. URL: https://www.ecmwf.int/node/16953.

Benito-Barca, S., M. Abalos, N. Calvo, H. Garny, T. Birner, N. L. Abraham, H. Akiyoshi, F. Dennison, P. Jöckel, B. Josse, J. Keeble, D. Kinnison, M. Marchand, O. Morgenstern, D. Plummer, E. Rozanov, S. Strode, T. Sukhodolov, S. Watanabe, and Y. Yamashita (2025). “Recent Lower Stratospheric Ozone Trends in CCMI-2022 Models: Role of Natural Variability and Transport”. In: *Journal of Geophysical Research: Atmospheres* 130.9. ISSN: 2169-8996. DOI: 10.1029/2024jd042412.

Bethan, S., G. Vaughan, and S. J. Reid (1996). “A comparison of ozone and thermal tropopause heights and the impact of tropopause definition on quantifying the ozone content of the troposphere”. In: *Quarterly Journal of the Royal Meteorological Society* 122.532, pp. 929–944. ISSN: 1477-870X. DOI: 10.1002/qj.49712253207.

Birner, T. and H. Bönisch (2011). “Residual circulation trajectories and transit times into the extratropical lowermost stratosphere”. In: *Atmospheric Chemistry and Physics* 11.2, pp. 817–827. ISSN: 1680-7324. DOI: 10.5194/acp-11-817-2011.

Birner, T. (2010a). “Recent widening of the tropical belt from global tropopause statistics: Sensitivities”. In: *Journal of Geophysical Research: Atmospheres* 115.D23. ISSN: 0148-0227. DOI: 10.1029/2010jd014664.

Birner, T. (2010b). “Residual Circulation and Tropopause Structure”. In: *Journal of the Atmospheric Sciences* 67.8, pp. 2582–2600. ISSN: 0022-4928. DOI: 10.1175/2010jas3287.1.

Bjerknes, J. (1938). “Saturated ascent of air through a dry-adiabatically descending environment”. In: *Quarterly Journal of the Royal Meteorological Society* 64, pp. 325–330.

Bony, S. and J.-L. Dufresne (2005). “Marine boundary layer clouds at the heart of tropical cloud feedback uncertainties in climate models”. In: *Geophysical Research Letters* 32.20. ISSN: 1944-8007. DOI: 10.1029/2005gl023851.

Bony, S. and K. A. Emanuel (2001). “A Parameterization of the Cloudiness Associated with Cumulus Convection; Evaluation Using TOGA COARE Data”. In: *Journal of the Atmospheric Sciences* 58.21, pp. 3158–3183. ISSN: 1520-0469. DOI: 10.1175/1520-0469(2001)058<3158:apotca>2.0.co;2.

Bony, S., B. Stevens, D. M. W. Frierson, C. Jakob, M. Kageyama, R. Pincus, T. G. Shepherd, S. C. Sherwood, A. P. Siebesma, A. H. Sobel, M. Watanabe, and M. J. Webb (2015). “Clouds, circulation and climate sensitivity”. In: *Nature Geoscience* 8.4, pp. 261–268. ISSN: 1752-0908. DOI: 10.1038/ngeo2398.

Bourke, W. (1988). “Physically-Based Modelling and Simulation of Climate and Climatic Change - Part 1”. In: ed. by M. E. Schlesinger. Kluwer Academic Publishers. Chap. 2, pp. 169–220.

Braconnot, P., F. Hourdin, S. Bony, J. L. Dufresne, J. Y. Grandpeix, and O. Marti (2007). “Impact of different convective cloud schemes on the simulation of the tropical seasonal cycle in a coupled ocean–atmosphere model”. In: *Climate Dynamics* 29.5, pp. 501–520. ISSN: 1432-0894. DOI: 10.1007/s00382-007-0244-y.

Brewer, A. W. (1949). “Evidence for a world circulation provided by the measurements of helium and water vapour distribution in the stratosphere”. In: *Quarterly Journal of the Royal Meteorological Society* 75.326, pp. 351–363. ISSN: 1477-870X. DOI: 10.1002/qj.49707532603.

Butchart, N. (2014). “The Brewer-Dobson circulation”. In: *Reviews of Geophysics* 52.2, pp. 157–184. ISSN: 1944-9208. DOI: 10.1002/2013rg000448.

Cariolle, D. and H. Teyssèdre (2007). “A revised linear ozone photochemistry parameterization for use in transport and general circulation models: multi-annual simulations”. In: *Atmospheric Chemistry and Physics* 7.9, pp. 2183–2196. ISSN: 1680-7324. DOI: 10.5194/acp-7-2183-2007.

Chabrillat, S., S. Rémy, Q. Errera, V. Huijnen, C. Bingen, J. Debosscher, F. Hendrick, S. Metzger, A. Mora, D. Minganti, M. Op de beek, L. Reisenfeld, J. E. Williams, H. Eskes, and J. Flemming (2025). “Modelling stratospheric composition for the Copernicus Atmosphere Monitoring Service: multi-species evaluation of IFS-COMPO Cy49”. In: *Geoscientific Model Development* 18.22, pp. 8973–9014. ISSN: 1991-9603. DOI: 10.5194/gmd-18-8973-2025.

Chapman, S. (1930). “XXXV.On ozone and atomic oxygen in the upper atmosphere”. In: *The London, Edinburgh, and Dublin Philosophical Magazine and Journal of Science* 10.64, pp. 369–383. ISSN: 1941-5990. DOI: 10.1080/14786443009461588.

Charlesworth, E., F. Plöger, T. Birner, R. Baikhadzhaev, M. Abalos, N. L. Abraham, H. Akiyoshi, S. Bekki, F. Dennison, P. Jöckel, J. Keeble, D. Kinnison, O. Morgenstern, D. Plummer, E. Rozanov, S. Strode, G. Zeng, T. Egorova, and M. Riese (2023). "Stratospheric water vapor affecting atmospheric circulation". In: *Nature Communications* 14.1. ISSN: 2041-1723. DOI: 10.1038/s41467-023-39559-2.

Chau, C. H., P. Hoor, and H. Tost (2025). "Simulated mixing in the UTLS by small-scale turbulence using multi-scale chemistry-climate model MECO(n)". In: *Atmospheric Chemistry and Physics* 25.20, pp. 13123–13140. ISSN: 1680-7324. DOI: 10.5194/acp-25-13123-2025.

Chen, D., M. Rojas, B. Samset, K. Cobb, A. Diongue Niang, P. Edwards, S. Emori, S. Faria, E. Hawkins, P. Hope, P. Huybrechts, M. Meinshausen, S. Mustafa, G.-K. Plattner, and A.-M. Tréguier (2021a). "Framing, Context, and Methods". In: *Climate Change 2021: The Physical Science Basis. Contribution of Working Group I to the Sixth Assessment Report of the Intergovernmental Panel on Climate Change*. Ed. by V. Masson-Delmotte, P. Zhai, A. Pirani, S. Connors, C. Péan, S. Berger, N. Caud, Y. Chen, L. Goldfarb, M. Gomis, M. Huang, K. Leitzell, E. Lonnoy, J. Matthews, T. Maycock, T. Waterfield, O. Yelekçi, R. Yu, and B. Zhou. Cambridge, United Kingdom and New York, NY, USA: Cambridge University Press, pp. 147–286. DOI: 10.1017/9781009157896.003.

Chen, D., A. Dai, and A. Hall (2021b). "The Convective-To-Total Precipitation Ratio and the "Drizzling" Bias in Climate Models". In: *Journal of Geophysical Research: Atmospheres* 126.16. ISSN: 2169-8996. DOI: 10.1029/2020jd034198.

Chen, P. (1995). "Isentropic cross-tropopause mass exchange in the extratropics". In: *Journal of Geophysical Research: Atmospheres* 100.D8, pp. 16661–16673. ISSN: 0148-0227. DOI: 10.1029/95jd01264.

Chepfer, H., S. Bony, D. Winker, G. Cesana, J. L. Dufresne, P. Minnis, C. J. Stubenrauch, and S. Zeng (2010). "The GCM-Oriented CALIPSO Cloud Product (CALIPSO-GOCCP)". In: *Journal of Geophysical Research: Atmospheres* 115.D4. ISSN: 0148-0227. DOI: 10.1029/2009jd012251.

Chim, M. M., T. J. Aubry, C. Smith, and A. Schmidt (2025). "Neglecting future sporadic volcanic eruptions underestimates climate uncertainty". In: *Communications Earth & Environment* 6.1. ISSN: 2662-4435. DOI: 10.1038/s43247-025-02208-1.

Chiodo, G., M. Friedel, S. Seeber, D. Domeisen, A. Stenke, T. Sukhodolov, and F. Zilker (2023). "The influence of future changes in springtime Arctic ozone on stratospheric and surface climate". In: *Atmospheric Chemistry and Physics* 23.18, pp. 10451–10472. ISSN: 1680-7324. DOI: 10.5194/acp-23-10451-2023.

Chrysanthou, A., A. C. Maycock, M. P. Chipperfield, S. Dhomse, H. Garny, D. Kinnison, H. Akiyoshi, M. Deushi, R. R. Garcia, P. Jöckel, O. Kirner, G. Pitari, D. A. Plummer, L. Revell, E. Rozanov, A. Stenke, T. Y. Tanaka, D. Visioni, and Y. Yamashita (2019). "The effect of atmospheric nudging on the stratospheric residual circulation in chemistry–climate models". In: *Atmospheric Chemistry and Physics* 19.17, pp. 11559–11586. ISSN: 1680-7324. DOI: 10.5194/acp-19-11559-2019.

Cohen, Y., D. Hauglustaine, N. Bellouin, M. T. Lund, S. Matthes, A. Skowron, R. Thor, U. Bundke, A. Petzold, S. Rohs, V. Thouret, A. Zahn, and H. Ziereis (2025). "Evaluation of O3, H2O, CO, and NOy climatologies simulated by four global models in the upper troposphere–lower stratosphere with IAGOS measurements". In: *Atmospheric Chemistry and Physics* 25.11, pp. 5793–5836. ISSN: 1680-7324. DOI: 10.5194/acp-25-5793-2025.

Cohen, Y., H. Petetin, V. Thouret, V. Marécal, B. Josse, H. Clark, B. Sauvage, A. Fontaine, G. Athier, R. Blot, D. Boulanger, J.-M. Cousin, and P. Nédélec (2018). “Climatology and long-term evolution of ozone and carbon monoxide in the upper troposphere–lower stratosphere (UTLS) at northern midlatitudes, as seen by IAGOS from 1995 to 2013”. In: *Atmospheric Chemistry and Physics* 18.8, pp. 5415–5453. ISSN: 1680-7324. DOI: 10.5194/acp-18-5415-2018.

Copernicus (2026). *Global Climate Highlights 2025*. ECMWF & Copernicus Climate Change Service. DOI: 10.24381/b3nm-p354.

Crueger, T., M. A. Giorgetta, R. Brokopf, M. Esch, S. Fiedler, C. Hohenegger, L. Kornblueh, T. Mauritsen, C. Nam, A. K. Naumann, K. Peters, S. Rast, E. Roeckner, M. Sakradzija, H. Schmidt, J. Vial, R. Vogel, and B. Stevens (2018). “ICON-A, The Atmosphere Component of the ICON Earth System Model: II. Model Evaluation”. In: *Journal of Advances in Modeling Earth Systems* 10.7, pp. 1638–1662. ISSN: 1942-2466. DOI: 10.1029/2017ms001233.

Dai, A. (2006). “Precipitation Characteristics in Eighteen Coupled Climate Models”. In: *Journal of Climate* 19.18, pp. 4605–4630. ISSN: 0894-8755. DOI: 10.1175/jcli3884.1.

Dauhut, T. and C. Hohenegger (2022). “The Contribution of Convection to the Stratospheric Water Vapor: The First Budget Using a Global Storm-Resolving Model”. In: *Journal of Geophysical Research: Atmospheres* 127.5. ISSN: 2169-8996. DOI: 10.1029/2021jd036295.

Davis, N. and T. Birner (2016). “Climate Model Biases in the Width of the Tropical Belt”. In: *Journal of Climate* 29.5, pp. 1935–1954. ISSN: 1520-0442. DOI: 10.1175/jcli-d-15-0336.1.

Davis, N. and T. Birner (2017). “On the Discrepancies in Tropical Belt Expansion between Reanalyses and Climate Models and among Tropical Belt Width Metrics”. In: *Journal of Climate* 30.4, pp. 1211–1231. ISSN: 1520-0442. DOI: 10.1175/jcli-d-16-0371.1.

Davis, N. A., P. Callaghan, I. R. Simpson, and S. Tilmes (2022). “Specified dynamics scheme impacts on wave-mean flow dynamics, convection, and tracer transport in CESM2 (WACCM6)”. In: *Atmospheric Chemistry and Physics* 22.1, pp. 197–214. ISSN: 1680-7324. DOI: 10.5194/acp-22-197-2022.

Davis, S. M., K. H. Rosenlof, B. Hassler, D. F. Hurst, W. G. Read, H. Vömel, H. Selkirk, M. Fujiwara, and R. Damadeo (2016). “The Stratospheric Water and Ozone Satellite Homogenized (SWOOSH) database: a long-term database for climate studies”. In: *Earth System Science Data* 8.2, pp. 461–490. ISSN: 1866-3516. DOI: 10.5194/essd-8-461-2016.

Degen, J., B. C. Baier, P. Jöckel, J. M. Menken, T. J. Schuck, C. Sweeney, and A. Engel (2025). “CO 2 variability and seasonal cycle in the UTLS: insights from EMAC model and AirCore observational data”. In: *Atmospheric Chemistry and Physics* 25.22, pp. 15741–15763. ISSN: 1680-7324. DOI: 10.5194/acp-25-15741-2025.

Dessler, A. E., M. R. Schoeberl, T. Wang, S. M. Davis, K. H. Rosenlof, and J.-P. Vernier (2014). “Variations of stratospheric water vapor over the past three decades”. In: *Journal of Geophysical Research: Atmospheres* 119.22. ISSN: 2169-8996. DOI: 10.1002/2014jd021712.

Dietmüller, S., M. Ponater, and R. Sausen (2014). “Interactive ozone induces a negative feedback in CO2-driven climate change simulations”. In: *Journal of Geophysical Research: Atmospheres* 119.4, pp. 1796–1805. ISSN: 2169-897X. DOI: 10.1002/2013jd020575.

Dietmüller, S., P. Jöckel, H. Tost, M. Kunze, C. Gellhorn, S. Brinkop, C. Frömming, M. Ponater, B. Steil, A. Lauer, and J. Hendricks (2016). “A new radiation infrastructure for the Modular Earth Submodel System (MESSy, based on version 2.51)”. In: *Geoscientific Model Development* 9.6, pp. 2209–2222. ISSN: 1991-9603. DOI: 10.5194/gmd-9-2209-2016.

Dobson, G. M. B. (1956). "Origin and distribution of the polyatomic molecules in the atmosphere". In: *Proceedings of the Royal Society of London. Series A. Mathematical and Physical Sciences* 236.1205, pp. 187–193. ISSN: 2053-9169. DOI: 10.1098/rspa.1956.0127.

Dobson, G. M. B., D. N. Harrison, and J. Lawrence (1929). "Measurements of the amount of ozone in the Earth's atmosphere and its relation to other geophysical conditions. Part III". In: *Proceedings of the Royal Society of London. Series A, Containing Papers of a Mathematical and Physical Character* 122.790, pp. 456–486. ISSN: 2053-9150. DOI: 10.1098/rspa.1929.0034.

Donner, L. J., C. J. Seman, R. S. Hemler, and S. Fan (2001). "A Cumulus Parameterization Including Mass Fluxes, Convective Vertical Velocities, and Mesoscale Effects: Thermodynamic and Hydrological Aspects in a General Circulation Model". In: *Journal of Climate* 14.16, pp. 3444–3463. ISSN: 1520-0442. DOI: 10.1175/1520-0442(2001)014<3444:acpimf>2.0.co;2.

ECMWF (2024). "IFS Documentation CY49R1 - Part IV: Physical Processes". In: DOI: 10.21957/C731EE1102.

Eichinger, R. and P. Jöckel (2014). "The generic MESSy submodel TENDENCY (v1.0) for process-based analyses in Earth system models". In: *Geoscientific Model Development* 7.4, pp. 1573–1582. ISSN: 1991-9603. DOI: 10.5194/gmd-7-1573-2014.

Eichinger, R., S. Dietmüller, H. Garny, P. Šácha, T. Birner, H. Bönisch, G. Pitari, D. Visioni, A. Stenke, E. Rozanov, L. Revell, D. A. Plummer, P. Jöckel, L. Oman, M. Deushi, D. E. Kinnison, R. Garcia, O. Morgenstern, G. Zeng, K. A. Stone, and R. Schofield (2019). "The influence of mixing on the stratospheric age of air changes in the 21st century". In: *Atmospheric Chemistry and Physics* 19.2, pp. 921–940. ISSN: 1680-7324. DOI: 10.5194/acp-19-921-2019.

Eichinger, R., H. Garny, P. Šácha, J. Danker, S. Dietmüller, and S. Oberländer-Hayn (2020). "Effects of missing gravity waves on stratospheric dynamics; part 1: climatology". In: *Climate Dynamics* 54.5–6, pp. 3165–3183. ISSN: 1432-0894. DOI: 10.1007/s00382-020-05166-w.

Eichinger, R., S. Rhode, H. Garny, P. Preusse, P. Pisoft, A. Kuchař, P. Jöckel, A. Kerkweg, and B. Kern (2023). "Emulating lateral gravity wave propagation in a global chemistry–climate model (EMAC v2.55.2) through horizontal flux redistribution". In: *Geoscientific Model Development* 16.19, pp. 5561–5583. ISSN: 1991-9603. DOI: 10.5194/gmd-16-5561-2023.

Elsaesser, G. S., C. W. O'Dell, M. D. Lebsock, R. Bennartz, T. J. Greenwald, and F. J. Wentz (2017). "The Multisensor Advanced Climatology of Liquid Water Path (MAC-LWP)". In: *Journal of Climate* 30.24, pp. 10193–10210. ISSN: 1520-0442. DOI: 10.1175/jcli-d-16-0902.1.

Emanuel, K. A. (1991). "A Scheme for Representing Cumulus Convection in Large-Scale Models". In: *Journal of the Atmospheric Sciences* 48.21, pp. 2313–2329. ISSN: 1520-0469. DOI: 10.1175/1520-0469(1991)048<2313:asfrcc>2.0.co;2.

Emanuel, K. A. (1993). "A Cumulus Representation Based on the Episodic Mixing Model: The Importance of Mixing and Microphysics in Predicting Humidity". In: *The Representation of Cumulus Convection in Numerical Models*. American Meteorological Society, pp. 185–192. ISBN: 9781935704133. DOI: 10.1007/978-1-935704-13-3_19.

Emanuel, K. A. and M. Živković-Rothman (1999). "Development and Evaluation of a Convection Scheme for Use in Climate Models". In: *Journal of the Atmospheric Sciences* 56.11, pp. 1766–1782. ISSN: 1520-0469. DOI: 10.1175/1520-0469(1999)056<1766:daeoac>2.0.co;2.

Emmerichs, T., A. Kerkweg, H. Ouwersloot, S. Fares, I. Mammarella, and D. Taraborrelli (2021). “A revised dry deposition scheme for land–atmosphere exchange of trace gases in ECHAM/MESSy v2.54”. In: *Geoscientific Model Development* 14.1, pp. 495–519. ISSN: 1991-9603. DOI: 10.5194/gmd-14-495-2021.

Engel, A., T. Möbius, H. Bönisch, U. Schmidt, R. Heinz, I. Levin, E. Atlas, S. Aoki, T. Nakazawa, S. Sugawara, F. Moore, D. Hurst, J. Elkins, S. Schauffler, A. Andrews, and K. Boering (2008). “Age of stratospheric air unchanged within uncertainties over the past 30 years”. In: *Nature Geoscience* 2.1, pp. 28–31. ISSN: 1752-0908. DOI: 10.1038/ngeo388.

Engel, A., H. Bönisch, M. Ullrich, R. Sitals, O. Membrive, F. Danis, and C. Crevoisier (2017). “Mean age of stratospheric air derived from AirCore observations”. In: *Atmospheric Chemistry and Physics* 17.11, pp. 6825–6838. ISSN: 1680-7324. DOI: 10.5194/acp-17-6825-2017.

Forster, P. M. d. F. and K. P. Shine (2002). “Assessing the climate impact of trends in stratospheric water vapor”. In: *Geophysical Research Letters* 29.6. ISSN: 1944-8007. DOI: 10.1029/2001gl013909.

Forster, P. M. d. F. and K. P. Shine (1997). “Radiative forcing and temperature trends from stratospheric ozone changes”. In: *Journal of Geophysical Research: Atmospheres* 102.D9, pp. 10841–10855. ISSN: 0148-0227. DOI: 10.1029/96jd03510.

Forster, P. M. d. F. and K. Tourpali (2001). “Effect of tropopause height changes on the calculation of ozone trends and their radiative forcing”. In: *Journal of Geophysical Research: Atmospheres* 106.D11, pp. 12241–12251. ISSN: 0148-0227. DOI: 10.1029/2000jd900813.

Fricko, O., P. Havlik, J. Rogelj, Z. Klimont, M. Gusti, N. Johnson, P. Kolp, M. Strubegger, H. Valin, M. Amann, T. Ermolieva, N. Forsell, M. Herrero, C. Heyes, G. Kindermann, V. Krey, D. L. McCollum, M. Obersteiner, S. Pachauri, S. Rao, E. Schmid, W. Schoepp, and K. Riahi (2017). “The marker quantification of the Shared Socioeconomic Pathway 2: A middle-of-the-road scenario for the 21st century”. In: *Global Environmental Change* 42, pp. 251–267. ISSN: 0959-3780. DOI: 10.1016/j.gloenvcha.2016.06.004.

Friedel, M., G. Chiodo, T. Sukhodolov, J. Keeble, T. Peter, S. Seeber, A. Stenke, H. Akiyoshi, E. Rozanov, D. Plummer, P. Jöckel, G. Zeng, O. Morgenstern, and B. Josse (2023). “Weakening of springtime Arctic ozone depletion with climate change”. In: *Atmospheric Chemistry and Physics* 23.17, pp. 10235–10254. ISSN: 1680-7324. DOI: 10.5194/acp-23-10235-2023.

Fu, Q., S. Solomon, H. A. Pahlavan, and P. Lin (2019). “Observed changes in Brewer–Dobson circulation for 1980–2018”. In: *Environmental Research Letters* 14.11, p. 114026. ISSN: 1748-9326. DOI: 10.1088/1748-9326/ab4de7.

Fueglistaler, S., A. E. Dessler, T. J. Dunkerton, I. Folkins, Q. Fu, and P. W. Mote (2009). “Tropical tropopause layer”. In: *Reviews of Geophysics* 47.1. ISSN: 1944-9208. DOI: 10.1029/2008rg000267.

Funke, B., M. López-Puertas, G. P. Stiller, S. Versick, and T. von Clarmann (2016). “A semi-empirical model for mesospheric and stratospheric NOy produced by energetic particle precipitation”. In: *Atmospheric Chemistry and Physics* 16.13, pp. 8667–8693. ISSN: 1680-7324. DOI: 10.5194/acp-16-8667-2016.

Garny, H., F. Ploeger, M. Abalos, H. Bönisch, A. E. Castillo, T. von Clarmann, M. Diallo, A. Engel, J. C. Laube, M. Linz, J. L. Neu, A. Podglajen, E. Ray, L. Rivoire, L. N. Saunders, G. Stiller, F. Voet, T. Wagenhäuser, and K. A. Walker (2024). “Age of Stratospheric Air:

Progress on Processes, Observations, and Long-Term Trends". In: *Reviews of Geophysics* 62.4. ISSN: 1944-9208. DOI: 10.1029/2023rg000832.

Gentine, P., M. Pritchard, S. Rasp, G. Reinaudi, and G. Yacalis (2018). "Could Machine Learning Break the Convection Parameterization Deadlock?" In: *Geophysical Research Letters* 45.11, pp. 5742–5751. ISSN: 1944-8007. DOI: 10.1029/2018gl078202.

Gettelman, A. and T. Birner (2007). "Insights into Tropical Tropopause Layer processes using global models". In: *Journal of Geophysical Research: Atmospheres* 112.D23. ISSN: 0148-0227. DOI: 10.1029/2007jd008945.

Gettelman, A., M. I. Hegglin, S.-W. Son, J. Kim, M. Fujiwara, T. Birner, S. Kremser, M. Rex, J. A. Añel, H. Akiyoshi, J. Austin, S. Bekki, P. Braesike, C. Brühl, N. Butchart, M. Chipperfield, M. Dameris, S. Dhomse, H. Garny, S. C. Hardiman, P. Jöckel, D. E. Kinnison, J. F. Lamarque, E. Mancini, M. Marchand, M. Michou, O. Morgenstern, S. Pawson, G. Pitari, D. Plummer, J. A. Pyle, E. Rozanov, J. Scinocca, T. G. Shepherd, K. Shibata, D. Smale, H. Teyssèdre, and W. Tian (2010). "Multimodel assessment of the upper troposphere and lower stratosphere: Tropics and global trends". In: *Journal of Geophysical Research: Atmospheres* 115.D3. ISSN: 0148-0227. DOI: 10.1029/2009jd013638.

Gettelman, A., P. Hoor, L. L. Pan, W. J. Randel, M. I. Hegglin, and T. Birner (2011). "THE EXTRATROPICAL UPPER TROPOSPHERE AND LOWER STRATOSPHERE". In: *Reviews of Geophysics* 49.3. ISSN: 1944-9208. DOI: 10.1029/2011rg000355.

Gidden, M. J., K. Riahi, S. J. Smith, S. Fujimori, G. Luderer, E. Kriegler, D. P. van Vuuren, M. van den Berg, L. Feng, D. Klein, K. Calvin, J. C. Doelman, S. Frank, O. Fricko, M. Harmsen, T. Hasegawa, P. Havlik, J. Hilaire, R. Hoesly, J. Horing, A. Popp, E. Stehfest, and K. Takahashi (2019). "Global emissions pathways under different socioeconomic scenarios for use in CMIP6: a dataset of harmonized emissions trajectories through the end of the century". In: *Geoscientific Model Development* 12.4, pp. 1443–1475. ISSN: 1991-9603. DOI: 10.5194/gmd-12-1443-2019.

Giorgetta, M. A., R. Brokopf, T. Crueger, M. Esch, S. Fiedler, J. Helmert, C. Hohenegger, L. Kornblueh, M. Köhler, E. Manzini, T. Mauritsen, C. Nam, T. Raddatz, S. Rast, D. Reinert, M. Sakradzija, H. Schmidt, R. Schneck, R. Schnur, L. Silvers, H. Wan, G. Zängl, and B. Stevens (2018). "ICON-A, the Atmosphere Component of the ICON Earth System Model: I. Model Description". In: *Journal of Advances in Modeling Earth Systems* 10.7, pp. 1613–1637. ISSN: 1942-2466. DOI: 10.1029/2017ms001242.

Giorgetta, M. A., E. Manzini, E. Roeckner, M. Esch, and L. Bengtsson (2006). "Climatology and Forcing of the Quasi-Biennial Oscillation in the MAECHAM5 Model". In: *Journal of Climate* 19.16, pp. 3882–3901. ISSN: 0894-8755. DOI: 10.1175/jcli3830.1.

Goessling, H. F. and S. Bathiany (2016). "Why CO_2 cools the middle atmosphere - a consolidating model perspective". In: *Earth System Dynamics* 7.3, pp. 697–715. ISSN: 2190-4987. DOI: 10.5194/esd-7-697-2016.

Grabowski, W. W. (2016). "Towards Global Large Eddy Simulation: Super-Parameterization Revisited". In: *Journal of the Meteorological Society of Japan. Ser. II* 94.4, pp. 327–344. ISSN: 2186-9057. DOI: 10.2151/jmsj.2016-017.

Guenther, A., T. Karl, P. Harley, C. Wiedinmyer, P. I. Palmer, and C. Geron (2006). "Estimates of global terrestrial isoprene emissions using MEGAN (Model of Emissions of Gases and Aerosols from Nature)". In: *Atmospheric Chemistry and Physics* 6.11, pp. 3181–3210. ISSN: 1680-7324. DOI: 10.5194/acp-6-3181-2006.

Gulev, S., P. Thorne, J. Ahn, F. Dentener, C. Domingues, S. Gerland, D. Gong, D. Kaufman, H. Nnamchi, J. Quaas, J. Rivera, S. Sathyendranath, S. Smith, B. Trewin, K. von Schuckmann, and R. Vose (2021). "Changing State of the Climate System". In: *Climate Change 2021: The Physical Science Basis. Contribution of Working Group I to the Sixth Assessment Report of the Intergovernmental Panel on Climate Change*. Ed. by V. Masson-Delmotte, P. Zhai, A. Pirani, S. Connors, C. Péan, S. Berger, N. Caud, Y. Chen, L. Goldfarb, M. Gomis, M. Huang, K. Leitzell, E. Lonnoy, J. Matthews, T. Maycock, T. Waterfield, O. Yelekçi, R. Yu, and B. Zhou. Cambridge, United Kingdom and New York, NY, USA: Cambridge University Press, pp. 287–422. DOI: 10.1017/9781009157896.004.

Hall, T. M. and R. A. Plumb (1994). "Age as a diagnostic of stratospheric transport". In: *Journal of Geophysical Research: Atmospheres* 99.D1, pp. 1059–1070. ISSN: 0148-0227. DOI: 10.1029/93jd03192.

Harzer, F., H. Garny, F. Ploeger, H. Bönisch, P. Hoor, and T. Birner (2023). "On the pattern of interannual polar vortex–ozone co-variability during northern hemispheric winter". In: *Atmospheric Chemistry and Physics* 23.18, pp. 10661–10675. ISSN: 1680-7324. DOI: 10.5194/acp-23-10661-2023.

Harzer, F., H. Garny, F. Ploeger, J. M. Menken, and T. Birner (2025). "Adiabatic versus diabatic transport contributions to the ozone budget in the northern hemispheric upper troposphere and lower stratosphere". In: *Atmospheric Chemistry and Physics* 25.21, pp. 14909–14921. ISSN: 1680-7324. DOI: 10.5194/acp-25-14909-2025.

Hassler, B., I. Petropavlovskikh, J. Staehelin, T. August, P. K. Bhartia, C. Clerbaux, D. Degenstein, M. D. Mazière, B. M. Dinelli, A. Dudhia, G. Dufour, S. M. Frith, L. Froidevaux, S. Godin-Beekmann, J. Granville, N. R. P. Harris, K. Hoppel, D. Hubert, Y. Kasai, M. J. Kurylo, E. Kyrölä, J.-C. Lambert, P. F. Levelt, C. T. McElroy, R. D. McPeters, R. Munro, H. Nakajima, A. Parrish, P. Raspollini, E. E. Remsberg, K. H. Rosenlof, A. Rozanov, T. Sano, Y. Sasano, M. Shiotani, H. G. J. Smit, G. Stiller, J. Tamminen, D. W. Tarasick, J. Urban, R. J. van der A, J. P. Veefkind, C. Vigouroux, T. von Clarmann, C. von Savigny, K. A. Walker, M. Weber, J. Wild, and J. M. Zawodny (2014). "Past changes in the vertical distribution of ozone – Part 1: Measurement techniques, uncertainties and availability". In: *Atmospheric Measurement Techniques* 7.5, pp. 1395–1427. ISSN: 1867-8548. DOI: 10.5194/amt-7-1395-2014.

Haynes, P., J. Scinocca, and M. Greenslade (2001). "Formation and maintenance of the extratropical tropopause by baroclinic eddies". In: *Geophysical Research Letters* 28.22, pp. 4179–4182. ISSN: 1944-8007. DOI: 10.1029/2001gl013485.

Haynes, P. and E. Shuckburgh (2000). "Effective diffusivity as a diagnostic of atmospheric transport: 2. Troposphere and lower stratosphere". In: *Journal of Geophysical Research: Atmospheres* 105.D18, pp. 22795–22810. ISSN: 0148-0227. DOI: 10.1029/2000jd900092.

Hegglin, M. I., C. D. Boone, G. L. Manney, and K. A. Walker (2009). "A global view of the extratropical tropopause transition layer from Atmospheric Chemistry Experiment Fourier Transform Spectrometer O3, H2O, and CO". In: *Journal of Geophysical Research: Atmospheres* 114.D7. ISSN: 0148-0227. DOI: 10.1029/2008jd009984.

Hegglin, M. I., A. Gettelman, P. Hoor, R. Krichevsky, G. L. Manney, L. L. Pan, S.-W. Son, G. Stiller, S. Tilmes, K. A. Walker, V. Eyring, T. G. Shepherd, D. Waugh, H. Akiyoshi, J. A. Añel, J. Austin, A. Baumgaertner, S. Bekki, P. Braesicke, C. Brühl, N. Butchart, M. Chipperfield, M. Dameris, S. Dhomse, S. Frith, H. Garny, S. C. Hardiman, P. Jöckel, D. E. Kinnison, J. F. Lamarque, E. Mancini, M. Michou, O. Morgenstern, T. Nakamura, D. Olivié, S. Pawson, G. Pitari, D. A. Plummer, J. A. Pyle, E. Rozanov, J. F. Scinocca, K. Shibata, D.

Smale, H. Teyssèdre, W. Tian, and Y. Yamashita (2010). “Multimodel assessment of the upper troposphere and lower stratosphere: Extratropics”. In: *Journal of Geophysical Research: Atmospheres* 115.D3. ISSN: 0148-0227. DOI: 10.1029/2010jd013884.

Hegglin, M. I., S. Tegtmeier, J. Anderson, L. Froidevaux, R. Fuller, B. Funke, A. Jones, G. Lingenfelser, J. Lumpe, D. Pendlebury, E. Remsberg, A. Rozanov, M. Toohey, J. Urban, T. von Clarmann, K. A. Walker, R. Wang, and K. Weigel (2013). “SPARC Data Initiative: Comparison of water vapor climatologies from international satellite limb sounders”. In: *Journal of Geophysical Research: Atmospheres* 118.20. ISSN: 2169-8996. DOI: 10.1002/jgrd.50752.

Hegglin, M. I. and T. G. Shepherd (2009). “Large climate-induced changes in ultraviolet index and stratosphere-to-troposphere ozone flux”. In: *Nature Geoscience* 2.10, pp. 687–691. ISSN: 1752-0908. DOI: 10.1038/ngeo604.

Held, I. M. and B. J. Soden (2006). “Robust Responses of the Hydrological Cycle to Global Warming”. In: *Journal of Climate* 19.21, pp. 5686–5699. ISSN: 0894-8755. DOI: 10.1175/jcli3990.1.

Hersbach, H., B. Bell, P. Berrisford, S. Hirahara, A. Horányi, J. Muñoz-Sabater, J. Nicolas, C. Peubey, R. Radu, D. Schepers, A. Simmons, C. Soci, S. Abdalla, X. Abellan, G. Balsamo, P. Bechtold, G. Biavati, J. Bidlot, M. Bonavita, G. De Chiara, P. Dahlgren, D. Dee, M. Diamantakis, R. Dragani, J. Flemming, R. Forbes, M. Fuentes, A. Geer, L. Haimberger, S. Healy, R. J. Hogan, E. Hólm, M. Janisková, S. Keeley, P. Laloyaux, P. Lopez, C. Lupu, G. Radnoti, P. de Rosnay, I. Rozum, F. Vamborg, S. Villaume, and J.-N. Thépaut (2020). “The ERA5 global reanalysis”. In: *Quarterly Journal of the Royal Meteorological Society* 146.730, pp. 1999–2049. ISSN: 1477-870X. DOI: 10.1002/qj.3803.

Highwood, E. J. and B. J. Hoskins (1998). “The tropical tropopause”. In: *Quarterly Journal of the Royal Meteorological Society* 124.549, pp. 1579–1604. ISSN: 1477-870X. DOI: 10.1002/qj.49712454911.

Hoerling, M. P., T. K. Schaack, and A. J. Lenzen (1991). “Global Objective Tropopause Analysis”. In: *Monthly Weather Review* 119.8, pp. 1816–1831. ISSN: 1520-0493. DOI: 10.1175/1520-0493(1991)119<1816:gota>2.0.co;2.

Hoffmann, L. and R. Spang (2021). *Reanalysis Tropopause Data Repository*. DOI: 10.26165/JUELICH-DATA/UBNGI2.

Hohenegger, C., L. Kornblueh, D. Klocke, T. Becker, G. Cioni, J. F. Engels, U. Schulzweida, and B. Stevens (2020). “Climate Statistics in Global Simulations of the Atmosphere, from 80 to 2.5 km Grid Spacing”. In: *Journal of the Meteorological Society of Japan. Ser. II* 98.1, pp. 73–91. ISSN: 2186-9057. DOI: 10.2151/jmsj.2020-005.

Holton, J. R., P. H. Haynes, M. E. McIntyre, A. R. Douglass, R. B. Rood, and L. Pfister (1995). “Stratosphere-troposphere exchange”. In: *Reviews of Geophysics* 33.4, pp. 403–439. ISSN: 1944-9208. DOI: 10.1029/95rg02097.

Homeyer, C. R., L. L. Pan, S. W. Dorsi, L. M. Avallone, A. J. Weinheimer, A. S. O’Brien, J. P. DiGangi, M. A. Zondlo, T. B. Ryerson, G. S. Diskin, and T. L. Campos (2014). “Convective transport of water vapor into the lower stratosphere observed during double-tropopause events”. In: *Journal of Geophysical Research: Atmospheres* 119.18, pp. 10, 941–10, 958. ISSN: 2169-897X. DOI: 10.1002/2014jd021485.

Hoor, P., C. Gurk, D. Brunner, M. I. Hegglin, H. Wernli, and H. Fischer (2004). “Seasonality and extent of extratropical TST derived from in-situ CO measurements during SPURT”. In: *Atmospheric Chemistry and Physics* 4.5, pp. 1427–1442. ISSN: 1680-7324. DOI: 10.5194/acp-4-1427-2004.

Hoor, P., H. Wernli, M. I. Hegglin, and H. Bönisch (2010). “Transport timescales and tracer properties in the extratropical UTLS”. In: *Atmospheric Chemistry and Physics* 10.16, pp. 7929–7944. ISSN: 1680-7324. DOI: 10.5194/acp-10-7929-2010.

Houghton, J. T., G. J. Jenkins, and J. J. Ephraums, eds. (1990). *Climate Change: The IPCC Scientific Assessment*. Cambridge: Cambridge University Press.

Hourdin, F., T. Mauritsen, A. Gettelman, J.-C. Golaz, V. Balaji, Q. Duan, D. Folini, D. Ji, D. Klocke, Y. Qian, F. Rauser, C. Rio, L. Tomassini, M. Watanabe, and D. Williamson (2017). “The Art and Science of Climate Model Tuning”. In: *Bulletin of the American Meteorological Society* 98.3, pp. 589–602. ISSN: 1520-0477. DOI: 10.1175/bams-d-15-00135.1.

Hourdin, F., I. Musat, S. Bony, P. Braconnot, F. Codron, J.-L. Dufresne, L. Fairhead, M.-A. Filiberti, P. Friedlingstein, J.-Y. Grandpeix, G. Krinner, P. LeVan, Z.-X. Li, and F. Lott (2006). “The LMDZ4 general circulation model: climate performance and sensitivity to parametrized physics with emphasis on tropical convection”. In: *Climate Dynamics* 27.7–8, pp. 787–813. ISSN: 1432-0894. DOI: 10.1007/s00382-006-0158-0.

Huang, D., P. Yan, J. Zhu, Y. Zhang, X. Kuang, and J. Cheng (2017). “Uncertainty of global summer precipitation in the CMIP5 models: a comparison between high-resolution and low-resolution models”. In: *Theoretical and Applied Climatology* 132.1–2, pp. 55–69. ISSN: 1434-4483. DOI: 10.1007/s00704-017-2078-9.

Hwang, Y.-T., D. M. W. Frierson, B. J. Soden, and I. M. Held (2011). “CORRIGENDUM”. In: *Journal of Climate* 24.5, pp. 1559–1560. ISSN: 0894-8755. DOI: 10.1175/2010jcli4045.1.

Iglesias-Suarez, F., P. J. Young, and O. Wild (2016). “Stratospheric ozone change and related climate impacts over 1850–2100 as modelled by the ACCMIP ensemble”. In: *Atmospheric Chemistry and Physics* 16.1, pp. 343–363. ISSN: 1680-7324. DOI: 10.5194/acp-16-343-2016.

IPCC (2021). *Climate Change 2021: The Physical Science Basis*. Ed. by V. Masson-Delmotte, P. Zhai, A. Pirani, S. L. Connors, C. Péan, S. Berger, N. Caud, Y. Chen, L. Goldfarb, M. I. Gomis, M. Huang, K. Leitzell, E. Lonnoy, J. B. R. Matthews, T. K. Maycock, T. Waterfield, O. Yelekçi, R. Yu, and B. Zhou. Contribution of Working Group I to the Sixth Assessment Report of the Intergovernmental Panel on Climate Change. Cambridge, United Kingdom and New York, NY, USA: Cambridge University Press, p. 2391. ISBN: 978-1-009-15789-6. DOI: 10.1017/9781009157896.

Jarraud, M. and A. Simmons (1983). “The spectral technique”. eng. PhD thesis. Shinfield Park, Reading, pp. 1–59. URL: https://www.ecmwf.int/en/elibrary/75050-spectral-technique.

Jensen, E. J., L. L. Pan, S. Honomichl, G. S. Diskin, M. Krämer, N. Spelten, G. Günther, D. F. Hurst, M. Fujiwara, H. Vömel, H. B. Selkirk, J. Suzuki, M. J. Schwartz, and J. B. Smith (2020). “Assessment of Observational Evidence for Direct Convective Hydration of the Lower Stratosphere”. In: *Journal of Geophysical Research: Atmospheres* 125.15. ISSN: 2169-8996. DOI: 10.1029/2020jd032793.

Jeuken, A. B. M., P. C. Siegmund, L. C. Heijboer, J. Feichter, and L. Bengtsson (1996). “On the potential of assimilating meteorological analyses in a global climate model for the purpose of model validation”. In: *Journal of Geophysical Research: Atmospheres* 101.D12, pp. 16939–16950. ISSN: 0148-0227. DOI: 10.1029/96jd01218.

Jöckel, P., A. Kerkweg, J. Buchholz-Dietsch, H. Tost, R. Sander, and A. Pozzer (2008). “Technical Note: Coupling of chemical processes with the Modular Earth Submodel System (MESSy) submodel TRACER". In: *Atmospheric Chemistry and Physics* 8.6, pp. 1677–1687. ISSN: 1680-7324. DOI: 10.5194/acp-8-1677-2008.

Jöckel, P., A. Kerkweg, A. Pozzer, R. Sander, H. Tost, H. Riede, A. Baumgaertner, S. Gromov, and B. Kern (2010). "Development cycle 2 of the Modular Earth Submodel System (MESSy2)". In: *Geoscientific Model Development* 3.2, pp. 717–752. ISSN: 1991-9603. DOI: 10.5194/gmd-3-717-2010.

Jöckel, P., R. Sander, A. Kerkweg, H. Tost, and J. Lelieveld (2005). "Technical Note: The Modular Earth Submodel System (MESSy) - a new approach towards Earth System Modeling". In: *Atmospheric Chemistry and Physics* 5.2, pp. 433–444. ISSN: 1680-7324. DOI: 10.5194/acp-5-433-2005.

Jöckel, P., H. Tost, A. Pozzer, C. Brühl, J. Buchholz, L. Ganzeveld, P. Hoor, A. Kerkweg, M. G. Lawrence, R. Sander, B. Steil, G. Stiller, M. Tanarhte, D. Taraborrelli, J. van Aardenne, and J. Lelieveld (2006). "The atmospheric chemistry general circulation model ECHAM5/MESSy1: consistent simulation of ozone from the surface to the mesosphere". In: *Atmospheric Chemistry and Physics* 6.12, pp. 5067–5104. ISSN: 1680-7324. DOI: 10.5194/acp-6-5067-2006.

Jöckel, P., H. Tost, A. Pozzer, M. Kunze, O. Kirner, C. A. M. Brenninkmeijer, S. Brinkop, D. S. Cai, C. Dyroff, J. Eckstein, F. Frank, H. Garny, K.-D. Gottschaldt, P. Graf, V. Grewe, A. Kerkweg, B. Kern, S. Matthes, M. Mertens, S. Meul, M. Neumaier, M. Nützel, S. Oberländer-Hayn, R. Ruhnke, T. Runde, R. Sander, D. Scharffe, and A. Zahn (2016). "Earth System Chemistry integrated Modelling (ESCiMo) with the Modular Earth Submodel System (MESSy) version 2.51". In: *Geoscientific Model Development* 9.3, pp. 1153–1200. ISSN: 1991-9603. DOI: 10.5194/gmd-9-1153-2016.

Johnson, G. C., J. M. Lyman, and N. G. Loeb (2016). "Improving estimates of Earth's energy imbalance". In: *Nature Climate Change* 6.7, pp. 639–640. ISSN: 1758-6798. DOI: 10.1038/nclimate3043.

Jonsson, A. I., J. de Grandpré, V. I. Fomichev, J. C. McConnell, and S. R. Beagley (2004). "Doubled CO2-induced cooling in the middle atmosphere: Photochemical analysis of the ozone radiative feedback". In: *Journal of Geophysical Research: Atmospheres* 109.D24. ISSN: 0148-0227. DOI: 10.1029/2004jd005093.

Kaiser, J. W., A. Heil, M. O. Andreae, A. Benedetti, N. Chubarova, L. Jones, J.-J. Morcrette, M. Razinger, M. G. Schultz, M. Suttie, and G. R. van der Werf (2012). "Biomass burning emissions estimated with a global fire assimilation system based on observed fire radiative power". In: *Biogeosciences* 9.1, pp. 527–554. ISSN: 1726-4189. DOI: 10.5194/bg-9-527-2012.

Kaufmann, S., C. Voigt, R. Heller, T. Jurkat-Witschas, M. Krämer, C. Rolf, M. Zöger, A. Giez, B. Buchholz, V. Ebert, T. Thornberry, and U. Schumann (2018). "Intercomparison of midlatitude tropospheric and lower-stratospheric water vapor measurements and comparison to ECMWF humidity data". In: *Atmospheric Chemistry and Physics* 18.22, pp. 16729–16745. ISSN: 1680-7324. DOI: 10.5194/acp-18-16729-2018.

Keeble, J., B. Hassler, A. Banerjee, R. Checa-Garcia, G. Chiodo, S. Davis, V. Eyring, P. T. Griffiths, O. Morgenstern, P. Nowack, G. Zeng, J. Zhang, G. Bodeker, S. Burrows, P. Cameron-Smith, D. Cugnet, C. Danek, M. Deushi, L. W. Horowitz, A. Kubin, L. Li, G. Lohmann, M. Michou, M. J. Mills, P. Nabat, D. Olivié, S. Park, Ø. Seland, J. Stoll, K.-H. Wieners, and T. Wu (2021). "Evaluating stratospheric ozone and water vapour changes in CMIP6 models from 1850 to 2100". In: *Atmospheric Chemistry and Physics* 21.6, pp. 5015–5061. ISSN: 1680-7324. DOI: 10.5194/acp-21-5015-2021.

Kerkweg, A., J. Buchholz, L. Ganzeveld, A. Pozzer, H. Tost, and P. Jöckel (2006a). "Technical Note: An implementation of the dry removal processes DRY DEPosition and SEDImentation in the Modular Earth Submodel System (MESSy)". In: *Atmospheric Chemistry and Physics* 6.12, pp. 4617–4632. ISSN: 1680-7324. DOI: `10.5194/acp-6-4617-2006`.

Kerkweg, A. and P. Jöckel (2015). "The infrastructure MESSy submodels GRID (v1.0) and IMPORT (v1.0)". In: DOI: `10.5194/gmdd-8-8607-2015`.

Kerkweg, A., R. Sander, H. Tost, and P. Jöckel (2006b). "Technical note: Implementation of prescribed (OFFLEM), calculated (ONLEM), and pseudo-emissions (TNUDGE) of chemical species in the Modular Earth Submodel System (MESSy)". In: *Atmospheric Chemistry and Physics* 6.11, pp. 3603–3609. ISSN: 1680-7324. DOI: `10.5194/acp-6-3603-2006`.

Kerkweg, A., C. Hofmann, P. Jöckel, M. Mertens, and G. Pante (2018). "The on-line coupled atmospheric chemistry model system MECO(n) – Part 5: Expanding the Multi-Model-Driver (MMD v2.0) for 2-way data exchange including data interpolation via GRID (v1.0)". In: *Geoscientific Model Development* 11.3, pp. 1059–1076. ISSN: 1991-9603. DOI: `10.5194/gmd-11-1059-2018`.

Kirner, O., R. Ruhnke, J. Buchholz-Dietsch, P. Jöckel, C. Brühl, and B. Steil (2011). "Simulation of polar stratospheric clouds in the chemistry-climate-model EMAC via the submodel PSC". In: *Geoscientific Model Development* 4.1, pp. 169–182. ISSN: 1991-9603. DOI: `10.5194/gmd-4-169-2011`.

Knutti, R., D. Masson, and A. Gettelman (2013). "Climate model genealogy: Generation CMIP5 and how we got there". In: *Geophysical Research Letters* 40.6, pp. 1194–1199. ISSN: 1944-8007. DOI: `10.1002/grl.50256`.

Konjari, P., C. Rolf, M. I. Hegglin, S. Rohs, Y. Li, A. Zahn, H. Bönisch, P. Nedelec, M. Krämer, and A. Petzold (2025). "Technical note: Water vapour climatologies in the extra-tropical upper troposphere and lower stratosphere derived from a synthesis of passenger and research aircraft measurements". In: *Atmospheric Chemistry and Physics* 25.7, pp. 4269–4289. ISSN: 1680-7324. DOI: `10.5194/acp-25-4269-2025`.

Koskentausta, J., A. Y. Karpechko, R. H. Köhler, X. Levine, R. R. Wijngaard, and V. A. Sinclair (2025). "The Role of Model Biases in the Simulated North Atlantic Jet Stream Response to Global Warming". In: *Journal of Climate* 38.18, pp. 5007–5023. ISSN: 1520-0442. DOI: `10.1175/jcli-d-24-0648.1`.

Krishnamurti, T. N., J. Xue, H. S. Bedi, K. Ingles, and D. Oosterhof (1991). "Physical initialization for numerical weather prediction over the tropics". In: *Tellus B* 43.4, pp. 53–81. ISSN: 1600-0889. DOI: `https://doi.org/10.1034/j.1600-0889.1991.t01-2-00007.x`.

Krüger, K., A. Schäfler, M. Wirth, M. Weissmann, and G. C. Craig (2022). "Vertical structure of the lower-stratospheric moist bias in the ERA5 reanalysis and its connection to mixing processes". In: *Atmospheric Chemistry and Physics* 22.23, pp. 15559–15577. ISSN: 1680-7324. DOI: `10.5194/acp-22-15559-2022`.

Kuma, P., F. A.-M. Bender, and A. R. Jönsson (2023). "Climate Model Code Genealogy and Its Relation to Climate Feedbacks and Sensitivity". In: *Journal of Advances in Modeling Earth Systems* 15.7. ISSN: 1942-2466. DOI: `10.1029/2022ms003588`.

Kumar, V. V., A. Protat, C. Jakob, C. R. Williams, S. Rauniyar, G. L. Stephens, and P. T. May (2016). "The Estimation of Convective Mass Flux from Radar Reflectivities". In: *Journal of Applied Meteorology and Climatology* 55.5, pp. 1239–1257. ISSN: 1558-8432. DOI: `10.1175/jamc-d-15-0193.1`.

Kunz, A., L. L. Pan, P. Konopka, D. E. Kinnison, and S. Tilmes (2011). “Chemical and dynamical discontinuity at the extratropical tropopause based on START08 and WACCM analyses: CHEMICAL AND DYNAMICAL DISCONTINUITY”. In: *Journal of Geophysical Research: Atmospheres* 116.D24, n/a–n/a. ISSN: 0148-0227. DOI: 10.1029/2011jd016686.

Lan, X., K. Thoning, and E. Dlugokencky (2025). *Trends in globally-averaged CH4, N2O, and SF6*. DOI: 10.15138/P8XG-AA10.

Lawrence, M. G. and P. J. Rasch (2005). “Tracer Transport in Deep Convective Updrafts: Plume Ensemble versus Bulk Formulations”. In: *Journal of the Atmospheric Sciences* 62.8, pp. 2880–2894. ISSN: 0022-4928. DOI: 10.1175/jas3505.1.

Lee, J.-Y., J. Marotzke, G. Bala, L. Cao, S. Corti, J. P. Dunne, F. Engelbrecht, E. Fischer, J. C. Fyfe, C. Jones, A. Maycock, J. Mutemi, O. Ndiaye, S. Panickal, and T. Zhou (2021). “Future Global Climate: ScenarioBased Projections and NearTerm Information”. In: *Climate Change 2021: The Physical Science Basis. Contribution of Working Group I to the Sixth Assessment Report of the Intergovernmental Panel on Climate Change*. Ed. by V. Masson-Delmotte, P. Zhai, A. Pirani, S. L. Connors, C. Péan, S. Berger, N. Caud, Y. Chen, L. Goldfarb, M. I. Gomis, M. Huang, K. Leitzell, E. Lonnoy, J. B. R. Matthews, T. K. Maycock, T. Waterfield, O. Yelekçi, R. Yu, and B. Zhou. Cambridge, United Kingdom and New York, NY, USA: Cambridge University Press, pp. 553–672. DOI: 10.1017/9781009157896.006.

Lee, S. and H.-k. Kim (2003). “The Dynamical Relationship between Subtropical and Eddy-Driven Jets”. In: *Journal of the Atmospheric Sciences* 60.12, pp. 1490–1503. ISSN: 1520-0469. DOI: 10.1175/1520-0469(2003)060<1490:tdrbsa>2.0.co;2.

Lelieveld, J., B. Bregman, F. Arnold, V. Bürger, P. J. Crutzen, H. Fischer, A. Waibel, P. Siegmund, and P. F. J. van Velthoven (1997). “Chemical perturbation of the lowermost stratosphere through exchange with the troposphere”. In: *Geophysical Research Letters* 24.5, pp. 603–606. ISSN: 1944-8007. DOI: 10.1029/97gl00255.

Lelieveld, J. and P. J. Crutzen (1994). “Role of Deep Cloud Convection in the Ozone Budget of the Troposphere”. In: *Science* 264.5166, pp. 1759–1761. ISSN: 1095-9203. DOI: 10.1126/science.264.5166.1759.

Lin, J.-L. (2007). “The Double-ITCZ Problem in IPCC AR4 Coupled GCMs: Ocean–Atmosphere Feedback Analysis”. In: *Journal of Climate* 20.18, pp. 4497–4525. ISSN: 0894-8755. DOI: 10.1175/jcli4272.1.

Loeb, N. G., D. R. Doelling, H. Wang, W. Su, C. Nguyen, J. G. Corbett, L. Liang, C. Mitrescu, F. G. Rose, and S. Kato (2018). “Clouds and the Earth’s Radiant Energy System (CERES) Energy Balanced and Filled (EBAF) Top-of-Atmosphere (TOA) Edition-4.0 Data Product”. In: *Journal of Climate* 31.2, pp. 895–918. ISSN: 1520-0442. DOI: 10.1175/jcli-d-17-0208.1.

Luhar, A. K., I. E. Galbally, M. T. Woodhouse, and N. L. Abraham (2021). “Assessing and improving cloud-height-based parameterisations of global lightning flash rate, and their impact on lightning-produced NOx and tropospheric composition in a chemistry-climate model”. In: *Atmospheric Chemistry and Physics* 21.9, pp. 7053–7082. ISSN: 1680-7324. DOI: 10.5194/acp-21-7053-2021.

Machenhauer, B. (1979). “The Spectral Method”. In: *Numerical Methods used in Atmospheric Models*. Vol. II. 17. GARP Publications. Chap. 3, pp. 121–275.

Maher, P., M. E. Kelleher, P. G. Sansom, and J. Methven (2019). “Is the subtropical jet shifting poleward?” In: *Climate Dynamics* 54.3–4, pp. 1741–1759. ISSN: 1432-0894. DOI: 10.1007/s00382-019-05084-6.

Manabe, S., J. Smagorinsky, and R. F. Strickler (1965). "SIMULATED CLIMATOLOGY OF A GENERAL CIRCULATION MODEL WITH A HYDROLOGIC CYCLE". In: *Monthly Weather Review* 93.12, pp. 769–798. ISSN: 1520-0493. DOI: 10.1175/1520-0493(1965)093<0769:scoagc>2.3.co;2.

Manabe, S. and R. T. Wetherald (1967). "Thermal Equilibrium of the Atmosphere with a Given Distribution of Relative Humidity". In: *Journal of the Atmospheric Sciences* 24.3, pp. 241–259. ISSN: 1520-0469. DOI: 10.1175/1520-0469(1967)024<0241:teotaw>2.0.co;2.

Manney, G. L. and M. I. Hegglin (2017). "Seasonal and Regional Variations of Long-Term Changes in Upper-Tropospheric Jets from Reanalyses". In: *Journal of Climate* 31.1, pp. 423–448. ISSN: 1520-0442. DOI: 10.1175/jcli-d-17-0303.1.

Manney, G. L., M. I. Hegglin, Z. D. Lawrence, K. Wargan, L. F. Millán, M. J. Schwartz, M. L. Santee, A. Lambert, S. Pawson, B. W. Knosp, R. A. Fuller, and W. H. Daffer (2017). "Reanalysis comparisons of upper tropospheric–lower stratospheric jets and multiple tropopauses". In: *Atmospheric Chemistry and Physics* 17.18, pp. 11541–11566. ISSN: 1680-7324. DOI: 10.5194/acp-17-11541-2017.

Marsh, D. R., J.-F. Lamarque, A. J. Conley, and L. M. Polvani (2016). "Stratospheric ozone chemistry feedbacks are not critical for the determination of climate sensitivity in CESM1(WACCM)". In: *Geophysical Research Letters* 43.8, pp. 3928–3934. ISSN: 1944-8007. DOI: 10.1002/2016gl068344.

Match, A. and E. P. Gerber (2025). "The Double Dip: How Tropospheric Expansion Counteracts Increases in Extratropical Stratospheric Ozone Under Global Warming". In: *Geophysical Research Letters* 52.9. ISSN: 1944-8007. DOI: 10.1029/2024gl112409.

Mauritsen, T., J. Bader, T. Becker, J. Behrens, M. Bittner, R. Brokopf, V. Brovkin, M. Claussen, T. Crueger, M. Esch, I. Fast, S. Fiedler, D. Fläschner, V. Gayler, M. Giorgetta, D. S. Goll, H. Haak, S. Hagemann, C. Hedemann, C. Hohenegger, T. Ilyina, T. Jahns, D. Jimenéz-de-la-Cuesta, J. Jungclaus, T. Kleinen, S. Kloster, D. Kracher, S. Kinne, D. Kleberg, G. Lasslop, L. Kornblueh, J. Marotzke, D. Matei, K. Meraner, U. Mikolajewicz, K. Modali, B. Möbis, W. A. Müller, J. E. M. S. Nabel, C. C. W. Nam, D. Notz, S.-S. Nyawira, H. Paulsen, K. Peters, R. Pincus, H. Pohlmann, J. Pongratz, M. Popp, T. J. Raddatz, S. Rast, R. Redler, C. H. Reick, T. Rohrschneider, V. Schemann, H. Schmidt, R. Schnur, U. Schulzweida, K. D. Six, L. Stein, I. Stemmler, B. Stevens, J.-S. von Storch, F. Tian, A. Voigt, P. Vrese, K.-H. Wieners, S. Wilkenskjeld, A. Winkler, and E. Roeckner (2019). "Developments in the MPI-M Earth System Model version 1.2 (MPI-ESM1.2) and Its Response to Increasing CO2". In: *Journal of Advances in Modeling Earth Systems* 11.4, pp. 998–1038. ISSN: 1942-2466. DOI: 10.1029/2018ms001400.

Mauritsen, T., B. Stevens, E. Roeckner, T. Crueger, M. Esch, M. Giorgetta, H. Haak, J. Jungclaus, D. Klocke, D. Matei, U. Mikolajewicz, D. Notz, R. Pincus, H. Schmidt, and L. Tomassini (2012). "Tuning the climate of a global model". In: *Journal of Advances in Modeling Earth Systems* 4.3. ISSN: 1942-2466. DOI: 10.1029/2012ms000154.

Meinshausen, M., S. C. B. Raper, and T. M. L. Wigley (2011a). "Emulating coupled atmosphere-ocean and carbon cycle models with a simpler model, MAGICC6 Part 1: Model description and calibration". In: *Atmospheric Chemistry and Physics* 11.4, pp. 1417–1456. ISSN: 1680-7324. DOI: 10.5194/acp-11-1417-2011.

Meinshausen, M., T. M. L. Wigley, and S. C. B. Raper (2011b). "Emulating atmosphere-ocean and carbon cycle models with a simpler model, MAGICC6 Part 2: Applications". In: *Atmo-*

spheric Chemistry and Physics 11.4, pp. 1457–1471. ISSN: 1680-7324. DOI: 10.5194/acp-11-1457-2011.

Meinshausen, M., Z. R. J. Nicholls, J. Lewis, M. J. Gidden, E. Vogel, M. Freund, U. Beyerle, C. Gessner, A. Nauels, N. Bauer, J. G. Canadell, J. S. Daniel, A. John, P. B. Krummel, G. Luderer, N. Meinshausen, S. A. Montzka, P. J. Rayner, S. Reimann, S. J. Smith, M. van den Berg, G. J. M. Velders, M. K. Vollmer, and R. H. J. Wang (2020). "The shared socio-economic pathway (SSP) greenhouse gas concentrations and their extensions to 2500". In: *Geoscientific Model Development* 13.8, pp. 3571–3605. ISSN: 1991-9603. DOI: 10.5194/gmd-13-3571-2020.

Meinshausen, M., E. Vogel, A. Nauels, K. Lorbacher, N. Meinshausen, D. M. Etheridge, P. J. Fraser, S. A. Montzka, P. J. Rayner, C. M. Trudinger, P. B. Krummel, U. Beyerle, J. G. Canadell, J. S. Daniel, I. G. Enting, R. M. Law, C. R. Lunder, S. O'Doherty, R. G. Prinn, S. Reimann, M. Rubino, G. J. M. Velders, M. K. Vollmer, R. H. J. Wang, and R. Weiss (2017). "Historical greenhouse gas concentrations for climate modelling (CMIP6)". In: *Geoscientific Model Development* 10.5, pp. 2057–2116. ISSN: 1991-9603. DOI: 10.5194/gmd-10-2057-2017.

Meng, L., J. Liu, D. W. Tarasick, W. J. Randel, A. K. Steiner, H. Wilhelmsen, L. Wang, and L. Haimberger (2021). "Continuous rise of the tropopause in the Northern Hemisphere over 1980–2020". In: *Science Advances* 7.45. ISSN: 2375-2548. DOI: 10.1126/sciadv.abi8065.

Messori, G., N. Harnik, E. Madonna, O. Lachmy, and D. Faranda (2021). "A dynamical systems characterization of atmospheric jet regimes". In: *Earth System Dynamics* 12.1, pp. 233–251. ISSN: 2190-4987. DOI: 10.5194/esd-12-233-2021.

Millan, L., L. Millán, P. Hoor, M. I. Hegglin, G. L. Manney, P. S. Jeffery, F. M. Weyland, T. Leblanc, K. A. Walker, H. Boenisch, D. Kunkel, I. Petropavlovskikh, and H. Ye (2025). "Ozone trends in the upper troposphere-lower stratosphere using equivalent latitude-potential temperature". In: DOI: 10.22541/essoar.175516869.91250011/v1.

Millán, L. F., P. Hoor, M. I. Hegglin, G. L. Manney, H. Boenisch, P. Jeffery, D. Kunkel, I. Petropavlovskikh, H. Ye, T. Leblanc, and K. Walker (2024). "Exploring ozone variability in the upper troposphere and lower stratosphere using dynamical coordinates". In: *Atmospheric Chemistry and Physics* 24.13, pp. 7927–7959. ISSN: 1680-7324. DOI: 10.5194/acp-24-7927-2024.

Morgenstern, O., M. I. Hegglin, E. Rozanov, F. M. O'Connor, N. L. Abraham, H. Akiyoshi, A. T. Archibald, S. Bekki, N. Butchart, M. P. Chipperfield, M. Deushi, S. S. Dhomse, R. R. Garcia, S. C. Hardiman, L. W. Horowitz, P. Jöckel, B. Josse, D. Kinnison, M. Lin, E. Mancini, M. E. Manyin, M. Marchand, V. Marécal, M. Michou, L. D. Oman, G. Pitari, D. A. Plummer, L. E. Revell, D. Saint-Martin, R. Schofield, A. Stenke, K. Stone, K. Sudo, T. Y. Tanaka, S. Tilmes, Y. Yamashita, K. Yoshida, and G. Zeng (2017). "Review of the global models used within phase 1 of the Chemistry–Climate Model Initiative (CCMI)". In: *Geoscientific Model Development* 10.2, pp. 639–671. ISSN: 1991-9603. DOI: 10.5194/gmd-10-639-2017.

Morgenstern, O., K. A. Stone, R. Schofield, H. Akiyoshi, Y. Yamashita, D. E. Kinnison, R. R. Garcia, K. Sudo, D. A. Plummer, J. Scinocca, L. D. Oman, M. E. Manyin, G. Zeng, E. Rozanov, A. Stenke, L. E. Revell, G. Pitari, E. Mancini, G. Di Genova, D. Visioni, S. S. Dhomse, and M. P. Chipperfield (2018). "Ozone sensitivity to varying greenhouse gases and ozone-depleting substances in CCMI-1 simulations". In: *Atmospheric Chemistry and Physics* 18.2, pp. 1091–1114. ISSN: 1680-7324. DOI: 10.5194/acp-18-1091-2018.

Mote, P. W., K. H. Rosenlof, M. E. McIntyre, E. S. Carr, J. C. Gille, J. R. Holton, J. S. Kinnersley, H. C. Pumphrey, J. M. Russell, and J. W. Waters (1996). “An atmospheric tape recorder: The imprint of tropical tropopause temperatures on stratospheric water vapor”. In: *Journal of Geophysical Research: Atmospheres* 101.D2, pp. 3989–4006. ISSN: 0148-0227. DOI: 10.1029/95jd03422.

Müller, W. A., J. H. Jungclaus, T. Mauritsen, J. Baehr, M. Bittner, R. Budich, F. Bunzel, M. Esch, R. Ghosh, H. Haak, T. Ilyina, T. Kleine, L. Kornblueh, H. Li, K. Modali, D. Notz, H. Pohlmann, E. Roeckner, I. Stemmler, F. Tian, and J. Marotzke (2018). “A Higher-resolution Version of the Max Planck Institute Earth System Model (MPI-ESM1.2-HR)”. In: *Journal of Advances in Modeling Earth Systems* 10.7, pp. 1383–1413. ISSN: 1942-2466. DOI: 10.1029/2017ms001217.

Murphy, D. M. and T. Koop (2005). “Review of the vapour pressures of ice and supercooled water for atmospheric applications”. In: *Quarterly Journal of the Royal Meteorological Society* 131.608, pp. 1539–1565. ISSN: 1477-870X. DOI: 10.1256/qj.04.94.

Neu, J. L., T. Flury, G. L. Manney, M. L. Santee, N. J. Livesey, and J. Worden (2014). “Tropospheric ozone variations governed by changes in stratospheric circulation”. In: *Nature Geoscience* 7.5, pp. 340–344. ISSN: 1752-0908. DOI: 10.1038/ngeo2138.

Nordeng, T.-E. (1994). *Extended versions of the convective parametrization scheme at ECMWF and their impact on the mean and transient activity of the model in the tropics*. Tech. rep. DOI: 10.21957/E34XWHYSW.

Nowack, P. J., N. Luke Abraham, A. C. Maycock, P. Braesicke, J. M. Gregory, M. M. Joshi, A. Osprey, and J. A. Pyle (2014). “A large ozone-circulation feedback and its implications for global warming assessments”. In: *Nature Climate Change* 5.1, pp. 41–45. ISSN: 1758-6798. DOI: 10.1038/nclimate2451.

Nützel, M., L. Stecher, P. Jöckel, F. Winterstein, M. Dameris, M. Ponater, P. Graf, and M. Kunze (2024). “Updating the radiation infrastructure in MESSy (based on MESSy version 2.55)”. In: *Geoscientific Model Development* 17.15, pp. 5821–5849. ISSN: 1991-9603. DOI: 10.5194/gmd-17-5821-2024.

Oberländer-Hayn, S., E. P. Gerber, J. Abalichin, H. Akiyoshi, A. Kerschbaumer, A. Kubin, M. Kunze, U. Langematz, S. Meul, M. Michou, O. Morgenstern, and L. D. Oman (2016). “Is the Brewer-Dobson circulation increasing or moving upward?” In: *Geophysical Research Letters* 43.4, pp. 1772–1779. ISSN: 1944-8007. DOI: 10.1002/2015gl067545.

Orbe, C., D. A. Plummer, D. W. Waugh, H. Yang, P. Jöckel, D. E. Kinnison, B. Josse, V. Marecal, M. Deushi, N. L. Abraham, A. T. Archibald, M. P. Chipperfield, S. Dhomse, W. Feng, and S. Bekki (2020). “Description and Evaluation of the specified-dynamics experiment in the Chemistry-Climate Model Initiative”. In: *Atmospheric Chemistry and Physics* 20.6, pp. 3809–3840. ISSN: 1680-7324. DOI: 10.5194/acp-20-3809-2020.

Orbe, C., D. W. Waugh, H. Yang, J.-F. Lamarque, S. Tilmes, and D. E. Kinnison (2017). “Tropospheric transport differences between models using the same large-scale meteorological fields”. In: *Geophysical Research Letters* 44.2, pp. 1068–1078. ISSN: 1944-8007. DOI: 10.1002/2016gl071339.

Orbe, C., H. Yang, D. W. Waugh, G. Zeng, O. Morgenstern, D. E. Kinnison, J.-F. Lamarque, S. Tilmes, D. A. Plummer, J. F. Scinocca, B. Josse, V. Marecal, P. Jöckel, L. D. Oman, S. E. Strahan, M. Deushi, T. Y. Tanaka, K. Yoshida, H. Akiyoshi, Y. Yamashita, A. Stenke, L. Revell, T. Sukhodolov, E. Rozanov, G. Pitari, D. Visioni, K. A. Stone, R. Schofield, and A. Banerjee (2018). “Large-scale tropospheric transport in the Chemistry–Climate Model

Initiative (CCMI) simulations”. In: *Atmospheric Chemistry and Physics* 18.10, pp. 7217–7235. ISSN: 1680-7324. DOI: 10.5194/acp-18-7217-2018.

Ozone-Secretariat (2020). *Handbook for the Montreal Protocolon Substances that Deplete the Ozone Layer*. Ed. by T. S. for the Vienna Convention for the Protection of the Ozone Layer and for the Montreal Protocol on Substances that Deplete the Ozone Layer. 14th ed. Nairobi, Kenya: United Nations Environment Programme. ISBN: 978-9966-076-79-3. URL: https://ozone.unep.org/sites/default/files/Handbooks/MP-Handbook-2020-English.pdf.

Pan, L. L., W. J. Randel, B. L. Gary, M. J. Mahoney, and E. J. Hintsa (2004). “Definitions and sharpness of the extratropical tropopause: A trace gas perspective”. In: *Journal of Geophysical Research: Atmospheres* 109.D23. ISSN: 0148-0227. DOI: 10.1029/2004jd004982.

Pan, L. L., W. J. Randel, J. C. Gille, W. D. Hall, B. Nardi, S. Massie, V. Yudin, R. Khosravi, P. Konopka, and D. Tarasick (2009). “Tropospheric intrusions associated with the secondary tropopause”. In: *Journal of Geophysical Research: Atmospheres* 114.D10. ISSN: 0148-0227. DOI: 10.1029/2008jd011374.

Pierrehumbert, R. T. (2010). *Principles of planetary climate*. Cambridge: Cambridge University Press. 1652 pp. ISBN: 9780521865562.

Pincus, R. and B. Stevens (2013). “Paths to accuracy for radiation parameterizations in atmospheric models”. In: *Journal of Advances in Modeling Earth Systems* 5.2, pp. 225–233. ISSN: 1942-2466. DOI: 10.1002/jame.20027.

Plöger, F. and H. Garny (2022). “Hemispheric asymmetries in recent changes in the stratospheric circulation”. In: *Atmospheric Chemistry and Physics* 22.8, pp. 5559–5576. ISSN: 1680-7324. DOI: 10.5194/acp-22-5559-2022.

Plummer, D., T. Nagashima, S. Tilmes, A. Archibald, G. Chiodo, S. Fadnavis, H. Garny, B. Josse, J. Kim, J.-F. Lamarque, O. Morgenstern, L. Murray, C. Orbe, A. Tai, M. Chipperfield, B. Funke, M. Juckes, D. Kinnison, M. Kunze, B. Luo, K. Matthes, P. A. Newman, C. Pascoe, and T. Peter (2021). “CCMI2022: a new set of Chemistry-Climate Model Initiative (CCMI) community simulations to update theassessment of models and support upcoming ozone assessment activities”. In: *SPARC Newsletter* 57, pp. 22–30. ISSN: 1245-4680. eprint: https://www.aparc-climate.org/wp-content/uploads/2021/07/SPARCnewsletter_Jul2021_web.pdf. URL: https://blogs.reading.ac.uk/ccmi/ccmi-2022/.

Poluianov, S. V., G. A. Kovaltsov, A. L. Mishev, and I. G. Usoskin (2016). “Production of cosmogenic isotopes 7Be, 10Be, 14C, 22Na, and 36Cl in the atmosphere: Altitudinal profiles of yield functions”. In: *Journal of Geophysical Research: Atmospheres* 121.13, pp. 8125–8136. ISSN: 2169-8996. DOI: 10.1002/2016jd025034.

Polvani, L. M., J. Keeble, A. Banerjee, R. Checa-Garcia, G. Chiodo, H. E. Rieder, and K. H. Rosenlof (2023). “No evidence of worsening Arctic springtime ozone losses over the 21st century”. In: *Nature Communications* 14.1. ISSN: 2041-1723. DOI: 10.1038/s41467-023-37134-3.

Polvani, L. M., L. Wang, M. Abalos, N. Butchart, M. P. Chipperfield, M. Dameris, M. Deushi, S. S. Dhomse, P. Jöckel, D. Kinnison, M. Michou, O. Morgenstern, L. D. Oman, D. A. Plummer, and K. A. Stone (2019). “Large Impacts, Past and Future, of Ozone-Depleting Substances on Brewer-Dobson Circulation Trends: A Multimodel Assessment”. In: *Journal of Geophysical Research: Atmospheres* 124.13, pp. 6669–6680. ISSN: 2169-8996. DOI: 10.1029/2018jd029516.

Pöschl, U., R. von Kuhlmann, N. Poisson, and P. J. Crutzen (2000). “Development and Intercomparison of Condensed Isoprene Oxidation Mechanismsfor Global Atmospheric Modeling”. In: *Journal of Atmospheric Chemistry* 37.1, pp. 29–52. ISSN: 0167-7764. DOI: 10.1023/a:1006391009798.

Pozzer, A., P. Jöckel, R. Sander, J. Williams, L. Ganzeveld, and J. Lelieveld (2006). “Technical Note: The MESSy-submodel AIRSEA calculating the air-sea exchange of chemical species”. In: *Atmospheric Chemistry and Physics* 6.12, pp. 5435–5444. ISSN: 1680-7324. DOI: 10.5194/acp-6-5435-2006.

Prather, M. J. (2025). “Calibrating the Tropospheric Air and Ozone Mass”. In: *AGU Advances* 6.3. ISSN: 2576-604X. DOI: 10.1029/2025av001651.

Prather, M. J., C. D. Holmes, and J. Hsu (2012). “Reactive greenhouse gas scenarios: Systematic exploration of uncertainties and the role of atmospheric chemistry”. In: *Geophysical Research Letters* 39.9. ISSN: 1944-8007. DOI: 10.1029/2012gl051440.

Price, C., J. Penner, and M. Prather (1997). “NOx from lightning: 1. Global distribution based on lightning physics”. In: *Journal of Geophysical Research: Atmospheres* 102.D5, pp. 5929–5941. ISSN: 0148-0227. DOI: 10.1029/96jd03504.

Price, C. and D. Rind (1992). “A simple lightning parameterization for calculating global lightning distributions”. In: *Journal of Geophysical Research: Atmospheres* 97.D9, pp. 9919–9933. ISSN: 0148-0227. DOI: 10.1029/92jd00719.

Pringle, K. J., H. Tost, S. Message, B. Steil, D. Giannadaki, A. Nenes, C. Fountoukis, P. Stier, E. Vignati, and J. Lelieveld (2010). “Description and evaluation of GMXe: a new aerosol submodel for global simulations (v1)”. In: *Geoscientific Model Development* 3.2, pp. 391–412. ISSN: 1991-9603. DOI: 10.5194/gmd-3-391-2010.

Ramaswamy, V., M.-L. Chanin, J. Angell, J. Barnett, D. Gaffen, M. Gelman, P. Keckhut, Y. Koshelkov, K. Labitzke, J.-J. R. Lin, A. O’Neill, J. Nash, W. Randel, R. Rood, K. Shine, M. Shiotani, and R. Swinbank (2001). “Stratospheric temperature trends: Observations and model simulations”. In: *Reviews of Geophysics* 39.1, pp. 71–122. ISSN: 1944-9208. DOI: 10.1029/1999rg000065.

Ramaswamy, V. and M. D. Schwarzkopf (2002). “Effects of ozone and well-mixed gases on annual-mean stratospheric temperature trends”. In: *Geophysical Research Letters* 29.22. ISSN: 1944-8007. DOI: 10.1029/2002gl015141.

Randall, D., M. Khairoutdinov, A. Arakawa, and W. Grabowski (2003). “Breaking the Cloud Parameterization Deadlock”. In: *Bulletin of the American Meteorological Society* 84.11, pp. 1547–1564. ISSN: 1520-0477. DOI: 10.1175/bams-84-11-1547.

Randel, W. J. and E. J. Jensen (2013). “Physical processes in the tropical tropopause layer and their roles in a changing climate”. In: *Nature Geoscience* 6.3, pp. 169–176. ISSN: 1752-0908. DOI: 10.1038/ngeo1733.

Raymond, D. J. and A. M. Blyth (1992). “Extension of the Stochastic Mixing Model to Cumulonimbus Clouds”. In: *Journal of the Atmospheric Sciences* 49.21, pp. 1968–1983. ISSN: 1520-0469. DOI: 10.1175/1520-0469(1992)049<1968:eotsmm>2.0.co;2.

Raymond, D. J. and A. M. Blyth (1986). “A Stochastic Mixing Model for Nonprecipitating Cumulus Clouds”. In: *Journal of the Atmospheric Sciences* 43.22, pp. 2708–2718. ISSN: 1520-0469. DOI: 10.1175/1520-0469(1986)043<2708:asmmfn>2.0.co;2.

Reed, R. J. (1955). “A STUDY OF A CHARACTERISTIC TPYE OF UPPER-LEVEL FRONTOGENESIS”. In: *Journal of Meteorology* 12.3, pp. 226–237. ISSN: 0095-9634. DOI: 10.1175/1520-0469(1955)012<0226:asoact>2.0.co;2.

Reichler, T., M. Dameris, and R. Sausen (2003). “Determining the tropopause height from gridded data”. In: *Geophysical Research Letters* 30.20. ISSN: 1944-8007. DOI: 10.1029/2003gl018240.

Reutter, P. and P. Spichtinger (2025). “The frosty frontier: redefining the mid-latitude tropopause using the relative humidity over ice”. In: *Atmospheric Chemistry and Physics* 25.22, pp. 16303–16314. ISSN: 1680-7324. DOI: 10.5194/acp-25-16303-2025.

Richter, J. H., A. Solomon, and J. T. Bacmeister (2014). “Effects of vertical resolution and nonorographic gravity wave drag on the simulated climate in the Community Atmosphere Model, version 5”. In: *Journal of Advances in Modeling Earth Systems* 6.2, pp. 357–383. ISSN: 1942-2466. DOI: 10.1002/2013ms000303.

Riddaway, R. W. and M. Hortal (2002). *Numerical methods*. eng. URL: https://www.ecmwf.int/en/elibrary/79880-numerical-methods.

Riese, M., F. Ploeger, A. Rap, B. Vogel, P. Konopka, M. Dameris, and P. Forster (2012). “Impact of uncertainties in atmospheric mixing on simulated UTLS composition and related radiative effects”. In: *Journal of Geophysical Research: Atmospheres* 117.D16. ISSN: 0148-0227. DOI: 10.1029/2012jd017751.

Righi, M., J. Hendricks, U. Lohmann, C. G. Beer, V. Hahn, B. Heinold, R. Heller, M. Krämer, M. Ponater, C. Rolf, I. Tegen, and C. Voigt (2020). “Coupling aerosols to (cirrus) clouds in the global EMAC-MADE3 aerosol–climate model”. In: *Geoscientific Model Development* 13.3, pp. 1635–1661. ISSN: 1991-9603. DOI: 10.5194/gmd-13-1635-2020.

Rio, C., A. D. Del Genio, and F. Hourdin (2019). “Ongoing Breakthroughs in Convective Parameterization”. In: *Current Climate Change Reports* 5.2, pp. 95–111. ISSN: 2198-6061. DOI: 10.1007/s40641-019-00127-w.

Roeckner, E., G. Bäuml, L. Bonaventura, R. Brokopf, M. Esch, M. Giorgetta, S. Hagemann, I. Kirchner, L. Kornblueh, E. Manzini, A. Rhodin, U. Schlese, U. Schulzweida, and A. Tompkins (2003). *The atmospheric general circulation model ECHAM5. Part1: Model description*. MPI-Report 349. Max Planck Institute for Meteorology. URL: https://pure.mpg.de/rest/items/item_995269_2/component/file_995268/content.

Roeckner, E., R. Brokopf, M. Esch, M. Giorgetta, S. Hagemann, L. Kornblueh, E. Manzini, U. Schlese, and U. Schulzweida (2004). *The atmospheric general circulation model ECHAM5. Part2: Sensitivity of Simulated Climate toHorizontal and Vertical Resolution*. MPI-Report 354. Max Planck Institute for Meteorology. URL: https://pure.mpg.de/rest/items/item_995221_12/component/file_995220/content.

Rolf, C., B. Vogel, P. Hoor, A. Afchine, G. Günther, M. Krämer, R. Müller, S. Müller, N. Spelten, and M. Riese (2018). “Water vapor increase in the lower stratosphere of the Northern Hemisphere due to the Asian monsoon anticyclone observed during the TACTS/ESMVal campaigns”. In: *Atmospheric Chemistry and Physics* 18.4, pp. 2973–2983. ISSN: 1680-7324. DOI: 10.5194/acp-18-2973-2018.

Rosenlof, K. H., A. F. Tuck, K. K. Kelly, J. M. Russell, and M. P. McCormick (1997). “Hemispheric asymmetries in water vapor and inferences about transport in the lower stratosphere”. In: *Journal of Geophysical Research: Atmospheres* 102.D11, pp. 13213–13234. ISSN: 0148-0227. DOI: 10.1029/97jd00873.

Rybka, H. and H. Tost (2014). “Uncertainties in future climate predictions due to convection parameterisations”. In: *Atmospheric Chemistry and Physics* 14.11, pp. 5561–5576. ISSN: 1680-7324. DOI: 10.5194/acp-14-5561-2014.

Rybka, H. and H. Tost (2020). "Superparameterised cloud effects in the EMAC general circulation model (v2.50) – influences of model configuration". In: *Geoscientific Model Development* 13.6, pp. 2671–2694. ISSN: 1991-9603. DOI: `10.5194/gmd-13-2671-2020`.

Sander, R., P. Jöckel, O. Kirner, A. T. Kunert, J. Landgraf, and A. Pozzer (2014). "The photolysis module JVAL-14, compatible with the MESSy standard, and the JVal PreProcessor (JVPP)". In: *Geoscientific Model Development* 7.6, pp. 2653–2662. ISSN: 1991-9603. DOI: `10.5194/gmd-7-2653-2014`.

Sander, R., A. Baumgaertner, D. Cabrera-Perez, F. Frank, S. Gromov, J.-U. Grooß, H. Harder, V. Huijnen, P. Jöckel, V. A. Karydis, K. E. Niemeyer, A. Pozzer, H. Riede, M. G. Schultz, D. Taraborrelli, and S. Tauer (2019). "The community atmospheric chemistry box model CAABA/MECCA-4.0". In: *Geoscientific Model Development* 12.4, pp. 1365–1385. ISSN: 1991-9603. DOI: `10.5194/gmd-12-1365-2019`.

Santer, B. D., S. Po-Chedley, L. Zhao, C.-Z. Zou, Q. Fu, S. Solomon, D. W. J. Thompson, C. Mears, and K. E. Taylor (2023). "Exceptional stratospheric contribution to human fingerprints on atmospheric temperature". In: *Proceedings of the National Academy of Sciences* 120.20. ISSN: 1091-6490. DOI: `10.1073/pnas.2300758120`.

Satoh, M., B. Stevens, F. Judt, M. Khairoutdinov, S.-J. Lin, W. M. Putman, and P. Düben (2019). "Global Cloud-Resolving Models". In: *Current Climate Change Reports* 5.3, pp. 172–184. ISSN: 2198-6061. DOI: `10.1007/s40641-019-00131-0`.

Saunois, M., A. R. Stavert, B. Poulter, P. Bousquet, J. G. Canadell, R. B. Jackson, P. A. Raymond, E. J. Dlugokencky, S. Houweling, P. K. Patra, P. Ciais, V. K. Arora, D. Bastviken, P. Bergamaschi, D. R. Blake, G. Brailsford, L. Bruhwiler, K. M. Carlson, M. Carrol, S. Castaldi, N. Chandra, C. Crevoisier, P. M. Crill, K. Covey, C. L. Curry, G. Etiope, C. Frankenberg, N. Gedney, M. I. Hegglin, L. Höglund-Isaksson, G. Hugelius, M. Ishizawa, A. Ito, G. Janssens-Maenhout, K. M. Jensen, F. Joos, T. Kleinen, P. B. Krummel, R. L. Langenfelds, G. G. Laruelle, L. Liu, T. Machida, S. Maksyutov, K. C. McDonald, J. McNorton, P. A. Miller, J. R. Melton, I. Morino, J. Müller, F. Murguia-Flores, V. Naik, Y. Niwa, S. Noce, S. O'Doherty, R. J. Parker, C. Peng, S. Peng, G. P. Peters, C. Prigent, R. Prinn, M. Ramonet, P. Regnier, W. J. Riley, J. A. Rosentreter, A. Segers, I. J. Simpson, H. Shi, S. J. Smith, L. P. Steele, B. F. Thornton, H. Tian, Y. Tohjima, F. N. Tubiello, A. Tsuruta, N. Viovy, A. Voulgarakis, T. S. Weber, M. van Weele, G. R. van der Werf, R. F. Weiss, D. Worthy, D. Wunch, Y. Yin, Y. Yoshida, W. Zhang, Z. Zhang, Y. Zhao, B. Zheng, Q. Zhu, Q. Zhu, and Q. Zhuang (2020). "The Global Methane Budget 2000–2017". In: *Earth System Science Data* 12.3, pp. 1561–1623. ISSN: 1866-3516. DOI: `10.5194/essd-12-1561-2020`.

Savazzi, A. C. M., C. Jakob, and A. P. Siebesma (2021). "Convective Mass-Flux From Long Term Radar Reflectivities Over Darwin, Australia". In: *Journal of Geophysical Research: Atmospheres* 126.19. ISSN: 2169-8996. DOI: `10.1029/2021jd034910`.

Schmidt, A., M. J. Mills, S. Ghan, J. M. Gregory, R. P. Allan, T. Andrews, C. G. Bardeen, A. Conley, P. M. Forster, A. Gettelman, R. W. Portmann, S. Solomon, and O. B. Toon (2018). "Volcanic Radiative Forcing From 1979 to 2015". In: *Journal of Geophysical Research: Atmospheres* 123.22, pp. 12491–12508. ISSN: 2169-8996. DOI: `10.1029/2018jd028776`.

Schmidt, G. A., D. Bader, L. J. Donner, G. S. Elsaesser, J.-C. Golaz, C. Hannay, A. Molod, R. B. Neale, and S. Saha (2017). "Practice and philosophy of climate model tuning across six US modeling centers". In: *Geoscientific Model Development* 10.9, pp. 3207–3223. ISSN: 1991-9603. DOI: `10.5194/gmd-10-3207-2017`.

Schneider, T. (2004). “The Tropopause and the Thermal Stratification in the Extratropics of a Dry Atmosphere”. In: *Journal of the Atmospheric Sciences* 61.12, pp. 1317–1340. ISSN: 1520-0469. DOI: 10.1175/1520-0469(2004)061<1317:ttatts>2.0.co;2.

Schneider, T. (2006). “The General Circulation of the Atmosphere”. In: *Annual Review of Earth and Planetary Sciences* 34.1, pp. 655–688. ISSN: 1545-4495. DOI: 10.1146/annurev.earth.34.031405.125144.

Schneider, T., S. Lan, A. Stuart, and J. Teixeira (2017). “Earth System Modeling 2.0: A Blueprint for Models That Learn From Observations and Targeted High-Resolution Simulations”. In: *Geophysical Research Letters* 44.24. ISSN: 1944-8007. DOI: 10.1002/2017gl076101.

Schoeberl, M. R., E. J. Jensen, L. Pfister, R. Ueyama, M. Avery, and A. E. Dessler (2018). “Convective Hydration of the Upper Troposphere and Lower Stratosphere”. In: *Journal of Geophysical Research: Atmospheres* 123.9, pp. 4583–4593. ISSN: 2169-8996. DOI: 10.1029/2018jd028286.

Schuckmann, K. von, A. Minière, F. Gues, F. J. Cuesta-Valero, G. Kirchengast, S. Adusumilli, F. Straneo, M. Ablain, R. P. Allan, P. M. Barker, H. Beltrami, A. Blazquez, T. Boyer, L. Cheng, J. Church, D. Desbruyeres, H. Dolman, C. M. Domingues, A. García-García, D. Giglio, J. E. Gilson, M. Gorfer, L. Haimberger, M. Z. Hakuba, S. Hendricks, S. Hosoda, G. C. Johnson, R. Killick, B. King, N. Kolodziejczyk, A. Korosov, G. Krinner, M. Kuusela, F. W. Landerer, M. Langer, T. Lavergne, I. Lawrence, Y. Li, J. Lyman, F. Marti, B. Marzeion, M. Mayer, A. H. MacDougall, T. McDougall, D. P. Monselesan, J. Nitzbon, I. Otosaka, J. Peng, S. Purkey, D. Roemmich, K. Sato, K. Sato, A. Savita, A. Schweiger, A. Shepherd, S. I. Seneviratne, L. Simons, D. A. Slater, T. Slater, A. K. Steiner, T. Suga, T. Szekely, W. Thiery, M.-L. Timmermans, I. Vanderkelen, S. E. Wjiffels, T. Wu, and M. Zemp (2023). “Heat stored in the Earth system 1960–2020: where does the energy go?” In: *Earth System Science Data* 15.4, pp. 1675–1709. ISSN: 1866-3516. DOI: 10.5194/essd-15-1675-2023.

Schumann, U. and H. Huntrieser (2007). “The global lightning-induced nitrogen oxides source”. In: *Atmospheric Chemistry and Physics* 7.14, pp. 3823–3907. ISSN: 1680-7324. DOI: 10.5194/acp-7-3823-2007.

Seidel, D. J., Q. Fu, W. J. Randel, and T. J. Reichler (2007). “Widening of the tropical belt in a changing climate”. In: *Nature Geoscience* 1.1, pp. 21–24. ISSN: 1752-0908. DOI: 10.1038/ngeo.2007.38.

Seidel, D. J. and W. J. Randel (2006). “Variability and trends in the global tropopause estimated from radiosonde data”. In: *Journal of Geophysical Research: Atmospheres* 111.D21. ISSN: 0148-0227. DOI: 10.1029/2006jd007363.

Seinfeld, J. H. and S. N. Pandis (2016). *Atmospheric Chemistry and Physics. From Air Pollution to Climate Change*. 3rd ed. New York Academy of Sciences Series. John Wiley & Sons, Incorporated. 11149 pp. ISBN: 9781119221166.

Semmler, T., S. Danilov, P. Gierz, H. F. Goessling, J. Hegewald, C. Hinrichs, N. Koldunov, N. Khosravi, L. Mu, T. Rackow, D. V. Sein, D. Sidorenko, Q. Wang, and T. Jung (2020). “Simulations for CMIP6 With the AWI Climate Model AWI-CM-1-1”. In: *Journal of Advances in Modeling Earth Systems* 12.9. ISSN: 1942-2466. DOI: 10.1029/2019ms002009.

Shepherd, T. G. (2007). “Transport in the Middle Atmosphere”. In: *Journal of the Meteorological Society of Japan. Ser. II* 85B.0, pp. 165–191. ISSN: 2186-9057. DOI: 10.2151/jmsj.85b.165.

Shepherd, T. G. (2014). “Atmospheric circulation as a source of uncertainty in climate change projections”. In: *Nature Geoscience* 7.10, pp. 703–708. ISSN: 1752-0908. DOI: 10.1038/ngeo2253.

Shepherd, T. G. and C. McLandress (2011). “A Robust Mechanism for Strengthening of the Brewer–Dobson Circulation in Response to Climate Change: Critical-Layer Control of Subtropical Wave Breaking”. In: *Journal of the Atmospheric Sciences* 68.4, pp. 784–797. ISSN: 1520-0469. DOI: 10.1175/2010jas3608.1.

Sherwood, S. C., S. Bony, and J.-L. Dufresne (2014). “Spread in model climate sensitivity traced to atmospheric convective mixing”. In: *Nature* 505.7481, pp. 37–42. ISSN: 1476-4687. DOI: 10.1038/nature12829.

Shine, K. P., M. S. Bourqui, P. M. d. F. Forster, S. H. E. Hare, U. Langematz, P. Braesicke, V. Grewe, M. Ponater, C. Schnadt, C. A. Smith, J. D. Haigh, J. Austin, N. Butchart, D. T. Shindell, W. J. Randel, T. Nagashima, R. W. Portmann, S. Solomon, D. J. Seidel, J. Lanzante, S. Klein, V. Ramaswamy, and M. D. Schwarzkopf (2003). “A comparison of model-simulated trends in stratospheric temperatures”. In: *Quarterly Journal of the Royal Meteorological Society* 129.590, pp. 1565–1588. ISSN: 1477-870X. DOI: 10.1256/qj.02.186.

Smalley, K. M., A. E. Dessler, S. Bekki, M. Deushi, M. Marchand, O. Morgenstern, D. A. Plummer, K. Shibata, Y. Yamashita, and G. Zeng (2017). “Contribution of different processes to changes in tropical lower-stratospheric water vapor in chemistry–climate models”. In: *Atmospheric Chemistry and Physics* 17.13, pp. 8031–8044. ISSN: 1680-7324. DOI: 10.5194/acp-17-8031-2017.

Soden, B. J., I. M. Held, R. Colman, K. M. Shell, J. T. Kiehl, and C. A. Shields (2008). “Quantifying Climate Feedbacks Using Radiative Kernels”. In: *Journal of Climate* 21.14, pp. 3504–3520. ISSN: 0894-8755. DOI: 10.1175/2007jcli2110.1.

Solomon, S., K. H. Rosenlof, R. W. Portmann, J. S. Daniel, S. M. Davis, T. J. Sanford, and G.-K. Plattner (2010). “Contributions of Stratospheric Water Vapor to Decadal Changes in the Rate of Global Warming”. In: *Science* 327.5970, pp. 1219–1223. ISSN: 1095-9203. DOI: 10.1126/science.1182488.

SPARC (2010). *SPARC CCMVal Report on the Evaluation of Chemistry-Climate Models*. Tech. rep. SPARC Report No. 5. SPARC (Stratosphere-troposphere Processes and their Role in Climate). URL: http://www.sparc-climate.org/publications/.

SPARC (2013). *SPARC Report on the Lifetimes of Stratospheric Ozone-Depleting Substances, Their Replacements, and Related Species*. Tech. rep. SPARC Report No. 6. SPARC. URL: http://www.aparc-climate.org/publications/.

Spichtinger, P., K. Gierens, and H. Wernli (2005). “A case study on the formation and evolution of ice supersaturation in the vicinity of a warm conveyor belt’s outflow region”. In: *Atmospheric Chemistry and Physics* 5.4, pp. 973–987. ISSN: 1680-7324. DOI: 10.5194/acp-5-973-2005.

Staten, P. W., J. Lu, K. M. Grise, S. M. Davis, and T. Birner (2018). “Re-examining tropical expansion”. In: *Nature Climate Change* 8.9, pp. 768–775. ISSN: 1758-6798. DOI: 10.1038/s41558-018-0246-2.

Steiner, A. K., F. Ladstädter, W. J. Randel, A. C. Maycock, Q. Fu, C. Claud, H. Gleisner, L. Haimberger, S.-P. Ho, P. Keckhut, T. Leblanc, C. Mears, L. M. Polvani, B. D. Santer, T. Schmidt, V. Sofieva, R. Wing, and C.-Z. Zou (2020). “Observed Temperature Changes in the Troposphere and Stratosphere from 1979 to 2018”. In: *Journal of Climate* 33.19, pp. 8165–8194. ISSN: 1520-0442. DOI: 10.1175/jcli-d-19-0998.1.

Stengel, M., S. Stapelberg, O. Sus, C. Schlundt, C. Poulsen, G. Thomas, M. Christensen, C. Carbajal Henken, R. Preusker, J. Fischer, A. Devasthale, U. Willén, K.-G. Karlsson, G. R. McGarragh, S. Proud, A. C. Povey, R. G. Grainger, J. F. Meirink, A. Feofilov, R. Bennartz, J. S. Bojanowski, and R. Hollmann (2017). "Cloud property datasets retrieved from AVHRR, MODIS, AATSR and MERIS in the framework of the Cloud_cci project". In: *Earth System Science Data* 9.2, pp. 881–904. ISSN: 1866-3516. DOI: 10.5194/essd-9-881-2017.

Stenke, A., V. Grewe, and M. Ponater (2007). "Lagrangian transport of water vapor and cloud water in the ECHAM4 GCM and its impact on the cold bias". In: *Climate Dynamics* 31.5, pp. 491–506. ISSN: 1432-0894. DOI: 10.1007/s00382-007-0347-5.

Tebaldi, C., K. Debeire, V. Eyring, E. Fischer, J. Fyfe, P. Friedlingstein, R. Knutti, J. Lowe, B. O'Neill, B. Sanderson, D. van Vuuren, K. Riahi, M. Meinshausen, Z. Nicholls, K. B. Tokarska, G. Hurtt, E. Kriegler, J.-F. Lamarque, G. Meehl, R. Moss, S. E. Bauer, O. Boucher, V. Brovkin, Y.-H. Byun, M. Dix, S. Gualdi, H. Guo, J. G. John, S. Kharin, Y. Kim, T. Koshiro, L. Ma, D. Olivié, S. Panickal, F. Qiao, X. Rong, N. Rosenbloom, M. Schupfner, R. Séférian, A. Sellar, T. Semmler, X. Shi, Z. Song, C. Steger, R. Stouffer, N. Swart, K. Tachiiri, Q. Tang, H. Tatebe, A. Voldoire, E. Volodin, K. Wyser, X. Xin, S. Yang, Y. Yu, and T. Ziehn (2021). "Climate model projections from the Scenario Model Intercomparison Project (ScenarioMIP) of CMIP6". In: *Earth System Dynamics* 12.1, pp. 253–293. ISSN: 2190-4987. DOI: 10.5194/esd-12-253-2021.

Tegtmeier, S., M. I. Hegglin, J. Anderson, A. Bourassa, S. Brohede, D. Degenstein, L. Froidevaux, R. Fuller, B. Funke, J. Gille, A. Jones, Y. Kasai, K. Krüger, E. Kyrölä, G. Lingenfelser, J. Lumpe, B. Nardi, J. Neu, D. Pendlebury, E. Remsberg, A. Rozanov, L. Smith, M. Toohey, J. Urban, T. von Clarmann, K. A. Walker, and R. H. J. Wang (2013). "SPARC Data Initiative: A comparison of ozone climatologies from international satellite limb sounders". In: *Journal of Geophysical Research: Atmospheres* 118.21. ISSN: 2169-8996. DOI: 10.1002/2013jd019877.

Tegtmeier, S., J. Anstey, S. Davis, R. Dragani, Y. Harada, I. Ivanciu, R. Pilch Kedzierski, K. Krüger, B. Legras, C. Long, J. S. Wang, K. Wargan, and J. S. Wright (2020). "Temperature and tropopause characteristics from reanalyses data in the tropical tropopause layer". In: *Atmospheric Chemistry and Physics* 20.2, pp. 753–770. ISSN: 1680-7324. DOI: 10.5194/acp-20-753-2020.

Thompson, A. M., R. M. Stauffer, K. Wargan, J. C. Witte, D. E. Kollonige, and J. R. Ziemke (2021). "Regional and Seasonal Trends in Tropical Ozone From SHADOZ Profiles: Reference for Models and Satellite Products". In: *Journal of Geophysical Research: Atmospheres* 126.22. ISSN: 2169-8996. DOI: 10.1029/2021jd034691.

Thouret, V., J.-P. Cammas, B. Sauvage, G. Athier, R. Zbinden, P. Nédélec, P. Simon, and F. Karcher (2006). "Tropopause referenced ozone climatology and inter-annual variability (1994–2003) from the MOZAIC programme". In: *Atmospheric Chemistry and Physics* 6.4, pp. 1033–1051. ISSN: 1680-7324. DOI: 10.5194/acp-6-1033-2006.

Thuburn, J. and G. C. Craig (2000). "Stratospheric Influence on Tropopause Height: The Radiative Constraint". In: *Journal of the Atmospheric Sciences* 57.1, pp. 17–28. ISSN: 1520-0469. DOI: 10.1175/1520-0469(2000)057<0017:siotht>2.0.co;2.

Tiedtke, M. (1989). "A Comprehensive Mass Flux Scheme for Cumulus Parameterization in Large-Scale Models". In: *Monthly Weather Review* 117.8, pp. 1779–1800. ISSN: 1520-0493. DOI: 10.1175/1520-0493(1989)117<1779:acmfsf>2.0.co;2.

Tilmes, S., L. L. Pan, P. Hoor, E. Atlas, M. A. Avery, T. Campos, L. E. Christensen, G. S. Diskin, R.-S. Gao, R. L. Herman, E. J. Hintsa, M. Loewenstein, J. Lopez, M. E. Paige, J. V. Pittman, J. R. Podolske, M. R. Proffitt, G. W. Sachse, C. Schiller, H. Schlager, J. Smith, N. Spelten, C. Webster, A. Weinheimer, and M. A. Zondlo (2010). "An aircraft-based upper troposphere lower stratosphere O3, CO, and H2O climatology for the Northern Hemisphere". In: *Journal of Geophysical Research: Atmospheres* 115.D14. ISSN: 0148-0227. DOI: 10.1029/2009jd012731.

Tost, H., P. Jöckel, A. Kerkweg, R. Sander, and J. Lelieveld (2006a). "Technical note: A new comprehensive SCAVenging submodel for global atmospheric chemistry modelling". In: *Atmospheric Chemistry and Physics* 6.3, pp. 565–574. ISSN: 1680-7324. DOI: 10.5194/acp-6-565-2006.

Tost, H., P. Jöckel, and J. Lelieveld (2006b). "Influence of different convection parameterisations in a GCM". In: *Atmospheric Chemistry and Physics* 6.12, pp. 5475–5493. ISSN: 1680-7324. DOI: 10.5194/acp-6-5475-2006.

Tost, H., P. Jöckel, and J. Lelieveld (2007). "Lightning and convection parameterisations – uncertainties in global modelling". In: *Atmospheric Chemistry and Physics* 7.17, pp. 4553–4568. ISSN: 1680-7324. DOI: 10.5194/acp-7-4553-2007.

Tost, H., M. G. Lawrence, C. Brühl, and P. Jöckel (2010). "Uncertainties in atmospheric chemistry modelling due to convection parameterisations and subsequent scavenging". In: *Atmospheric Chemistry and Physics* 10.4, pp. 1931–1951. ISSN: 1680-7324. DOI: 10.5194/acp-10-1931-2010.

Tost, H. (2006). "Global Modelling of Cloud,Convection and Precipitation Influenceson Trace Gases and Aerosols". PhD thesis. Rheinischen Friedrich-Wilhelms-Universität Bonn. URL: https://d-nb.info/982575963/34.

Tummon, F., B. Hassler, N. R. P. Harris, J. Staehelin, W. Steinbrecht, J. Anderson, G. E. Bodeker, A. Bourassa, S. M. Davis, D. Degenstein, S. M. Frith, L. Froidevaux, E. Kyrölä, M. Laine, C. Long, A. A. Penckwitt, C. E. Sioris, K. H. Rosenlof, C. Roth, H.-J. Wang, and J. Wild (2015). "Intercomparison of vertically resolved merged satellite ozone data sets: interannual variability and long-term trends". In: *Atmospheric Chemistry and Physics* 15.6, pp. 3021–3043. ISSN: 1680-7324. DOI: 10.5194/acp-15-3021-2015.

Turhal, K., F. Plöger, J. Clemens, T. Birner, F. Weyland, P. Konopka, and P. Hoor (2024). "Variability and trends in the potential vorticity (PV)-gradient dynamical tropopause". In: *Atmospheric Chemistry and Physics* 24.23, pp. 13653–13679. ISSN: 1680-7324. DOI: 10.5194/acp-24-13653-2024.

Ueyama, R., M. Schoeberl, E. Jensen, L. Pfister, M. Park, and J.-M. Ryoo (2023). "Convective Impact on the Global Lower Stratospheric Water Vapor Budget". In: *Journal of Geophysical Research: Atmospheres* 128.6. ISSN: 2169-8996. DOI: 10.1029/2022jd037135.

Vogel, B., G. Günther, R. Müller, J.-U. Grooß, A. Afchine, H. Bozem, P. Hoor, M. Krämer, S. Müller, M. Riese, C. Rolf, N. Spelten, G. P. Stiller, J. Ungermann, and A. Zahn (2016). "Long-range transport pathways of tropospheric source gases originating in Asia into the northern lower stratosphere during the Asian monsoon season 2012". In: *Atmospheric Chemistry and Physics* 16.23, pp. 15301–15325. ISSN: 1680-7324. DOI: 10.5194/acp-16-15301-2016.

Wagenhäuser, T., A. Engel, H. Bönisch, E. Ray, H. Garny, and F. Voet (2024). *AtmosphericAngels/AoA_from_convolution: Software version as used in Garny et al. 2024*. DOI: 10.5281/ZENODO.11127613.

Wang, X., Y. Wu, W.-w. Tung, J. H. Richter, A. A. Glanville, S. Tilmes, C. Orbe, Y. Huang, Y. Xia, and D. E. Kinnison (2018). "The Simulation of Stratospheric Water Vapor Over the Asian Summer Monsoon in CESM1(WACCM) Models". In: *Journal of Geophysical Research: Atmospheres* 123.20. ISSN: 2169-8996. DOI: 10.1029/2018jd028971.

Wang, Y., J. A. Logan, and D. J. Jacob (1998). "Global simulation of tropospheric O3-NOx-hydrocarbon chemistry: 2. Model evaluation and global ozone budget". In: *Journal of Geophysical Research: Atmospheres* 103.D9, pp. 10727–10755. ISSN: 0148-0227. DOI: 10.1029/98jd00157.

Weyland, F., P. Hoor, D. Kunkel, T. Birner, F. Plöger, and K. Turhal (2025). "Long-term changes in the thermodynamic structure of the lowermost stratosphere inferred from reanalysis data". In: *Atmospheric Chemistry and Physics* 25.2, pp. 1227–1252. ISSN: 1680-7324. DOI: 10.5194/acp-25-1227-2025.

Wilks, D. S. (2016). ""The Stippling Shows Statistically Significant Grid Points": How Research Results are Routinely Overstated and Overinterpreted, and What to Do about It". In: *Bulletin of the American Meteorological Society* 97.12, pp. 2263–2273. ISSN: 1520-0477. DOI: 10.1175/bams-d-15-00267.1.

WMO (1957). "Meteorology: A Three-Dimensional Science". In: *WMO Bulletin* IV.4, pp. 134–138.

WMO (2018). *Scientific Assessment of Ozone Depletion: 2018*. Report No. 58. Geneva, Switzerland: Global Ozone Research and Monitoring Project, p. 588. URL: https://ozone.unep.org/science/assessment/sap.

World Meteorological Organization (2022). *Scientific Assessment of Ozone Depletion: 2022*. Tech. rep. GAW Report No. 278. Geneva: World Meteorological Organization, p. 509.

Xian, T. and C. R. Homeyer (2019). "Global tropopause altitudes in radiosondes and reanalyses". In: *Atmospheric Chemistry and Physics* 19.8, pp. 5661–5678. ISSN: 1680-7324. DOI: 10.5194/acp-19-5661-2019.

Yanai, M., S. Esbensen, and J.-H. Chu (1973). "Determination of Bulk Properties of Tropical Cloud Clusters from Large-Scale Heat and Moisture Budgets". In: *Journal of the Atmospheric Sciences* 30.4, pp. 611–627. ISSN: 1520-0469. DOI: 10.1175/1520-0469(1973)030<0611:dobpot>2.0.co;2.

Zahn, A. and C. A. M. Brenninkmeijer (2003). "New directions: A chemical tropopause defined". In: *Atmospheric Environment* 37.3, pp. 439–440. URL: https://hdl.handle.net/11858/00-001M-0000-0014-8F4E-0.

Zahn, A., E. Christner, P. F. J. van Velthoven, A. Rauthe-Schöch, and C. A. M. Brenninkmeijer (2014). "Processes controlling water vapor in the upper troposphere/lowermost stratosphere: An analysis of 8 years of monthly measurements by the IAGOS-CARIBIC observatory". In: *Journal of Geophysical Research: Atmospheres* 119.19. ISSN: 2169-8996. DOI: 10.1002/2014jd021687.

Danksagung

An dieser Stelle möchte ich mich von ganzem Herzen bei Professor Anja Schmidt bedanken. Neben ihrer neuen Position als Abteilungsleitung hat sie die Rolle meiner Doktormutter übernommen. Sie hat sich immer Zeit für mich genommen, um mich sowohl bei meiner wissenschaftlichen Arbeit als auch bei meiner persönlichen Entwicklung zu unterstützen. Insbesondere bin ich ihr für die Gelegenheit dankbar, eigene Lehrerfahrung sammeln zu können.
Zudem möchte ich mich bei meinem Zweitgutachter, Professor Thomas Birner, bedanken, der mir durch sein hilfreiches und ehrliches Feedback dabei geholfen hat, meinen Blick auf mein Thema zu schärfen. Durch den Austausch im Rahmen des Projektes TPChange habe ich die spannende erste Frage meiner Dissertation gefunden.
Ein ganz besonderer Dank gilt meinem Betreuer Dr. Patrick Jöckel. Egal, wie viele Aufgaben er für das gesamte MESSy-Konsortium auf dem Zettel hatte, hatte ich immer das Gefühl, dass ich mit meinen Problemen an erster Stelle stand, seien es Fragen bei der Erstellung meiner Simulationen oder den Überblick bei der schieren Anzahl an Daten zu behalten. Zudem danke ich Patrick für seinen enormen Einsatz, der dazu geführt hat, dass mein Projekt C07 von TPChange so bewilligt wurde und ich die sehr positive Erfahrung machen konnte, Teil eines so großen Projekts zu sein.
Außerdem möchte ich mich bei Professor Martin Dameris bedanken, der mich zusammen mit Patrick in den ersten drei Jahren bis zu seinem Ruhestand betreut hat. Ich durfte ihn bei seiner Arbeit am ESA Ozone CCI Projekt unterstützen und im Anschluss sogar in seine großen Fußstapfen treten und für ihn in der folgenden Projektphase übernehmen.
Ebenso möchte ich mich bei Professor Holger Tost bedanken, der zusammen mit Patrick das TPChange Projekt C07 entworfen und mir mit seiner Erfahrung im Bereich der globalen Konvektionsmodellierung jederzeit mit Rat zur Seite gestanden hat.
Ich möchte mich bei Dr. Hella Garny bedanken, die jederzeit bereit war, meine Fragen zur Dynamik der Stratosphäre zu beantworten und mir Ratschläge zur Analyse zu geben. Ihre aktive Unterstützung bei der Betreuung meiner Arbeit hat mir sehr geholfen.
Ein besonderer Dank gilt der TPChange Community, die mich während meiner Promotion begleitet hat. In einem großen Team an den gleichen großen Fragestellungen mit verschiedenen Methoden zu arbeiten, hat die letzten Jahre sehr bereichert. Hervorheben möchte ich die Kooperation mit Johannes Degen und Dr. Frederik Harzer, die mir neue Anwendungsmöglichkeiten gezeigt haben und mit denen ich die Promotion im Rahmen von TPChange gemeinsam erleben durfte. Ich bedanke mich herzlich bei Professor Peter Hoor und Dr. Vera Bense dafür, dass sie dieses große Projekt so wunderbar geleitet haben.
Außerdem möchte ich mich beim DKRZ dafür bedanken, dass sie mir die Ressourcen auf Levante bewilligt haben, damit ich meine Simulationen wie geplant durchführen konnte. Zudem danke ich dem DKRZ User Support, insbesondere Dr. Daniel Heydebreck, die mir bei Anfragen

und Problemen mit Levante und dem SLK Archiv immer direkt weitergeholfen haben.
Außerdem möchte ich der gesamten ESM Abteilung für die gemeinsame Zeit auf und neben der Arbeit danken – für die Teepausen, die gemeinsamen Mittagessen oder die Spieleabende. Vor allem möchte ich mich für die Unterstützung und Hilfsbereitschaft bedanken, die mir alle immer entgegengebracht haben. Besonders erwähnen möchte ich Dr. Sabine Brinkop und Dr. Matthias Nützel für den wissenschaftlichen Austausch wenn ich mal wieder mehr Fragen als Antworten hatte, Dr. Bastian Kern und Dr. Kerstin Hartung für die Geduld bei meinen Fragen zu MESSy sowie die gemeinsamen Abenteuer durch Mittelerde, Dr. Franziska Winterstein, Dr. Mattia Righi und Dr. Jan Christopher Kaiser für die Entwicklung und Pflege der Software Pakete emacutils, emactuner und pa-emac, die so vielen aus ESM nützen, und Dr. Laura Stecher, für die Hilfe beim tunen meiner Simulationen mit PSrad und dem generellen Hinweisen zur Anwendung von EMAC.
Ein großer Dank gilt den lieben Kolleginnen und Kollegen, mit denen ich das Glück hatte, das Büro zu teilen: Anja, Adrienne, Anna, Dario, Ismail, Patrick und Sina. Die gegenseitige Unterstützung bei der Bearbeitung der Aufgaben, die Ablenkungen und Aufmunterungen haben meine Promotionszeit geprägt und unvergesslich gemacht.
Abschließend möchte ich mich bei meinen Freunden und meiner Familie bedanken, ohne deren emotionale Unterstützung dieses wahnsinnige Vorhaben nicht möglich gewesen wäre. Mein größter Dank gilt meiner Frau Julia, die mich auf jede noch erdenkliche Art unterstützt und an mich geglaubt hat.